University of Southampton

Faculty of Engineering and Physical Sciences

Physics and Astronomy

Design of Nanomaterials for Oligonucleotide Detection

by

Konstantina Alexaki

ORCID ID 0000-0002-8702-2696

Thesis for the degree of Doctor of Philosophy

July 2022

University of Southampton

Abstract

Faculty of Engineering and Physical Sciences

Physics and Astronomy

Thesis for the degree of Doctor of Philosophy

Design of Nanomaterials for Oligonucleotide Detection

by

Konstantina Alexaki

Nanoparticles are considered a powerful tool for novel applications ranging from imaging and sensing to therapy. In this thesis, gold nanoparticles functionalised with DNA strands were used for the detection of target oligonucleotides in live cells while upconversion nanoparticles functionalised with DNA strands were used for the detection of target oligonucleotides in a tube.

Gold nanoparticles functionalised with synthetic DNA oligonucleotides were used to identify and sort skeletal stem cells upon specific mRNA detection. Human bone marrow stromal cells include a population of skeletal stem cells, with the capacity to differentiate along the osteogenic, adipogenic, and chondrogenic lineages. According to current techniques, the isolation and enrichment of skeletal stem cells from human tissues face challenges when there is no specific skeletal stem cell marker. DNA functionalised AuNPs were able to detect skeletal stem cells based on endocellular mRNA expression and to rapidly sort these cells from human bone marrow. This is a significant approach for tissue engineering as skeletal stem cells can be harnessed to help bone regeneration.

The enhancement of the endosomal escape of DNA functionalised gold nanoparticles *via* the incorporation of a cell-penetrating peptide has been studied in order to maximize the concentration of gold nanoparticles that can detect mRNA and therefore reduce their total amount when incubating with cells. Two different approaches for the functionalisation of gold nanoparticles' surfaces with peptides are presented. In the first case, gold nanoparticles were functionalised with thiol terminated DNA strands followed by functionalisation with cysteine terminated cell-penetrating peptides. In the second instance, the peptide was conjugated on the 5' end of the DNA strand. Then, the gold nanoparticles were modified with these conjugate sequences. All the above probes exhibited similar stability towards degradation by endocellular enzymes and similar specificity towards the detection of specific mRNA targets.

Finally, the fabrication of an oligonucleotide sensor was developed based on the emissive optical properties of oligonucleotide-coated lanthanide-doped upconversion nanoparticles and the quenching ability of two-dimensional materials; MoS_2, WS_2 and graphene oxide. In the first system, it was investigated the development of an upconversion nanoparticles sensor that detected polyA sequences and used the two-dimensional materials, MoS_2 and WS_2, as quenchers. In the second system, the fabrication of a DNA sensor for SARS-CoV-2 oligonucleotide detection was demonstrated while in this case, graphene oxide was the quencher. In both cases, monodisperse upconversion nanoparticles were functionalised with single-stranded DNA. In the presence of a complementary oligonucleotide target and the formation of double-stranded DNA, the upconversion nanoparticles could not interact with two-dimensional materials, thus retaining their fluorescence properties. The high sensitivity and specificity of this sensor to detect specific target oligonucleotides were also monitored.

Table of Contents

Table of Tables

Table of Figures

Table of Equations

Research Thesis: Declaration of Authorship

Print name: Konstantina Alexaki

Title of thesis: Design of Nanomaterials for Oligonucleotide Detection

I declare that this thesis and the work presented in it are my own and has been generated by me as the result of my own original research.

I confirm that:

1. This work was done wholly or mainly while in candidature for a research degree at this University;
2. Where any part of this thesis has previously been submitted for a degree or any other qualification at this University or any other institution, this has been clearly stated;
3. Where I have consulted the published work of others, this is always clearly attributed;
4. Where I have quoted from the work of others, the source is always given. With the exception of such quotations, this thesis is entirely my own work;
5. I have acknowledged all main sources of help;
6. Where the thesis is based on work done by myself jointly with others, I have made clear exactly what was done by others and what I have contributed myself;
7. Parts of this work have been published as:

Articles in Academic Press:

1) Alexaki, Konstantina; Kyriazi, Maria-Eleni; Greening, Joshua; Taemaitree, Lapatrada; El-Sagheer, Afaf; Brown, Tom; Zhang, Xunli; Muskens, Otto L. and Kanaras, Antonios G. "A SARS-CoV-2 sensor based on upconversion nanoparticles and graphene oxide", *RSC Advances* 12, 18445-18449 (2022); DOI: https://doi.org/10.1039/D2RA03599E

2) Xavier, Miguel; Kyriazi, Maria-Eleni; Lanham, Stuart; Alexaki, Konstantina; Matthews, Elloise; El-Sagheer, Afaf H.; Brown, Tom; Kanaras, Antonios G. and Oreffo, Richard O. C. "Enrichment of Skeletal Stem Cells from Human Bone Marrow Using Spherical Nucleic Acids", *ACS Nano* 15 (4), 6909-6916 (2021); DOI: https://doi.org/10.1021/acsnano.0c10683

3) Alexaki, Konstantina; Giust, Davide; Kyriazi, Maria-Eleni; El-Sagheer, Afaf H.; Brown, Tom; Muskens, Otto L. and Kanaras, Antonios G.

"A DNA Sensor Based on Upconversion Nanoparticles and Two-Dimensional Dichalcogenide Materials", *Frontiers of Chemical Science and Engineering* 15, 935-943 (2021); DOI: https://doi.org/10.1007/s11705-020-2023-9

4) Matthews, Elloise; Lanham, Stuart; White, Kate; Kyriazi, Maria-Eleni; Alexaki, Konstantina; El-Sagheer, Afaf H.; Brown, Tom; Kanaras, Antonios G.; West, Jonathan; MacArthur, Ben D.; Stumpf, Patrick S. and Oreffo, Richard O. C.
"Single Cell RNA Sequence Analysis of Human Bone Marrow Samples Reveals New Targets for Isolation of Skeletal Stem Cells using DNA-coated Gold Nanoparticles", *bioRxiv* 2020.06.17.156836; DOI: https://doi.org/10.1101/2020.06.17.156836

5) Alexaki, Konstantina; Kyriazi, Maria-Eleni; El-Sagheer, Afaf H.; Brown, Tom and Kanaras, Antonios G.
"Engineering functional nanoparticles for delivery in cells", Proc. SPIE 11255, Colloidal Nanoparticles for Biomedical Applications XV, 112550K (21 February 2020); DOI: https://doi.org/10.1117/12.2538470

Posters:

1) NaNaX 9 (September 2019, Hamburg, Germany)

Signature: Date: 04/07/2022

Acknowledgements

Firstly, I would like to thank my supervisor Prof. Antonios Kanaras for giving me the opportunity to carry out my PhD research project in his group and to develop a great toolkit of skills such as the preparation of academic journals and the mentoring of MSc students. My great appreciation for his guidance and advice throughout my PhD programme as well as for his time for reading my drafts and thesis.

I would also like to thank the School of Physics and Astronomy for the Mayflower studentship.

My thanks and appreciation to the entire Biomedical Imaging Unit and PCD team from the University Hospital of Southampton. Especially, I would like to thank James Thompson, Lizzie West, Regan Doherty, Janice Coles, Dr Anton Page, Patricia Goggin and Dr Peter Lackie for teaching and helping me with the cell cultures and the imaging techniques. Special thanks to Dr Dave Johnston for the confocal sessions and for always being available to teach microscopy-related topics.

I would like to thank Prof. Tom Brown and Dr Afaf El-Sagheer who have synthesised all the oligonucleotides used in this thesis as well as provided scientific advice in the process of oligonucleotide design. This project would not have been possible without them.

Many thanks to Prof. Otto Muskens for allowing me to use his laser lab and for his scientific support on photonic topics.

I would like to thank Prof. Richard Oreffo and his group for the collaboration on the project for the use of spherical nucleic acids in the enrichment of skeletal stem cells from human bone marrow as well as for providing me with the SAOS-2 cell line.

A big thank you to all the present and previous members of the LICNA group as well as the people from the 2nd floor of Chemistry: Doxi, Elena, Toni, Pete, Joshua, James, Tom, Molly and Maria. I would like to thank my friends Maribel and Angela for their support and help. I am so grateful for our friendship and all you have taught me in the lab. Thank you very much Vikesh, Dan, Joseph and Hiroki for making the long hours in the lab so much fun! My thanks and appreciation to Marilena for her constant guidance and help throughout my PhD programme.

I am so grateful for meeting Magda, Loukas and Wilma during this PhD journey. My life in Soton wouldn’t be the same without your friendship and support. I would like to thank my precious friends Ntina, Efi and Ioanna for always being an inspiration. A big thanks to my friends Elena, Angelos, Antonia, Christina, Maria, Vangelis and Michalis. A special thank you to my friends Eva, Nikos, Evi and Andreas for their help and support. Katerina, Sakis, Cilia, Nikos and little Dioni; I’m so lucky to have you in my life. You will always be my mentors. I would also like to thank my cousins Charis, Konstantinos, Dora and Efi for their love and support throughout the years. My dearest friends Angeliki, Christos, Orsalia, Maria and Dimitra thank you; I’m so proud to have you in my life. You are the most caring and supportive friends that someone can have. My deepest gratitude to my best friend Olia. Thank you for being my *sister* since I remember myself.

I'm eternally grateful to the most inspiring and kind person; my partner Panagiotis. Your love and support cannot be described in words. I couldn't have done it without you.

Finally, I would like to thank my brother Dimitris for being my friend for life that I will always love and admire. Thank you to my amazing parents, Thomas and Anastasia, for their unconditional love and support in everything in my life – μαμά και μπαμπά σας αγαπώ και σας ευχαριστώ για όλα!

στην Αννούλα –

τον άνθρωπο που με έφερε σε επαφή

με επιστημονικό εργαστήριο

για πρώτη φορά –

θα σε θυμάμαι για πάντα

Definitions and Abbreviations

^{o}C	degree Celsius
3D	three-dimensional
A	adenine
a.u.	arbitrary units
AMP	antimicrobial peptide
APS	ammonium persulfate
Ar	argon
AR	aspect ratio
ATP	adenosine triphosphate
Au	gold
AuNPs	gold nanoparticles
AuNRs	gold nanorods
BLAST	Basic Local Alignment Search Tool
BM	bone marrow
BMSCs	bone marrow stromal cells
BSPP	bis(p-sulfonatophenyl) phenyl phosphine dehydrate dipotassium salt
c	concentration
C	cytosine
cDNA	complementary deoxyribonucleic acid
CFU-Fs	colony-forming units fibroblastic cells
cm	centimetre (10^{-2} metre)
CR	cross-relaxation upconversion
CTAB	cetyltrimethylammonium bromide
Da	Dalton
DDA	discrete dipole approximations
DLS	dynamic light scattering

Definitions and Abbreviations

DLVO theory	Derjaguin, Landau, Verwey and Overbeek theory
DMEM	Dulbecco's modified eagle medium
DMF	dimethylformamide
DMSO	dimethyl sulfoxide
DNA	deoxyribonucleic acid
DNase	deoxyribonuclease
dsDNA	double-stranded deoxyribonucleic acid
EDC	N-(3-(dimethylamino)propyl)-N’-ethylcarbodiimide hydrochloride
EDTA	(ethylenedinitrilo)tetraacetic acid
EMT	epithelial to mesenchymal transition
ESA	excited state absorption
EtOH	ethanol
ETU	energy transfer upconversion
FACS	fluorescence activated cell sorting
FBS	fetal bovine serum
FDTD method	finite-difference-time-domain method
fM	femtomolar (10^{-15} molar)
FRET	Förster resonance energy transfer
fs	femtosecond
FT-IR	Fourier-transform infrared
G	guanine
g/mol	grams per mole
GO	graphene oxide
h	hour
HBSS	Hank’s balanced salt solution
HSCs	hematopoietic stem cells
kV	kilo Volt
LSPR	local surface plasmon resonance

M	molar
MACS	magnetic activated cell sorting
MEM	minimum essential medium
MeOH	methanol
MES buffer	4-morpholineethanesulfonic acid buffer
MET	mesenchymal to epithelial transition
mg	milligram (10^{-3} gram)
min	minute
mL	millilitre (10^{-3} litre)
mm	millimetre (10^{-3} metre)
mM	millimolar (10^{-3} molar)
mmol	millimole (10^{-3} mole)
mol	mole
mRNA	messenger ribonucleic acid
MSCs	mesenchymal stem/stromal cells
mW	milliwatt (10^{-3} watt)
MW	molecular weight
NaCl	sodium chloride
NCBI	National Centre for Biotechnology Information
NLS	nuclear localisation signal
nm	nanometre (10^{-9} metre)
nM	nanomolar (10^{-9} molar)
O.D.	optical density
PAA	poly(acrylic acid)
PAGE	polyacrylamide gel electrophoresis
PAMAM	poly(amidoamine)
PBS	phosphate buffer saline
PEI	polyethylenimine

pH	potential hydrogen
PIPES	piperazine-N,N′-bis(2-ethanesulfonic acid)
pM	picomolar (10^{-12} molar)
pmol	picomole (10^{-12} mole)
PVP	polyvinylpyrrolidone
RE	rare earth
RNA	ribonucleic acid
RPA	ribonuclease protection assay
rpm	revolutions per minute
RT-PCR	real-time reverse transcription-polymerase chain reaction
s	second
s/v	surface to volume
SDS	sodium dodecyl sulphate
SNAs	spherical nucleic acids
SR-A	scavenger receptor class A
SSCs	skeletal stem cells
ssDNA	single-stranded deoxyribonucleic acid
sulfo-NHS	N-hydroxysulfosuccinimide sodium salt
T	thymine
TBE	Tris Borate EDTA
TEAB	triethylammonium bicarbonate
TEM	transmission electron microscopy
TEMED	N, N, N', N'-tetramethylethylenediamine
THF	tetrahydrofuran
T_m	melting temperature
UCNPs	upconversion nanoparticles
UV-Vis	ultraviolet-visible
VDW	Van der Walls

XRD	X-ray diffraction
µL	microlitre (10^{-6} litre)
µm	micrometre (10^{-6} metre)
µM	micromolar (10^{-6} molar)

Chapter 1 Introduction

In recent years nanotechnology has become one of the most exciting and important forefront fields. Nanotechnology is referred to the design, characterisation, production and application of materials that belong to the nanoscale which is about 1 to 100 nanometers [1]. Nanoscale particles are considered an important class of nanomaterials and have attracted considerable attention as a valuable tool for various novel applications ranging from imaging and sensing to therapy [2-4].

Among the various noble metal nanoparticles, gold nanoparticles (AuNPs) are the most extensively studied and well-established due to their size- and shape-dependant optical, electronic and thermal properties [5-7]. They can also be modified with a variety of chemical functional groups such as thiols, phosphines and amines, which exhibit affinity for gold surface [8]. By using these functional groups to anchor the ligands, additional moieties such as oligonucleotides, peptides and antibodies can offer even greater functionality to AuNPs' surface [9].

Lanthanide-doped upconversion nanoparticles (UCNPs) are a widely used type of nanoparticles that can turn lower energy photons into higher energy photons. Their unique properties such as chemical stability, narrow emission bands, absence of photobleaching and multiband emission make them suitable for many applications such as bioassays, biomedical imaging and photodynamic therapy [10]. Moreover, UCNPs can be easily functionalised by linking specific targeting ligands such as oligonucleotides, peptides or antibodies to their surface and can be used as probes to detect specific targets with high sensitivity and selectivity [11, 12].

The aim of the research presented in this thesis has focused on the synthesis and functionalisation of AuNPs and UCNPs with oligonucleotides for the detection of biomolecules.

In detail, in order to identify and sort skeletal stem cells upon specific mRNA detection, AuNPs functionalised with synthetic DNA oligonucleotides were used in live cells. Skeletal stem cells with the ability to differentiate along the osteogenic, adipogenic, and chondrogenic lineages are present in human bone marrow stromal cells. The isolation and enrichment of skeletal stem cells from human tissues are currently difficult due to the lack of a unique skeletal stem cell marker. Based on endocellular mRNA expression, DNA functionalised AuNPs could effectively sort skeletal stem cells from human bone marrow.

Then, in order to increase the concentration of AuNPs that can detect mRNA and subsequently decrease their total amount when incubating with cells, the enhancement of the endosomal escape of DNA functionalised AuNPs by the incorporation of a cell-penetrating peptide has been investigated. Two methods for functionalising the surfaces of AuNPs with peptides are demonstrated. In the first case, thiol-terminated DNA strands were used to functionalize AuNPs, and then cell-penetrating peptides containing cysteine ends were used. In the second case, the peptide was conjugated on the 5’ end of the DNA strand, and then these conjugate sequences were attached to the AuNPs' surface.

Also, an oligonucleotide sensor was designed based on the emissive optical properties of oligonucleotide-coated UCNPs and the quenching ability of two-dimensional materials; MoS_2, WS_2 and graphene oxide. The fabrication of a UCNPs sensor that detected polyA sequences and utilised the two-dimensional materials, MoS_2 and WS_2, as quenchers was examined. In the second system, the development of a DNA sensor for SARS-CoV-2 oligonucleotide detection was performed by using graphene oxide as the quencher. Monodisperse UCNPs were functionalised with single-stranded DNA in both systems. The formation of double-stranded DNA in the presence of a complementary oligonucleotide target, prevented the UCNPs from interacting with two-dimensional materials, maintaining their fluorescent characteristics. In both cases, the sensor's sensitivity and specificity for detecting specific target oligonucleotides were observed.

Chapter 3 includes all the experimental procedures for the synthesis and surface modification of nanoparticles. The techniques used for the characterisation of nanomaterials and experimental details for the cell culture studies are also presented in this chapter.

Chapter 4 discusses the results for the synthesis of various types of colloidal nanoparticles such as spherical AuNPs, gold nanorods (AuNRs) and branched AuNPs as well as core and core-shell UCNPs. Modified synthetic protocols have been used for the synthesis of these biocompatible nanoparticles. The synthesis of highly monodisperse particles with precise control over size, shape and surface chemistry is of utmost importance for the fabrication of functional nanomaterials.

Chapter 5 presents the design of DNA functionalised AuNPs and their ability to identify and sort skeletal stem cells (SSCs) upon specific mRNA detection. Human bone marrow stromal cells (BMSCs) contain a population of SSCs, with the capacity to differentiate along the osteogenic, adipogenic, and chondrogenic lineages. Since current methods to isolate and enrich SSCs from human tissues remain challenging when there is no specific SSC marker, DNA functionalised AuNPs are able to detect and sort SSCs displaying specific mRNA signatures as well as enable their use in clinical therapies.

Chapter 6 demonstrates a new design strategy to enhance the endosomal escape of DNA functionalised AuNPs *via* the incorporation of a cell-penetrating peptide that facilitates effective escape within cells. DNA coated AuNPs are suitable tools for sensing applications as they can detect specific targets *in vitro* and *in vivo*. However, a common barrier in nanoparticle delivery methods is endosomal entrapment. Two different types of surface functionalisation with peptides are presented in this chapter. In the first case, AuNPs have been firstly modified with thiol terminated DNA strands and then with cysteine terminated cell-penetrating peptides. In the second case, the peptide has been conjugated on the 5’ end of the DNA strand and then the functionalisation of AuNPs with these conjugate sequences follows. The aforementioned probes show similar stability towards degradation by endocellular enzymes and similar specificity towards the detection of specific mRNA targets.

Chapter 7 presents a sensor that combines the emissive optical properties of UCNPs and the quenching ability of two-dimensional materials for the detection of biomolecules. The detection of DNA and RNA biomolecules is of increasing interest in order to monitor different biological processes such as protein production, gene regulation and various diseases such as cancer [13-15]. Then, the fabrication of a UCNPs sensor that detects polyA sequences and uses two-dimensional materials (MoS_2 and WS_2) as quenchers is investigated. Moreover, during the COVID-19 pandemic, the development of a DNA sensor for SARS-CoV-2 oligonucleotide detection was significantly important. The ability of oligonucleotide coated UCNPs to detect a DNA target and SARS-CoV-2 oligonucleotides is demonstrated.

Chapter 2 Theoretical Background

The research presented in this thesis focuses on the synthesis and functionalisation of AuNPs and UCNPs with oligonucleotides for the detection of biomolecules. This chapter provides relevant theoretical background information about the materials and techniques used in this project. **Section 2.1** discusses the basic principles of AuNPs and UCNPs preparation while their unique optical properties are presented in **Section 2.2**. This is followed by a general overview of the structure and properties of oligonucleotides and cell-penetrating peptides in **Section 2.3** and **Section 2.4**, respectively. **Section 2.5** demonstrates the surface modification of spherical AuNPs with oligonucleotides and further modifications with cell-penetrating peptides, as well as the surface functionalisation of UCNPs with oligonucleotides. Finally, **Section 2.6** discusses how spherical AuNPs can be used within live cells for mRNA detection and imaging.

2.1 Colloidal Nanoparticles

Wet chemistry methods provide versatile routes for the synthesis of monodispersed colloidal suspensions of nanoparticles with various compositions, sizes and shapes. The synthetic approaches and detailed reaction mechanisms involved in the synthesis of gold and upconversion nanoparticles are presented in this section.

2.1.1 Synthesis of gold nanoparticles

It is still vague when humans first began to exploit nanosized materials. In the fourth century A.D., Roman glassmakers were fabricating glasses containing nanosized metals. The Lycurgus cup is an artefact from this period that resides in the British Museum in London. This cup, which depicts the death of King Lycurgus, is made from soda-lime glass containing Ag and AuNPs. When a light source is placed inside it, the colour of the cup changes from green to a deep red [16]. Then, the presence of metal nanoparticles in the glass offers a great variety of colours in the windows of medieval cathedrals. The first systematic study of the synthesis and colours of colloidal AuNPs dating back to 1857 was reported by Michael Faraday [17]. Over a century later, Turkevich developed a new method to synthesise AuNPs based on the reduction of gold salt with citrate which was further refined by Frens in 1973 and Schultz in 2014 [18-21].

The most widely applied method for the synthesis of monodisperse spherical AuNPs with an average diameter of 15 nm, is the citrate reduction method. This method involves the reduction of an aqueous solution of sodium tetrachloroaurate ($NaAuCl_4$) by an aqueous solution of trisodium citrate (see **Section 3.1.1** for synthetic protocol). The size of the resulting nanoparticles can be tuned by mixing both solutions at 100 °C in different molar ratios [20, 22]. This reaction relies on the use of trisodium citrate as a reducing agent and capping ligand, providing increased stability to the formed nanoparticles [21, 22]. The proposed mechanism behind the formation of colloidal AuNPs involves a multistep reaction as seen in **Figure 2.1** [23].

(A) RedOx reaction between citrate and gold precursor

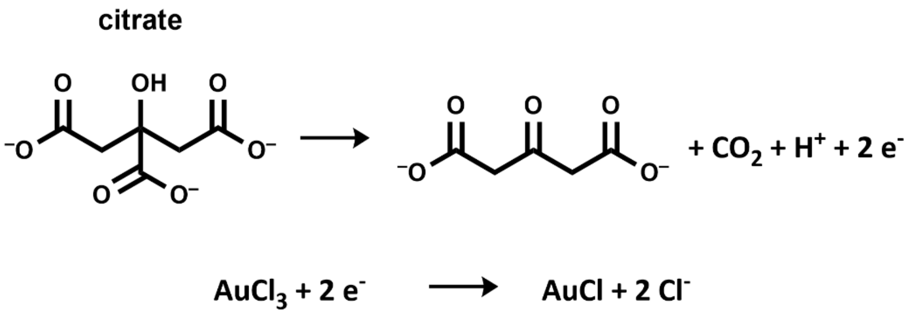

(B) Complexation of gold chloride and acetone dicarboxylate anion

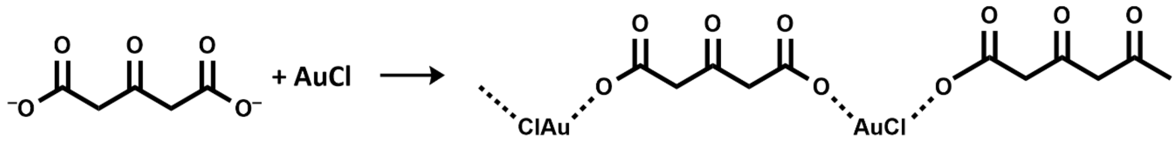

(C) Decomposition of acetone dicarboxylate

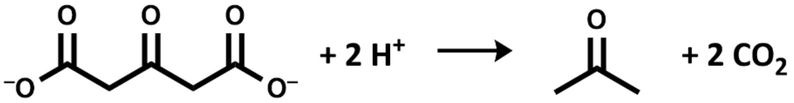

(D) RedOx reaction between acetone and $AuCl_3$ and disproportionation of AuCl into Au^0

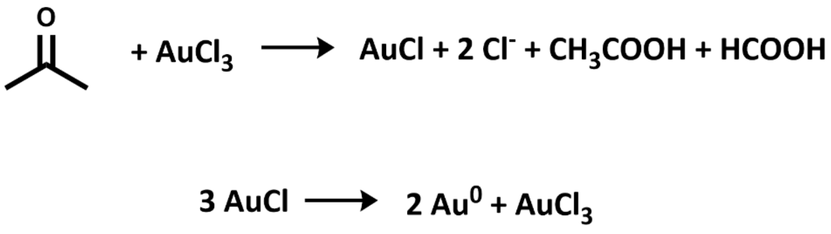

Figure 2.1 Reaction mechanism of the reduction of gold precursors by citrate for the synthesis of AuNPs. In the initial step (**A**), the gold salt is reduced by the citrate precursor. In the second step (**B**), a complex between gold chloride and acetone dicarboxylate anion is formed. In the third step (**C**), acetone dicarboxylate is decomposed into acetone. In the final step (**D**), the disproportionation of AuCl into Au^0 and $AuCl_3$ occurs. Adapted from reference [24].

The initial step of this process involves the oxidation of citrate into acetone dicarboxylate and the simultaneous reduction of Au^{3+} precursor into Au^{1+} to form gold monochloride (AuCl) (see **Figure 2.1 Reaction A**). In the second step, complexes between dicarboxylate anions and AuCl are formed (see **Figure 2.1 Reaction B**). These complexes then coagulate into precursors followed by the disproportionation of AuCl into gold nuclei (Au^0) (see **Figure 2.1 Reaction D**). The nuclei promote an autocatalytic reaction with AuCl molecules, which are absorbed onto the nuclei leading to nanoparticle growth. The surface of the nanoparticles is covered loosely by excess citrate ions providing colloidal stability against irreversible aggregation phenomena [25].

The formation of nanoparticles is based on the formation of nuclei and then the growth of the nuclei into nanoparticles of the desired size. The simultaneous formation of all the nuclei and the absence of secondary nucleations are essential for the synthesis of nanoparticles with a narrow size distribution. Privman and co-workers reported that AuNPs' monodispersity is dependent on rapid coagulation [26]. Then, Xia *et al*. showed that a rapid formation of acetone dicarboxylate promoted rapid coagulation and hence monodisperse particles [24]. According to **Figure 2.1 Reaction C**, in a side reaction, acetone dicarboxylate is decomposed into acetone. This decomposition is enhanced at high temperatures and pH as demonstrated by Privman and co-workers [26]. **Figure 2.1 Reaction D** demonstrates that acetone can also reduce the gold precursor (Au^{3+}) [27]. This leads to further nucleation events at different time points resulting in particles with a wide size distribution. However, Kumar *et al*. presented that this side reaction (**Figure 2.1 Reaction C**) is slower compared to the citrate reaction (**Figure 2.1 Reaction A**) and only affects the growth process when low citrate concentrations are used [23].

The role of citrate in this reaction is three-fold according to Ji and co-workers [22]. It acts as a reducing agent inducing the formation of Au^{1+} from Au^{3+}, a capping agent in particle stabilisation by electrostatically binding to the surface and a pH modulator influencing the reaction kinetics. In more detail, pH plays an important role in the reaction as pH changes lead to two different reaction pathways for the AuNPs formation. At low pH, the nucleation is very fast and results in small highly reactive nuclei that grow to bigger structures. This is a common mechanism at low pH where the citrate is fully protonated and its ability to bind the nanoparticles’ surface is reduced affecting the electrostatic stabilisation of AuNPs. At higher pH, the nucleation is slower and the slow growth that follows leads to uniform spherical nanoparticles (**Figure 2.2**).

$$C_6H_5O_7^{3-} + H_2O \rightleftharpoons C_6H_6O_7^{2-} + OH^- \qquad pKa = 6.4$$

$$C_6H_6O_7^{2-} + H_2O \rightleftharpoons C_6H_7O_7^{-} + OH^- \qquad pKa = 4.8$$

$$C_6H_7O_7^{-} + H_2O \rightleftharpoons C_6H_8O_7 + OH^- \qquad pKa = 3.2$$

Figure 2.2 Citrate protonation equilibrium reactions. Citrate can be found in different protonation states at different pH values, hence its ability as a capping agent is pH-dependent. The three pKa values of citric acid are 3.2, 4.8, and 6.4. Adapted from reference [21].

The major drawback of the Turkevich method is the synthesis of nanoparticles with a narrow size distribution only in the range of 10 to 20 nm. Larger nanoparticles can be synthesised by varying the reaction conditions (pH, citrate to gold salt molar ratio), however, the resulting particles have wide size distributions and non-uniform shapes, such as triangles and ellipsoids [28]. To face this challenging issue, a seeding mediated synthesis strategy based on separating nucleation and growth has been developed for the synthesis of larger monodisperse AuNPs [29-31]. This synthetic method is based on the growth of Au seeds *via* the reduction of Au^{3+} to Au^{1+} using a mild reducing agent. The reaction conditions of the nanoparticles' growth need to be carefully controlled to avoid secondary nucleation and wide size distribution. In this approach, small spherical Au seeds are synthesised at 100 ^{o}C *via* the citrate reduction method. The enlargement of these Au seeds and subsequently the formation of larger AuNPs happen when the temperature is lowered to 90 °C and more gold and citrate precursors are added. By decreasing the reaction temperature to 90 ^{o}C the formation of new seeds is prevented since the citrate reduction ability is remarkably lower at a temperature below 100 ^{o}C. The use of weak reducing agents such as ascorbic acid and hydroxylamine was proposed by Brown *et al*. for the synthesis of larger AuNPs [30]. However, the synthesised nanoparticles of this method were rod-shaped particles [30, 32, 33]. The need for further improvements in this protocol was covered by Murphy and Liz-Marzan groups who synthesised uniform spherical nanoparticles by using ascorbic acid and cetyltrimethylammonium bromide (CTAB) as a cationic surfactant. The synthesised AuNPs were up to 180 nm in size with narrow size distributions [34, 35]. CTAB offers precise control of the synthesis of nanoparticle morphology and binds strongly to the AuNPs' surface. This limits the further functionalisation of the surface or the replacement of the CTAB with thiol terminated ligands. The next step to face this issue was realised by Bastus and co-workers by proposing a kinetically controlled synthesis of up to 200 nm sized particles *via* the use of citrate as a mild reducing agent [29]. By adjusting the ratio between Au seeds and added Au precursor, as well as the concentration of added citrate, new nucleation events or irregular growth due to Ostwald ripening, were prevented. According to the Ostwald ripening phenomenon, smaller particles in solution dissolve and deposit on larger particles to reach a more thermodynamically stable state wherein the surface-to-area ratio is minimised [36]. Moreover, Bastus and co-workers managed to get a narrower size distribution of citrate stabilised spherical nanoparticles by lowering the temperature to 90 °C and controlling the amount of gold precursor added by successive injections [29].

2.1.2 Synthesis of gold nanorods

A seed mediated synthetic route has been followed for the synthesis of AuNRs as it leads to tunable-aspect ratio nanoparticles and high nanoparticle uniformity (see **Section 3.1.3** for synthetic protocol) [37, 38]. The mechanism for the synthesis of AuNRs is still not clear and it can be categorised into two synthetic paths depending on the presence of Ag^+ ions [39, 40]. In the absence of Ag^+ ions, growth is caused by the preferential binding of CTAB to the specific crystal facets of the Au seed. The surfactant CTAB preferentially binds to the (100) facet more strongly than to other facets and as a result, newly reduced Au atoms deposit on the available (111) facet resulting in structure elongation along the (100) direction. In the presence of Ag^+ ions, preferential reduction to Ag atoms occurs on the AuNR side due to underpotential deposition [41]. The deposition of Au atoms is blocked as a strong interaction is formed between the deposited Ag atoms and the Br^- ions of CTAB. Therefore the Au seeds will grow along the longitudinal direction. Jana *et al*. have first introduced the seed mediated protocol for the synthesis of AuNRs [37]. A two-step procedure was followed where citrate stabilised AuNPs (2 – 3 nm in diameter) were synthesised and used as seeds and then a strong reducing agent ($NaBH_4$) in the presence of citrate was used for the gold salt reduction (**Figure 2.3**). The second step involved the growth by adding the citrate stabilised seeds into the growth solution containing CTAB, ascorbic acid, gold salt and silver nitrate. Nevertheless, the product of this synthesis contained a large portion of spherical nanoparticles apart from AuNRs. Nikoobakht and co-workers improved this protocol by replacing the citrate with CTAB during seed synthesis [42]. Also, the nanorod aspect ratio could be controlled by tuning the Ag^+ ion concentration in the growth solution. After these adjustments, a detailed mechanism for the nanorod formation was presented by Orendorff *et al*. where $AuCl^{4-}$ bound to CTAB formed $AuCl^{2-}$ *via* the reduction of Au^{3+} to Au^+ due to the addition of ascorbic acid. The collision of $AuCl^{2-}$ - CTAB complexes with CTAB-protected seed particles led to the formation of growing Au particles. The rate of the nanorod growth was determined by the frequency of collisions. The fast deposition of silver on the (110) facet was followed by strong CTAB binding that hindered the gold growth on the side of the rods and led to preferential growth at the ends [40].

$$2\ AuCl_4^- + 2\ Na^+ + 18\ H_2O + 6\ NaBH_4 \longrightarrow 2\ Au^0 + 8\ NaCl + 21\ H_2\uparrow + 6\ B(OH)_3$$

Figure 2.3 Reduction of the gold precursor with sodium borohydride.

2.1.3 Synthesis of branched gold nanoparticles

Branched AuNPs have an anisotropic structure and tunable optical properties similar to AuNRs [43-46]. The growth mechanism for the branched AuNPs is quite challenging since anisotropic growth must be initiated at multiple sites of seed and maintained to form branched arms with controlled lengths (see **Section 3.1.4** for synthetic protocol). There are two proposed mechanisms for the formation of these nanostructures [46, 47]. According to the first method, there is a site-selective deposition of Au^0 atoms on a gold seed and then the attachment of many seed particles promoting growth. The reaction temperature is kept low in this synthesis as higher temperatures can lead to more thermodynamically favoured shapes [47]. The second mechanism involves the seed mediated approach for the synthesis of branched AuNPs. By following this method, there is better control over the morphology and size distribution. The first report for using Ag nanoplates as seeds to form single-crystal Au multipods was presented by Chen and co-workers [46]. Sau *et al*. showed the synthesis of gold nanostructures with branched arms with dimensions from 70 to 300 nm by modifying the seeded growth protocol for AuNRs [48]. The deposition rates of Au^0 on different gold facets could be affected by changing the surfactant and additive concentrations. CTAB acted as the surfactant and silver nitrate was used as the additive to promote anisotropic growth while the Br^- ions from CTAB played a crucial role in the growth of branches. L-ascorbic acid was used as the reducing agent in the reaction, reducing the gold ions from the gold precursor into gold atoms. According to Day and co-workers, an increase in the concentration of the reducing agent (L-ascorbic acid) led to AuNPs with a higher degree of branching while an increase in the concentration of the additive (silver nitrate) resulted in spherical AuNPs [49]. In more detail, the Au seeds presented (100) and (111) facets. The gold deposition was promoted on the (111) facet leading to anisotropic growth since silver atoms showed preferential deposition on the (100) facet followed by strong CTAB binding. When the concentration of silver nitrate increased, the deposition of silver atoms would occur on the (100) facet as well as the (111) facet. Consequently, all facets would be coated with CTAB before excessive gold could be placed on them causing larger spherical AuNPs. When the concentration of L-ascorbic acid increased, a faster reduction process was promoted leading to an increase in the rate at which gold ions became available. This resulted in more reactive species that led to the generation of particles with more branches [49].

There are several surfactants aside from CTAB that induce the formation of branched structures. By replacing CTAB with sodium dodecyl sulphate (SDS), small branched nanoparticles (40 nm) are formed whereas polyvinylpyrrolidone (PVP) can lead to an overall branched AuNP size ranging from 45 to 60 nm [50-52]. The type of the reducing agent can also affect the formation of the particles as it induces the reaction kinetics. In particular, Zou *et al*. demonstrated the use of hydroxylamine sulfate with sulphuric acid to generate nanoparticles with branched arms [53]. Furthermore, NH_2OH was used as the reducing agent in the presence of silver nitrate and citrate stabilised seeds in order to obtain thorny AuNPs [54]. The synthesis of branched AuNPs using dimethylformamide (DMF) as the reducing agent was reported by Liz-Marzan's group. The tuning of the concentration of the seeds could change the size of the nanostructures with branched arms ranging from 45 to 160 nm whilst maintaining structure uniformity [51, 52]. To sum up, the synthesis of uniform branched AuNPs with a well-controlled yield remains challenging. Despite the existence of numerous synthetic protocols, the mechanism for the synthesis of branched AuNPs depends on many parameters such as the temperature, the reducing agent and the seed concentration.

2.1.4 Synthesis of upconversion nanoparticles

UCNPs are named after the fluorescence process of photon upconversion and have interesting optical properties. In photon upconversion, UCNPs are able to convert lower energy photons (near-infrared light) into higher energy photons (visible light); hence a certain frequency of light is absorbed and then emitted at lower wavelengths [55]. The first reference to a bulk material able to absorb and convert energy goes back to the 1970s [56, 57]. There are several synthetic techniques to prepare lanthanide-doped UCNPs with different compositions, shapes and sizes [58-61]. The reproducibility of fabrication of monodispersed UCNPs and the narrow size distribution are two of the major challenges in the synthesis of UCNPs. The most commonly used methods for the preparation of UCNPs doped with Ln^{3+} are co-precipitation, thermal decomposition, microwave-assisted heating and hydro(solvo)thermal synthesis.

2.1.4.1 Chemical co-precipitation method

Co-precipitation is a convenient technique to synthesise ultrasmall lanthanide-doped nanocrystals with narrow size distribution and involves the precipitation of desired products out of the precursor solution. This method is less time consuming since there is no need for meticulous reaction conditions, expensive equipment and complex procedures [62]. The earliest example of synthesising crystalline $NaYF_4$:Yb, Pr UCNPs by a co-precipitation technique at a low temperature of 80 ^oC was presented by Martin and co-workers [63]. In 2002, Stouwdam *et al*. made down-conversion LaF_3 nanocrystals doped with Ln^{3+} where Ln = Eu, Er, Nd, and Ho [64]. Then, Yi and co-workers refined this technique by synthesising LaF_3 nanocrystals with smaller particle sizes and narrower size distribution from water-soluble inorganic precursors [65]. Apart from LaF_3

nanocrystals, several groups have synthesised $NaYF_4$:Yb/Er, $LuPO_4$:Yb/Tm and $YbPO_4$:Er nanocrystals by using the co-precipitation approach coupled with heat treatment or post-annealing process for enhanced upconversion emission [66-69]. In 2008, Li and co-workers introduced a ''user-friendly'' high-temperature co-precipitation method where 1-octadecane was used as the solvent and oleic acid was used as a capping ligand to generate crystalline, highly uniform, purely hexagonal phase $NaYF_4$ UCNPs with narrow size distributions and high luminescence efficiencies [70, 71]. By tuning the oleic acid to 1-octadecane ratio in the synthesis, hexagonal-phase nanoplates, nanoellipses and nanospheres were produced with narrow size distributions. The decrease in the content of toxic byproducts generated at high temperatures renders this method ''user-friendly''. In the initial step of this method, a yttrium oleate precursor is formed followed by the addition of NH_4F and NaOH. Consequently, small amorphous aggregates are formed. The increase of the temperature at ~300 ^oC for 1 h facilitates the particle growth of these aggregates and the development of uniform nanocrystals *via* the Ostwald ripening mechanism. This thermodynamically-driven process consists of the dissolution of small crystals and then the redeposition of the dissolved species on the surfaces of larger particles. Furthermore, several water-soluble organic ligands such as PVP and polyethylenimine (PEI) are used to control particle growth and provide solubility to the nanocrystals [72, 73]. Specifically, Wang *et al*. showed that PEI-coated nanoparticles are a great platform for the direct surface functionalisation of biomolecules [74]. The co-precipitation technique was used to prepare UCNPs for the experiments reported in this thesis (see **Section 3.1.5** for synthetic protocol) since highly monodisperse, uniform and phase pure nanoparticles are produced in comparison with other techniques.

2.1.4.2 Thermal decomposition method

Thermal decomposition is a synthetic method for the synthesis of monodispersed UCNPs in which metal-organic precursors are dissolved in the high-boiling organic solvents and then decomposed at elevated temperatures. The commonly used metal-organic precursors are rare-earth (RE) organic compounds, such as metallic or lanthanide trifluoroacetate, lanthanide oleates, lanthanide acetates, and lanthanide chlorides, which decompose at a high boiling point [75]. After decomposition at high temperatures, the seeds ripe into nanoparticles with the aid of a surfactant that prevents agglomeration. Zhang and co-workers first reported the fabrication of single-crystalline and monodisperse LaF_3 nanoplates *via* thermal decomposition of $La(CF_3COO)_3$ precursors in the presence of oleic acid and 1-octadecene [76]. Since then, high-quality UCNP crystals such as $NaYF_4$ [77], $LiYF_4$ [78, 79], $NaGdF_4$ [77] and $NaLuF_4$ [77] have been synthesised. By adjusting the reaction temperature and time, the nature and the concentration of solvents, and the concentration of precursors, a variety of sizes and shapes of UCNPs can be produced [80, 81]. In 2009, Wang *et al*. used ethylene glycol as solvent and PEI as capping ligand [82]. As a result, easily dispersed in aqueous media UCNPs were synthesised but only in the cubic α-$NaYF_4$ phase. Although thermal decomposition has become an effective strategy to synthesise UCNPs, there are certain disadvantages such as the generation of toxic volatile species by the decomposition of the fluoride reactants, the need for expensive air-sensitive metallic precursors and the low upconversion efficiency of the synthesised nanoparticles [81, 83].

2.1.4.3 Microwave-assisted heating method

In the microwave-assisted heating method, the reactants are exposed to electromagnetic waves and heated in a very short time [84]. This technique is considered a green approach since it requires less reaction time and less energy consumption [85, 86]. The first approach for the synthesis of monodisperse $NaYF_4$ nanocrystals by microwave irradiation in a closed vessel was presented by Nann and Wang [87]. In 2010, the factors that control the size and shape of AYF_4:Yb, Er (with A = Na, Li) nanocrystals by using the microwave-assisted heating method were investigated by Wang and co-workers [88]. This study revealed the dependence of the nanocrystals' size on the reaction time while the reactant concentration and composition controlled the morphology. By increasing the concentration, flower shape nanocrystals were formed whilst the decrease of the concentration led to spherical morphology nanoparticles.

2.1.4.4 Hydro(solvo)thermal synthesis

Hydro(solvo)thermal synthesis is another solution-based technique to grow monodispersed $NaYF_4$ UCNPs. This method has become an effective way to synthesise UCNPs with controllable shape, size and phase by taking advantage of the high solubility and reactivity of reactants at high pressure and temperature conditions [89-91]. Li's group was the first to report the synthesis of $NaYF_4$ by using the hydro(solvo)thermal method [66, 92]. They synthesised hexagonal $NaYF_4$: Yb^{3+}, Er^{3+} UCNPs in ethanol, acetic acid and distilled water by using CTAB and (ethylenedinitrilo)tetraacetic acid (EDTA) as capping ligands. In a typical hydro(solvo)thermal synthesis, RE chloride, nitrate or acetate are mixed with the surfactant in an aqueous solution and then it is heated at 160 ^{0}C – 220 ^{0}C. By varying the reaction pH, the temperature, the time and the precursors' concentration, the morphologies of the nanoparticles can be tuned to have desired structures [83]. However, the main drawback is the use of a reaction PTFE vessel for the synthesis which prevents monitoring the growth of nanoparticles [93].

2.2 Optical Properties of Colloidal Nanoparticles

2.2.1 Optical properties of gold nanoparticles

Colloidal metallic nanoparticles exhibit remarkably different properties compared to their corresponding bulk material due to their unique interactions with light [94]. Gold is considered to have a characteristic golden yellow colour while on the nanometre scale AuNPs solutions can vary in colour ranging from wine red to blue depending on the nanoparticle size and shape [95]. By solving Maxwell's equation, Gustav Mie was the first to correlate the colour of the AuNP solution with the absorption and scattering of light by the AuNPs in the solution [96]. Metallic nanoparticles such as AuNPs have free conduction band electrons on their surface [16]. According to the Drude-Sommerfeld model developed in 1927, these electrons form an electron cloud around the particle core [94]. When the electromagnetic radiation interacts with AuNPs, there is an electron cloud displacement relative to the nanoparticle core, creating a dipole [16]. This electron cloud displacement induces a restoring force based on attractive Coulomb interactions between electrons and AuNPs core [97]. As a result, there is a coherent oscillation of the electron cloud [16]. This phenomenon of collective oscillation of free conduction band electrons is known as local surface plasmon resonance (LSPR). **Figure 2.4** presents a schematic illustration of this phenomenon for spherical AuNPs.

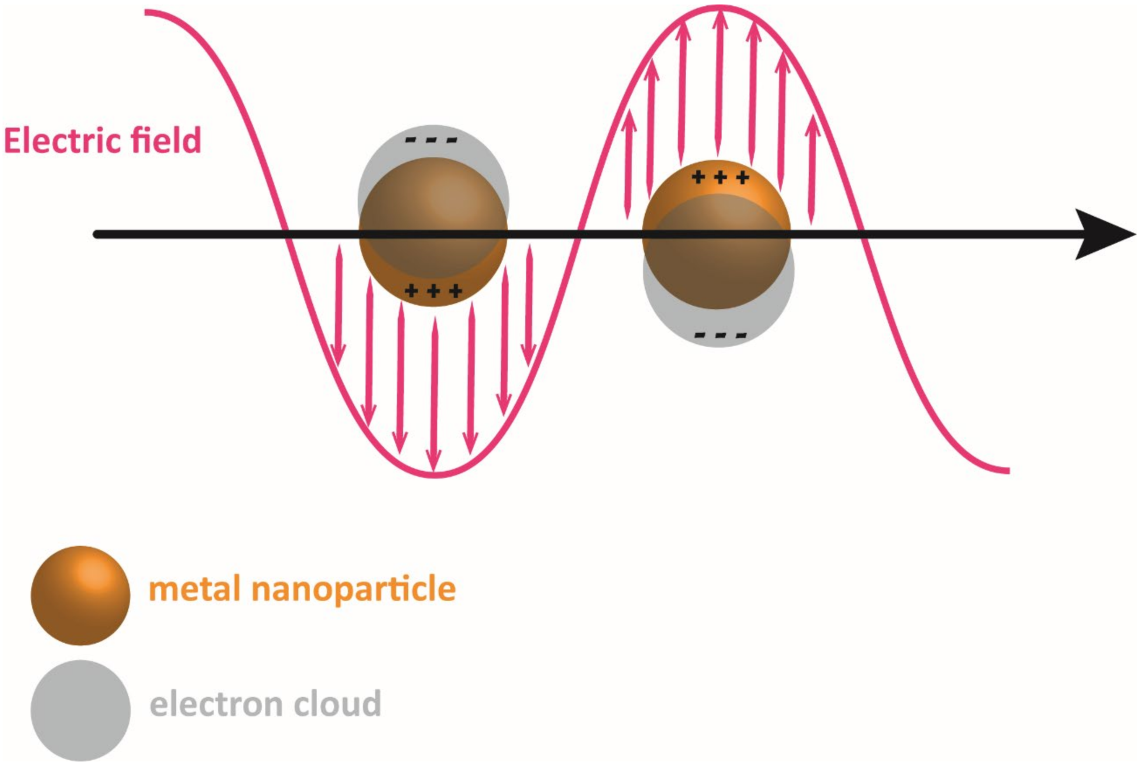

Figure 2.4 Schematic illustration of the LSPR on metal nanoparticles resulting from the interaction between metal nanoparticles and the electromagnetic radiation of incident light. Adapted from reference [98].

In 1908, a paper by Mie presented the interaction of light with a particle smaller than or comparable to the wavelength of light. Gustav Mie combined the theory with the scattering and absorption of light, the polarization, and the colour phenomena observed for gold colloids. This was the first quantitative description of the LSPR [99]. Mie solved Maxwell's equations using boundary conditions for spherical particles. He assumed that the electric field around a particle that is smaller than the wavelength of light is constant [97]. When the free conduction band electrons are excited to oscillate by an externally applied electric field, their return to the ground state can be either radiative or nonradiative (absorption or scattering). As a result, the extinction cross-section (C_{ext}) is expressed as the sum of both the absorption (C_{abs}) and the scattering (C_{sca}) cross-section as seen in **Equation 2.1** [94]. The dielectric constant of the nanoparticle is a complex number with a real part ε_r and an imaginary part ε_i, while the surrounding medium is characterised by a dielectric constant ε_m. The position of the peak is determined by the real part of the dielectric constant as the extinction cross-section reaches a maximum at $\varepsilon_r = -2\,\varepsilon_m$ while the width of the peak is determined by the imaginary part of the dielectric constant [95].

$$c_{ext} = \frac{24\pi^2 r^3 {\varepsilon_m}^{3/2}}{\lambda} \frac{\varepsilon_i}{(\varepsilon_r + 2\varepsilon_m)^2 + {\varepsilon_i}^2}$$

Equation 2.1 Calculation of the total extinction cross-section, where r = radius of the nanoparticle, λ = wavelength, ε_m = dielectric constant of the medium, ε_r and ε_i = express the dielectric constant of the metal.

However, Mie's theory is based on some assumptions so as to express spherical nanoparticles smaller than 25 nm. In the first place, the nanoparticle and the surrounding medium dielectric constants are homogenous and can be described as their bulk dielectric functions. Secondly, the size of the nanoparticle is much smaller compared to the wavelength of incident light so only dipolar oscillations are considered. Finally, the local electric field of light in the nanoparticle is considered uniform and constant and the retardation effect is ignored [100, 101]. Although the retardation effect can not be neglected for larger gold nanospheres as it gives rise to oscillation modes in higher orders and at lower frequencies leading to a red-shift (longer wavelengths) of the overall LSPR peaks [95].

More advanced methods and approximations are employed for more complex geometries such as AuNRs or branched AuNPs to precisely describe their optical properties. Discrete dipole approximations (DDA) and finite-difference-time-domain method (FDTD) are two computing methods for these types of nanoparticles [95]. In the case of nanorods, free electrons can oscillate in two different directions, parallel to the short and the long axis. Consequently, the LSPR peak splits into the transverse mode and the longitudinal mode. The transverse mode is perpendicular to the long axis of the rod and the longitudinal mode is parallel to the long rod axis [102]. The longitudinal mode depends linearly on the aspect ratio as observed by Link and co-workers [103]. In the case of branched AuNPs, Shao *et al*. proposed that their LSPR spectral features are highly dependent upon the number and orientation of the extended spikes when a broad spectrum of average particles is obtained. When clear peaks are observed, they can be attributed to a specific spike in the structure [104]. Further growth of branched AuNPs leads to broadening of the peaks and reduced absorption as there is an increase in the Rayleigh scattering [53]. An increase in the extinction cross-section at the spike tips was also studied by Nehl and co-workers which may be responsible for their effective scattering properties [105].

2.2.2 Upconversion processes

Photon upconversion is characterised by the conversion of long-wavelength radiation to short-wavelength radiation. Several upconversion mechanisms have been discussed to be involved in the upconversion processes but this thesis focuses on the three main mechanisms: the excited state absorption (ESA), the energy transfer upconversion (ETU) and the cross-relaxation upconversion (CR). These three mechanisms are discussed in **Section 2.2.2** and are based on the sequential absorption of two or more excitation photons to generate an emission photon.

2.2.2.1 Excited state absorption

ESA is a single-ion process and involves multistep excitation by sequentially absorbing one or more photons from the ground state to the intermediate metastable excited state (E1) and finally populates at the excited state (E2). The emission is generated from the radiative relaxation from the excited state (E2) to the ground state (G), thus resulting in the emission of a photon with higher energy than the exciting one [61, 106-108]. This mechanism is presented in **Figure 2.5**.

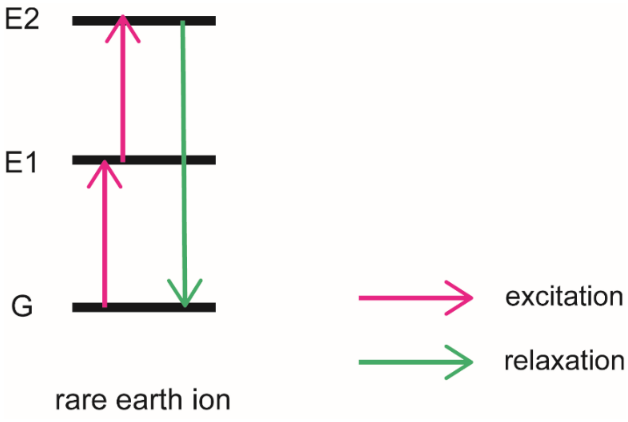

Figure 2.5 Schematic illustration of the excited state absorption process. G, E1 and E2 indicate the ground state, the intermediate excited state, and the excited state, respectively.

2.2.2.2 Energy transfer upconversion

ETU requires energy transfer between two neighbouring ions where one ion acts as a donor of energy and the second ion as the acceptor of energy [55, 106, 107]. For ETU, co-doped materials are needed where a ‘‘donor sensitiser ion’’ non-radiatively transfers the energy to an ‘‘acceptor activator ion’’ [83, 109]. In this process due to successive energy transfers, the sensitiser ion is excited by a first photon absorption from the ground state to its intermediate state E1. Then, due to the interaction between the sensitiser and the activator ions when they are in close vicinity, the energy is transferred by the sensitiser to the activator which is thus excited in its intermediate state E1. This is a nonradiative energy transfer (ETU1). Further excitation of the sensitiser into its E1 state may lead to energy transfer where both sensitiser and activator ions are initially in their excited state E1 promoting the activator to the higher energy excited state E2 (ETU2) and the sensitiser in the ground state (G) [83, 108, 109]. The upconversion luminescence will occur from the excited state (E2) to the ground state (G) of the activator ion, thus releasing a photon with higher energy than the exciting ones [110]. The ETU process utilises sensitisers, like Yb^{3+} or Nd^{3+} with larger absorption cross-sections as compared to other lanthanide ions. The Eu^{3+}/Yb^{3+}, Tm^{3+}/Yb^{3+}, Er^{3+}/Yb^{3+} and Ho^{3+}/Yb^{3+} are the most frequently used as sensitiser and activator pairs for the enhanced upconversion emission intensity [111-114]. This mechanism is presented in **Figure 2.6**.

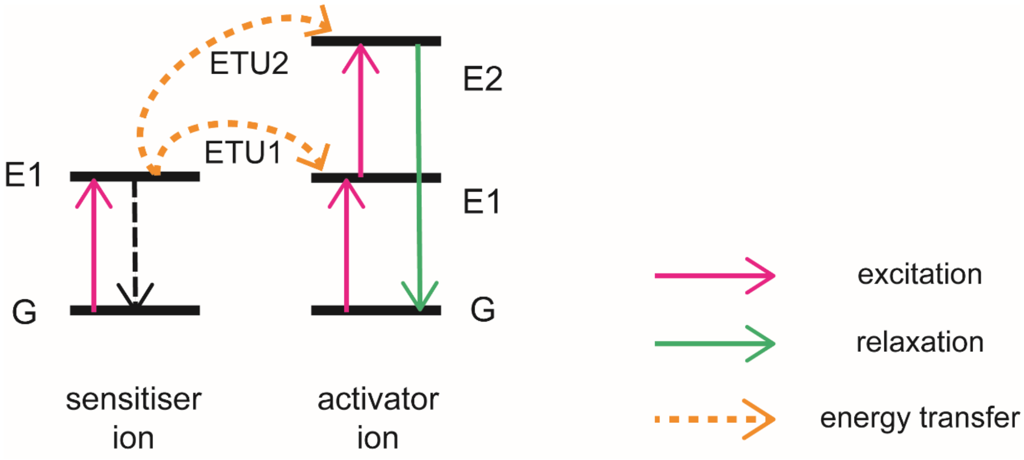

Figure 2.6 Schematic illustration of the energy transfer upconversion process. G, E1 and E2 indicate the ground state, the intermediate excited state, and the excited state, respectively.

2.2.2.3 Cross-relaxation upconversion

CR upconversion is an energy transfer phenomenon that results from an ion to ion interaction. In this interaction, the donor ion is in the excited energy state E2 and transfers part of its energy to the acceptor ion which is in the ground state. This results in the emission of two photons of low energy [83, 109, 115-117]. In this process, the donor and the acceptor ion may be similar or dissimilar, and the acceptor can also be in the excited state [107]. The efficiency of the CR process is related to the dopant concentration. It is one of the reasons for the concentration quenching mechanism which is used to tune the output colour upconversion [118-120]. This mechanism is presented in **Figure 2.7**.

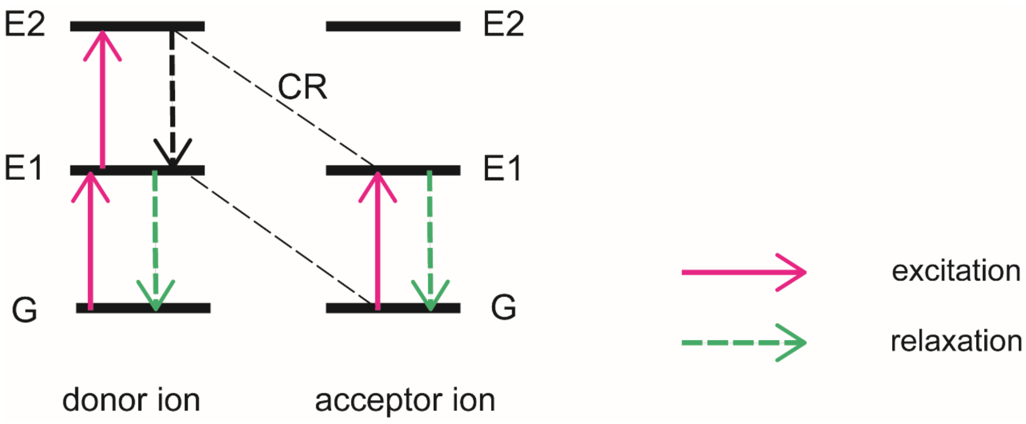

Figure 2.7 Schematic illustration of the cross-relaxation upconversion process. G, E1 and E2 indicate the ground state, the intermediate excited state, and the excited state, respectively.

2.2.3 Upconversion composition

The chemical composition of UCNPs plays a major role in their upconversion efficiency and their optical properties. The host matrix, the activator ions and the sensitiser ions are the three parameters that can affect the nanoparticles’ characteristics. In general, low concentrations of Ln^{3+} ions act as dopants on the inorganic host matrix. By tuning the amount and the type of dopants, several emissions can be achieved over a wide spectral range.

2.2.3.1 Host matrix

The appropriate host matrix can control the optical properties of UCNPs such as quantum efficiency. Notably, the crystal structure of the host material can affect the efficiency of upconversion luminescence [121]. Thus, the ideal host material should have low phonon energy to minimise nonradiative relaxations, high transparency in the spectral range of interest and excellent chemical and thermal stability to retain the original crystal structures [122]. The RE ion-based inorganic compounds are usually considered for the host material due to their similar valence states and chemical and physical properties. According to the literature, RE based oxides, oxysulfides, oxysalts and fluorides as well as alkaline earth ion and transition metal ion-based compounds have been investigated as host materials [68, 69, 123-125]. However, the $NaREF_4$ has been chosen as the optimum option due to its low phonon energy and excellent chemical stability [56, 115]. $NaREF_4$ nanocrystals can be found in two phases, the cubic phase and the hexagonal phase. The hexagonal $NaREF_4$ is one of the most transparent matrices in the NIR range and with the lowest phonon losses [114]. As a result, hexagonal $NaREF_4$ is the most commonly chosen host lattice in the literature.

2.2.3.2 Sensitiser and activator

According to the ETU mechanism, the ideal sensitiser ions should have large absorption cross-sections as well as energy levels matching those of the activator ions. The optimum choice among Ln^{3+} ions is Yb^{3+} since its absorption cross-section is relatively large ($9.11 \cdot 10^{-21}$ cm^{-2} at 980 nm). In detail, at 980 nm the absorption cross-section of Yb^{3+} is about an order of magnitude larger than that of Er^{3+} [126]. The energy level diagram of Yb^{3+} is quite simple since there is only one excited state ($^2F_{5/2}$). **Figure 2.8** demonstrates that the energy level of the excited state of Yb^{3+} is similar to this of Er^{3+} [82, 83, 109]. Hence, Yb^{3+} stands as an excellent choice of sensitiser to donate energy to other ions [127, 128].

According to the ETU process, the activator ions should have long-lived intermediate energy levels [129]. When the electrons from the ground level are excited to the intermediate level, activator ions can absorb energy from other excited sensitisers in order to promote further transitions to higher energy states. However, the energy states of the activator ions should not be close since nonradiative relaxation events may cause quenching effects [55]. Taking these into consideration, Er^{3+}, Tm^{3+} and Ho^{3+} are the best candidates for ETU activators due to the ladderlike arrangement of their energy levels [82, 130, 131]. Particularly, Er^{3+} shows the highest upconversion efficiency because of the large energy gaps between energy levels that prevent nonradiative transitions [132].

In general, by increasing the concentration of the dopant in a nanoparticle, the upconversion efficiency can be improved. However, the distance between dopant ions in the host lattice would decrease and the probability of radiationless deactivation through cross-relaxation would increase [55]. The percentage for activators' concentration in UCNPs is 3% for Er^{3+} and 0.5% for Tm^{3+} [75, 82, 109, 132]. To enable effective energy transfer to activator ions, sensitiser ions are used, which absorb at the excitation wavelength of interest. This allows an appropriate distance between sensitisers and activators.

In the case of Yb^{3+}/Er^{3+} co-doped UCNPs, there are four distinct emissions observed under 980 nm excitation, the green at 525 nm and 540 nm, the red at 655 nm and the violet at 415 nm. The green and the red emissions derive from two-photon processes whilst the violet emission comes from a three-photon process. **Figure 2.8** demonstrates the mechanism of Yb^{3+}/Er^{3+} co-doped UCNP where the $^2H_{11/2} \rightarrow {}^4I_{15/2}$ and the $^4S_{3/2} \rightarrow {}^4I_{15/2}$ transitions are responsible for the green and the $^4F_{9/2} \rightarrow {}^4I_{15/2}$ transition is responsible for the red emission [74, 133-135]. In detail, when UCNPs are under 980 nm laser irradiation, Yb^{3+} absorbs NIR photons and the $^2F_{7/2} \rightarrow {}^2F_{5/2}$ transition happens. The $^4I_{11/2}$ energy level of Er^{3+} resonates and there is an efficient energy transfer process from the $^2F_{5/2}$ energy level of Yb^{3+} to Er^{3+}, while Yb^{3+} results back to its $^2F_{7/2}$ ground level. The Er^{3+} can also be populated to the higher excited states ($^4F_{7/2}$, $^4F_{9/2}$) through resonant energy transfer from the sensitiser because of the energy level match. Then, there is relaxation to the $^2H_{11/2}$ and $^4S_{3/2}$ levels and the green emissions corresponding to 525 nm and 540 nm come from the radiative decay to the $^4I_{15/2}$ ground level. The red emission corresponding to 655 nm comes from the $^4F_{9/2}$ state due to either relaxation from the higher $^4S_{3/2}$ level or exciting Er^{3+} ions from the $^4I_{13/2}$ level to the $^4F_{9/2}$ level *via* energy transfer from the $^2F_{5/2}$ of Yb^{3+} [83, 109, 136].

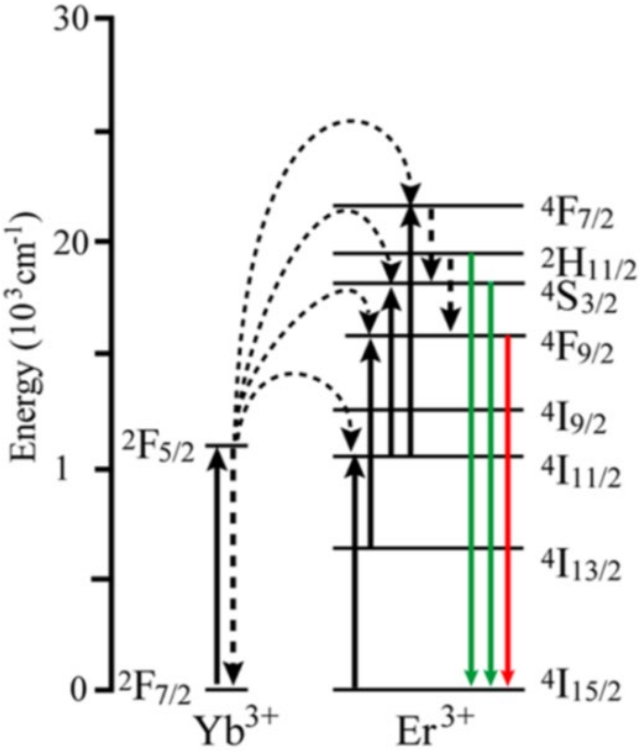

Figure 2.8 Simplified energy level diagram showing the upconversion processes in Yb^{3+} and Er^{3+} doped crystals under 980 nm diode laser excitation. To improve upconversion efficiency, Yb^{3+} is typically doped into the host lattice as a sensitizer ion at higher molar concentrations (18 – 20%), while activator ions are kept low, usually under 3% to minimise undesirable cross-relaxation events. Adapted from references [61, 83].

2.3 Structure and Properties of Oligonucleotides

Deoxyribonucleic acid (DNA) is a large polymeric molecule composed of two chains that twist around each other to form a double helix, rendering it the molecule of all known forms of life. It contains the information all organisms need to develop, live and reproduce. DNA is composed of monomers known as nucleotides (**Figure 2.9**). Each nucleotide consists of a pentose sugar, a phosphate group and a heterocyclic base. In DNA there are four different heterocyclic bases: the purines adenine (A) and guanine (G) and the pyrimidines cytosine (C) and thymine (T).

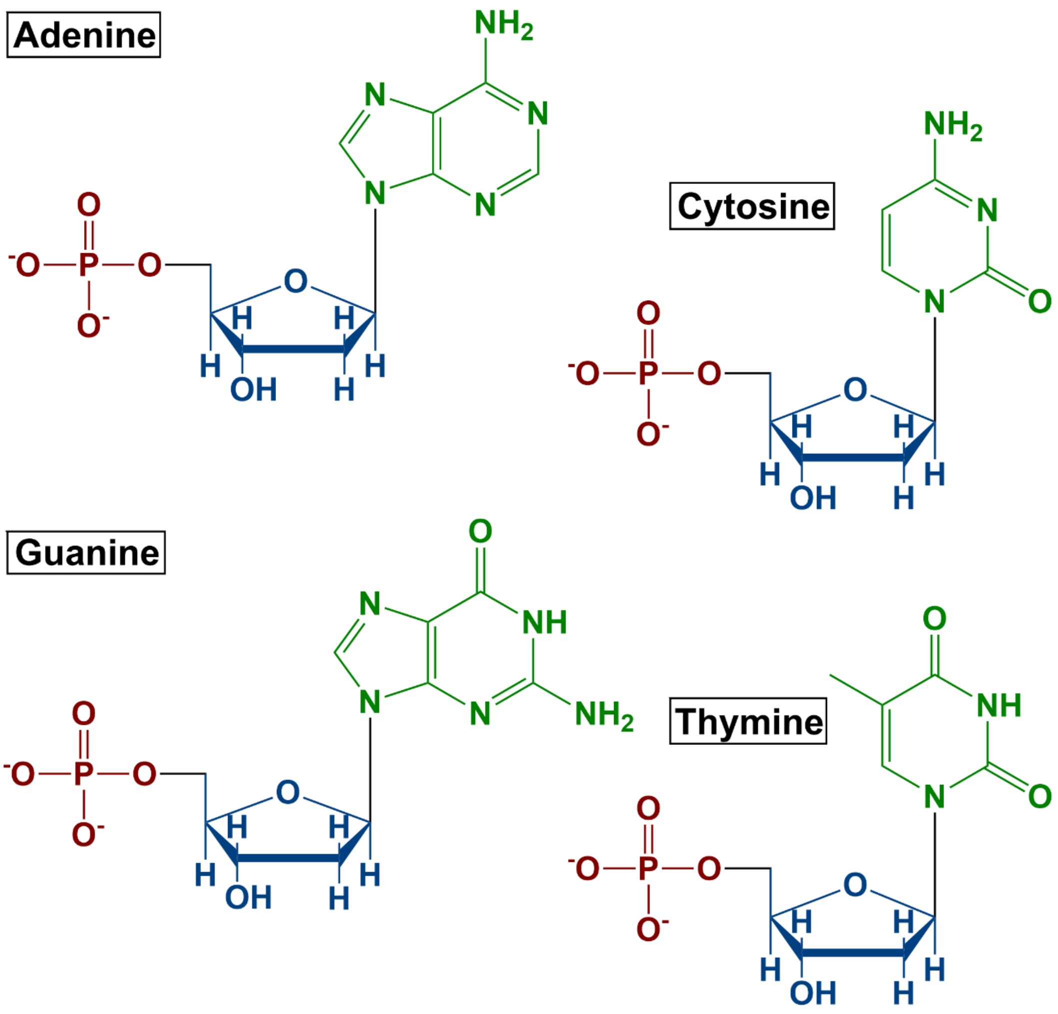

Figure 2.9 Chemical structures of the DNA nucleotides. The phosphate is highlighted in red, the deoxyribose ring is marked in blue and the different nucleobases in green.

Each nucleobase is linked to a deoxyribose, and the deoxyribose molecules are linked to each other by a phosphodiester bond resulting in the formation of the phosphate backbone as shown in **Figure 2.10** [137]. Phosphate groups in DNA are negatively charged at pH > 2 causing a highly charged anionic polymer. Each deoxyribose is oriented in the same way and the phosphodiester linkage is created between the 5’ phosphate group of one nucleotide to the 3’ hydroxyl group of another.

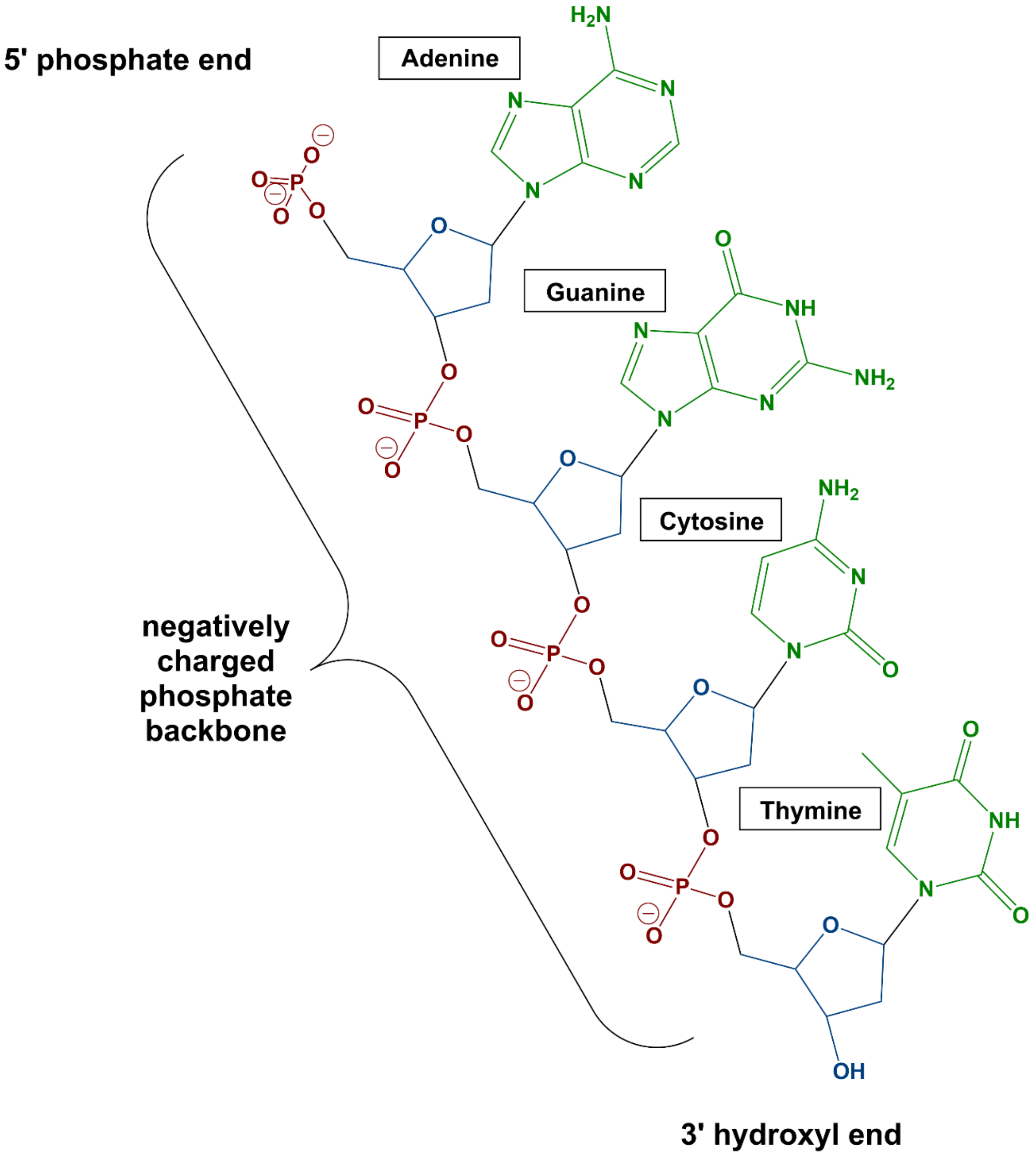

Figure 2.10 Chemical structure of a single DNA strand with the sequence 5' AGCT 3’. The phosphate groups are highlighted in red, the deoxyribose rings are marked in blue and the different nucleobases are shown in green. The nucleotides are linked through the phosphate groups connected between the 5' carbon and the 3’ carbon of adjacent deoxyribose sugar molecules. The DNA chain has a negatively charged phosphate backbone.

Ribonucleic acid (RNA) is created using DNA strands as a template through the process of transcription [138]. Some organisms such as retroviruses, use RNA instead of DNA to store their genetic information. In most cases, RNA carries messages that are stored in DNA to the ribosome for processing decoded into the sequence of a protein. This type of RNA is called messenger RNA (mRNA) [139]. RNA is chemically very similar to DNA although there are two fundamental differences. RNA has a hydroxyl group attached to the sugar, and uracil replaces thymine.

In 1953 James Watson and Francis Crick explained that DNA adopts a double-stranded (dsDNA) helical structure (duplex). This made the mechanism of DNA replication (copying) apparent [137]. Rosalind Franklin and Maurice Wilkins acquired X-ray fibre diffraction data of the double-helical structure. The fact that the molar amount of adenine in DNA was always equal to that of thymine and it was the same for guanine and cytosine was discovered by Erwin Chargaff [140]. By building models, Watson and Crick demonstrated that the two strands of DNA are held together by hydrogen bonds between individual bases on opposite strands. The purine base A pairs with the pyrimidine T and the purine G pairs with the pyrimidine C [141].

In the double helix of DNA, the two strands are complementary as the sequence of one strand defines the sequence of the other. The 5' end of one strand matches with the 3' end of the other since the two strands are antiparallel. Also, the two strands form a right-handed double helix where the hydrophobic base pairs are in the centre and the sugars and negatively charged phosphates form the external hydrophilic backbone. RNA can also form a right-handed duplex using the same base-pairing rules where the A pairs with the U base and the G pairs with the C base. Moreover, the forces that hold the double-stranded helix of DNA together are bifold: a) attractive hydrogen bonding and π-π stacking between the nucleobases and b) repulsive between the negatively charged phosphate backbone [142]. The conditions in the surrounding environment such as the pH, ionic strength and temperature of the solution affect the DNA hybridisation, due to the presence of the repulsive forces between the negatively charged phosphate backbone [143]. To maintain the intermolecular forces that hold the double helix together, the monitoring of the temperature is important. By increasing the temperature, the bonds tend to break and the double-strand system detaches to its respective single strands [144]. The pH value of the solution can also affect the structure of DNA due to the protonation of the bases in an acidic environment or the deprotonation of the bases in a basic environment. In the presence of cations that shield the negative charge of the phosphate backbone, successful hybridisation is possible as the electrostatic repulsion barrier is surpassed [145].

An essential characteristic for the design of DNA strands is the melting temperature (T_m) of DNA. At this temperature, 50% of the double-stranded DNA is dehybridised into single strands [146]. To monitor this variable experimentally, a melting curve is performed where the temperature is gradually increased whilst observing the changes in the UV absorption of DNA. Purine and pyrimidine rings are aromatic and absorb UV light with a max at 260 nm. The base stacking in a double-stranded conformation reduces the resonance of the rings and thus their corresponding absorbance. As a result, the absorbance of a DNA duplex is always lower than the sum of the absorbances of the two individual strands due to the π-π stacking of bases in the double helix [147]. This decrease in absorbance is called hypochromicity. The DNA duplex in an aqueous buffer solution is heated slowly until it dissociates into two single strands. This happens by disrupting the ordered stacking of the bases and breaking hydrogen bonds. A graph of UV absorbance against temperature gives a characteristic sigmoidal curve. The T_m is found at the mid-point of the melting curve. By using different models such as the nearest neighbour method, the T_m can be calculated theoretically. The enthalpy of the formation of a double-strand and the stacking of the nearest neighbours are considered in this method. The result is a good approximation and agrees with the experimentally calculated values [148].

Synthetic DNA strands, termed oligonucleotides, can be produced by automated solid phase phosphoramidite synthesis, which allows for the synthesis of any sequence of bases [149-151]. The oligonucleotides can be functionalised with a wide range of functional groups such as fluorescent dyes or molecules that can enable further chemical reactions [152, 153]. These modifications can be incorporated into the sequences *via* either a functionalised column used for solid-phase synthesis (only for 3’ modifications) or pre-modified nucleoside phosphoramidite monomers. The oligonucleotides can be also synthesised with aminoalkyl linkers for post-synthetic modifications. In this work, synthetic DNA strands were modified with fluorescent dyes, peptides and two different modifier groups in order to attach multiple single strands to the surface of nanoparticles. A thiol group attached to a DNA strand was used for the functionalisation of the gold surface since the linkage gold-sulfur is well-established in the literature [154, 155]. An amino group attached to a DNA strand was used for the functionalisation of the UCNPs surface. The amino group can covalently bound a carboxy group located on the surface of the UCNPs [156]. **Figure 2.11** demonstrates the anchoring group structures of thiol and amino attached to a nucleotide of the oligonucleotide sequence.

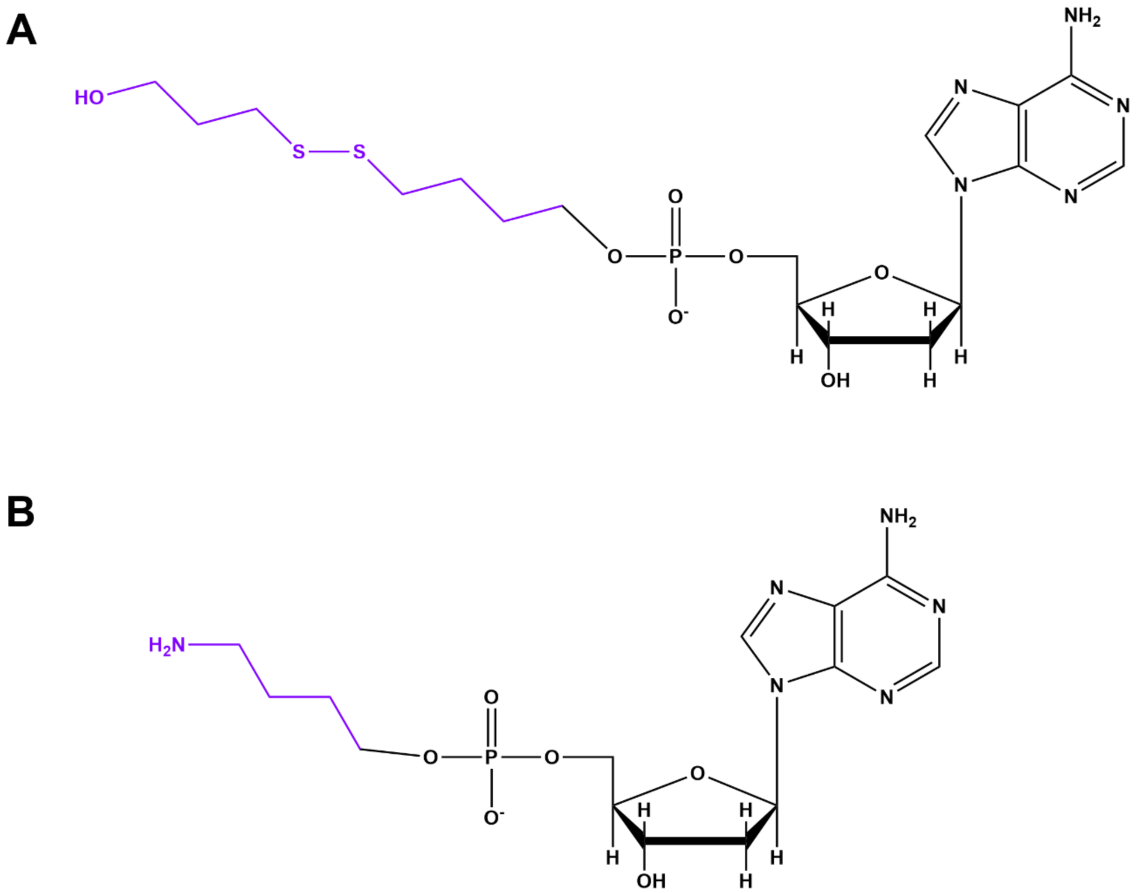

Figure 2.11 Chemical structures of modifications to the oligonucleotide sequences used in this study. The functional groups are highlighted in purple and are attached to the 5’ end. (**A**) The sulphur bridge was used for oligonucleotide coating of AuNPs surfaces while (**B**) the aminohexyl was used for the DNA attachment *via* EDC/sulfo-NHS coupling on UCNPs.

2.4 Cell-Penetrating Peptides

Peptides consist of a small chain of two or more amino acids that are connected by their peptide bonds. Cell-penetrating peptides are short peptides (5-30 amino acids) that unlike most peptides can cross the cellular membrane and show nearly non-toxic and non-immunogenic behaviour. In 1988 cell-penetrating peptides were discovered by two research groups independently and first called ‘protein transduction domains (PTDs)’ [157, 158]. Since then they have been widely used in experimental studies as effective delivery systems.

The cell-penetrating peptides can be classified into two categories based on the origin of peptides and their physicochemical properties. According to the origin of peptides, cell-penetrating peptides are divided into chimeric, protein-derived and synthetic. Chimeric cell-penetrating peptides consist of two or more motifs from dissimilar peptides such as transportan. Protein-derived cell-penetrating peptides stem from natural proteins such as TAT and penetratin. Synthetic cell-penetrating peptides are rationally designed sequences based on structure-activities studies. A characteristic example is the polyarginine family [159, 160]. According to their physicochemical properties, cell-penetrating peptides are divided into three classes: cationic, amphipathic and hydrophobic. Most cell-penetrating peptides are cationic due to their positive charge. An example of a cationic peptide is TAT, a transcriptional activator protein in HIV-1 which involves arginine and lysine residues [161]. Amphipathic cell-penetrating peptides are the sequences with a high degree of amphipathicity due to lysine residues in their structures such as transportan [162]. Hydrophobic cell-penetrating peptides consist of only hydrophobic motif/non-polar sequences. However, there are not many references for using the hydrophobic peptides as carriers compared to cationic and amphipathic cell-penetrating peptides [163].

The exact mechanism of cell-penetrating peptide transport across biological membranes is still vague, however, there are three proposed pathways for the internalisation of peptides; direct penetration, endocytosis pathway and translocation through the formation of a transitory structure [164, 165].

Direct penetration is an energy-independent pathway that includes several mechanisms such as the carpet-like model [166], the pore formation [167], and the membrane thinning model [168]. The first stage of all these mechanisms is the interaction of the positively charged cell-penetrating peptide with negatively charged membrane components followed by the destabilisation of the membrane and the folding of the peptide on the lipid membrane. The attachment of the cell-penetrating peptide to the membrane happens through electrostatic interactions. Then, the cellular membrane is disrupted in the binding sites in order to allow the cell-penetrating peptide into the cell [169].

Endocytosis or cellular digestion is an energy-dependent pathway in which the plasma membrane folds inward to carry materials from the outside of cells and absorb them. The three classes of endocytosis are pinocytosis, phagocytosis and receptor-mediated endocytosis. During phagocytosis, the plasma membrane absorbs the large particles. In pinocytosis, solutes are taken in by the membrane. In receptor-mediated endocytosis, also called clathrin-mediated endocytosis, there is a selective translocation of material into cells through the binding of this material to specific receptors on the surface of the cell. The material absorbed by cells includes mainly proteins, metabolites and hormones. This process is based on the formation of vesicles that contain the absorbed substances and are mediated by specific receptors on the surface of the cell. Hence through this mechanism, only the receptor-specific material can enter the cell [170]. According to the literature, the endocytosis pathway is the dominant mechanism of cell-penetrating peptides' internalisation [171].

In the translocation through the formation of a transitory structure method, the lipid bilayer of the membrane can be disrupted by the interaction of the cell-penetrating peptide with the cellular membrane. As a result, the formation of inverted structures/micelles is followed. Firstly, the cell-penetrating peptides are trapped in the hydrophilic environment of the micelle core. Then, the inverted micelles interact with the membrane components and consequently, the destabilisation of the inverted micelles happens. Finally, the cell-penetrating peptides are released into the cytoplasm [172, 173]. This mechanism is suitable for the translocation of small hydrophilic peptides. In general, in this uptake method, there is an electrostatic interaction between the cell-penetrating peptide and the components of the lipid membrane as well as an interaction between hydrophobic residues and the hydrophobic part of the membrane. Thus this mechanism is not suitable for the highly cationic cell-penetrating peptides such as TAT [174].

The cell-penetrating peptide used in this thesis is Aurein 1.2 and belongs to a large family of peptides discovered in the skin secretions of the Litoria genus of Australian frogs with various degrees of antimicrobial activity. The Aurein peptides are classified based on their lengths. Aurein 1.2 is one of the shortest in the family with only 13 amino acids [175]. Referring to its structural properties, it is amphipathic with well-defined hydrophobic and hydrophilic sides along its helical axis [175, 176]. It has been observed to reside on the surface of a lipid bilayer and permeabilise bacterial membranes at high concentrations. Aurein 1.2 inhibits both intact Gram-negative and Gram-positive bacteria like many other antimicrobial peptides (AMP) [177]. It also demonstrates a moderate anticancer activity at concentrations that can kill both bacterial and cancer cells without killing healthy mammalian cells [175]. Furthermore, Li and co-workers presented the enhancement of the endosomal escape when Aurein 1.2 peptide is conjugated with a cationic protein by up to around 5-fold in a cytosolic fractionation assay in cultured cells [178]. Based on the above characteristics, the use of the membrane-active Aurein 1.2 peptide was considered an effective choice for a better understanding of the interaction between cell-penetrating peptides and membranes.

2.5 Surface Functionalisation of Colloidal Nanoparticles

Functionalised nanoparticles are characterised by stability, functionality and biocompatibility. Nanoparticles can act as a scaffold for attaching a variety of surface ligands that give new functional properties to the system [179]. Consequently, the nanoparticle surface chemical composition and its modification should be controlled for their application in nanomedicine, nanosensors and nanofabrication.

2.5.1 Surface functionalisation of spherical gold nanoparticles with oligonucleotides

In 1996, Mirkin *et al*. presented a 13 nm spherical gold core functionalised with a dense shell of synthetic oligonucleotides [180] while Alivisatos and co-workers demonstrated that it was equally possible to conjugate a discrete number of oligonucleotides on the surface of AuNPs [181]. The structures synthesised by Mirkin *et al*. are also termed spherical nucleic acids (SNAs) and exhibit functional properties such as higher binding constants, increased resistance to degradation by nucleases, sharp melting transitions and the capability of uptake by many cell lines in comparison with free strands of the same sequence [182-184]. The previously listed properties mainly result from the density and orientation of the oligonucleotides on the surface of nanoparticles [179].

The core material is a major design parameter for SNA conjugates. AuNP cores functionalised with alkylthiolated oligonucleotides connected *via* a gold-sulfur bond constitute the majority of conjugates that have been widely investigated [185, 186]. AuNPs were selected as the first candidates for the core material since they are easily synthesised over a wide range of particle diameters [20], have plasmon resonances with high extinction coefficients, have well-defined catalytic properties and can be easily functionalised with a wide range of chemical reagents. Aside from gold, the physical properties of other inorganic nanoparticles provide distinct benefits within the SNA concept. Towards this direction, a great effort has been made to build SNA architectures by attaching oligonucleotides to a variety of particle types, including silver [187], semiconductor quantum dots [188], silica [189] and metal oxides [190]. However, it is significant to mention that each of these approaches involves specific chemistry customised to the target particles, which is a hard task given the high oligonucleotide densities required to obtain the special properties of SNAs. In particular, it is challenging to create stable conjugates from monodentate alkylthiols because the surfaces of aqueous silver nanoparticles are easily oxidised [191, 192]. As a result, oligonucleotides containing many cyclic disulfide anchoring groups are usually used to synthesise SNAs from silver nanoparticles [187]. Similarly, silver nanoprisms have been functionalised with DNA by first coating them with a silica shell and then conjugating them [189]. Finally, the simplicity in synthesis renders SNAs with AuNP cores as the best candidate.

A well-established synthetic method leading to the synthesis of robust SNAs was followed by using thiol-terminated oligonucleotides. This method is called the salt-ageing procedure and allows for the conjugation of multiple oligonucleotides by screening the negative charge of the phosphate backbone of neighbouring strands, as well as the repulsive charges between the AuNP surface and the negatively charged phosphate backbone on the DNA [193, 194]. To achieve high loading of oligonucleotides on the surface of the nanoparticle, the NaCl concentration is increased in a solution containing AuNPs and thiol-modified oligonucleotides over an 8 h period [179, 195]. Higher salt concentrations can lead to higher oligonucleotide densities where the 3D monolayer of oligonucleotides is especially stable due to the strong gold-sulfur bond (40 kcal/mol). However, there are steric constraints after a critical point that prohibit further adsorption onto the surface of the nanoparticle [179, 196, 197]. The maximum number of oligonucleotides attached to the gold core is dependent on the dimensions of the nanoparticle. Nanoparticles of a smaller size can be covered by a larger oligonucleotide density due to a higher radius curvature. Nanoparticles' curvature modulates the forces and molecular interactions [198]. A larger curvature results in a natural deflection angle between the neighbouring oligonucleotides and creates additional space. This reduces the electrostatic and steric repulsion constraints. When the size of the nanoparticles increases, the radius curvature decreases and the effect of the natural deflection angle between the neighbouring oligonucleotides is reduced. As a result, the conjugation becomes less effective [199]. The type of nucleobases that is near the AuNP surface also plays an important role. A spacer sequence of approximately 8 – 10 bases (~3 nm) offers an extension to the active oligonucleotide sequence away from the surface. This increases the flexibility in binding and minimises steric barriers when it comes to complementary hybridisation. A and T spacers show increased rigidity in comparison to C and G bases [194, 200]. The surface density of oligonucleotides has been also increased by using sonication, which facilitates the kinetics of immobilization, orientation and packing of the oligonucleotides on the surface of the particle [194].

Another important design parameter is the density of oligonucleotides around a nanoparticle since it can protect the oligonucleotides' integrity against hydrolysis in the presence of enzymes. There are several studies where the enzymatic degradation of the oligonucleotide shell around nanoparticles is inhibited at a high DNA surface loading (~100 oligonucleotides/nanoparticle) [14, 179, 201, 202]. This observed resistance in enzymatic degradation may be due to a high local sodium concentration in the surrounding vicinity of the nanoparticles created by the dense oligonucleotide shell [203-205]. Moreover, it was proposed by Cutler *et al*. that oligonucleotides' degradation by nucleases is prevented by steric hindrance due to the dense packing of oligonucleotides around an AuNP [206]. A low surface density of oligonucleotides on the nanoparticles would lead to DNA enzymatic degradation. Seferos and co-workers used 13 nm AuNPs functionalised with DNA strands composed of 30 bases and varied oligonucleotide densities. By incubating with DNase I the half-life of oligonucleotide-coated AuNPs decreased with decreasing density. This indicated that by lowering the oligonucleotide density, enzymatic degradation was observed. This effect was investigated for up to 6 h post-incubation time and in the presence of

DNase I only [201]. Recently, Kyriazi and co-workers presented an interesting approach to how modified oligonucleotides can be used to build SNAs in which density is no longer an important design criterion for preserving SNA stability. By replacing the phosphodiester bond on the oligonucleotide backbone with a phosphorothioate bond, SNAs with low DNA loading exhibited great stability in the presence of nucleases [207].

There have been reported other techniques apart from the well-established salt-ageing method for the functionalisation of AuNPs. In 2003, Kanaras *et al*. obtained a similar result by applying careful vacuum centrifugation of a nanoparticle solution with 0.1 M NaCl. This involved a gradual and steady increase in ionic strength and oligonucleotide concentration as the reaction volume of the solution decreased resulting in stable DNA functionalisation of AuNPs with a calculated density of approximately 230 oligonucleotides per AuNP [208]. In 2012, Zhang and co-workers presented a pH-assisted route to achieve quantitative DNA adsorption within 3 min while using a citrate buffer at pH 3 [209]. Liu *et al*. demonstrated experimental design conditions for attaching thiolated DNA strands on AuNPs by simply freezing the sample resulting in high-quality conjugates after thawing it [210, 211].

2.5.2 Surface functionalisation of spherical gold nanoparticles with cell-penetrating peptides

Peptides are one type of ligand that can also be conjugated to a nanoparticle surface and give new properties to the nanoparticles [3]. Peptide coated nanoparticles demonstrated changes in intracellular localisation and increased the efficacy of conjugated biomolecules [212]. The functionalisation of AuNPs with cell-penetrating peptides is mainly based on the ligand exchange method which involves the displacement of one ligand by another. Hostetler *et al*. were the first to explore the replacement of simple thiol ligands on AuNPs with more complex thiols [213]. According to the literature, the use of cysteine modified peptides is an effective way to obtain peptide functionalised AuNPs after ligand exchange on the surface of the citrate stabilised AuNPs [214, 215]. The cysteine modified peptides form a thiol bond with AuNPs' surface. Peng and co-workers used peptide sequences derived from the HIV Tat protein to increase the delivery of synthetic materials to the cell nucleus and study the delivery mechanism. AuNPs were functionalised *via* partial ligand exchange with thiol-TAT peptides [216]. Khamehchian *et al*. presented the successful conjugation of two peptides containing extra cysteine residue at the C-terminus, $\text{MCa}_{\text{UF1–9 (Ala)}}$-C and TAT-C, on the surface of AuNPs. Maurocalcine (MCa) is the first animal toxin peptide with great cell penetration properties that has been discovered [217]. In 2018, the cell-penetrating peptide CRRRRRRRRGDS was conjugated with AuNPs *via* cross-linking of the cysteine's thiol group to the gold surface by Boussoufi and co-workers. The peptide functionalised

AuNPs showed limited cytotoxicity toward human dermal fibroblasts and promoted their growth [218]. Kumar *et al*. demonstrated the functionalisation of tannic acid coated AuNPs with two TAT derived cell-penetrating peptides *via* an electrostatic and a ligand exchange approach. The internalisation of 5 nm AuNPs functionalised with cell-penetrating peptides was reported to be efficient in bacteria [219]. Yan and co-workers created a series of tumour targeting and redox-responsive AuNPs coupled with three different functional polypeptides; the targeting peptide GE11, the cell-penetrating peptide octaarginine (R8), and the polyhistidine. The peptides were attached to AuNPs through gold-sulfur bonds to improve the gene-binding ability [220]. Finally, another approach based on chemical conjugation was used by Xie and co-workers to present a novel nuclear targeting nanoprobe based on nuclear localisation signal (NLS) peptide functionalised AuNPs. The nanoparticles were modified with 11-mercaptoundecanoic acid and then the NLS peptide was attached to the modified AuNPs by carbodiimide coupling [221].

2.5.3 Surface functionalisation of upconversion nanoparticles with oligonucleotides

UCNPs have applications in biological environments that require a high dispersibility and stability in aqueous media. However, the majority of uniform UCNPs are synthesised in organic solvents. As a result, the surfaces of these UCNPs are covered by hydrophobic organic ligands such as oleic acid that inhibit the dispersion in biocompatible media [75, 80, 222]. There are different approaches for the functionalisation of the hydrophobic surfaces of UCNPs, which can be divided into two main categories, ligand exchange and encapsulation techniques. This study is focused on the ligand exchange approach where the hydrophobic capping agents such as oleic acid are replaced by hydrophilic ligands. This straightforward technique allows the transfer to the aqueous phase and provides colloidal stability [223]. According to the literature, the ligand exchange process can be realised by direct substitution of the primary ligands with new ligands [224], by a ligand-free procedure [225] or by using BF_4^--capped UCNPs as an intermediate step [226]. The direct replacement of the stabilising capping ligands with water-soluble organic polymers offers a strong bond of their functional groups to the particle surface. The water-soluble organic polymers used in the bibliography for this purpose are poly(acrylic acid) (PAA) [227-230], PVP [231, 232], branched PEI [227], poly(amidoamine) (PAMAM) [233] and multidentate thiolate-grafting polymers [234]. The attachment of polymers with reactive amino- or carboxylic acid groups such as PEI and PAA gives the advantage of the facile conjugation of molecules such as oligonucleotides to the nanoparticles. In 2010, Xiong and co-workers demonstrated a direct ligand exchange with PAA to achieve water-dispersible UCNPs [229]. By functionalising the surface of particles with PAA which gives a coverage of carboxyl groups, amine-terminated oligonucleotides can be conjugated *via* the use of EDC/sulfo-NHS coupling chemistry [156, 235]. N-(3-(dimethylamino)propyl)-N'-

ethylcarbodiimide hydrochloride (EDC) is a cross-linking reagent used for the coupling of a primary amine with a carboxylic group. N-hydroxysulfosuccinimide sodium salt (sulfo-NHS) increases the stability of active intermediates in coupling reactions by forming active ester functional groups with carboxylates. The reaction mechanism involves the coupling of a primary amine with a carboxylic acid in the presence of EDC and sulfo-NHS as demonstrated in **Figure 2.12**. During the first step, the carboxylic acid is activated by EDC to form an unstable intermediate (**Figure 2.12 Step 1**). This highly reactive intermediate tends to hydrolyse. To avoid subsequent reformation of the carboxylic group, sulfo-NHS is employed to react with the intermediate and form an active ester (**Figure 2.12 Step 2**) which has a higher selectivity to react with primary amine to form a stable amide bond between UCNPs and amine-terminated oligonucleotides (**Figure 2.12 Step 3**).

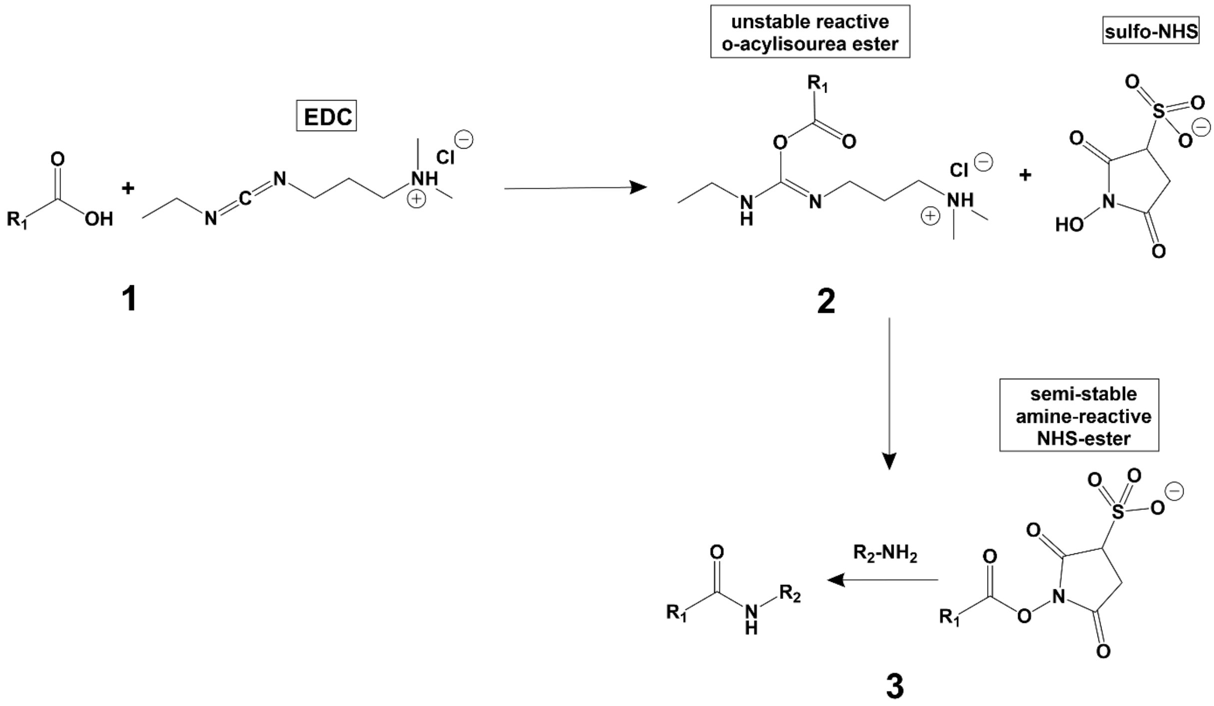

Figure 2.12 Reaction mechanism of EDC/sulfo-NHS coupling. Initially, a highly reactive intermediate is formed *via* the activation of the carboxylic acid by EDC. In the second step, an active ester is formed when sulfo-NHS is employed while in the third step it selectively reacts with a primary amine to form an amide. Adapted from reference [235].

2.6 Interaction of Functionalised Spherical Gold Nanoparticles with Mammalian Cells

The functionalisation of spherical AuNPs with oligonucleotides has increased the scientific interest in using them within cells for *in vitro* applications, especially in the detection of RNA [182, 202, 236-238]. Several biological processes such as cancer progression are based on both bulk mRNA expression and cell-to-cell variations in mRNA levels [202, 239, 240]. There are many methods for the detection of mRNA in the literature such as real-time reverse transcription-polymerase chain reaction (RT-PCR) and microarray analysis. However, these techniques are not able to detect cell-to-cell variations but can only detect an average mRNA expression from cell lysates [202, 239]. Another technique that can be used within cells is the synthetic fluorophore labelled oligonucleotides (molecular beacons or FRET) where the target binding is translated into a fluorescence signal. Although these methods are quite unstable in biological environments and they require transfection agents to assist with cellular uptake that can be toxic [3, 241-243].

The use of SNAs for live cell mRNA detection was an approach to overcome the weaknesses of previously mentioned methods. In detail, SNA consists of the AuNP core and a thiol modified sense strand attached to AuNP's surface. A shorter fluorophore modified oligonucleotide is hybridised into the sense strand. It is termed flare strand. The design of the sense sequence is towards the detection of a specific mRNA target. Thus when the mRNA target binds, the flare strand will be released due to competitive hybridisation. This indicates the detection of the mRNA target since a fluorescence signal will be detected. In the absence of the target, the flare will remain attached to the sense strand and there will be no fluorescence signal from the dye since it will be quenched by the gold core [236, 237]. The fact that SNAs can enter a wide variety of cells without the need for transfection agents is a useful property for probes [3, 179, 244]. The internalisation of SNAs by various cell lines including primary cells and neurons after their addition to cell media was demonstrated by Giljohann and co-workers. It was presented the dependence of cellular uptake on the cell type, concentration, incubation time and especially DNA density. Bare citrate stabilised nanoparticles were tested as a control experiment and the cellular uptake was orders of magnitude lower than SNAs [200].

By observing the ability of SNAs to enter cells, there was a need for investigating the mechanism of uptake. Giljohann *et al*. proposed that the adsorption of proteins from cell culture media on the SNAs could be a possible mechanism of recognition and their subsequent internalisation [200]. It was supported that a decrease in oligonucleotide loading could lead to a decrease in protein adsorption and consequently, the cellular uptake was affected [200]. According to Narayan and co-workers, the sequence composition can also influence the intracellular delivery of SNAs by affecting the protein corona. It was observed that SNAs with G-rich content can have higher cellular uptake rates as they increased protein binding in number and type [245]. A proposed mechanism for SNA endocytosis suggested that SNAs bind strongly to scavenger receptors class A (SR-A) which mediate cellular uptake. As a result, SNAs enter the cells *via* the caveolae-mediated pathway since SNAs, SR-A and lipid-raft micro-domains are in close proximity [246, 247].

The use of SNAs is a promising tool for cancer diagnosis and treatment due to their great selectivity in cancer-related oligonucleotide sequences [240, 248-250]. In this thesis, the concept of the detection of vimentin cell-type-specific mRNA was developed. Vimentin has shown to be a marker of invasive epithelial cell-based lung cancer in conjunction with epithelial to mesenchymal transition.

Epithelial cells form primary tissues and are located throughout the body by developing sheets. They have many different functions based on morphology and location and they are non-motile, uniformly shaped and stationary cells [251]. Mesenchymal cells have an irregular shape and non-uniform composition or density. They do not display tight adhesion with other cells and are highly motile [251]. During embryonic development, wound healing, tissue regeneration, organ fibrosis, and cancer progression, the biological process of epithelial to mesenchymal transition (EMT) is crucial [252, 253]. EMT is a cellular process where epithelial cells obtain mesenchymal phenotypes and behaviour by downregulating the epithelial characteristics [254, 255]. This repression of the epithelial features and the acquisition of mesenchymal features can happen after changes in gene expression and post-translational regulation mechanisms [256]. The reverse process is called mesenchymal to epithelial transition (MET) and occurs frequently during development [255]. It has been proposed to classify EMTs into three subtypes based on the biological and biomarker context [254]. Type 1 EMT generates cells with a mesenchymal phenotype to create new tissue with various functions while type 2 EMT is associated with wound healing, tissue regeneration and organ fibrosis. In types 1 and 2, cells undergo either apoptosis or MET after completing their task [252]. In type 3 EMT, epithelial cancer cells migrate from the primary tumour location to a secondary tumour site [252, 257].

After the completion of EMT, previously stationary epithelial cells can migrate from the original epithelial layer. The biochemical changes depend on the up- or down-regulation of certain proteins. The intermediate filament protein and mesenchymal cell marker vimentin is a protein strongly up-regulated [258-260], while the epithelial cell marker cytokeratin 8 is strongly down-regulated [251]. Vimentin is a type III intermediate filament mostly expressed in mesenchymal cells of various types of tissue [14, 261]. It also represents a cell marker for cancerous cell types such as adenocarcinomic human alveolar basal epithelial cells (A 549) [262, 263] and human osteosarcoma cells (SAOS-2) [264]. Vimentin can be overexpressed and is correlated with tumour growth and progression [260, 261, 265]. Similarly, cytokeratin proteins are expressed in epithelial cells such as human bronchial epithelial cells (16 HBE) and are located in the intracytoplasmic cytoskeleton of epithelial tissue where they help resist mechanical stress [14, 266, 267].

Chapter 3 Experimental Procedures

This chapter includes all the experimental procedures for the synthesis and surface modification of nanoparticles described in **Sections 3.1** and **3.2**. Characterisation techniques for nanomaterials and cell culture studies are presented in **Sections 3.3** and **3.4**.

3.1 Synthesis of Colloidal Nanoparticles

3.1.1 Synthesis of 15 ± 1 nm spherical gold nanoparticles

Spherical AuNPs were synthesised based on wet chemistry approaches by producing monodisperse particles suspended in water. 15 ± 1 nm spherical AuNPs were synthesised using a citrate reduction method, developed by Turkevich and modified by Frens [20]. A solution of $NaAuCl_4$ in water (1 mM, 100 mL) was heated up to the boiling point under stirring at 700 rpm. Then, a hot sodium citrate solution in water (2% wt in water, 5 mL) was added under vigorous stirring. A colour change from yellow to colourless, and then to deep purple was observed. The final colour of the solution was wine red, indicating the formation of nanoparticles. The solution was left under stirring at 100 ^{o}C for 15 min and then cooled down to room temperature under slow stirring (200 rpm). When the solution reached room temperature, bis(p-sulfonatophenyl) phenyl phosphine dehydrate dipotassium salt (BSPP, 20 mg, MW = 534.62) was added to it to replace the citrate ligands on the surface of the nanoparticles. After stirring overnight at 125 rpm, a concentrated solution of sodium chloride (NaCl) was added until observing a colour change. The colour of the solution turned from a clear wine red to a cloudy dark brown indicating particle aggregation *via* charge screening. The solution was purified by centrifugation (5,000 rpm, 25 min) and re-dispersed in Milli-Q water. Further purification by filtration (syringe filter, 0.2 µm) was used to remove large aggregates. The final solution was stored at 4 ^{o}C.

3.1.2 Synthesis of large spherical gold nanoparticles

Large spherical AuNPs (> 20 nm) were synthesised following a kinetically controlled seeded growth strategy *via* the reduction of $NaAuCl_4$ by sodium citrate developed by Bastus *et al.* [29]. The Au seed solution was firstly prepared by heating a solution of sodium citrate in Milli-Q water (2.2 mM, 150 mL) under vigorous stirring. The solution was placed in a 250 mL three-neck round-bottom flask and a condenser was used to avoid solvent evaporation. Once the temperature reached 100 ^{o}C, the solution was left under stirring for 15 min, and then a solution of $NaAuCl_4$ (25 mM, 1 mL) was quickly injected. A colour change from yellow to bluish grey and then to light pink was observed within 10 min. The solution was cooled to 90 ^{0}C and a solution of $NaAuCl_4$ (25 mM, 1 mL) was immediately injected. After 30 min the initial generation of particles (g0) was formed. Then, the solution was diluted by extracting 55 mL of sample and adding 53 mL of Milli-Q water and 2 mL of sodium citrate solution (60 mM). This solution was then used as a seed solution and was injected with three consecutive $NaAuCl_4$ (25 mM, 1 mL) additions every 30 min at 90 °C to generate the next generation of particles (g1). This process was repeated to produce AuNPs of increasing sizes. After reaching the desired size of nanoparticles, the heating mantle was removed and the citrate-capped AuNPs were left to cool down to room temperature. The solution was purified by centrifugation (7,000 rpm, 15 min) and re-dispersed in Milli-Q water. The final solution was stored at 4 ^{0}C.

3.1.3 Synthesis of gold nanorods

Anisotropic AuNRs were synthesised using a modified seed-mediated protocol [40, 42, 268]. The seed solution was firstly prepared by heating a solution of CTAB (0.2 M, 1 mL) to 40 °C (see **Figure 3.1**). An aqueous solution of $NaAuCl_4$ (5 mM, 1 mL) was added to this. Then, an ice-cold solution of sodium borohydride ($NaBH_4$, 0.01 M, 0.5 mL) was injected dropwise into the solution under intense stirring. A colour change from yellow to brown was observed indicating the formation of small nanoparticles (~2 nm). The solution was left to stand at 40 ^{0}C after 2 min of intense stirring until the growth solution was prepared. The growth solution was prepared by heating a solution of CTAB (0.2 M, 14.24 mL) to 40 °C. An aqueous solution of $NaAuCl_4$ (5 mM, 2 mL) was added to this. Then, a solution of silver nitrate (5 mM, 50 – 400 µL) was pipetted into the reaction mixture. The AuNR aspect ratio can be adjusted by varying the volume of silver nitrate. A freshly prepared L-ascorbic acid solution (78.8 mM, 160 µL) was injected under gentle stirring and a colour change to colourless was noticed. After 30 s of slow stirring, the seed solution (16 µL) was added to the growth solution. The stirring was immediately interrupted and AuNPs were left to grow overnight at 40 °C. The colour of the solution changed depending on the amount of silver nitrate added and therefore the aspect ratio of AuNRs synthesised. AuNRs were purified by two rounds of centrifugation (6,000 rpm, 15 min) to remove excess CTAB and re-dispersed in Milli-Q water. The final solution was stored at 4 ^{0}C.

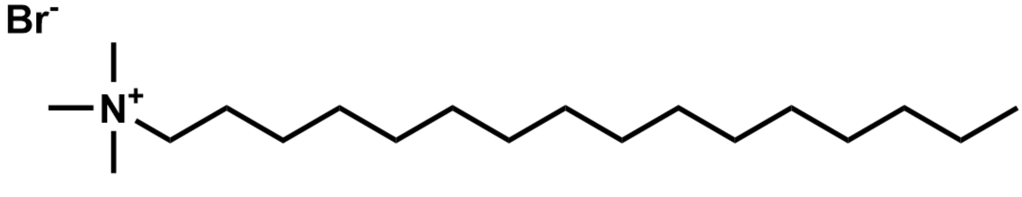

Figure 3.1 Chemical structure of CTAB.

3.1.4 Synthesis of branched gold nanoparticles

Branched AuNPs were synthesised using a modified seed-mediated growth protocol [269]. The growth solution was prepared by heating a solution of CTAB (0.2 M, 14.24 mL) to 40 °C. An aqueous solution of $NaAuCl_4$ (5 mM, 2 mL) and silver nitrate (5 mM, 410 µL) was added to this. 15 nm BSPP coated AuNPs (5 mM, 16 µL) were pipetted into the reaction mixture followed by a freshly prepared L-ascorbic acid solution (157.6 mM, 180 µL) under gentle stirring. The solution was left to slowly stir at 40 °C for 1 h 30 min. A colour change from colourless to blue was observed after the addition of L-ascorbic acid, indicating the formation of anisotropic AuNPs. Particles were purified by two rounds of centrifugation (8,000 rpm, 10 min) to remove excess CTAB and re-dispersed in Milli-Q water. The final solution was stored at 4 ^oC.

3.1.5 Synthesis of lanthanide-doped $NaYF_4$ (core upconversion nanoparticles)

The mechanism behind the synthesis of lanthanide-doped nanoparticles is based on the co-precipitation procedure involving the nucleation of $NaYF_4$ at a low temperature *via* the diffusion of metallic ions, and then the Ostwald ripening process at a higher temperature [112].

In more detail, hexagonal phase $NaYF_4$:Yb^{3+} (20%), Er^{3+} (2%) UCNPs were synthesised using a modified solvothermal method [70, 112]. The RE salts, $YCl_3·6H_2O$ (236 mg, 0.78 mmol), $YbCl_3·6H_2O$ (77.5 mg, 0.20 mmol), and $ErCl_3·6H_2O$ (7.63 mg, 0.02 mmol) were put in a 100 mL round-bottom flask together with oleic acid (6 mL, 90%) and 1-octadecene (15 mL, 90%). The solution was heated up to 150 ^oC under Argon (Ar) flow and left at this temperature for 1 h and 30 min. Then, the reaction mixture was cooled down to room temperature. A solution of NaOH (100 mg, 2.5 mmol) and NH_4F (148.16 mg, 4 mmol) dissolved in 10 mL of dry methanol (MeOH) was injected into the reaction mixture. After 45 min of stirring at room temperature, the solution was gradually heated up to 100 ^oC under Ar for other 30 min. Then, the reaction mixture was stirred under vacuum for 30 min to reassure the complete evaporation of the MeOH. Next, the temperature was increased to 310 ^oC under Ar and the solution was left under stirring for 1h 20 min to form the particles. Finally, the particles were left to cool down to room temperature. The solution was rinsed with ethanol (EtOH, 20 mL) and centrifuged (8,000 rpm, 15 min) three times so as to purify the particles. The nanoparticles' pellet was let to dry for several hours and its weight was measured. The resulting nanoparticles were re-dispersed in hexane or chloroform ($CHCl_3$) before using for further experiments.

Hexagonal phase $NaYF_4$:Yb^{3+} (20%), Tm^{3+} (0.5%) UCNPs were synthesised using a similar protocol by adding the corresponding $YCl_3·6H_2O$ (241.17 mg, 0.795 mmol), $YbCl_3·6H_2O$ (77.5 mg, 0.20 mmol) and $TmCl_3·6H_2O$ (1.92 mg, 0.005 mmol) at the initial step of the reaction.

Hexagonal phase NaYGd(30%)F_4:Yb^{3+} (20%), Er^{3+} (2%) UCNPs were synthesised following a similar protocol with some modifications in the $RECl_3 \cdot 6H_2O$ concentrations and the reaction time. The salt concentrations were $YCl_3 \cdot 6H_2O$ (145.61 mg, 0.48 mmol), $YbCl_3 \cdot 6H_2O$ (77.5 mg, 0.20 mmol), $ErCl_3 \cdot 6H_2O$ (7.63 mg, 0.02 mmol) and $GdCl_3 \cdot 6H_2O$ (111.51 mg, 0.30 mmol) and the solution in the final step of the reaction was maintained at 310 °C for 1 h 10 min under Ar.

Lanthanide-doped NPs are typically suspended in organic ligands, such as oleic acid or oleylamine, which bind to the nanoparticle surface to control the particle growth and stabilise the particles against aggregation. By modifying the amount of oleic acid as organic ligand, different shapes with different aspect ratios (AR) can be obtained.

3.1.6 Synthesis of a shell of lanthanide-doped $NaYF_4$ (core-shell upconversion nanoparticles)

Core-shell lanthanide-doped UCNPs were prepared following a previously published protocol [270]. Briefly, $YCl_3 \cdot 6H_2O$ (151.68 mg, 0.5 mmol) was dissolved in a solution of 1-octadecene (15 mL, 90%) and oleic acid (6 mL, 90%) and stirred for 1h under Ar at 150 °C. The solution was cooled down to 80 °C and core UCNPs (125 mg) in $CHCl_3$ (20 mg/mL) were added dropwise. After 20 min at 80 °C, the solution was gradually heated up to 100 °C under Ar and stirred for 45 min. Once the mixture was cooled down to room temperature under the Ar flux, a solution of NaOH (50 mg, 1.25 mmol) and NH_4F (74.08 mg, 2 mmol) dissolved in dry MeOH (5 mL) was added dropwise. Then, the solution was stirred for another 45 min at room temperature and it was gradually heated up to 100 °C under Ar. After 30 min at 100 °C under Ar, it was stirred for other 30 min at 100 °C under vacuum to ensure the complete evaporation of MeOH. Finally, the temperature was raised to 310 °C at a 15 °C/min rate under Ar and the mixture was stirred for 1 h 40 min to form the core-shell UCNPs. After completion of the reaction, the nanoparticles were left to cool down to room temperature. Then, EtOH (20 mL) was added to the nanoparticles solution and the mixture was centrifuged (8,000 rpm, 15 min). This process was repeated three times to purify the nanoparticles. The core-shell UCNPs were collected as white powder and re-dispersed in hexane or tetrahydrofuran (THF) before using for further experiments.

3.1.7 Wet annealing treatment of core-shell upconversion nanoparticles

A wet annealing protocol was used in order to improve the dispersibility of the UCNPs by increasing the amount of oleic acid molecules around each nanoparticle. Core-shell lanthanide-doped UCNPs were annealed following a previously published protocol [271]. In detail, core-shell UCNPs (10 mg/mL in hexane, 10 mL) were put in a 100 mL round-bottom flask together with oleic acid (8 mL, 90%) and 1-octadecene (12 mL, 90%). The solution was gradually heated up to 100 °C under Ar and stirred for 40 min. After evaporation of the hexane, the solution was heated up to 240 ^{0}C and maintained for 1 h 30 min under an Ar atmosphere. The resulting annealed UCNPs were left to cool down to room temperature. The solution was rinsed with EtOH (20 mL) and centrifuged (8,000 rpm, 15 min) three times so as to purify the particles. The annealed UCNPs were re-dispersed in hexane forming a transparent solution and stored for further use.

3.2 Surface Modification of Colloidal Nanoparticles

The surface of different types of nanoparticles was modified by single-stranded DNA or peptide sequences. All modified oligonucleotides were synthesised by Dr Afaf El-Sagheer in Prof. Tom Brown's group at the University of Oxford. All the sequences used in this work are reported in **Table 3.1** and **Table 3.2** below.

3.2.1 Design of oligonucleotide sequences

The National Centre for Biotechnology Information (NCBI) database (https://www.ncbi.nlm.nih.gov/nucleotide/) was used for the design of appropriate oligonucleotide sequences. The Basic Local Alignment Sense Tool (BLAST) was used with the following settings: Nucleotide-specific blast (blastn), Database: RefSeq mRNA, Species: Homo Sapiens, Expected Threshold: 10 Match/Mismatch scores: 2/-3. A sense sequence was designed to have a length of 21-30 bases, a GC content of < 50%, an E value of < 0.05 and an E value of nearest match > 1. A flare strand was designed to be complementary to the sense sequence with a length of 11-14 bases and a melting temperature of > 40 °C.

3.2.2 Synthesis of oligonucleotide sequences

Oligonucleotides were synthesised on an Applied Biosystems 394 automated DNA/RNA synthesizer using a standard 1.0 µmole phosphoramidite cycle of acid-catalyzed detritylation, coupling, capping and iodine oxidation. Stepwise coupling efficiencies and overall yields were determined by the automated trityl cation conductivity monitoring facility and were > 98%. Solid support 3' thiol-modifier C3 S-S CPG, 1000/110, item number: 2361, fluorescein-dT-CE phosphoramidite (6-FAM), item number: 2068, 5' fluorescein-CE phosphoramidite (6-FAM), item number: 2134, Cy-5-CE phosphoramidite (Cyanine 650), item number: 2521 and 5' TFA-Amino-Modifier C6-CE phosphoramidite, item number: 2124 were purchased from Link Technologies Ltd. Additional reagents were purchased from Link Technologies Ltd, Sigma-Aldrich, Glen research and Applied Biosystems Ltd. All β-cyanoethyl phosphoramidite monomers were dissolved in anhydrous acetonitrile to a concentration of 0.1 M immediately prior to use with a coupling time of 50 s for normal A, G, C, and T monomers and was extended to 600 s for modified monomers. The solid support was washed with 20% diethylamine in acetonitrile for 10 min. Cleavage and deprotection were achieved by exposure to concentrated aqueous ammonia solution for 60 min at room temperature followed by heating in a sealed tube for 5 h at 55 °C. Purification was carried out by reversed-phase HPLC on a Gilson system using a Brownlee Aquapore column (C8, 8 mm x 250 mm, 300Å pore) with a gradient of acetonitrile in triethylammonium bicarbonate (TEAB) increasing from 0% to 50% buffer B over 30 min with a flow rate of 4 mL/min (buffer A: 0.1 M TEAB, pH 7.0, buffer B: 0.1 M TEAB, pH 7.0 with 50% acetonitrile). Elution was monitored by ultraviolet absorption at 298 nm. After HPLC purification, oligonucleotides were freeze-dried and then dissolved in water without the need for desalting. All purified oligonucleotides were characterised by electrospray mass spectrometry. Mass spectra of oligonucleotides were recorded either using a Bruker micrOTOFTM II focus ESI-TOF MS instrument in ES-mode or a XEVO G2-QTOF MS instrument in ES-mode. Data were processed using MaxEnt and in all cases confirmed the integrity of the sequences.

3.2.3 Synthesis of peptide-DNA conjugate sequences

The peptide sequences were purchased from Peptide Protein Research Ltd in a lyophilised off-white powdered solid form with an azide modification. The oligonucleotide sequences were synthesised as described above. After HPLC purification and freeze-drying, the 5’ amine-modified oligonucleotides (20 nmol) were dissolved in 30 µL $Na_2CO_3/NaHCO_3$ buffer (0.5 M, pH 8) and labelled with DBCO-NHS (0.4 mg, 50 eq) in 20 µL of dimethyl sulfoxide (DMSO). The reaction mixture was incubated at 25 °C with shaking (750 rpm) for 4 h followed by desalting using a NAP-10 column. The DBCO labelled oligonucleotides were HPLC purified as discussed above. After freeze-drying, oligonucleotide sequences were diluted to 10 mM in water and peptide (10 mM in DMSO) was added. The reaction mixture was left overnight. Then, the use of a NAP-10 column followed by HPLC (as discussed above) gave the desired peptide-oligonucleotide conjugate.

Table 3.1 Oligonucleotide sequences used in the experiments.

Name	**Oligonucleotide Sequences (5’ to 3’) and Modifications**
vimentin (sense strand)	5’ FAM – CTT TGC TCG AAT GTG CGG ACT TAA AAA AAA – thiol 3’
vimentin (flare strand)	5’ Cy5 – AAG TCC GCA CA 3’
vimentin perfect DNA target	5’ AAG TCC GCA CAT TCG AGC AAA G 3’
vimentin perfect RNA target	5’ AAG UCC GCA CAU UCG AGC AAA G 3’
hspa8 (sense strand)	5’ FAM – AGC AGT ACG GAG GCG TCT TAC AAA AAA AAA – thiol 3’
hspa8 (flare strand)	5’ Cy5 – TGT AAG ACG CCT C 3’
hspa8 perfect DNA target	5’ GTA AGA CGC CTC CGT ACT GCT 3’
runx2 (sense strand)	5’ FAM – TGT GGT TGT TTG TGA GGC GAA TAA AAA AAA – thiol 3’
runx2 (flare strand)	5’ Cy5 – ATT CGC CTC ACA 3’
runx2 perfect DNA target	5’ ATT CGC CTC ACA AAC AAC CAC A 3’
scramble (sense strand)	5’ FAM – ATG GTA TAC CGA AAG ACT GTT AAA AA – thiol 3’
scramble (flare strand)	5’ Cy5 – AAC AGT CTT TCG 3’
scramble perfect DNA target	5’ AAC AGT CTT TCG GTA TAC CAT 3’
PolyT	5’ aminohexyl – TTT TTT TTT TTT TTT TTT TTT 3’
PolyA	5’ AAA AAA AAA AAA AAA AAA AAA AAA AAA AAA 3’
Non-complementary sequence (ncDNA)	5’ CTA GAT CCG TGT CCT CGT 3’
SARS-CoV-2 RdRP/Hel (sense strand)	5’ aminohexyl – GTC TAC GTA TGC AAG CAC CAC ATC TTA A 3’
SARS-CoV-2 RdRP/Hel (DNA target sequence)	5’ TTA AGA TGT GGT GCT TGC ATA CGT AGA C 3’
SARS-CoV-2 RdRP/Hel (RNA target sequence)	5’ UUA AGA UGU GGU GCU UGC AUA CGU AGA C 3’

Table 3.2 Peptide and peptide-DNA conjugate sequences used in the experiments.

Name	**Peptide Sequences and Modifications**
Aurein 1.2	GLFDIIKKIAESF – NH_2
Cysteine modified Aurein 1.2	CGLFDIIKKIAESF – NH_2
Name	**Peptide-DNA Conjugate Sequence**
vimentin conjugate	5’ GLFDIIKKIAESF – FAM – CTT TGC TCG AAT GTG CGG ACT TAA AAA AAA – thiol 3’
scramble conjugate	5’ GLFDIIKKIAESF – ATG GTA TAC CGA AAG ACT GTT AAA AA – thiol 3’

3.2.4 Synthesis of 15 ± 1 nm spherical nucleic acids

15 ± 1 nm spherical AuNPs were modified with a shell of oligonucleotides according to a well-established literature procedure which is known as the salt-ageing procedure [182]. The negative charge of the oligonucleotide phosphate backbone and the AuNP surface was screened by the gradual addition of a NaCl solution [199]. In this method, BSPP coated 15 nm spherical AuNPs (10 nM, 1 mL) in Milli-Q water were incubated with thiol-terminated oligonucleotides (3 µM, 1 mL) overnight so as to allow the solution to equilibrate. BSPP (1 mg/20 µL, 10 µL), phosphate buffer (0.1 M, pH 7.4) and SDS (10%) were added to the solution to reach a final concentration of 0.01 M phosphate and 1% SDS, respectively. The addition of NaCl was realised over a period of 8 h by six equal additions with a final concentration of 0.3 M. Following each salt addition, the solution was sonicated well to keep the particles well-dispersed during the salting procedure. After the NaCl additions, the solution was shaken overnight for further functionalisation of the AuNPs. Then, the sample was purified by three rounds of centrifugation (16,400 rpm, 20 min) to remove unbound oligonucleotides and re-dispersed in phosphate buffer saline (PBS). The solution was stored at 4 °C. The next step was the flare hybridisation where SNAs (16 nM, 500 µL) were mixed with an excess of complementary flare sequence (960 nM, 500 µL). The solution was heated to 75 °C for 2 min and then, was left to gradually cool to room temperature. The solution was purified by three rounds of centrifugation (16,400 rpm, 15 min) to remove unbound strands. Fully assembled SNAs were finally re-suspended in sterile PBS buffer and stored at 4 °C.

3.2.5 Surface modification of DNA functionalised 15 ± 1 nm spherical gold nanoparticles with peptide

The attachment procedure of peptide to the surface of 15 nm spherical oligonucleotide-coated AuNPs (10 nM, 1 mL) in PBS was conducted *via* incubation of the two solutions in an AuNP to peptide ratio of 1:3000. The peptide used for this functionalisation was cysteine modified Aurein 1.2 (MW = 1634.92). The sample was shaken overnight for further functionalisation of the DNA-AuNPs. Then, the solution was purified by one round of centrifugation (16,400 rpm, 20 min, 4 °C) to remove unbound peptides and re-dispersed in PBS. The supernatant solution was kept at 4 °C for further measurements.

3.2.6 Synthesis of DNA and peptide-coated gold nanoparticles

DNA and peptide-coated AuNPs were functionalised with numerous strands of DNA sense and cysteine modified Aurein 1.2 strands. The prepared conjugates in PBS were then mixed with the corresponding flare sequence (60 equivalents) and heated to 75 °C for 2 min. The sample was left to gradually cool to room temperature in order to allow for hybridisation to occur. The solution was then purified by centrifugation (16,400 rpm, 15 min) three times to remove unbound strands. Fully assembled nanoprobes were finally re-suspended in sterile PBS buffer and stored at 4 °C.

3.2.7 Surface modification of 15 ± 1 nm spherical gold nanoparticles with peptide-DNA conjugate sequences

15 ± 1 nm spherical AuNPs were incubated with different ratios of peptide-DNA conjugate sequences and DNA sequences to investigate the impact on the endosomal escape and then on the mRNA expression. The salt-ageing procedure was followed to screen the negative charge of the oligonucleotide phosphate backbone and the AuNP surface. Firstly, BSPP coated 15 nm spherical AuNPs (10 nM, 1 mL) in Milli-Q water were incubated with thiol-terminated oligonucleotides and thiol-terminated peptide-DNA conjugate sequences in different ratios (3 µM, 1 mL) overnight. Then, BSPP (1 mg/20 µL, 10 µL), phosphate buffer (0.1 M, pH 7.4) and SDS (10%) were added to the solution to reach a final concentration of 0.01 M phosphate and 1% SDS, respectively. The NaCl was added over an 8 h period by 6 additions with a final concentration of 0.3 M. After each salt addition, the solution was sonicated well to keep the particles well-dispersed during the salting procedure. Following the NaCl additions, the solution was shaken overnight for further functionalisation of the AuNPs. Then, the sample was purified by three rounds of centrifugation (16,400 rpm, 20 min) to remove unbound oligonucleotides and re-dispersed in PBS. The final solution was stored at 4 °C.

3.2.8 Ligand exchange on core-shell upconversion nanoparticles

A ligand exchange protocol was followed to coat the nanoparticle surface with PAA in order to bring the UCNPs into water [272]. In a typical reaction, PAA (0.25 g, MW ≈ 1.8 kDa) in THF (3 mL) was added to the core-shell UCNPs nanoparticles coated with oleic acid (21 mg) and redispersed in 7mL THF. The solution was stirred for 96h at room temperature and then centrifuged at 5,000 rpm for 15 min. After decanting the THF, the particles were washed twice with EtOH (20 mL) and isolated *via* centrifugation (5,000 rpm, 15 min) as a pellet. After drying for several hours, the particles were suspended in borate buffer (1 mM, pH 8.5) and stored at 4 °C.

3.2.9 Surface modification of PAA coated core-shell upconversion nanoparticles with synthetic oligonucleotides

The amino-modified oligonucleotides were attached to the surface of the PAA coated core-shell UCNPs *via* the carboxylic groups on the PAA ligand using EDC amino-coupling chemistry. A solution of EDC (0.3 M, 20 µL) and sulfo-NHS (0.3 M, 40 µL) in 4-morpholineethanesulfonic acid buffer (MES, 0.1 M, pH 5.5) was added to PAA coated core-shell UCNPs (0.5 mg/mL) suspended in borate buffer (1 mM, pH 8.5). The solution was shaken for 1 h and the desired amino-terminated oligonucleotide sequence was added (9 nmol). The reaction was stirred overnight, and the particles were purified by centrifugation (16,400 rpm, 4 °C, 30 min). The functionalised with DNA core-shell UCNPs were re-suspended in sterile PBS or DNase/RNase free Milli-Q water and stored at 4 °C.

3.3 Characterisation Techniques

3.3.1 Gel electrophoresis

3.3.1.1 Agarose gel electrophoresis

Gel electrophoresis is an essential tool for the purification of nanoparticles with DNA sequences. It depicts the movement of particles or molecules in a gel matrix under the presence of an electric field. The size and charge of particles or molecules determine the separation of the objects being analysed. Gel matrices have different pore sizes and densities in order to separate different populations within the same sample as the electrophoretic mobility changes. Agarose gel electrophoresis was applied for sample analysis and purification of nanoparticles because of the larger pore size within the matrix, which lies from a few hundred nanometres for a 1% gel [273, 274].

Gels were prepared by dissolving agarose (2%) in 0.5 × Tris borate EDTA (TBE). Then, this was heated in a microwave oven for 5 min avoiding to boil the solution. Once all agarose had completely dissolved and melted, the solution was poured into a gel cast and combs were inserted to form wells. After letting it stand for 2 h, the gel was placed in the electrophoretic buffer chamber containing 0.5 × TBE to cover its surface. Before adding the samples to the wells, they were mixed with a Ficoll solution, a high-mass polysaccharide (15% in 3 × TBE) to increase the density of the sample. The loaded gel was electrophoresed at 10 V/cm for approximately 50 min or until having a clear visual separation between the bands. The resulting bands of interest were extracted from the gel and cut into small pieces. They left overnight shaking in 0.5 × TBE buffer to allow the sample to dissolve out of the gel. The recovered sample was then filtered (syringe filter, 0.2 µm) and centrifuged three times (16,400 rpm, 15 min). The final sample was re-dispersed in Milli-Q water or PBS.

3.3.1.2 Polyacrylamide gel electrophoresis (PAGE)

Polyacrylamide gel electrophoresis (PAGE) is used as a technique for separating small molecules such as nucleic acids depending on their electrophoretic mobility [275]. According to the concentration of the polyacrylamide, the pore size of PAGE gels can range from a few tens of nanometres to several hundred nanometres.

A 6% PAGE gel was prepared in a 70 mL volume. A solution containing a 40% acrylamide: bis-acrylamide (19:1) solution (10.5 mL), 5 × TBE (14 mL) and Milli-Q water (45.5 mL) was prepared. The addition of an initiator, an ammonium persulfate (APS, 560 µL) and a crosslinker, N, N, N', N'-tetramethylethylenediamine (TEMED, 56 µL) initiated the polymerization process. The solution was immediately syringed into the glass cast and a comb was placed to create the wells on top of the gel. After leaving to polymerise for 2 h at 4 °C, the comb was removed, and the gel was placed in a 1 × TBE buffer inside the electrophoresis chamber. The oligonucleotide samples (40 µL) were mixed with a Ficoll solution (15% in 3 × TBE, 5 µL) to increase the density of the sample and avoid floating. Then, the samples were loaded into the wells of the gel. A molecular marker (ladder) of known molecular weight (10 µL) was loaded in a separate lane in the gel to calibrate the gel. A power supply from BioRad was used for running the gel at 110 W for 25 min. Subsequently, the gel was removed from the glass cast and stained with a Diamond^{TM} Nucleic Acid Dye (20 µL) for 10 min before imaging on a tray in a Syngene Gene Genius bioimaging system under UV illumination.

3.3.2 Spectroscopy techniques

3.3.2.1 Ultraviolet-Visible spectroscopy

Ultraviolet-Visible Spectroscopy (UV-Vis) is widely used as a technique for monitoring the intensity of absorbing materials which are scanned over the ultraviolet and visible range of light. The concentration of gold colloids and oligonucleotide solutions was determined by observing the absorption intensity over a wavelength scanning from 200 to 800 nm. A black low volume quartz cuvette was placed in a Shimadzu UV-Visible spectrophotometer (UV-2700) to collect the spectra. The concentration of the solution can be calculated from the corresponding absorption spectrum by using the Beer-Lambert law:

$$A = \frac{\varepsilon \cdot c \cdot l}{D} \Rightarrow c = \frac{A \cdot D}{\varepsilon \cdot l}$$

Equation 3.1 Rearranged Beer-Lambert equation used to calculate the concentration of solutions, where A = absorbance at the peak maximum (a.u.), c = concentration of the compound in the solution (M), ε = extinction coefficient ($L \cdot mol^{-1} \cdot cm^{-1}$), D = dilution factor, l = path length of light (cm).

The type and the size of the AuNPs define the extinction coefficient value [276] while for the oligonucleotides it is sequence-dependent and is calculated using the nearest neighbour or base composition model [277, 278]. The extinction coefficient value for 15 ± 1 nm spherical AuNPs is $\varepsilon = 2.27 \cdot 10^8\ L \cdot mol^{-1} \cdot cm^{-1}$.

3.3.2.2 Oligonucleotide loading on spherical gold nanoparticles

The quantification of the number of oligonucleotides attached to the surface of AuNP after the salt-ageing procedure was determined *via* dissolution of the gold core using a solution of KI/I_2 in a ratio of I_2 to KI at 1:6. The KI/I_2 solution was slowly added (1 µL per addition) to the oligonucleotide-coated AuNPs solution (8.33 nM, 120 µL) and a colour change was observed from wine red to yellow which means the successful gold core dissolution [279]. The total solution was diluted with MilliQ water up to 1 mL and loaded onto a NAP-10 desalting column. After this volume entered the column, it was eluted with MilliQ (1.5 mL). A DeNovix DS-11 spectrophotometer was used to measure the oligonucleotide absorbance (also referred to as optical density or O.D.) at 260 nm. Both the obtained and the initial absorbance value of the oligonucleotide solution synthesised by Dr Afaf El-Sagheer were used for calculating the concentration and therefore the number of moles of oligonucleotides in the solution. Then, using this information and the Beer-Lambert law it was calculated the number of oligonucleotide sense strands attached to the surface of each AuNP.

3.3.2.3 Peptide sequence loading on DNA-coated spherical gold nanoparticles

It is essential to quantify the number of peptides attached to the surface of DNA-coated AuNP after the incubation procedure. Ellman introduced 5,5'-dithio-bis-(2-nitrobenzoic acid), also known as DTNB, as a versatile water-soluble compound for quantitating free sulfhydryl groups in solution. The materials needed for the quantification were the reaction buffer which consisted of sodium phosphate (0.1 M, pH 8.0) containing EDTA (1 mM) and the Ellman's reagent solution (see **Figure 3.2**) which consisted of Ellman's Reagent (4 mg, MW = 396.35) dissolved in 1mL of reaction buffer. A tube containing 50 µL of Ellman's reagent solution and 2.5 mL of reaction buffer was prepared and then 250 µL of the supernatant which contained the free non-conjugated peptide was added. The solution was mixed and incubated at room temperature for 15 minutes. The concentration of the free sulfhydryls and hence the number of peptides were calculated by measuring the absorption at 412 nm.

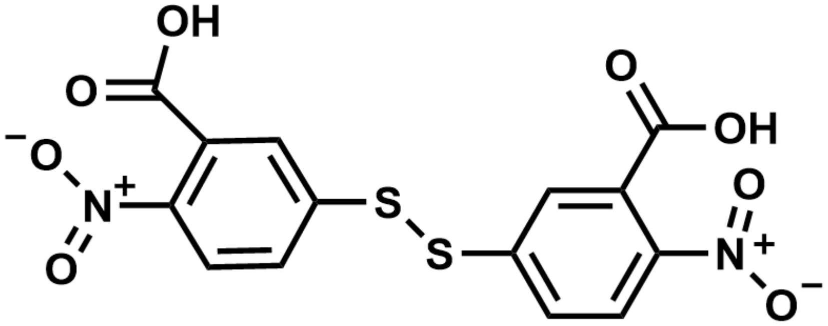

Figure 3.2 Chemical structure of Ellman's reagent.

3.3.2.4 Fluorescence melting analysis of sense/flare oligonucleotides

Fluorescence spectroscopy is a method to analyse light-emitting specimens and is based on the radiative relaxation of a molecule from an excited to a lower state. Samples are excited at a specific wavelength (647 nm for Cy5) and the emitted light is recorded at higher wavelengths (665 nm for Cy5).

The increase in fluorescence intensity of the fluorophore modified oligonucleotide flare strand was monitored as the temperature gradually increased on the sense/flare duplex [280]. Fluorescence melting analysis of all samples was performed on a Carry Eclipse Fluorescence Spectrophotometer using a low volume black quartz fluorescence cuvette. Functionalised AuNPs (2.5 nM, 200 µL) in PBS were gradually heated (0.1 ^{o}C / min) from 25 ^{o}C to 70 ^{o}C and then the solution was cooled to room temperature at the same rate.

3.3.2.5 DNase I nuclease assay

Functionalised AuNPs (150 µL, 2.5 nM) were incubated with Deoxyribonuclease I (DNase I, from bovine pancreas, Sigma Aldrich, 2 U/L) in a solution containing Tris-HCl (10 mM), $MgCl_2$ (2.5 mM) and $CaCl_2$ (0.5 mM) at pH 7.4. The sample was incubated at 37 °C and the fluorescence of the dye at the 5' end of the sense strand (FAM) was monitored during a 72 h incubation period to determine the degree of degradation to the sense strands (excitation: 495 nm, emission: 505 – 800 nm). All experiments were performed in triplicates. If the oligonucleotides were attached to the surface, the fluorescence from the dye would be quenched by the gold core. If the oligonucleotides were cleaved due to enzymatic degradation, there would be a fluorescence signal due to the dyes' release.

3.3.2.6 Fluorescence measurements of upconversion nanoparticles

The emitted fluorescence of a suspension of UCNPs was monitored in a home-built setup with a continuous wave 980 nm 300 mW diode laser (Thorlabs) as the excitation source and a fibre-coupled grating SpectraSuite Spectrometer detector (USB4000, OceanOptics, USA). The emission was collected at an angle of 90° using a 35 mm focal length lens. A short pass IR-blocking filter (Schott KG3) and a narrowband optical filter centred at 545 nm (Thorlabs) were used to suppress scattered excitation light and select only the fluorescence emission. The setup was built and aligned by Prof. Otto Muskens. All samples were measured using a quartz cuvette with a path length of 10 mm and each measurement was performed with 1 second of integration time and 10 scans to average. Three independent measurements were collected for each result and the fitted data corresponded to the mean value ± standard error of the mean (see **Appendix B**).

3.3.2.7 Sensor calibration

In order to accurately calibrate the DNA sensor based on UCNPs and two-dimensional materials, increasing concentrations of two-dimensional materials were added to a solution containing a fixed concentration of functionalised UCNPs (0.5 mg/mL) dispersed in sterile PBS or DNase/RNase free Milli-Q water. The corresponding fluorescence spectra of the DNA coated UCNPs were monitored to determine the concentration of the two-dimensional materials that would result in optimum fluorescence quenching.

3.3.2.8 Targeted DNA/RNA detection using DNA coated UCNPs

To prevent the interaction between the single-stranded DNA coated UCNPs and the two-dimensional materials, the single-stranded DNA was hybridised with its complementary sequence before incubating with the two-dimensional material. For this purpose, 0.5 mg/mL of single-stranded DNA coated UCNPs were incubated in PBS or DNase/RNase free Milli-Q water with various concentrations of the complementary DNA or RNA strand (ranging from 5 fM to 50 nM) while shaking. After this, a solution of two-dimensional material dispersed in PBS was added and left incubating for 10 min before performing the fluorescence measurements.

3.3.2.9 Fourier-transform infrared spectroscopy

Fourier-transform infrared spectroscopy (FT-IR) was used to observe the successful ligand exchange and DNA attachment *via* EDC/sulfo-NHS coupling on UCNPs. In detail, 5 mg of PAA coated UCNPs and single-stranded DNA coated UCNPs were dried and deposited directly on the instrument surface. A Nicolet iS5 FT-IR Spectrometer (Thermo Fisher) was used for samples' measurements. Each measurement was collected in the spectral range of 525 and 4000 cm^{-1} at room temperature.

3.3.3 Microscopy techniques

3.3.3.1 Transmission electron microscopy

Transmission electron microscopy (TEM) relies on the transmission of a beam of electrons through a specimen to form an image. The size and the morphology of the synthesised nanoparticles were observed on a Hitachi HT7700 TEM operating at an accelerating voltage of 100 kV. A small amount (~7 µL) of all samples were deposited on 400 mesh copper grids with a Formvar and a carbon coating and then left to air to dry overnight. Images of the nanoparticles were analysed by using ImageJ software (National Institutes of Health, USA) and the size distribution histograms were obtained by using Origin software.

3.3.3.2 Confocal microscopy

Confocal microscopy is an optical imaging technique used for the analysis of fluorescent specimens. Direct non-invasive imaging of thick specimens such as cells *via* the use of fluorescent dyes or probes is provided by confocal observation. The fluorescence of modified AuNPs with fluorescent oligonucleotides and peptides incubated with cells was monitored on a Leica TCS SP8 confocal microscope using a x 63 oil immersion objective. A Diode 505, a He-Ne 633, an Argon and a DPSS 561 were the lasers that were used for imaging. The appropriate settings are presented in the following table (**Table 3.3**).

Table 3.3 Confocal microscope imaging settings used to monitor the fluorescence of each dye.

Fluorescent dyes	Excitation laser line
Hoechst 33342	405 nm UV
FAM	488 nm VIS
Cy5	633 nm VIS

3.3.4 Scattering techniques

3.3.4.1 Dynamic light scattering

Dynamic light scattering (DLS) was used to monitor the size of colloidal nanoparticles suspended in a liquid medium. This technique relies on the Brownian motion and the Rayleigh scattering. During this process, the sample is illuminated using a monochromatic light source (laser beam), which causes the molecules to scatter light in all directions. This scattered light creates an interference pattern, which due to the constant movement of particles within the liquid medium constantly fluctuates. The hydrodynamic diameter is calculated with the Stokes-Einstein relation by analysing the fluctuations within the sample and correlating them to the diffusion coefficient of the sample (**Equation 3.2**).

$$R_H = \frac{k\,T}{6\,\pi\,\eta\,D}$$

Equation 3.2 Stokes-Einstein equation used to calculate the hydrodynamic radius of colloidal nanoparticles, where R_H = hydrodynamic radius, k = Boltzmann's constant, T = temperature, D = diffusion coefficient and η = viscosity of the medium.

All samples (1 mL) were placed in disposable cuvettes and measured on a Malvern Zetasizer Nano ZS with a He-Ne light source at 633 nm wavelength. Each measurement was performed with a 173° backscattering arrangement and consisted of 10 sub-runs of 15 s in three independent measurements at 25 °C.

3.3.4.2 Zeta potential

Zeta potential is the charge developed at the interface between the solid surface of the nanoparticle and its liquid medium. It is a useful tool to shed light on the state of the nanoparticle surface and to monitor the stability of a colloidal dispersion. An electric field is applied across the sample and the velocity of the particles moving through the solution is measured in order to determine the zeta potential. This is the electrophoretic mobility which is correlated with the zeta potential as described in **Equation 3.3**. The electrophoretic mobility is measured by a laser light source that is split to give an incident and a reference beam. The incident beam passes through the solution and the scattered light is detected. When an electric field is present, the nanoparticles move in the solution and pass through the measurement volume which causes fluctuations proportional to the particle speed. For the calculation of zeta potentials of dispersed colloidal systems containing spherical particles, the Smoluchowski approximation is used in Henry's function. For a low κα, Henry's function approaches the value 1 while for large κα, it approaches the value 1.5. These values refer to the borderline values that Henry's function can obtain and are known as Hückel and Smoluchowski equation.

$$U_E = \frac{2\,\varepsilon\,\zeta\,f(\kappa\alpha)}{3\,\eta}$$

Equation 3.3 Henry equation used to present the relationship between zeta potential (ζ) and electrophoretic mobility (U_E), where ε = dielectric constant, η = viscosity of the medium and f(κα) = Henry's function.

Zeta potential measurements of suspended nanoparticles in solution were recorded by a Malvern Zetasizer Nano ZS with a He-Ne light source at 633 nm wavelength and collection angle 173°. All nanoparticles were dispersed in Milli-Q water. Disposable capillary cells were used for all measurements. Average net charges were determined from at least 10 sub-runs in three independent measurements at 25 °C.

3.4 Cell Cultures

Two model cell lines were used to investigate the interaction of nanoparticles with live cells. Adenocarcinomic human alveolar basal epithelial cells (A 549) and human osteosarcoma cells (SAOS-2) were cultured to observe the intracellular behaviour of nanoparticles for mRNA detection.

3.4.1 Subculturing of cells

A 549 and SAOS-2 cell lines were cultured in Corning cell culture flasks using Minimum Essential Medium (MEM), which was supplemented with 100 U penicillin - 100 mg streptomycin, 0.29 mg/mL of L-glutamine, 1 mL nystatin and 10% fetal bovine serum (FBS). The cells were kept at 37 °C in a 5% CO_2 atmosphere in a Sanyo CO_2 incubator. Cells were left to grow up to 90% confluency after which they were passaged. For passaging, the medium was first removed and replaced with Hank's Balanced Salt Solution (HBSS, 10 mL, 5 min) after which cells were displaced using trypsin (5 mL, 0.25% trypsin, 0.01% EDTA solution). After 3 minutes of incubation with the trypsin, a full growth medium with serum (13 mL) was added to inactivate the trypsin. The cell suspension was pelleted by centrifugation (1,000 rpm, 5 min) and re-suspended in MEM (600 – 1200 µL). To maintain cell stocks a small amount of cell suspension (100 µl) was seeded in a new cell culture flask already containing MEM (13 mL). For building up cell stocks, the whole amount of cell suspension was seeded in several new cell culture flasks.

3.4.2 Cell incubation with functionalised gold nanoparticles

A µ-slide with 8 wells and a glass bottom was used to grow cells at a density that reached 90% confluent within 3 days. Once cells reached 90% confluency, they were incubated with Hoechst 33342 (2 µL, 30 min) to stain the nuclei. Then, the medium was replaced by a fresh medium containing surface-modified nanoparticles. The imaging was performed on a Leica SP8 confocal microscope at 37 °C under a constant flow of CO_2 to provide a healthy environment for the cells. Images of cell behaviour upon nanoparticles' uptake were recorded at different time points.

3.4.3 Ultra-thin sectioning of cells for transmission electron microscopy

The intracellular fate and location of functionalised nanoparticles after cellular uptake was investigated. Cells were fixed and embedded in resin and ultra-thin sections were cut and observed by TEM. Prior to fixation, cells were seeded on cellulose transwell inserts in 12 well plates at a cell concentration of 1×10^5 cells/mL for SAOS-2 and 0.5×10^5 cells/mL for A 549 cells. When cells reached 90% confluency, they were incubated with functionalised nanoparticles for 18 h. Then, they were fixed for 1 h in 4% formaldehyde/3% glutaraldehyde in piperazine-N,N′-bis(2-ethanesulfonic acid) (PIPES, 0.1 M, pH 7.2). Two washing steps followed (10 min each) with PIPES buffer. Cells were treated for 1h with a 1% osmium tetroxide in PIPES buffer and then two more steps of PIPES buffer (10 min each) followed. After rinsing briefly with deionized water, cells were stained with a solution of 2% (aq) uranyl acetate for 20 min. Samples were then dehydrated by incubating with increasing percentages of EtOH solutions (30, 50, 70, 95%) for 10 min each. After incubation in 50% EtOH, transwell inserts were cut from the plastic wells to avoid plastic dissolution from EtOH in high alcohol concentrations. Transwell membranes were placed in glass vials and allowed for complete dehydration by two more washes (20 min each) in absolute EtOH. Due to further preparation for resin embedding, samples were treated with acetonitrile for 10 min followed by 1:1 acetonitrile:SPURR resin overnight. The sample was then completely embedded in pure SPURR resin and left for 6 h, after which transwell samples were cut in half. Each part of the sample was embedded in fresh SPURR resin in small embedding capsules and polymerized at 60 °C for 24 h. Resin blocks were cut using a Leica RM 2255 ultramicrotome. Ultrathin sections of cells

(~100 nm) were collected and placed on TEM grids. Reynold's lead stain was used to stain the sections. Samples were observed under a Hitachi HT7700 TEM.

3.4.4 AlamarBlue® cell viability assay

AlamarBlue® cell viability assay was used as its cell viability reagent used the reducing power of living cells to measure the proliferation of various cell lines. When cells are alive they maintain a reducing environment within the cytosol of the cell. The active ingredient of the AlamarBlue® reagent is resazurin which is non-toxic, cell-permeable, blue in colour and optically non-fluorescent. When resazurin entered cells, it was reduced to resorufin, a compound that is red in colour and highly fluorescent. Viable cells converted resazurin to resorufin continuously and as a result, the colour of the medium and the overall fluorescence increased. Cells were seeded in 24 well plates up to 90% confluency. Then, they were incubated with surface-modified nanoparticles. After, cells were washed with warm PBS and replaced by a 10% AlamarBlue® solution in a warm complete medium (MEM) including the blank cells. After 3 h of incubation at 37 °C in the dark, a small amount (100 µL) of cell medium with AlamarBlue® was transferred to a black flat-bottomed 96 well plate. Cell viability was calculated based on triplicates of experiments.

Chapter 4 Synthesis of Colloidal Nanoparticles

The fabrication of highly monodisperse particles with precise control over shape, size and surface chemistry is crucial for the synthesis of functional nanomaterials. Biocompatible colloidal nanoparticles have been synthesised and further functionalised by using modified synthetic protocols. This chapter includes the results and discussion of the synthesis of various types of colloidal nanoparticles. The synthesis of AuNPs of different shapes and sizes such as spherical AuNPs (see **Section 4.1.1** and **4.1.2**), AuNRs (see **Section 4.1.3**) and branched AuNPs (see **Section 4.1.4**) is presented in **Section 4.1**. The synthesis of core and core-shell UCNPs is demonstrated in **Section 4.2.1** and **Section 4.2.2**, respectively.

4.1 Synthesis of Gold Nanoparticles

4.1.1 Synthesis of 15 ± 1 nm spherical gold nanoparticles

15 ± 1 nm AuNPs were synthesised in an aqueous solution using a bottom-up approach which was based on the reduction of Au(III) to metallic Au(0) by trisodium citrate. This method was initially introduced in 1951 by J. Turkevich [18, 19] and improved by G. Frens [20]. The use of trisodium citrate plays an important role in the synthesis of spherical and monodisperse nanoparticles as it is the reducing agent and acts as the capping ligand that electrostatically stabilises the formed AuNPs and protects against aggregation. Trisodium citrate adsorbs onto the surface of Au atoms through its carboxylate groups with various binding modes [281]. Hence AuNPs have a net negative charge that results in their electrostatic repulsion according to the Derjaguin, Landau, Verwey and Overbeek (DLVO) theory. According to this theory, this negative charge is based on the combined effect of van der Waals and electrical double layer forces [282]. Although, at higher salt concentrations or in the presence of divalent cations, AuNPs are still prone to aggregation due to the weak electrostatic interactions between the AuNP surface and the citrate ligand [283]. As a result, the bulky phosphine ligand BSPP is used to replace citrate molecules *via* a ligand exchange process as presented in **Figure 4.1**.

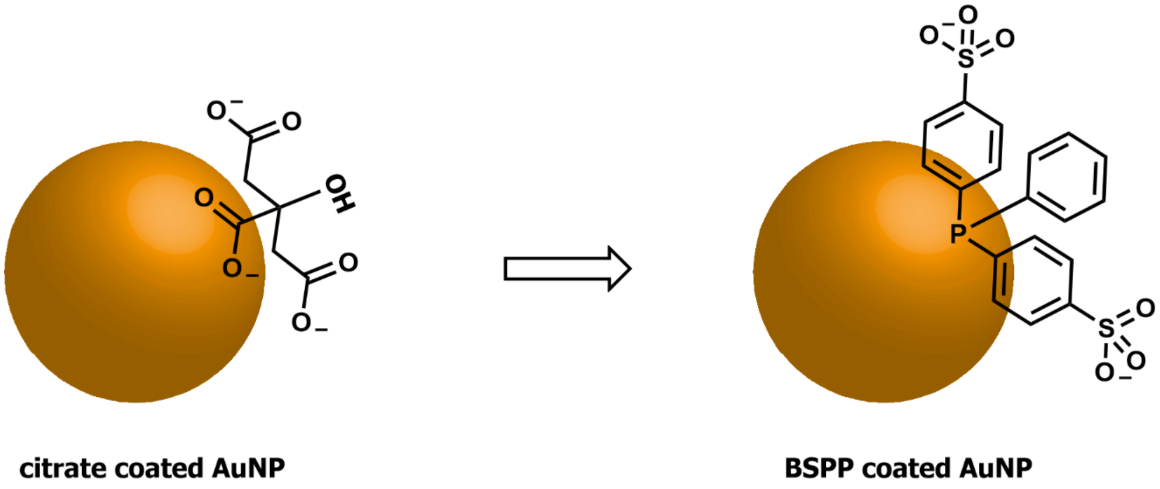

Figure 4.1 Schematic representation of citrate coated spherical AuNP and BSPP coated spherical AuNP.

The use of BSPP as a capping agent was first introduced by Schmid *et al*. in 1991 [284]. The phosphine group replaces the citrate ligand due to its higher affinity for the gold surface. Phosphines bind to the gold surface *via* the phosphorus' lone electron pair which is a stronger bond than the electrostatic interactions between citrate and gold but not as strong as the gold-sulfur bond [285]. BSPP is water-soluble and improves the stability of the spherical AuNPs [286]. This enhanced stability stems from the steric hindrance due to the large aromatic rings of the BSPP molecules and the negative charges of the sulfonate groups [285]. AuNPs functionalised with BSPP remain stable for high nanoparticle concentrations and can be reversibly aggregated by using salt which allows the precipitation of a nanoparticle solution by centrifugation [287].

Synthesised particles were characterised by TEM and UV-Vis. **Figure 4.2** shows a representative TEM image of spherical AuNPs with a size distribution of 15 ± 1 nm. The size distribution of the particles was determined by counting ~200 spherical AuNPs using ImageJ software (National Institutes of Health, USA). The absence of larger aggregates was a strong indication that the particles were colloidally stable in solution.

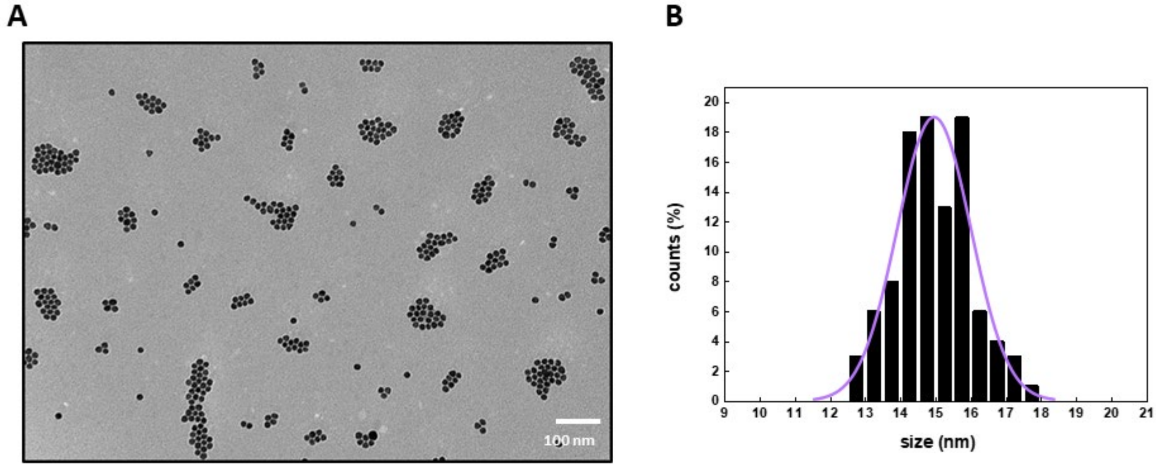

Figure 4.2 (**A**) TEM image of 15 ± 1 nm spherical AuNPs synthesised according to the citrate reduction method. (**B**) Histogram showing the size distribution of the spherical AuNPs. Scale bar is 100 nm.

Colloidal stability was also assessed by UV-Vis spectroscopy. **Figure 4.3** shows a representative UV-Vis spectrum of the synthesised AuNPs. A characteristic narrow peak was observed at 518 nm, which is typical for monodisperse 15 nm spherical AuNPs. The extinction peak for citrate coated spherical AuNPs had a maximum at 518 nm while after ligand exchange with BSPP, the BSPP coated spherical AuNPs had a slight red-shift peak (~1.5 nm). This red-shift is due to an increase in the refractive index of the immediate environment surrounding the nanoparticle core induced by the adsorption of BSPP molecules on the AuNPs' surface [288].

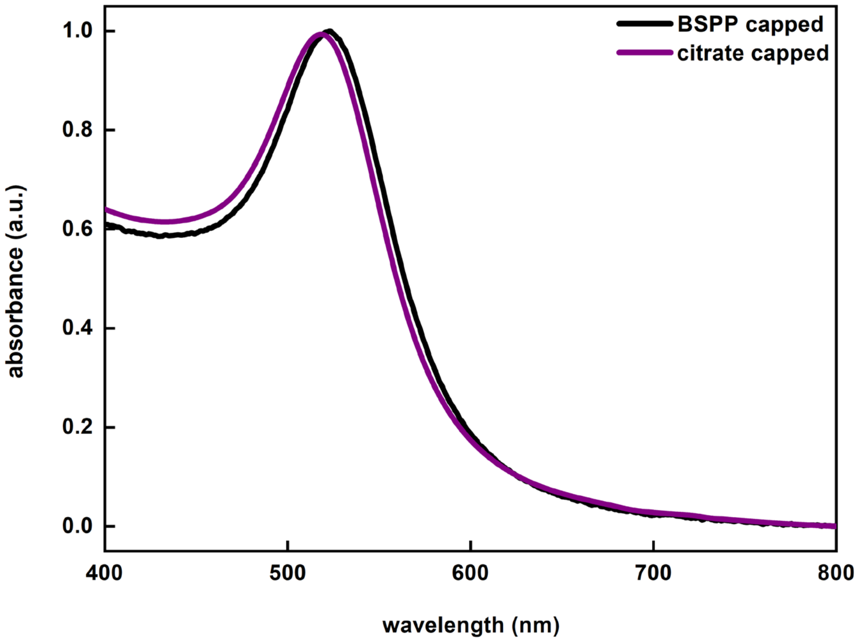

Figure 4.3 Normalised UV-Vis spectra of citrate and BSPP coated 15 ± 1 spherical AuNPs.

The formation of a monodisperse colloidal solution is demonstrated in **Figure 4.3** due to the single and sharp peak at 518 nm. A broad peak would indicate a polydisperse colloid solution, whereas aggregation would be visible as a secondary peak in the 700 nm region.

4.1.2 Synthesis of large spherical gold nanoparticles

Larger spherical AuNPs were synthesised in an aqueous solution using a seed-mediated growth approach developed by the Puntes group (see **Section 3.1.2**) [29]. This method involved the use of small spherical AuNPs as seeds that were firstly synthesised by the reduction of sodium tetrachloroaurate (III) dihydrate by sodium citrate at 100 °C. To prevent the formation of new seeds, the temperature was lowered to 90 °C and more gold and citrate precursors were added to enlarge the pre-synthesised AuNPs. After every three consecutive gold precursor additions, part of the solution was extracted for further analysis (termed generation *n*) and the rest was further grown into larger size AuNPs. In this thesis, AuNPs of up to generation 6 (g6) were synthesised and analysed. The success of this reproducible approach was based on the detailed adjustment of the different conditions such as temperature, seed concentration and reaction pH. The decrease in the temperature of the solution allowed the slowing of the reaction and prevented any secondary nucleation. The control of the number of Au atoms injected in each growth step allowed the shifting of the system towards the focusing conditions and narrowed the AuNP final distributions. The control of the pH level allowed control of the reactivity of the gold species, which was a crucial point in improving the monodispersity of the particles.

Synthesised particles were characterised by TEM and UV-Vis. **Figure 4.4** shows the morphological characterisation of AuNPs obtained after different growth steps and their size distribution. The final size of the particles increased as the number of growth steps increased. The size distributions were measured showing an average size of 12.8 ± 0.1 nm for the seeds (g0), 20.7 ± 0.2 nm for the first growth (g1), 26.2 ± 0.2 nm for the second growth (g2), 31.2 ± 0.2 nm for the third growth (g3), 38.6 ± 0.8 nm for the fourth growth (g4), 45.5 ± 2.6 nm for the fifth growth (g5) and 56.4 ± 0.6 nm for the sixth growth (g6). The size distribution of the particles was determined by counting ~200 AuNPs using ImageJ software (National Institutes of Health, USA).

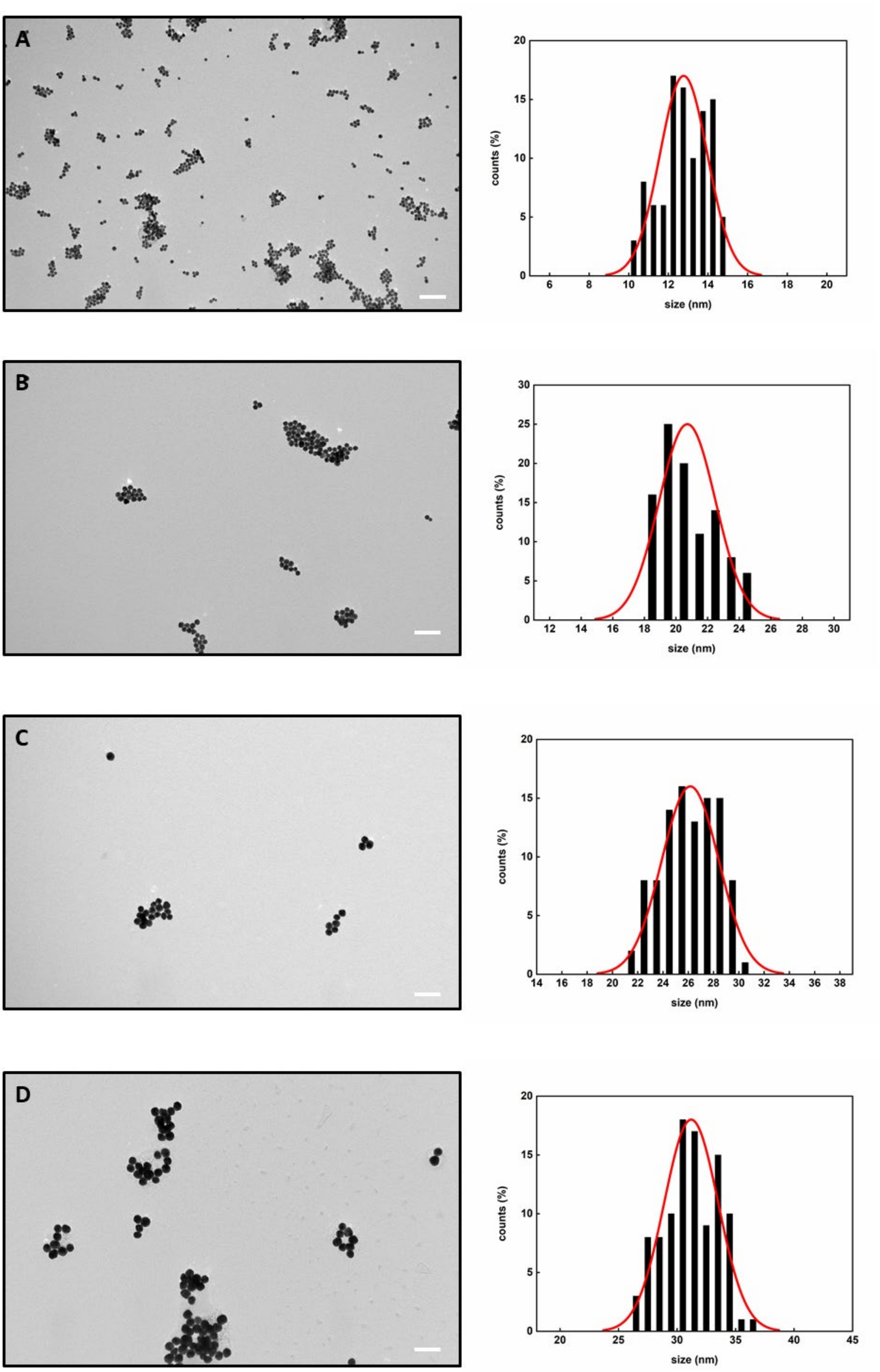
A
B
C
D
counts (%)
size (nm)
0
5
10
15
20
25
30
6
8
10
12
14
16
18
20
22
24
26
28
30
32
34
36
38
40
45

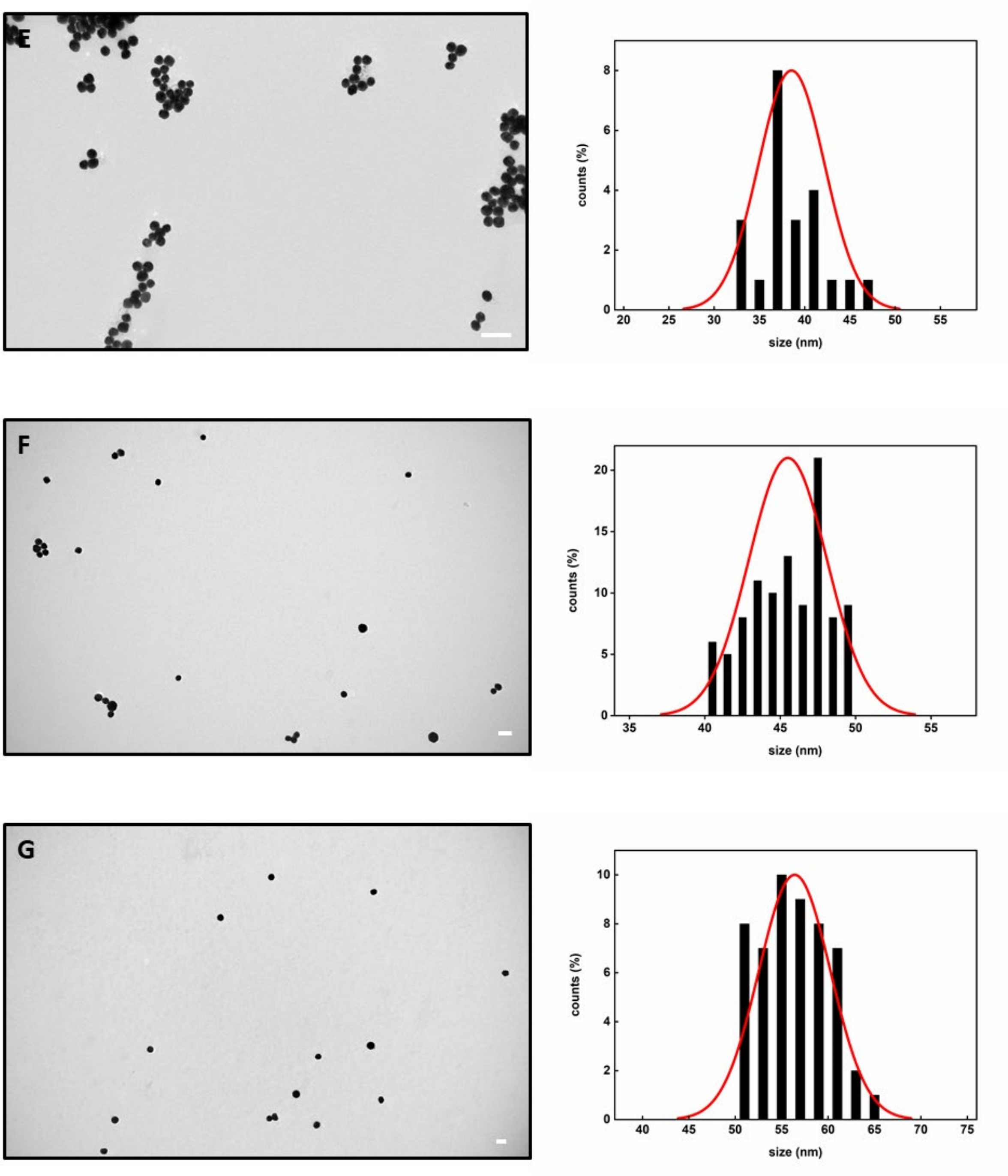

Figure 4.4 TEM images and corresponding size distribution histograms of spherical AuNPs at different stages of the synthesis: (**A**) seeds, (**B**) first growth, (**C**) second growth, (**D**) third growth, (**E**) fourth growth, (**F**) fifth growth and (**G**) sixth growth. Scale bars are 100 nm.

The optical properties of the gold colloidal solutions were measured by UV-Vis spectroscopy. **Figure 4.5** presents the normalised surface plasmon absorption spectra, which redshifted as a consequence of particle growth. The plasmon resonance peak was at 520 nm for the seeds (g0), 523 nm for the first growth (g1), 527 nm for the second growth (g2), 528 nm for the third growth (g3), 532 nm for the fourth growth (g4), 537 nm for the fifth growth (g5) and 544 nm for the sixth growth (g6) spherical nanoparticles. This shift of the plasmon band was in good agreement with previously published results [29]. For larger nanoparticles, this red-shift was due to the phase retardation of the light as it interacted with a particle of size comparable to its wavelength [94, 289, 290]. Moreover, the lack of shoulders or secondary peaks indicated that the nanoparticles were spherical and uniform.

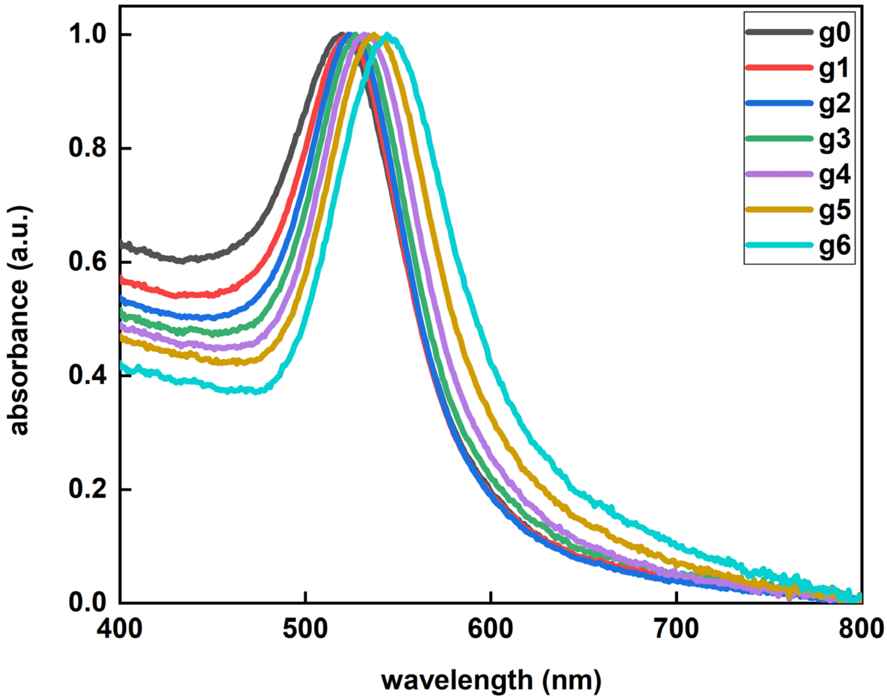

Figure 4.5 Normalised UV-Vis spectra of seeds (**g0**), first growth (**g1**), second growth (**g2**), third growth (**g3**), fourth growth (**g4**), fifth growth (**g5**) and sixth growth (**g6**) spherical nanoparticles, normalised to the maximum. A distinct red-shift of the maximum LSPR peak is observed as the average size of the AuNPs is increased.

4.1.3 Synthesis of gold nanorods

As opposed to spherical gold nanoparticles, AuNRs have an anisotropic shape with a tuneable aspect-ratio LSPR, which can range from visible to near-infrared [268]. Anisotropic AuNRs coated with CTAB of varying aspect ratios were synthesised using a modified seed mediated growth protocol (see **Section 3.1.3**), which included the addition of silver [38, 40, 42]. The seed-mediated growth synthesis for AuNRs was first introduced by Jana *et al.* who followed a two-step procedure [37]. The first step involved the synthesis of 'seed' nanoparticles (2 - 3 nm in diameter) *via* the reduction of the gold salt by a reducing agent ($NaBH_4$) in the presence of CTAB. Finally, AuNR synthesis was achieved *via* the addition of the seed solution to a 'growth' solution containing gold salt, CTAB, silver nitrate and ascorbic acid. During this step, $AuCl^{4-}$ bound to CTAB formed $AuCl^{2-}$ *via* the reduction of Au^{3+} to Au^{+} due to the addition of ascorbic acid. The collision of $AuCl^{2-}$ - CTAB complexes with CTAB-protected seed particles led to the formation of growing Au particles [40, 291]. Preferential reduction of Ag atoms on the sides of the AuNRs, known as underpotential deposition, followed by strong CTAB binding inhibited gold growth on the side of the rods and promoted directional growth at the ends. In more detail, a strong interaction between the deposited Ag^{+} ions and the Br^{-} ions of CTAB blocked the deposition of Au atoms and consequently, the Au seeds elongated along the longitudinal direction [40, 41].

Synthesised AuNRs were characterised by TEM and UV-Vis. **Figure 4.6** shows representative TEM images with size distribution histograms of AuNRs, where the aspect ratio varied by adjusting the concentration of silver nitrate in the growth solution in agreement with previously published results [292]. An increase in silver nitrate concentration resulted in the formation of nanorods with a length-to-width aspect ratio extended from 2.78 to 3.65 (see **Table 4.1** for the dimensions and aspect ratios of the synthesised AuNRs) [292]. The size distribution of the structures was determined by counting ~200 AuNRs using ImageJ software (National Institutes of Health, USA).

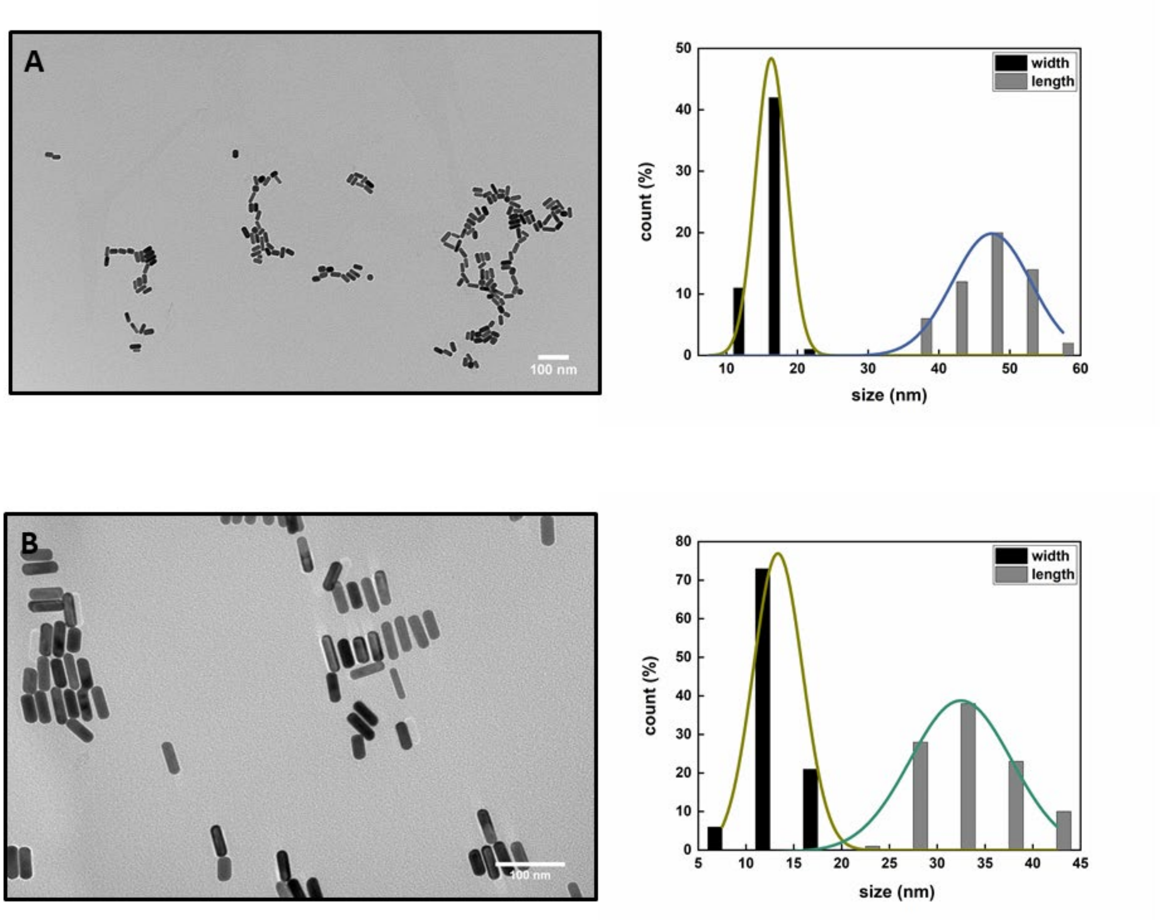

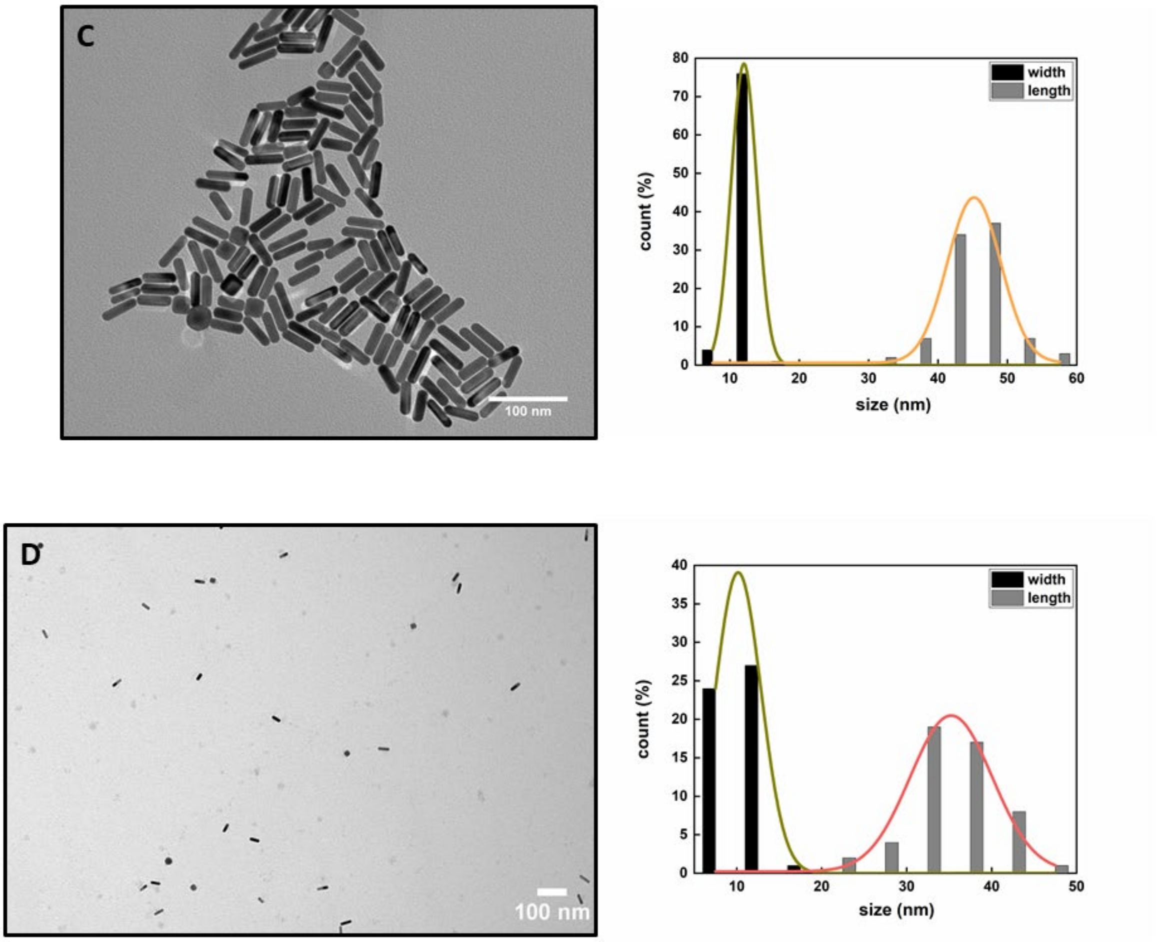

Figure 4.6 TEM images and representative size distribution histograms of AuNRs prepared with (**A**) 0.15 mL, (**B**) 0.21 mL, (**C**) 0.3 mL and (**D**) 0.4 mL of silver nitrate. Aspect ratios increase from approximately (**A**) 2.78, to (**B**) 2.81, to (**C**) 3.59 and (**D**) 3.65 while there is a decrease in their diameter. Scale bars are 100 nm.

Table 4.1 Dimensions and aspect ratio of the synthesised AuNRs obtained by using different silver nitrate amounts.

silver nitrate (mL)	length (nm)	width (nm)	aspect ratio
0.15	45.4 ± 0.3	16.3 ± 0.1	2.78
0.21	34.6 ± 0.5	12.3 ± 0.1	2.81
0.3	43.1 ± 0.1	12.0 ± 0.1	3.59
0.4	37.2 ± 0.4	10.2 ± 0.1	3.65

The change in aspect ratio was also exhibited by UV-Vis spectroscopy. Two plasmon peaks were observed by AuNR absorption spectra, which corresponded to LSPR along their length (longitudinal resonance) and diameter (transverse resonance) [97, 293, 294]. A red-shift of the longitudinal peak was also recorded as the aspect ratio increased (**Figure 4.7 (B)**). This resulted in colloidal AuNR solutions of variable colours due to the variation of the silver nitrate concentration added which is indicative of AuNRs with different aspect ratios (**Figure 4.7 (A)**).

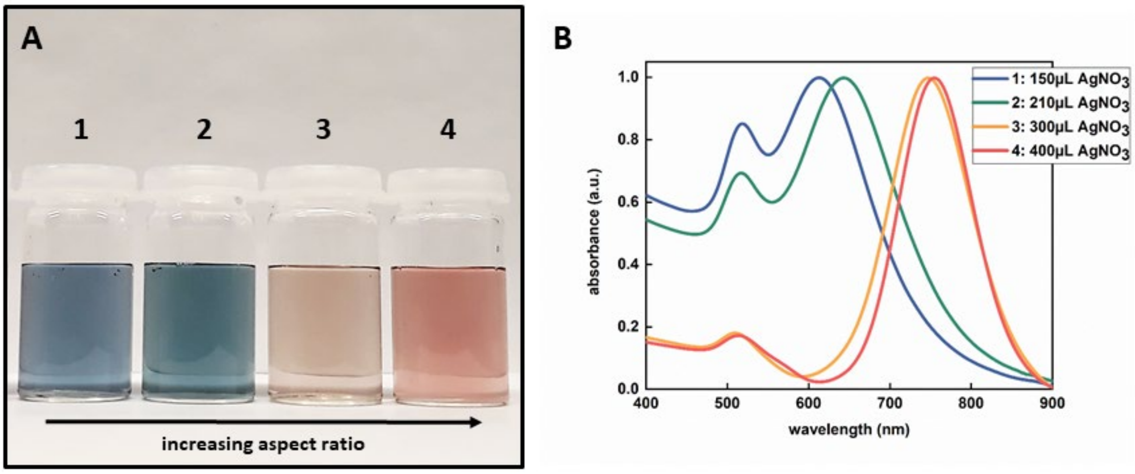

Figure 4.7 (**A**) Digital image and (**B**) Normalised UV-Vis spectra of AuNRs prepared with (**1**) 0.15 mL, (**2**) 0.21 mL, (**3**) 0.3 mL and (**4**) 0.4 mL of silver nitrate ($AgNO_3$).

4.1.4 Synthesis of branched gold nanoparticles

Branched AuNPs with an anisotropic structure were also synthesised using a modified seed mediated two-step growth protocol [44, 45]. Chen *et al.* were the first to introduce a seed mediated approach for the synthesis of branched nanoparticles, which provided better control over the size distribution and morphology of the branched structure [46]. The mechanism behind the two-step growth synthesis was based on the growth of seeds using a reducing agent (L-ascorbic acid solution) and the initiation of the nanocrystal growth using a surfactant (CTAB) (see **Section 3.1.4** for synthetic protocol). CTAB and silver nitrate were used as the surfactant and additive, respectively, to promote anisotropic growth. CTAB was used as the capping reagent, which in the presence of Ag^+ ions kinetically controlled the growth rate of various facets of the Au seeds to create branched structures [295]. A high increase in the concentration of the reducing agent (L-ascorbic acid solution) could lead to the formation of larger AuNPs with a higher degree of branching possibly due to the acceleration of the reduction rate of gold precursor on the nanoparticle surface [49].

Synthesised branched AuNPs were characterised by TEM and UV-Vis. **Figure 4.8 (A)** displays a representative TEM image with the size of branched AuNPs ranging from 85 to 110 nm, depending on the degree of branching. The size of the structures was determined by using ImageJ software (National Institutes of Health, USA).

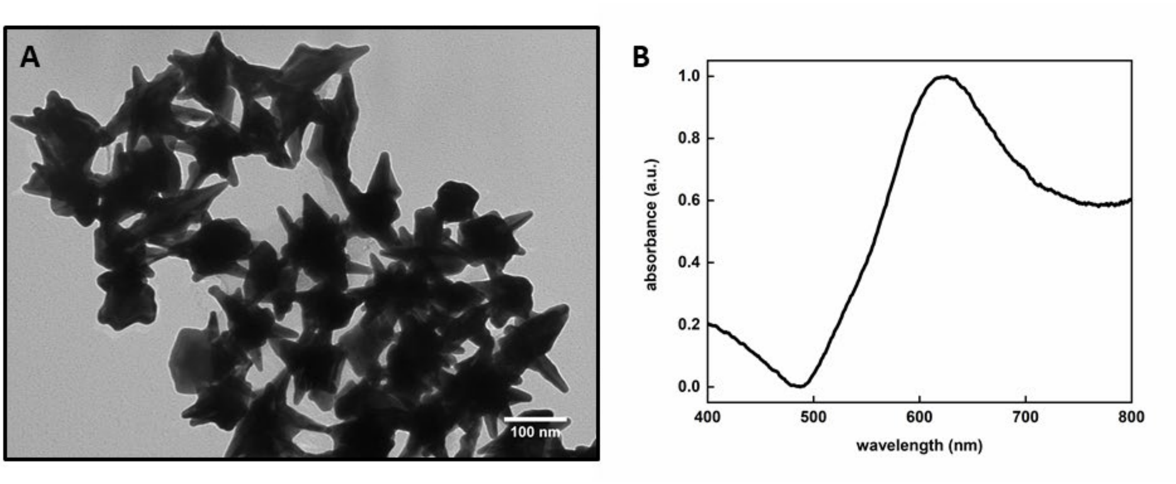

Figure 4.8 (**A**) Representative TEM image of anisotropic branched AuNPs. (**B**) Normalised UV-Vis spectrum shows a strong SPR maximum peak at 630 nm. Scale bar is 100 nm.

Figure 4.8 (B) also shows a representative UV-Vis spectrum. The branched AuNPs demonstrated a strong SPR peak. By comparing the absorption band of branched AuNPs with spherical AuNPs peaks of similar size, it can be stated that branched nanoparticles were found to be more red-shifted and have broader peaks. This shift was associated with the size of the branches around the AuNPs' core while the broadening of the peak was a result of the Rayleigh light scattering from particles with a diameter smaller than the radiation wavelength [53].

4.2 Synthesis of Upconversion Nanoparticles

4.2.1 Synthesis of core upconversion nanoparticles

Hexagonal phase $NaYF_4$:Yb^{3+} (20%), Er^{3+} (2%) UCNPs were synthesised based on a modified solvothermal method (see **Section 3.1.5** for synthetic protocol), which is a typical solution-based approach and is usually employed under high temperatures and pressures [112]. In the first step of this synthesis, the yttrium, ytterbium and erbium chloride salts were dissolved in oleic acid and octadecene at 150 ^{0}C. Oleic acid was used as a capping ligand to control particle growth and stabilise the particles against aggregation. A specific concentration of oleic acid was used in this synthesis to promote the growth of hexagonal platelet shape nanoparticles. The size and shape of the upconversion nanocrystals were dependent on the concentration of the oleic acid [71]. Oleic acid was able to direct the preferential growth of specific facets. The use of a constant Ar flow was critical at this step of the synthesis as Ar prevented the oxidation of the oleic acid from the air and the formation of oleate forms of the precursors. After the solubilisation of the chloride salts, the reaction was cooled to room temperature. In the next step, NaOH and NH_4F dissolved in dry MeOH were injected into the solution to form the host matrix together with yttrium at room temperature. By performing the addition at room temperature conditions, the risk of producing fluorinated compounds was eliminated and the synthesis of β-phase UCNPs (hexagonal phase) was enhanced [70]. Then, MeOH was evaporated at 100 ^{0}C and a degassing step under vacuum was realised to ensure the complete evaporation. This step was crucial in the prevention of the oxidation of the oleates, which would change the number of oleic ligands available to bind the surface of the nanoparticles once formed. Finally, the solution was heated up to 310 ^{0}C under Ar to allow the homogeneous growth of the seeds and avoid the creation of secondary nuclei.

Synthesised particles were characterised by TEM. **Figure 4.9** shows a representative TEM image of core $NaYF_4$:Yb^{3+} (20%), Er^{3+} (2%) UCNPs with a size distribution histogram, which depicts high uniformity in shape and size. The particles had a hexagonal phase. The size distribution of the core UCNPs was determined to be 21.6 ± 0.8 nm by counting ∼200 nanoparticles using ImageJ software (National Institutes of Health, USA).

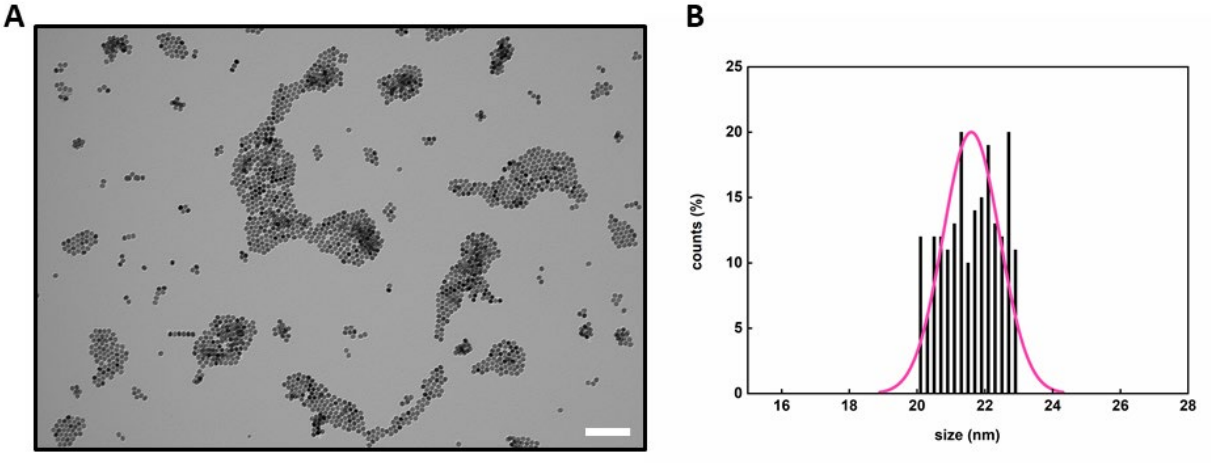

Figure 4.9 (**A**) TEM image of core UCNPs showing hexagonal particles with an average size of 21.6 ± 0.8 nm. (**B**) Histogram showing the size distribution of core UCNPs. Scale bar is 200 nm.

4.2.2 Synthesis of core-shell upconversion nanoparticles

Lanthanide-doped UCNPs usually have a larger number of dopant ions distributed on the surface of the nanoparticles. Due to a lack of adequate protection by the host lattice, luminescence is easily quenched by high-energy oscillators emerging from surface defects and weakly bound ligands, solvents and impurities. The inner ions' excitation energy can also be transmitted to the surface by neighbouring dopant ions and subsequently dissipated non-radiatively. By growing a shell with a small lattice mismatch around the core, the non-radiative decay losses of the surface luminescence can be reduced and the optical properties of UCNPs can be enhanced. As a result, in a core-shell structure, the dopant ions are contained in the inner core of the nanocrystals. The deposition of an un-doped $NaYF_4$ shell over the core UCNPs surface can effectively reduce energy loss on the crystal surface resulting in enhanced luminescence efficiency [270]. Core-shell UCNPs have also an improved fluorescent emission in water where the upconversion processes can be strongly affected by vibrational scattering of water molecules adsorbed onto the crystal surface [296, 297]. In 2006 Lezhnina *et al*. were the first to report core-shell structured UCNPs by focusing on $EuF_3@GdF_3$, $GdF_3@EuF_3$, LaF_3:Yb, $Ho@LaF_3$ and $LaF_3:Nd@LaF_3$ core@shell nanoparticles [298]. Then, in 2007, the improvement of luminescence by ~7 and 29 times for $NaYF_4$:Yb, Er and $NaYF_4$:Yb, Tm nanocrystals after coating with $NaYF_4$ shells, respectively, was presented by Yi and co-workers [299]. Several core-shell nanocomposites have been developed since then to increase upconversion efficiency [300-303]. In this thesis, previously synthesised hexagonal phase $NaYF_4:Yb^{3+}$ (20%), Er^{3+} (2%) core UCNPs were utilised to grow a β-$NaYF_4$ shell on their surface by following a solvothermal method (see **Section 3.1.6** for synthetic protocol).

Synthesised particles were characterised by TEM. **Figure 4.10** shows a representative TEM image of core-shell UCNPs with a size distribution histogram. The synthesis yielded highly monodisperse hexagonal-shaped core-shell UCNPs with an average nanocrystal size of 27.4 ± 0.1 nm by counting ~200 nanoparticles using ImageJ software (National Institutes of Health, USA).

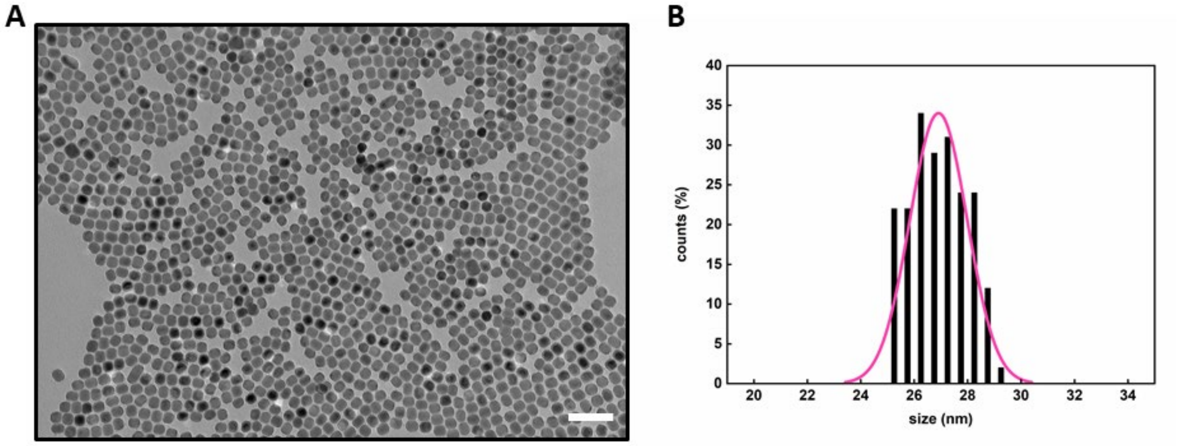

Figure 4.10 (**A**) TEM image of core-shell UCNPs showing hexagonal particles with an average size of 27.4 ± 0.1 nm. (**B**) Histogram showing the size distribution of core-shell UCNPs. Scale bar is 100 nm.

In **Figure 4.11** core-shell UCNPs showed improved fluorescence emission compared to core UCNPs. This was due to the shell formation on the core surface. To do a quantitative measurement of fluorescent properties of core and core-shell UCNPs, the fluorescence emission was recorded under the excitation of a 980 nm laser. The laser excitation was chosen at 980 nm due to the distinct experimentally observed emission spectra at the violet at 415 nm, the green at 525 nm and 540 nm and the red at 655 nm as well as the occurring transitions $^2H_{11/2} \rightarrow {}^4I_{15/2}$, $^4S_{3/2} \rightarrow {}^4I_{15/2}$ and $^4F_{9/2} \rightarrow {}^4I_{15/2}$ [74, 133-135] (see **Section 2.2.3.2**). The increase in fluorescence intensity of core-shell UCNPs was significant in comparison with core UCNPs (**Figure 4.12**). By comparing the two spectra, no peak shifting was observed, confirming that the energy level distribution for the $NaYF_4:Yb^{3+}$ (20%), Er^{3+} (2%) UCNPs was not affected by the formation of a shell. For the core-shell UCNPs, ytterbium (Yb^{3+}) served as an efficient photo-sensitizer with high absorption at 976 nm. The absorbed energy was transferred to Er^{3+}, an activator within the matrix that emitted the energy in the visible spectrum. The emissions were in the green at 522 nm and 540 nm and in the red at 655 nm.

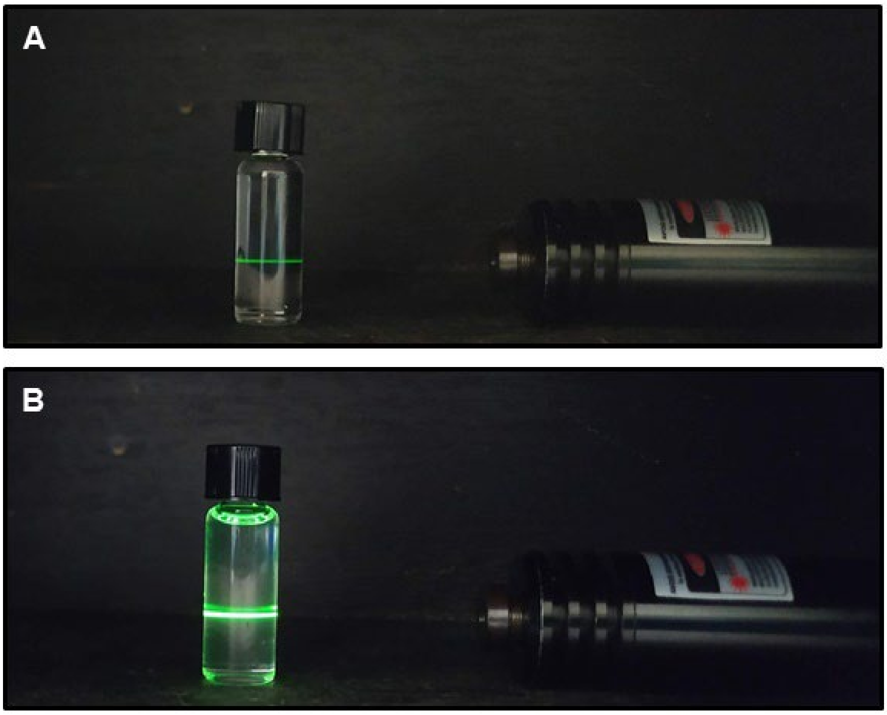

Figure 4.11 Digital images of (**A**) core UCNPs and (**B**) core-shell UCNPs in hexane irradiated with a 980 nm laser beam.

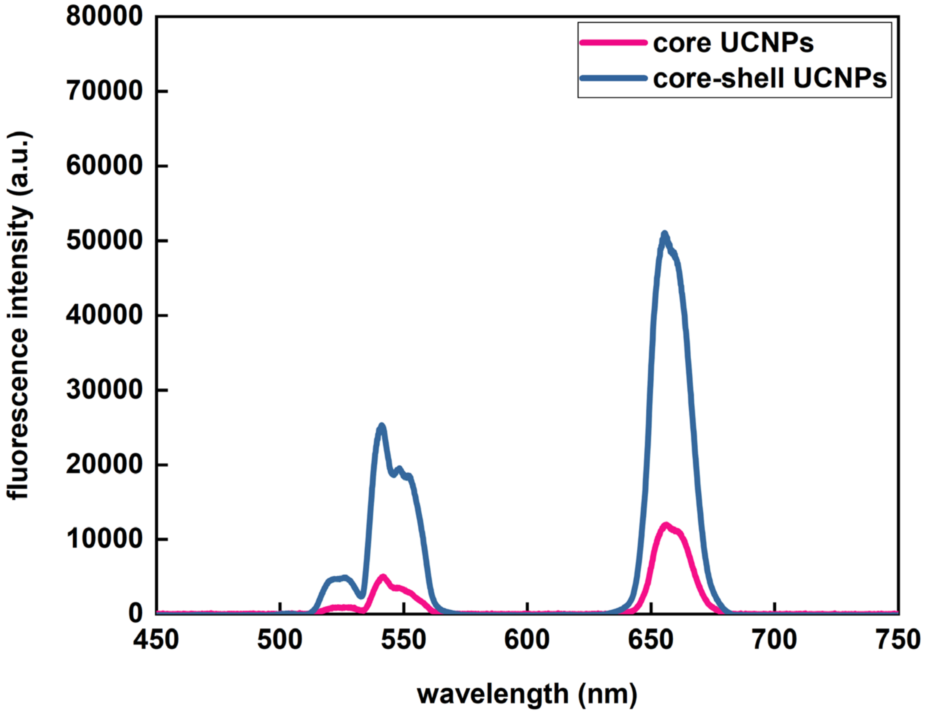

Figure 4.12 Fluorescence emission spectra of core UCNPs (pink line) and core-shell UCNPs (blue line) in hexane irradiated with a 980 nm laser beam. The peak positions remained the same since the percentage of erbium and ytterbium was constant in both samples.

Overall, the synthesis and characterisation of different types of colloidal nanoparticles such as spherical AuNPs, AuNRs and branched AuNPs as well as core and core-shell UCNPs, are presented in this chapter. These nanoparticles were synthesised with the use of modified synthetic routes. The production of highly monodisperse nanoparticles with precise control over size, shape, and surface chemistry is critical for the development of functional nanomaterials.

Chapter 5 Design of Functionalised Gold Nanoparticles for Enrichment of Skeletal Stem Cells from Human Bone Marrow

Human bone marrow (BM)-derived stromal cells contain a population of SSCs, with the capacity to differentiate along the osteogenic, adipogenic, and chondrogenic lineages, enabling their application to clinical therapies. In the absence of a specific SSC marker, current methods to isolate and enrich SSCs from human tissues remain challenging. A homogeneous cell population with the ability to form bone, cartilage and adipose tissue in humans cannot be isolated by the currently available markers alone. This chapter includes the results and discussion of the design of DNA functionalised AuNPs (**Section 5.1**) and their ability to identify and sort SSCs upon specific mRNA detection (**Section 5.2**). This approach presents the significant enrichment achieved in the isolation of SSCs, with the potential to enhance our understanding of bone cell biology and translational applications. The results of this chapter have been published in the article: ‘‘Enrichment of Skeletal Stem Cells from Human Bone Marrow Using Spherical Nucleic Acids’’, Miguel Xavier, Maria-Eleni Kyriazi, Stuart Lanham, Konstantina Alexaki, Elloise Matthews, Afaf H. El-Sagheer, Tom Brown, Antonios G. Kanaras, and Richard O. C. Oreffo, *ACS Nano* **2021** *15* (4), 6909-6916, DOI: https://doi.org/10.1021/acsnano.0c10683.

5.1 Design of Spherical Nucleic Acids for mRNA Detection

In recent years spherical AuNPs have been at the forefront of research and represented attractive candidates for biomedical applications due to the facile and efficient functionalisation of their surface with a variety of capping ligands including synthetic oligonucleotides [304, 305]. The modification of the surface of AuNPs with thiol-terminated synthetic DNA sequences was first introduced by Mirkin and co-workers who showed that AuNP surface could be functionalised with a shell of oligonucleotides and by Alivisatos *et al*. who achieved surface modification with a defined number of oligonucleotides [180, 181]. A thiol linker chemically modified to either the 5’ or 3’ end was used for the conjugation of the oligonucleotides to the AuNP surface as thiols have a very strong affinity for gold [306, 307]. By exploiting this property, spherical AuNPs modified with a shell of oligonucleotides were synthesised creating a three-dimensional (3D) oligonucleotide structure [180, 181, 308] as shown in **Figure 5.1**. These structures are SNAs and combine both the properties of the gold inorganic core and the dense oligonucleotide shell (see **Section 2.5.1**). The extensive use of SNAs for intracellular applications has been found to provide high specificity, binding of complementary oligonucleotide strands, intracellular stability towards DNA enzymatic degradation and enhanced uptake of SNAs by multiple types of cells [179, 309].

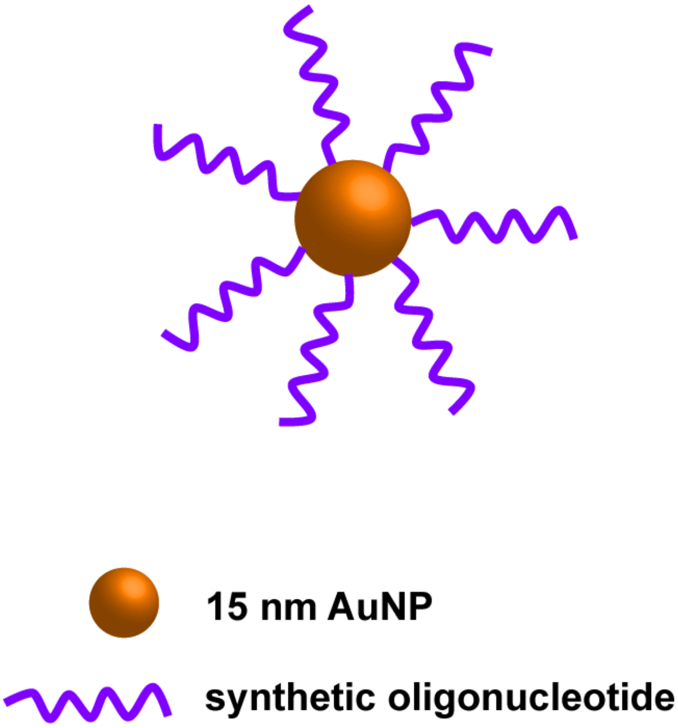

Figure 5.1 Schematic illustration of a spherical nucleic acid that consists of an AuNP core functionalised with multiple synthetic oligonucleotides.

Seferos and co-workers demonstrated how SNAs could be hybridized into shorter fluorophore-bearing oligonucleotides for the targeted detection of mRNA. In more detail, they showed a significant increase in fluorescence intensity for the detection of survivin mRNA compared to the treatment with nontargeting nanoparticles [236]. After this work, several studies have used SNAs for the detection of mRNA targets with high accuracy and specificity. The use of SNAs for the detection of Nanog and Gdf3 mRNA in embryonic stem cells as well as induced pluripotent stem (iPS) cells of murine, porcine, and human origin was demonstrated by Lahm and co-workers. Target gene positive cells were sorted and Nanog-specific probes identified reprogrammed murine iPS cells based on their Cy3-fluorescence [310]. In contrast, the use of SNAs to enable self-activation and imaging of mRNA sequential expression (tubb3 and fox 3 mRNA) was presented by Wang *et al.* during the neural stem cell differentiation process [311]. Vilela *et al.* have shown that SNAs can detect vimentin mRNA in skin wounds. Vimentin mRNA is expressed during the epithelial to mesenchymal transition that happens during wound healing [312]. In addition, the group of Kanaras has developed SNAs and dimer SNAs that can detect up to two different mRNA targets and at the same time deliver two different types of anticancer drugs (doxorubicin and mitoxantrone) in live cells [14, 313].

Spherical AuNPs with a size of 15 ± 1 nm were functionalised with synthetic oligonucleotides bearing a terminal 3′ thiol modification and a terminal 5′ FAM dye. The oligonucleotides directly attached to the AuNP surface are termed "sense" strands. Shorter oligonucleotide complements modified with a Cy5 dye at their 5′ end were hybridised to these sense strands. The shorter fluorophore modified oligonucleotides are termed "flare" strands. The sequence of the sense strand was designed to bind only a specific mRNA. When the sense strand was bound to the AuNP core and the flare strand hybridised with the sense oligonucleotide, the oligonucleotide dyes were quenched (OFF state) due to the close proximity to the AuNP surface. In the presence of the mRNA target, the flare strand was released and the target mRNA was bound to the sense strand due to competitive hybridisation [236, 237]. This displacement was detected as an increase in fluorescence at the specific wavelength of the Cy5 fluorophore (ON state) as demonstrated in **Figure 5.2**. The fluorophore on the flare strand acted as a reporter for mRNA detection. The excitation wavelength for Cy5 dye is 647 nm and the emission wavelength is 665 nm. The FAM dye on the sense strand was introduced to monitor the integrity of the sense strand, with the FAM dye released and detectable, only if the sense strand was degraded by nucleases or detached from the nanoparticle surface. The excitation wavelength for FAM dye is 494 nm and the emission wavelength is 519 nm.

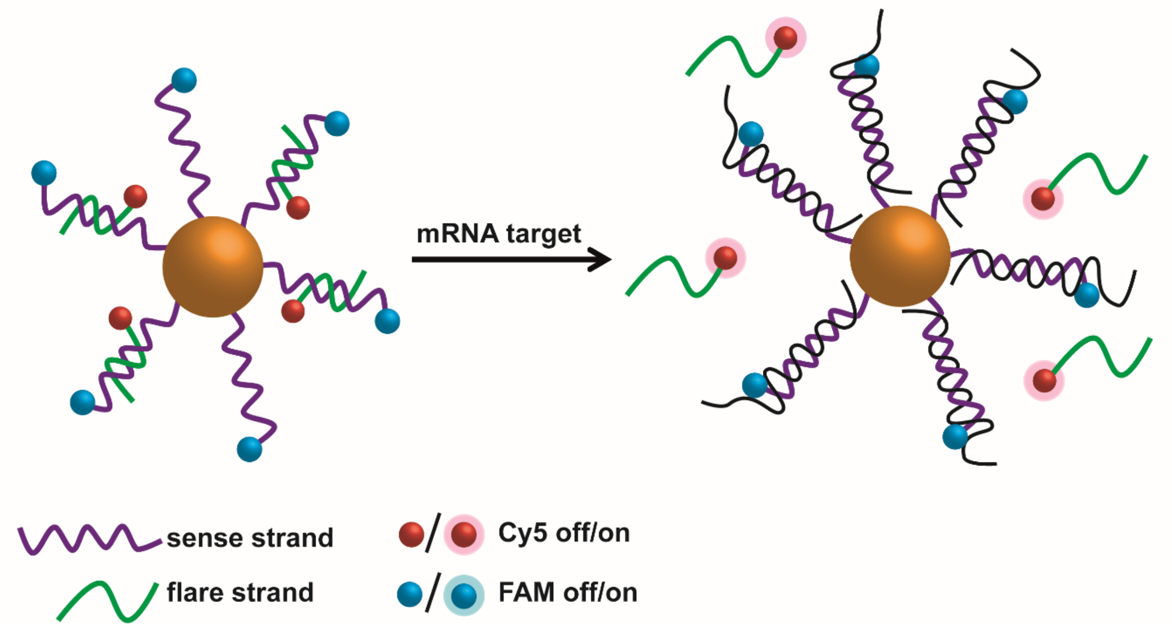

Figure 5.2 Schematic illustration of SNAs that detect mRNA. When both sense and flare strands are close to the AuNP core, fluorescence is quenched. When the target mRNA binds to the sense strand, the release of the flare can be detected as an increase in its fluorescence signature.

5.1.1 Synthesis and characterisation of spherical nucleic acids

Cells isolated from human BMSCs directly collected from patients were incubated with SNAs for the detection of specific mRNAs. The oligonucleotide sequences on the surface of the AuNPs were customised for the detection of the bone cell mRNAs, hspa8 and runx2 (see **Table 3.1** for oligonucleotide sequences). Runx2 is known as a bone-specific transcription factor critical in osteogenic differentiation and as a regulator of bone development. Runx2 is also involved in the expression of osteogenesis related genes, the regulation of the cell cycle progression, and the improvement of the bone microenvironment [314-317]. Concerning hspa8, it was selected as a target since the hspa8 gene encodes for the STRO-1 antigen [318, 319]. STRO-1 is a cell surface protein expressed by BMSCs and erythroid precursors. It has been routinely used as a marker for SSC analysis and SSC sorting [320, 321]. STRO-1 provides enrichment specificity for SSCs, as STRO-1 positive cell populations exhibit enhanced osteogenic differentiation both *in vitro* and *ex vivo* [319]. To test the specificity of the SNAs toward the targeted detection of mRNA, a scrambled control sequence was designed to not detect any cellular mRNA.

To achieve an efficient packing of the oligonucleotides on the AuNP surface is necessary to control the repulsive interactions between adjacent DNA strands, as well as the charges between the AuNP surface and the negatively charged phosphate backbone on the DNA. A commonly used strategy to screen these charges is NaCl additions as presented in **Figure 5.3**.

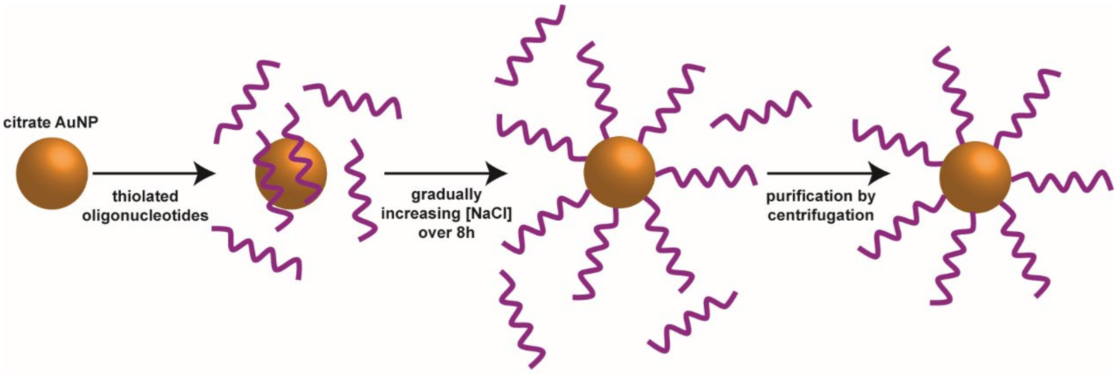

Figure 5.3 Schematic representation of oligonucleotide attachment to an AuNP surface *via* the salt-ageing procedure.

Mirkin’s group has quantified the loading number per AuNP that can be attached to a spherical AuNP depending on the experimental conditions and the size of the NP [199, 322]. Moreover, this method can be applied to any oligonucleotide sequence. By applying the quantification procedure for the attached DNA strands to the surface of AuNP after salt-ageing and the quantitative analysis of the oligonucleotides in solution, it was found the number of oligonucleotide sense strands attached to each 15 ± 1 nm AuNP surface with no significant variation between oligonucleotides of varying sequences (**Table 5.1**).

Table 5.1 Determination of oligonucleotide loading for each type of SNA. Values based on triplicate experiments.

oligonucleotide	**average number of oligonucleotides / AuNP**	**standard error of the mean**
hspa8	111	4
runx2	109	4
scramble	109	5

The method that was followed in this study for determining the degree of oligonucleotide loading was the dissolution of the AuNP core using a solution of KI/I_2 (see **Section 3.3.2.2**). To assess the number of oligonucleotides attached per AuNP, the absorbance of free oligonucleotides in the solution was monitored. The triiodide ion (I_3^-) is the oxidant in this system formed by the reaction of I_2 with I^-. The anodic and cathodic reactions that lead to the etching of the AuNP are:

$$I_2 + I^- \rightarrow I_3^-$$

$$I_3^- + 2e^- \rightarrow 3I^-$$

$$Au + 2I^- \rightarrow AuI_2^- + e^-$$

Equation 5.1 RedOx reaction resulting in the dissolution of the gold core.

The successful DNA conjugation to the AuNP surface to form a 3D shell was qualitatively observed by UV-Vis and gel electrophoresis. UV-Vis analysis of oligonucleotide coated spherical AuNPs revealed a sharp peak that is slightly red-shifted compared to BSPP functionalised AuNPs (**Figure 5.4**). This was attributed to an increase in the refractive index of the sample due to successful oligonucleotide attachment [288]. Agarose gel electrophoresis was also used as another method to assure oligonucleotide attachment [323]. The different samples of 15 nm spherical AuNPs coated with a shell of oligonucleotides were run against a sample of unmodified spherical AuNPs stabilised by BSPP. **Figure 5.5** depicts a delay in the bands of DNA functionalised AuNPs (lane 2 - 4) compared to unmodified AuNPs (lane 1), which indicates a decrease in the electrophoretic mobility due to an increase in AuNP size and therefore validates oligonucleotide conjugation.

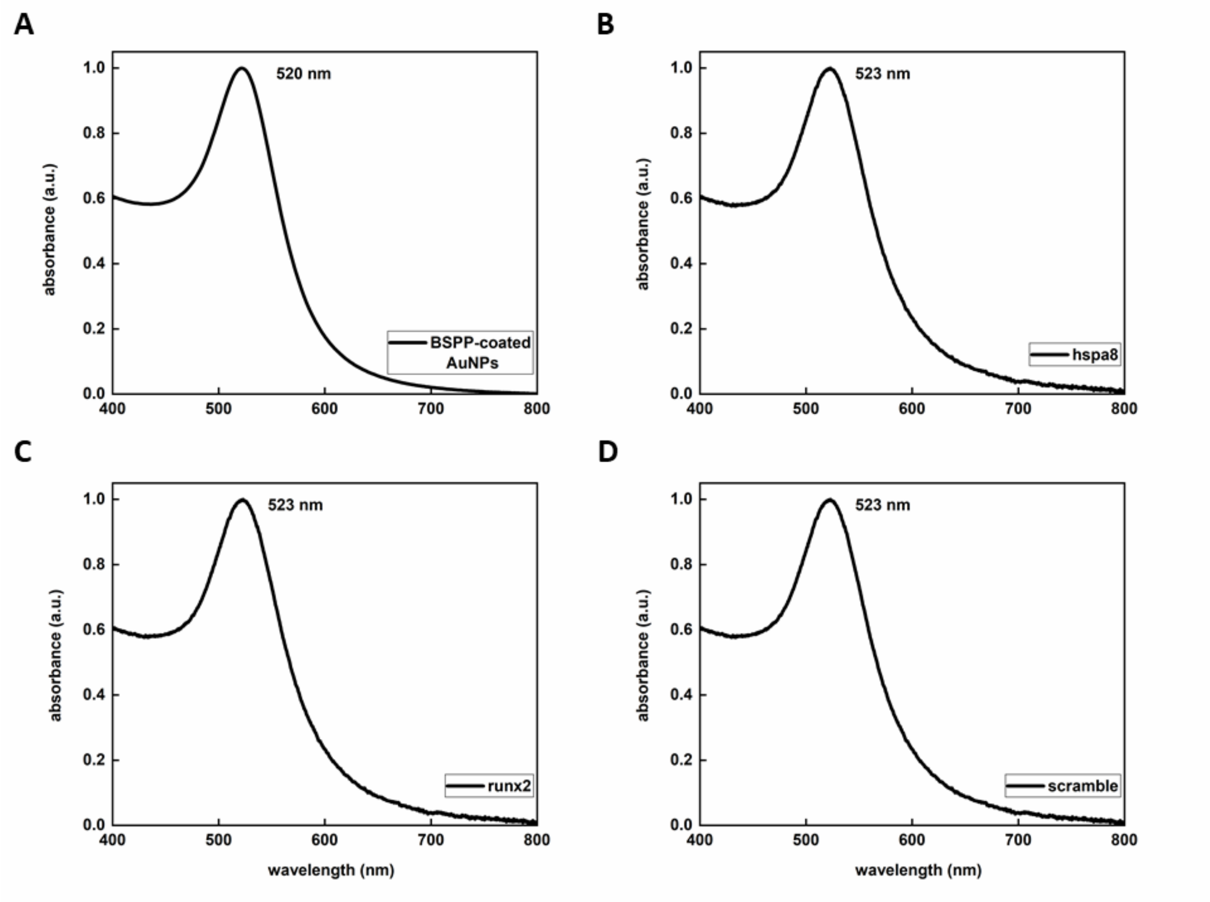

Figure 5.4 Normalized visible spectra of (**A**) BSPP coated AuNPs, (**B**) hspa8 coated AuNPs, (**C**) runx2 coated AuNPs and (**D**) scramble coated AuNPs. A 3 nm shift was observed after oligonucleotide functionalisation indicating a change in the refractive index and successful surface functionalisation.

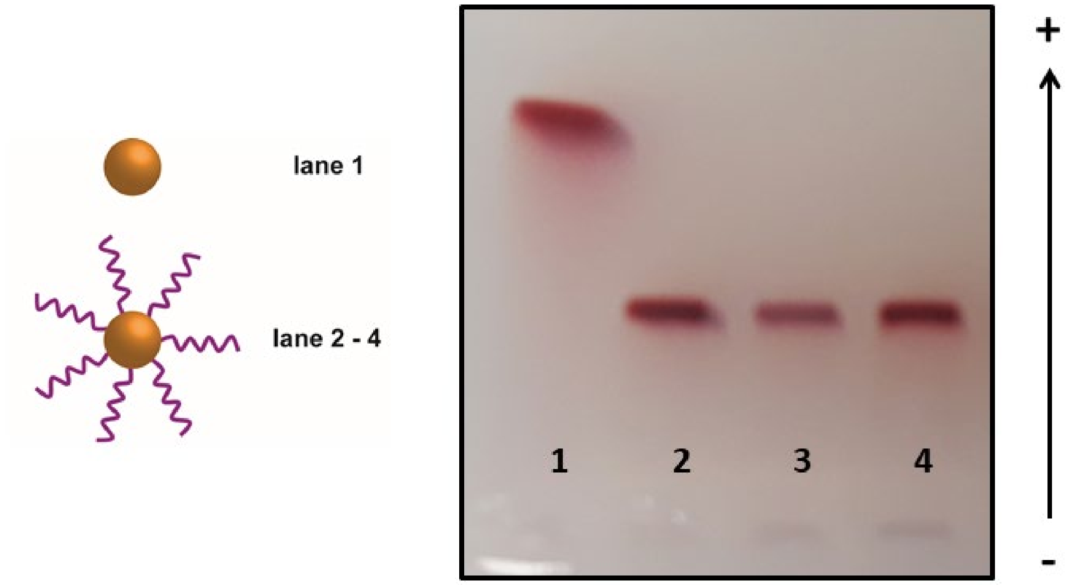

Figure 5.5 Agarose gel electrophoresis comparing (**lane 1**) 15 ± 1 nm BSPP coated AuNPs and 15 ± 1 nm AuNPs coated with a shell of (**lane 2**) hspa8 oligonucleotides, (**lane 3**) runx2 oligonucleotides and (**lane 4**) scramble oligonucleotides.

The oligonucleotide-coated nanoparticles had a stronger net negative charge compared to BSPP AuNPs according to ζ-potential measurements (**Figure 5.6**).

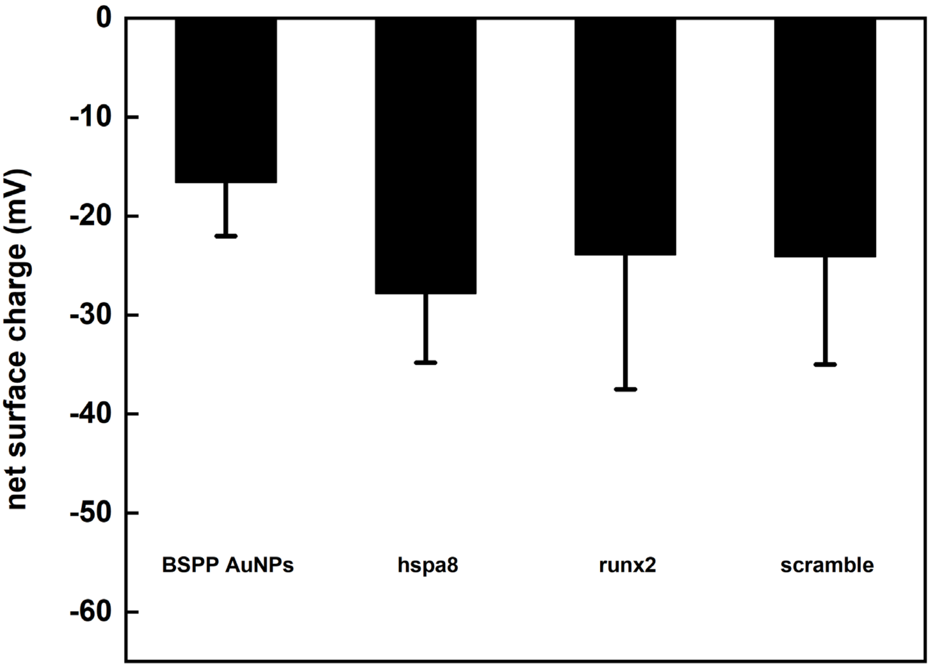

Figure 5.6 Net surface charge of BSPP AuNPs and oligonucleotide-coated AuNPs. After ligand replacement of BSPP with thiol modified oligonucleotides, a decrease in the net surface charge was observed as a result of the negatively charged oligonucleotides.

5.1.2 Stability of spherical nucleic acids against nuclease

Enzymatic hydrolysis is a process of nucleic acid degradation in biological environments in which enzymes enhance the cleavage of bonds with the addition of water molecules [324]. Hence, the system of oligonucleotide-based nanoparticles for intracellular application is susceptible to degradation by enzymes. DNase I is an endonuclease that cleaves the DNA preferentially at phosphodiester linkages adjacent to a pyrimidine nucleotide. It is present in the cytoplasm, in the serum and the extracellular space. The pH range that DNase I remains active in the presence of bivalent magnesium and calcium cations, is 6.5 − 8.0 [325]. It is calcium that keeps the optimal enzyme conformation and the magnesium ions that initiate the cleavage of the phosphodiester bond [326]. Single-stranded DNA, double-stranded DNA and chromatin can be affected by DNase I [327]. However, SNAs present a better resistance to nucleases according to several studies [3, 14, 207, 328]. This is due to the close packing of oligonucleotides on the AuNP surface which creates a high concentration of cations around the surface [182, 329]. Compared to molecular DNA when incubated with DNase I under the same conditions, it displays no stability towards degradation. A free dsDNA was incubated with DNase I and analysed *via* PAGE. In **Figure 5.7**, lane 1 shows the band of a single DNA strand, lane 3 shows the band of a DNA duplex and lane 2 shows that after a 24 h incubation at 37 °C with DNase I the DNA duplex was fully degraded indicating efficient enzyme activity.

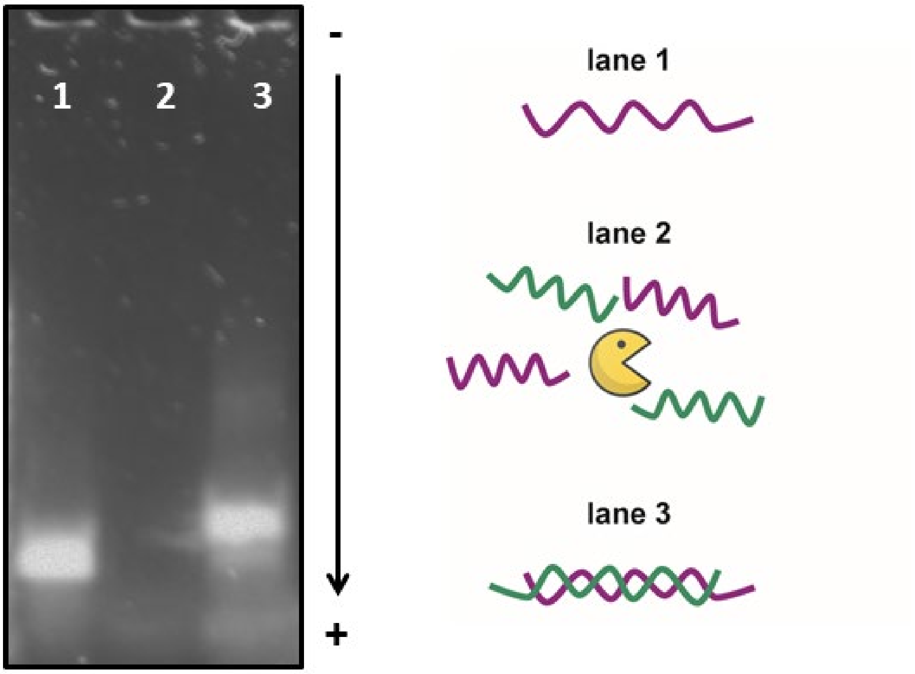

Figure 5.7 PAGE gel displaying ssDNA (**lane 1**), dsDNA incubated with DNase I for 24 h (**lane 2**) and dsDNA not incubated with DNase I (**lane 3**). The disappearance of a clear band in lane 2 indicated that DNase I was active in the presence of a free duplex.

The stability of SNAs was investigated in the presence of DNase I. Prior to the SSC isolation experiment, SNAs (2.5 nM, 150 µL) in a DNase I buffer containing Tris-HCl (10 mM), $MgCl_2$ (2.5 mM) and $CaCl_2$ (0.5 mM) at pH 7.4 were incubated with DNase I (from bovine pancreas, Sigma Aldrich, 2 U/L). Samples were then incubated at 37 °C for 24 h. By monitoring the fluorescence intensity of the sense strand (FAM), the % of oligonucleotides remaining on the AuNP was determined. **Figure 5.8** shows that in the presence of DNase I, SNAs retained more than 95% of oligonucleotide surface coating suggesting that our SNAs displayed unique stability.

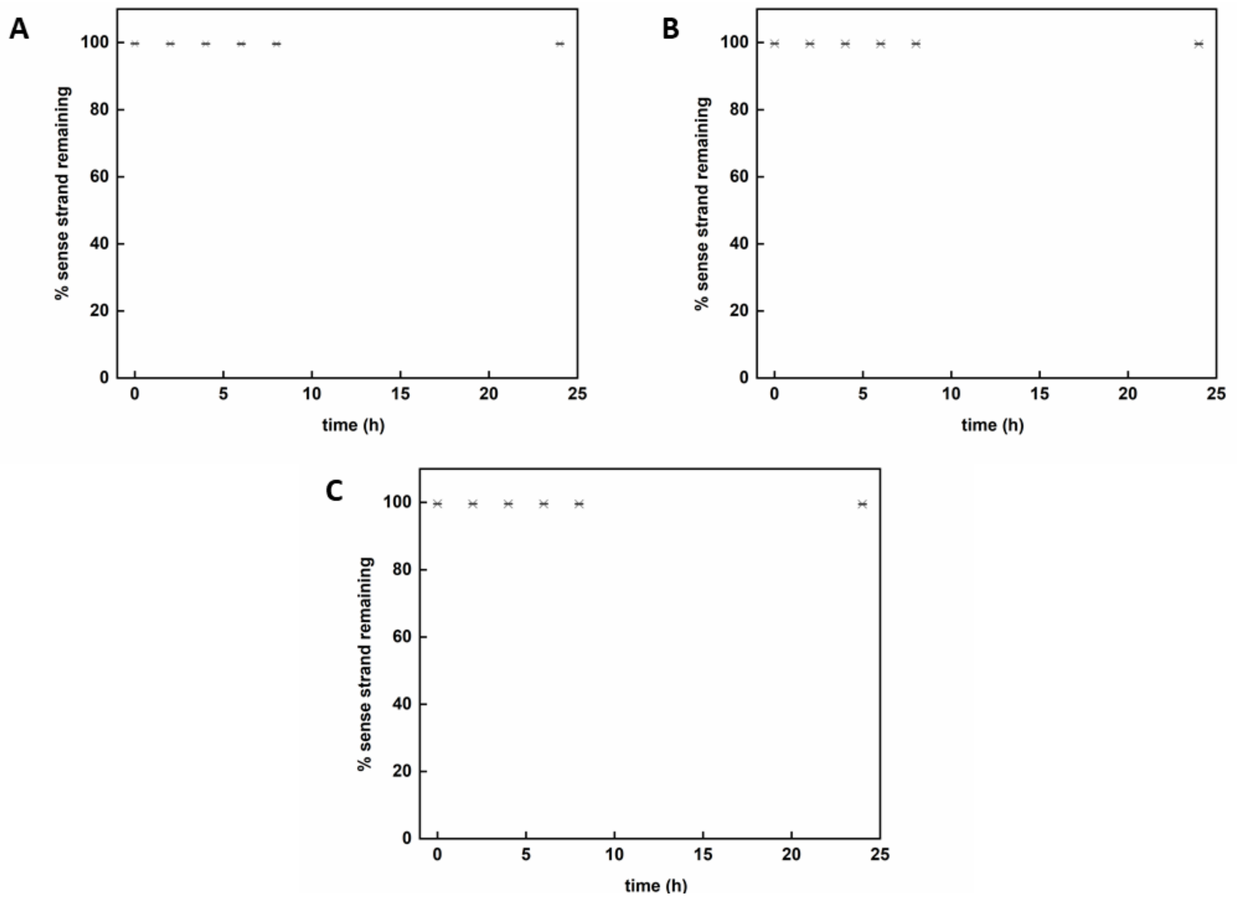

Figure 5.8 SNAs for the detection of hspa8 (**A**) and runx2 (**B**) mRNA including a scramble SNA (**C**) were incubated with DNase I over a 24 h period. By monitoring the fluorescence intensity, the percentage (%) of oligonucleotides on the AuNP surface was determined. Data are shown as mean ± standard error of the mean (n = 3).

Based on previous work it is suggested that the increased resistance within cells is due to the high local salt concentration at the NP surface [3, 201, 203, 205]. The inhibition of DNase I and related nucleases by monovalent cations, including Na^+, is caused by the displacement of Ca^{2+} and Mg^{2+} by Na^+ ions that are bound to the enzyme and are required for efficient activity. Nuclease resistance is also correlated with the charge due to a greater amount of charge-balancing Na^+ counterions [201]. Wu *et al*. proposed that the resistance to enzymatic degradation is attributed to the arrangement of DNA oligonucleotides in a dense 3D shell [330]. To experimentally demonstrate the effect of oligonucleotide density on the NPs, an SNA with a lower oligonucleotide density (40 oligonucleotides/AuNP) was subjected to the same nuclease conditions. The FAM signal from the sense strand was monitored over 24 h and compared to the fluorescence signal obtained from a higher density SNA. A clear increase in the FAM intensity was observed after 2 h for the SNA with a lower oligonucleotide density indicating that oligonucleotide degradation occurred. In comparison, SNA coated with a larger number of oligonucleotides had no significant degradation thus proving that dense packing of oligonucleotides on the AuNP surface can prevent enzyme activity (**Figure 5.9**).

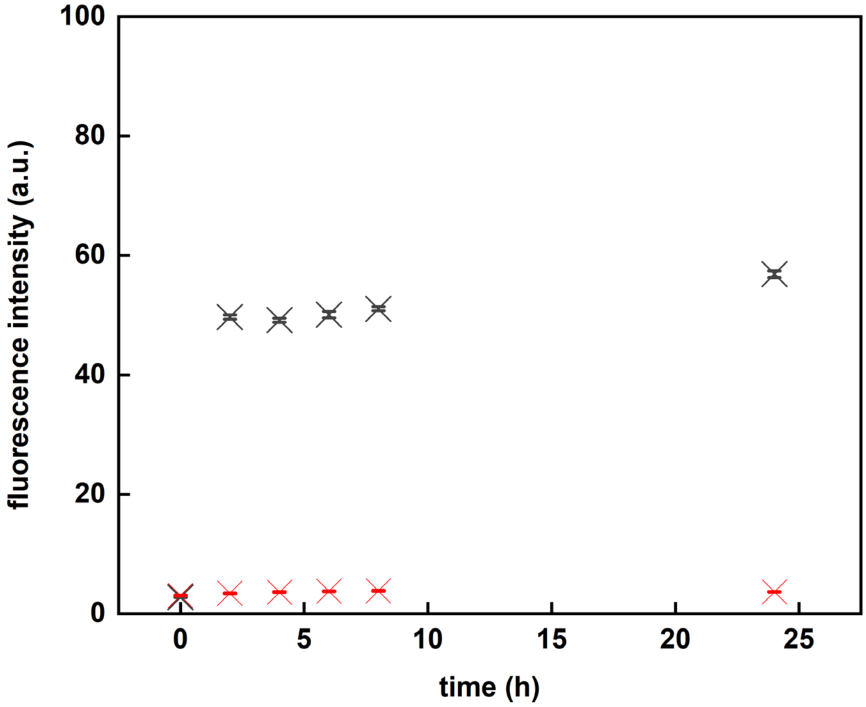

Figure 5.9 Fluorescence intensity of FAM signal monitored over 24 h of low oligonucleotide density (black) and high oligonucleotide density (red) SNAs incubated with DNase I. Data are shown as mean ± standard error of the mean (n = 3).

5.1.3 Specificity of spherical nucleic acids

To detect target mRNA within living cells, the SNAs must respond to their target rapidly and efficiently. Binding studies were performed in a tube using synthetic fully complementary oligonucleotide targets for each mRNA. SNAs (6.7 nM, 150 µL) in PBS were incubated with their fully complementary target. **Figure 5.10** shows that in the presence of the fully complementary target, SNAs responded with an increase in the Cy5 fluorescence signal upon recognition and binding within the first 2 min. This indicated their efficiency at signalling in the presence of a specific target in buffered conditions within a tube.

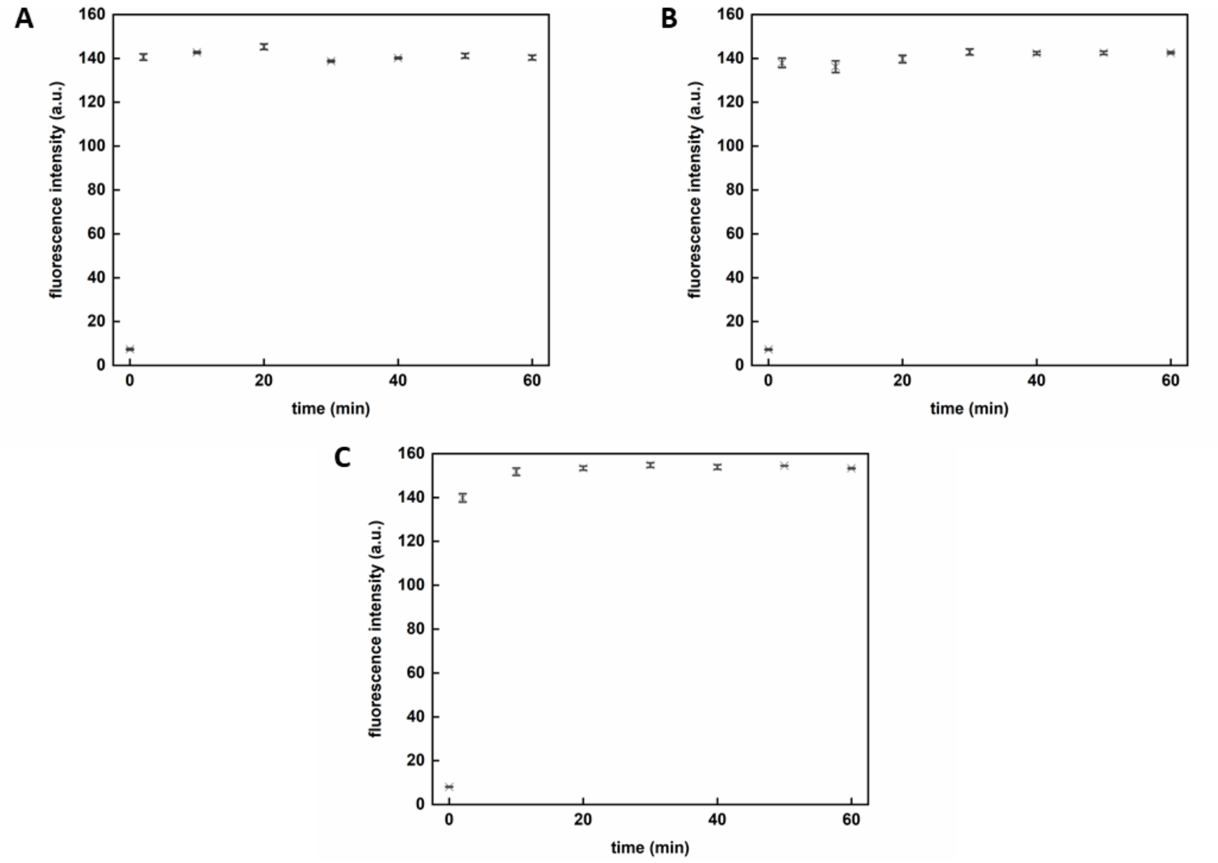

Figure 5.10 Time course of fluorescence associated with flare release when SNAs were incubated with a synthetic and fully complementary oligonucleotide sequence within a tube leading to the displacement of the hspa8 (**A**), runx2 (**B**) and scramble (**C**) flare. Data are shown as mean ± standard error of the mean (n = 3).

5.2 Spherical Nucleic Acids for Skeletal Stem Cell Isolation and Enrichment

The application of stem cells in regenerative medicine is an area of research of great importance in recent years. The ability of human BMSCs from BM to differentiate into bone-forming osteoblasts when implanted *in vivo* has driven the application of these cells in the clinic [331]. BM is the soft connective tissue that resides inside bone cavities, produces blood cells and stores fat. BM has been studied as an organ with two main systems: the hematopoietic tissue and the supportive stroma [332]. Hematopoietic stem cells (HSCs) are responsible for the production of all blood cell types and are very important for the treatment of hematopoietic disorders [333]. The BM supportive stroma contains the unspecialised mesenchymal stem/stromal cells (MSCs) that lack tissue-specific characteristics [334]. By the term MSC, it is represented a heterogeneous cell population when cultured *in vitro* and is likely to include cells with a wide spectrum of regenerative potential from specific terminal cell type progenitors to multipotent stem cells, named skeletal stem cells (SSCs)

[320, 335]. The term SSC represents the self-renewing stem cell of the BM stroma responsible for the regenerative capacity inherent to the bone with osteogenic, adipogenic, and chondrogenic differentiation potential *in vivo*. However, there are several limitations in SSC isolation techniques due to their low abundance in BM aspirates (1 in 10 – 100,000 mononuclear cells) [336], the absence of specific markers causing the phenotypic ambiguity of the SSCs [337] and the complexity of BM tissue [320]. Hence, there is a restricted understanding of SSC fate, immunophenotype and selection criteria that results in the limited clinical application of these cells [320].

The current approaches for SSC sorting are FACS (Fluorescence Activated Cell Sorting) and MACS (Magnetic Activated Cell Sorting). FACS can purify the cells by labelling them with fluorescence-tagged biochemical antibodies resulting in cells isolation by various parameters. FACS is capable of processing millions of cells and isolating multiple, high purity subpopulations. MACS is based on the purification of cells by using magnetic beads attached to specific antibodies. MACS is less time consuming and less expensive [338]. The use of both techniques is hindered by the requirement for the cells to be fixed and the lack of specific cell membrane markers for SSCs [320]. Widely used markers, such as STRO-1, interact with only a small percentage of BM cells that contain a subpopulation that includes the SSC/progenitor population. A combinatorial approach that used MACS to sort STRO-1^+ cells followed by dual-colour FACS to sort STRO-1^{bright} and $CD146^+$ cells was used by Shi and Gronthos to achieve a 2×10^3-fold enrichment of the CFU-F population compared with unfractionated marrow. Although the use of both FACS and MACS can cause cell damage and loss, it is time-consuming and impractical for clinical application [339]. It remains elusive the use of a specific marker, in isolation, to isolate single cells with the ability to form bone, cartilage, and adipose tissue in humans.

In this study, SNAs are used not only to detect SSCs based on mRNA expression but also to isolate SSCs from human BM, which is essential for tissue engineering applications. SNAs detect endocellular mRNA targets rather than antigens present on the cells' membrane. FACS was used to isolate BMSCs expressing specific mRNA and subsequently isolate SSCs. Due to the SNA specificity for mRNA detection, the enrichment was 1 in 200 SSCs isolated from BM aspirates although the number of SSCs is low in BM aspirates. This is translated to a 50 – 500-fold enrichment demonstrating the potential of this SNA method for different strategies. **Figure 5.11** presents a schematic illustration of the experimental approach. In detail, the SNAs were incubated with BMSCs for 1 h and then FACS was used to separate the target positive from target negative cells based on their fluorescence signature. Target positive cells were plated and stained to observe the number of colonies formed. SSCs can form colonies, termed colony-forming units fibroblastic cells (CFU-Fs), when plated and cultured at limiting dilutions [321]. The CFU-F assay utilises the ability to identify

SSCs and progenitor cells, as each colony is derived from a single stem/early progenitor cell. Upon CFU-F formation, SSCs have a fibroblastic appearance after isolation and culture [340].

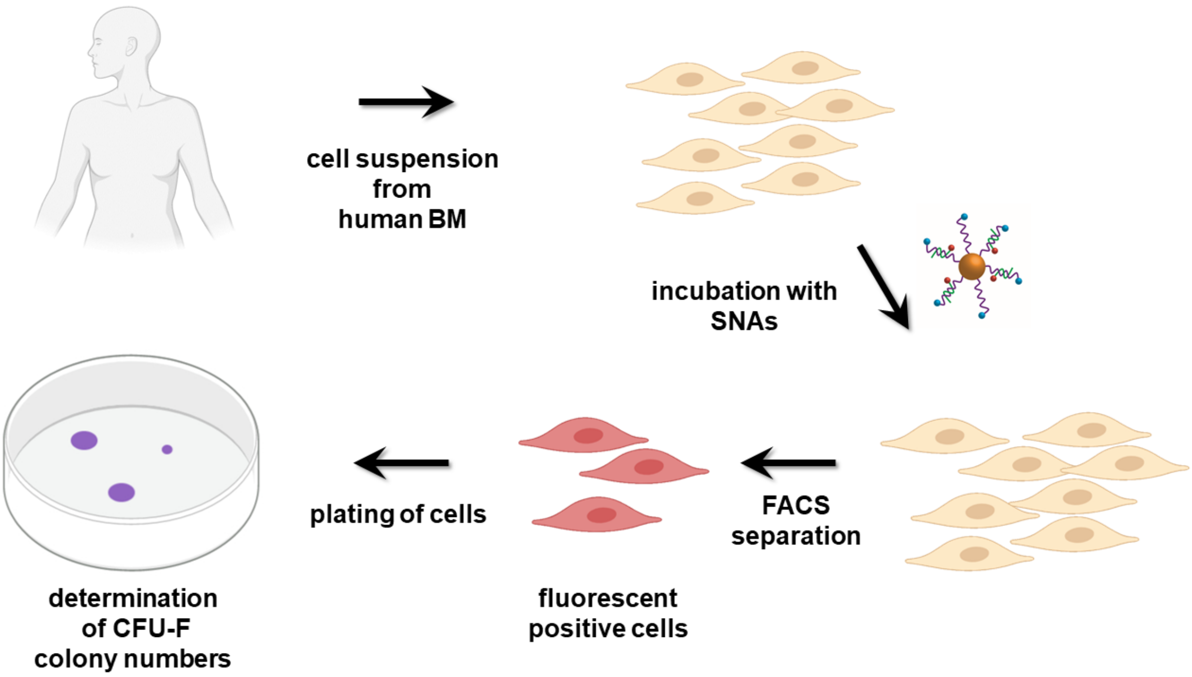

Figure 5.11 Schematic illustration of the isolation of SSCs and the formation of their colonies.

SNAs for the detection of runx2 and hspa8 mRNA were incubated with human BMSCs for 1, 2, or 3 h at 0.2 nM final concentration. After the establishment of the appropriate settings for FACS separation, the fluorescence signal of the flare release was monitored. An increase in Cy5 fluorescence was observed compared to cells incubated with no SNAs. These experiments were carried out by the collaborators in Prof. Richard Oreffo's lab based at Cancer Research Building, Southampton General Hospital (see **Appendix D**).

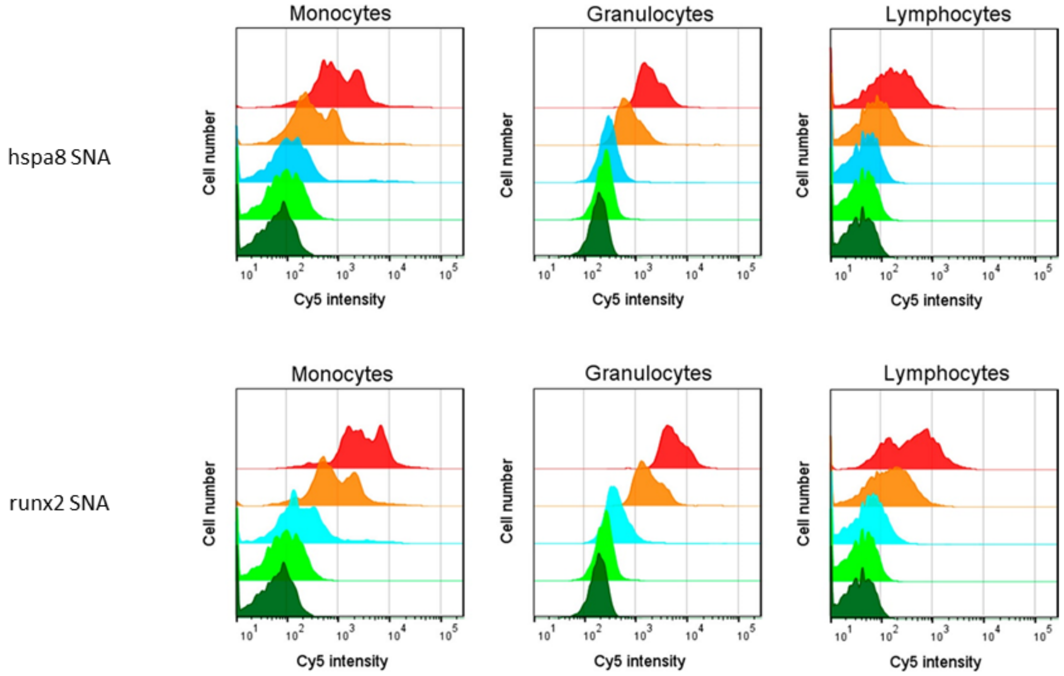

Figure 5.12 SNAs for the detection of hspa8 and runx2 mRNA including a scrambled SNA were incubated with human BMSCs for 1, 2, or 3 h. Cy5 intensity *vs* cell number overlay plots for the different SNAs for different cell types within the BM as determined by the FACS selection criteria. Colour guide: red, 3 h incubation; orange, 2 h incubation; light blue, 1 h incubation; light green, scrambled control at 3 h incubation; dark green, no SNAs at 3 h incubation.

According to **Figure 5.12**, after the addition of hspa8 and runx2 SNAs, Cy5 positive cells could be detected within 1 h of incubation in the different subpopulations of BM cells including lymphocytes, granulocytes, and monocytes. The fluorescence intensity was observed to increase with longer incubation times (2−3 h). **Figure 5.13** confirms the absence of signal from the FAM dye that is conjugated to the sense strand regardless of the target detected and indicates the stability of the sense strand. Thus the presence of a Cy5 fluorescence is due to target detection and not to degradation. A scramble SNA designed to not detect any intracellular mRNA was used as a control in both cases. Not only the stability against nuclease degradation but also the specificity of SNAs for the detection of mRNA were confirmed by the absence of both Cy5 and FAM signals from the flare and sense strands, respectively, after a 3 h incubation period.

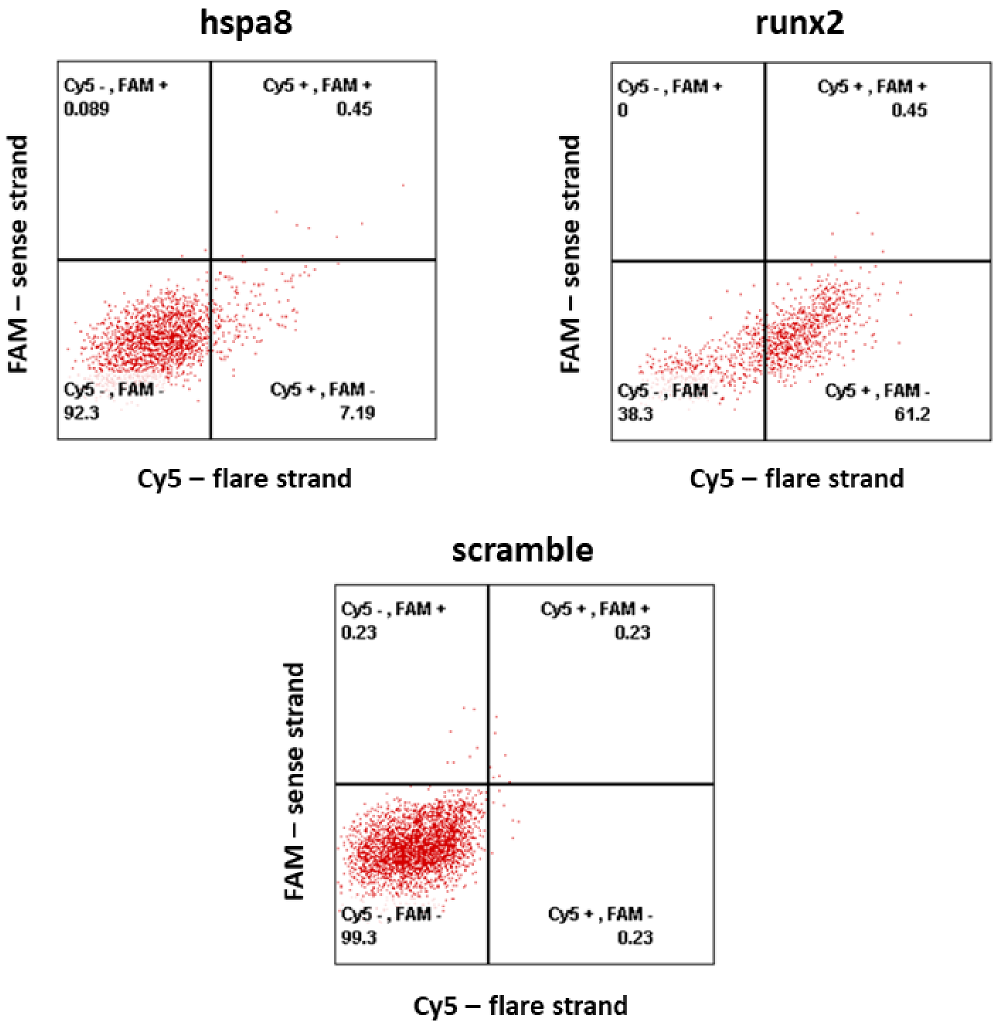

Figure 5.13 Representative FACS Cy5 *vs* FAM dot plots shown for human BM samples used to isolate and enrich human SSCs.

After the sorting of Cy5 positive cells for hspa8 and runx2 mRNA, the recovered cells were grown for 14 days. To determine the number of colonies formed, the cells were stained. Only cells of monocyte size and granularity were collected by FACS, while the rest of the cell types were discarded. This happened as this gate has been shown to contain the largest fraction of SSCs in a typical BM sample [341, 342].

Isolated cells produced varying levels of CFU-Fs as shown in **Figure 5.14**. Cells sorted from SNAs designed for the detection of runx2 mRNA produced a higher number of cell colonies than hspa8. Although, it was observed a significant enrichment in comparison to unsorted cells. On the contrary Cy5 negative cells expressed either no or negligible CFU-F formation. In **Figure 5.14 (B)** and **(C)** the cells isolated by the SNAs for the detection of hspa8 (**B**) and runx2 (**C**) mRNA expressed a fibroblastic phenotype. During the collection of different proportions of the brightest Cy5 cells (15 – 60%) with the two different types of SNAs, it was observed that CFU-Fs occurred in the top 15% of brightest cells for these two targets.

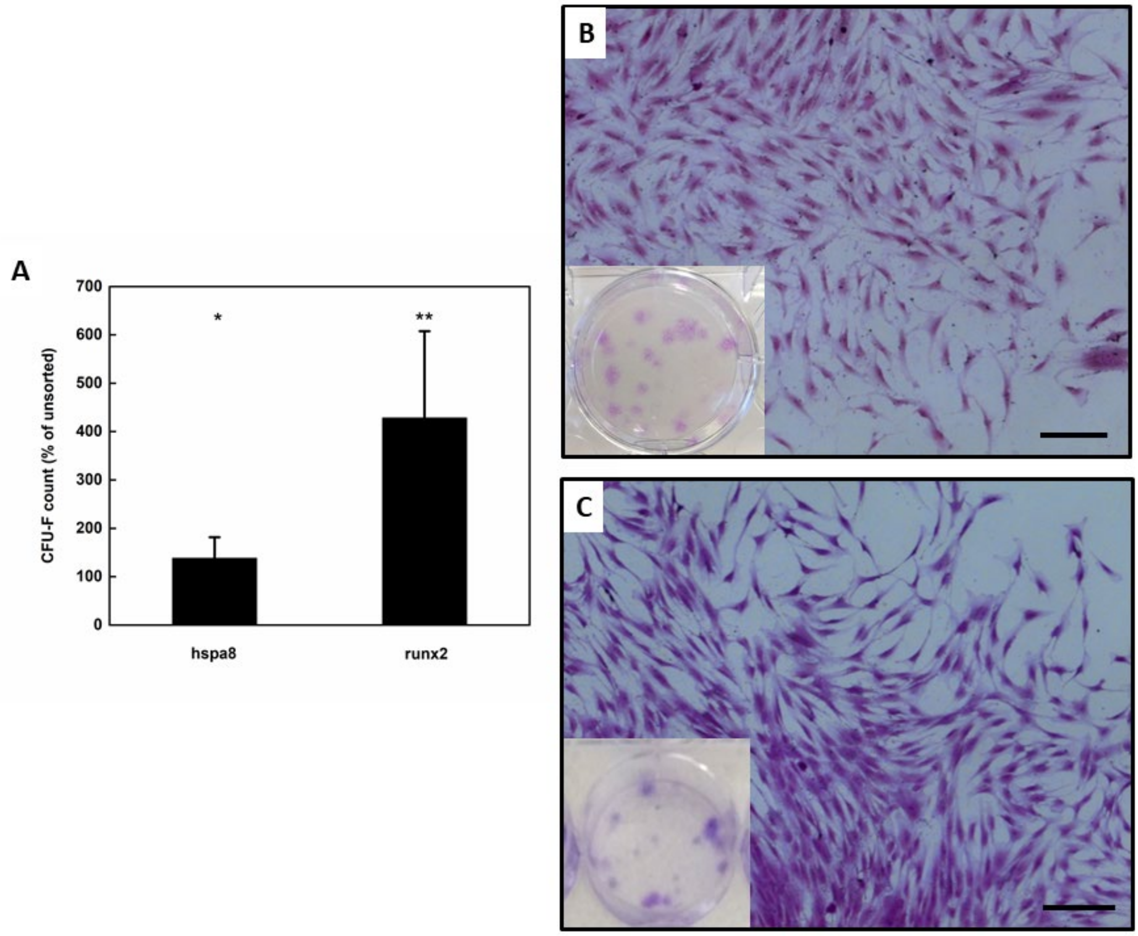

Figure 5.14 (**A**) Graph shows CFU-F count for cells sorted using hspa8 and runx2 SNAs. The statistical analysis was run comparing the number of colonies formed from cells sorted using the two types of SNAs *vs* unsorted cells, which were plated to give the equivalent of 10,000 cells in the monocyte region per well. Graphs show the mean with SD from n = 3 patients for each SNA. * $p < 0.05$, ** $p < 0.01$. (**B** and **C**) Representative images of cells within individual CFU-F colonies isolated with SNAs for the detection of (**B**) hspa8 and (**C**) runx2 mRNA. Cells isolated using SNAs displayed a fibroblastic phenotype, characteristic of such colonies. Insets show individual colonies in a 6-well plate. Scale bar is 200 µm.

Cells isolated using the runx2 SNA were grown, expanded and then subjected to different culture conditions to generate osteogenic, adipogenic, and chondrogenic stromal populations. This aimed to determine if the cells isolated were indeed SSCs with trilineage potential and the capacity to generate the requisite stromal lineages. To investigate the negative control, cells were collected using a scramble SNA and cultured for differentiation studies. It was observed insufficient SSCs that were enriched to facilitate the setup of differentiation assays. A total of 25,000 cells were seeded at a density of 800 cells/cm^2. **Figure 5.15** shows that the majority of cells had not adhered to the bottom of the culture flask and only one SSC colony was observed, after 16 days of culture. This slow cell growth confirms that the scramble SNAs are unable to enrich SSCs.

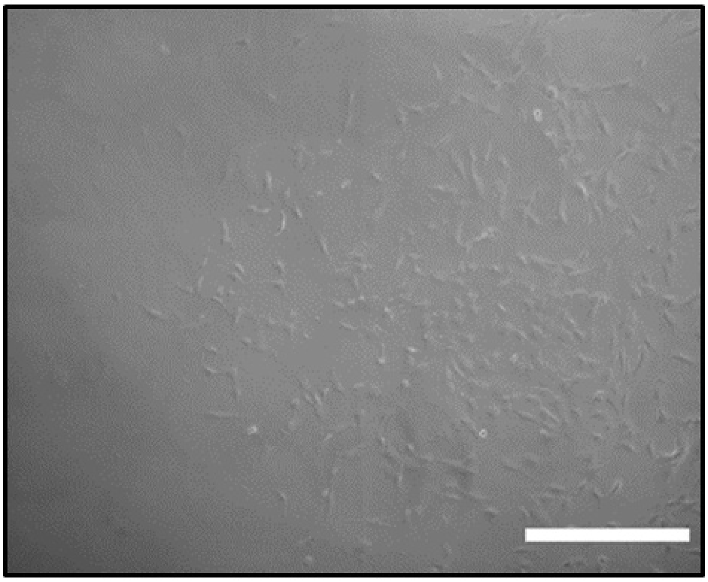

Figure 5.15 Culture of human BMSCs following selection with scramble control SNA does not provide sufficient SSCs for differentiation studies. Scale bar is 500 µm.

Cell populations were isolated by using SNAs targeting hspa8, runx2 and scramble DNA sequences. In hspa8 and runx2 Cy5 positive fractions, a consistent enrichment of CFU-F was observed, while in Cy5 negative fractions a negligible CFU-F formation occurred. In scramble Cy5 positive or Cy5 negative fractions, no consistent enrichment of CFU-F was observed confirming the non-specificity of the scramble sequence for the enrichment of SSCs.

Figure 5.16 (A) presents that the cells maintained under osteogenic conditions produced enhanced positive staining for alkaline phosphatase than the cells kept to basal conditions. **Figure 5.16 (B)** shows that Alcian Blue staining of the chondrogenic pellets revealed proteoglycan synthesis, whereas Sirius Red stain retention was absent in pellets, indicating an absence of collagenous matrix formation. **Figure 5.16 (C)** presents the Oil-Red-O staining of lipids which provided evidence of adipogenesis and lipid droplet formation, while there was no lipid visible in basal conditions.

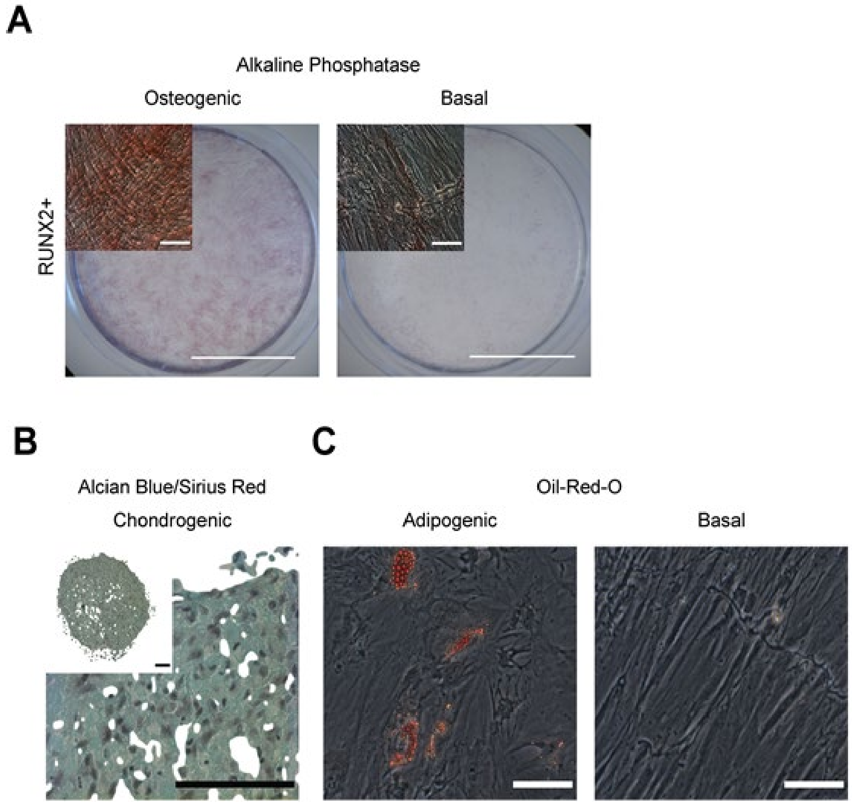

Figure 5.16 Cells isolated using the runx2 SNA demonstrate a capacity for trilineage stromal cell differentiation. Isolated populations showed (**A**) osteogenic, (**B**) chondrogenic, and (**C**) adipogenic induction indicating the presence of SSCs.

The above results demonstrate that the cells isolated by the runx2 SNA displayed trilineage potential and generated stromal populations with osteogenic, chondrogenic and adipogenic potentials. This was a strong indication that the isolated cells contained SSCs.

Overall, the development of SNAs for the detection of runx2 and hspa8 mRNA targets in human BM stromal populations, which enables the isolation and enrichment of human SSCs, is presented in this study. FACS was used to sort fluorescent cells, after incubating human BMSCs with runx2 and hspa8 SNAs. The isolated mRNA target positive cells were further plated and showed significant enrichment in CFU-F formation. There were up to 1 in 200 of the Cy5 positive cells isolated by FACS that formed colonies with CFU-F levels on culture despite the limited number of SSCs in human BM.

Chapter 6 Surface Modification of DNA-Coated Gold Nanoparticles with Peptides

The ability of DNA functionalised AuNPs to detect specific targets *in vitro* and *in vivo* has led to their development as suitable tools for sensing applications. However, endosomal entrapment is a common barrier in various nanoparticle delivery approaches. A new design strategy to enhance the endosomal escape of DNA-coated AuNPs *via* the incorporation of a cell-penetrating peptide has been attempted to promote effective escape within cells. This chapter is divided into sections based on the type of surface functionalisation with the peptide sequences. In **Section 6.1**, AuNPs have been firstly modified with thiol terminated DNA strands followed by further surface functionalisation with cysteine terminated cell-penetrating peptides. **Section 6.2** shows the conjugation of the peptide on the 5′ end of the DNA strand and then the functionalisation of AuNPs with these conjugate sequences. DNA and peptide coated AuNP hybrids demonstrate similar stability towards degradation by endocellular enzymes and similar specificity towards the detection of specific mRNA targets. The first part of this chapter's results has been published in the article: ''Engineering functional nanoparticles for delivery in cells'', Konstantina Alexaki, Maria-Eleni Kyriazi, Afaf H. El-Sagheer, Tom Brown, and Antonios G. Kanaras, *Proc. SPIE 11255*, *Colloidal Nanoparticles for Biomedical Applications XV*, 112550K (21 February 2020), DOI: https://doi.org/10.1117/12.2538470.

6.1 Surface Modification of 15 ± 1 nm Spherical Gold Nanoparticles with DNA and Peptide

6.1.1 Synthesis and characterisation of DNA-peptide-coated spherical nucleic acids

Gold nanoconjugates functionalised with both oligonucleotides and NLS or HIV Tat peptides were demonstrated by Patel and co-workers. In more detail, thiolated oligonucleotides and cysteine-terminated peptides were used to functionalize the AuNPs surfaces in the presence of salt [343]. The addition of salt is required to screen the oppositely charged oligopeptides and oligonucleotides during synthesis. After testing in cell cultures, the resultant conjugates were internalised and localised in the perinuclear region.

In this study, spherical AuNPs with a size of 15 ± 1 nm were functionalised with synthetic oligonucleotides bearing a terminal 3′ thiol modification and a terminal 5′ FAM dye (see **Section 2.5.1**). Shorter complementary oligonucleotides modified with a Cy5 dye at their 5′ end were hybridised to these sense strands. The sequence of the oligonucleotide used in this study was specific for the detection of vimentin mRNA (see **Table 3.1** for oligonucleotide sequence). After applying the quantification procedure for the attached DNA strands to the surface of AuNP, it was found that approximately 92 ± 10 oligonucleotide sense strands were attached to each 15 ± 1 nm AuNP surface.

The successful DNA conjugation to the AuNP surface was qualitatively monitored by UV-Vis and gel electrophoresis. UV-Vis analysis of oligonucleotide coated spherical AuNPs revealed a sharp peak with an SPR maximum at 524 nm as demonstrated in **Figure 6.1 (A)**. This was slightly red-shifted compared to BSPP functionalised AuNPs due to an increase in the refractive index of the sample. Agarose gel electrophoresis was another method to assure oligonucleotide attachment [323]. The sample of 15 nm spherical AuNPs coated with a shell of oligonucleotides specific for the detection of vimentin mRNA was run against a sample of unmodified spherical AuNPs stabilised by BSPP. **Figure 6.1 (B)** shows a delay in the band of DNA functionalised AuNPs (lane 2) compared to unmodified AuNPs (lane 1), which indicates the oligonucleotide conjugation due to a decrease in the electrophoretic mobility.

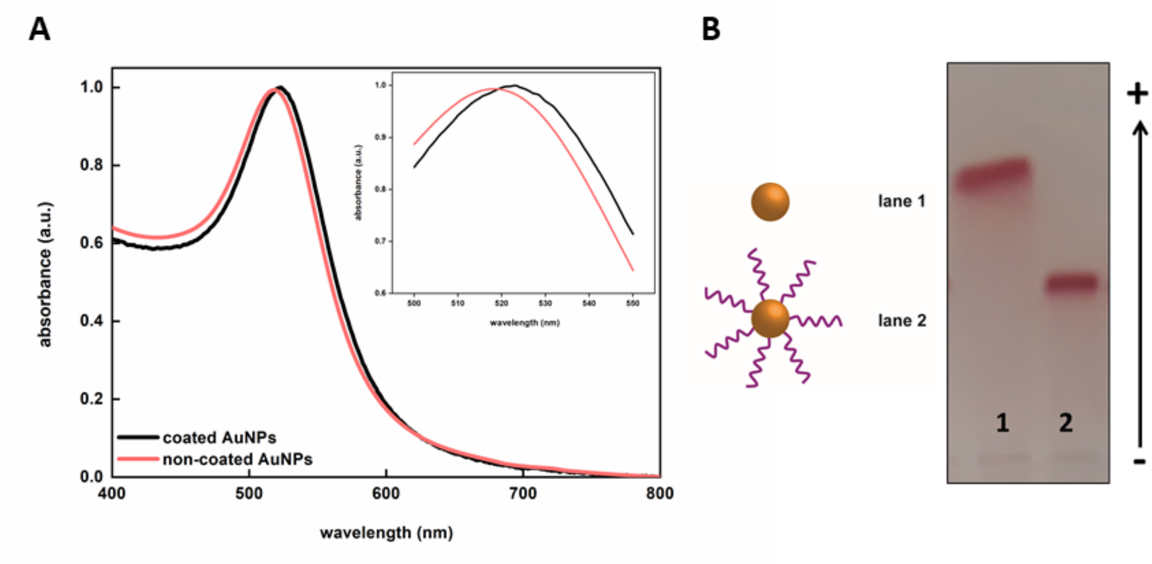

Figure 6.1 (**A**) Normalised UV-Vis spectra comparing the SPR peak maximum of DNA-coated and non-coated (BSPP stabilised) 15 ± 1 nm spherical AuNPs and (**B**) agarose gel electrophoresis comparing 15 ± 1 nm BSPP coated AuNPs (**lane 1**) and 15 ± 1 nm AuNPs coated with a shell of oligonucleotides specific for the detection of vimentin mRNA (**lane 2**).

Endocytosis is the cellular process in which different macromolecules and particles from the surrounding medium can be internalized into the cell (see **Section 2.4**). In endocytosis, the substance is surrounded by an area of the plasma membrane, which then is assembled into a vesicle inside the cell. DNA functionalised AuNPs can undergo endocytosis. The DNA-coated AuNPs were found within early endosomes after an incubation time of 1 h with live cells, while after 4 h of incubation DNA-coated AuNPs were trafficked to late endosomes where they reside. Only a small percentage of DNA-coated AuNPs escape endosomes. The use of certain peptides can facilitate the entry of other peptides, oligonucleotides, and even proteins into the cytoplasm of cells. Previous studies have shown that the path of nanoparticles conjugated with these peptides is different from a regular endosome-lysosome pathway [344, 345]. Nativo *et al*. proposed the approach of evading the endosome-lysosome pathway of uptake to a significant extent by surface modification of the nanoparticles with cell-penetrating peptides [346]. In our study, a short 14 amino acid AMP, which is called Aurein 1.2 and is expressed in the skin secretions of various species of the Litoria genus of Australian frogs [347, 348] was used to increase the endosomal escape. The surface of the AuNP with attached ssDNA was further functionalised with the Aurein 1.2 peptide by overnight incubation (see **Section 2.5.2**). A cysteine modification to one end of the Aurein 1.2 peptide (see **Table 3.2** for peptide sequence) was used for the conjugation of the peptides to the AuNP surface to facilitate the binding to the gold surface (**Figure 6.2**).

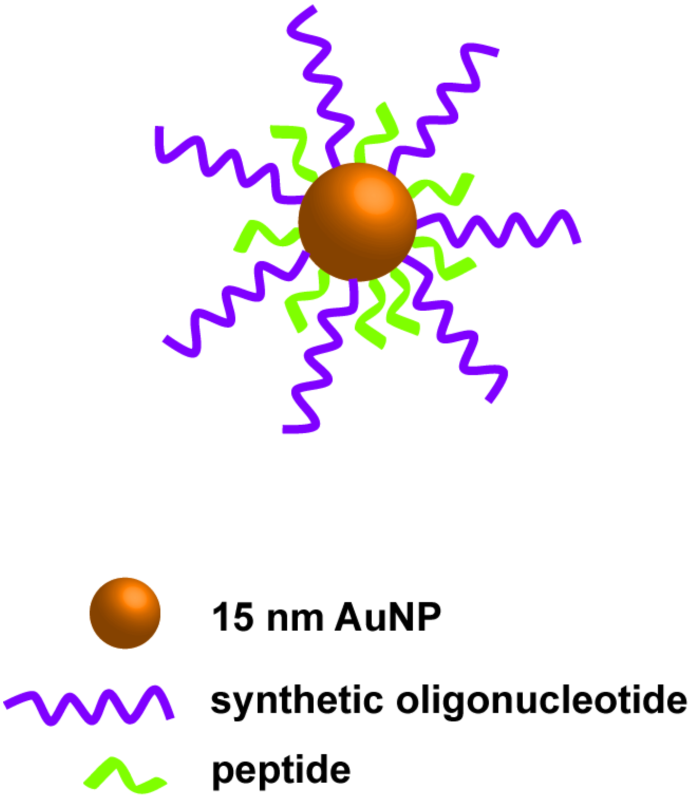

Figure 6.2 Schematic illustration of an AuNP core functionalised with multiple synthetic oligonucleotides specific for the detection of vimentin mRNA (5′ FAM – CTT TGC TCG AAT GTG CGG ACT TAA AAA AAA – thiol 3′) and cysteine modified Aurein 1.2 peptide sequences (CGLFDIIKKIAESF – NH_2).

After the peptide attachment to the DNA-coated AuNPs, the sample was centrifuged and the supernatant was recovered for peptide quantification. The number of peptides attached to the surface of each AuNP was determined by using Ellman's quantification (see **Section 3.3.2.3**). Loading of 173 ± 7 peptide strands for each 15 ± 1 nm AuNP surface was calculated by the quantification procedure.

Following the DNA and peptide functionalisation of the AuNPs' surface, the ability of these probes to detect oligonucleotide targets was checked. **Figure 6.3** demonstrates a schematic illustration of DNA-peptide-coated SNAs that detect mRNA. In the presence of the mRNA target, the flare strand was released due to competitive hybridisation and a fluorescence signal could be detected. When the mRNA target was not present, the flare remained attached and the fluorescence signal corresponding to the Cy5 dye was quenched by the gold core [236, 237].

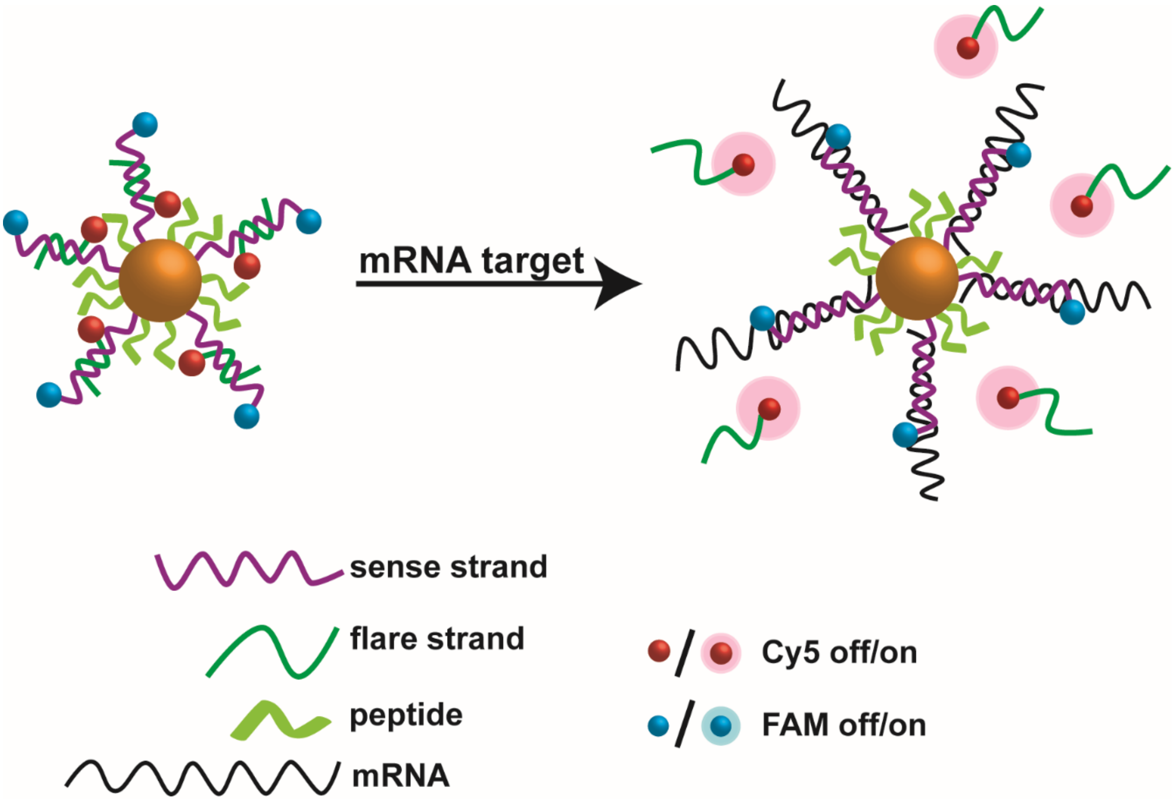

Figure 6.3 Schematic illustration of DNA-peptide-coated SNAs for live mRNA detection. When both sense and flare strands are close to the AuNP core, fluorescence is quenched. When the target mRNA binds to the sense strand, the release of the flare can be detected as an increase in its fluorescence signature.

The control of the temperature is crucial for maintaining the intermolecular forces holding the double-stranded helix together as an increase in temperature can cause the breaking of the bonds and dissociation of the double-strand. When the melting temperature (T_m) is reached, 50% of the dsDNA dehybridises into single strands [44]. Prior to DNA melting, the fluorescent signal from Cy5-capped flare strands was quenched by the AuNPs due to energy transfer from the excited fluorophores to the nanoparticles. The temperature was gradually increased whilst monitoring changes in the fluorescence intensity of the flare strand. After DNA melting, the flare strands were released and the fluorescence signal was recovered, providing a way of monitoring the melting process. After reaching and surpassing the T_m, the DNA-peptide-coated SNA duplex disassociated and the donor Cy5 fluorophore strands were released into the solution. This increased the fluorophore concentration in the solution which resulted in self-quenching hence a large decrease in fluorescence intensity in the melting curve for higher temperatures [349, 350]. **Figure 6.4** presents the melting curve of vimentin DNA-peptide-coated SNAs where the T_m corresponds to the mid-point of a smooth transition.

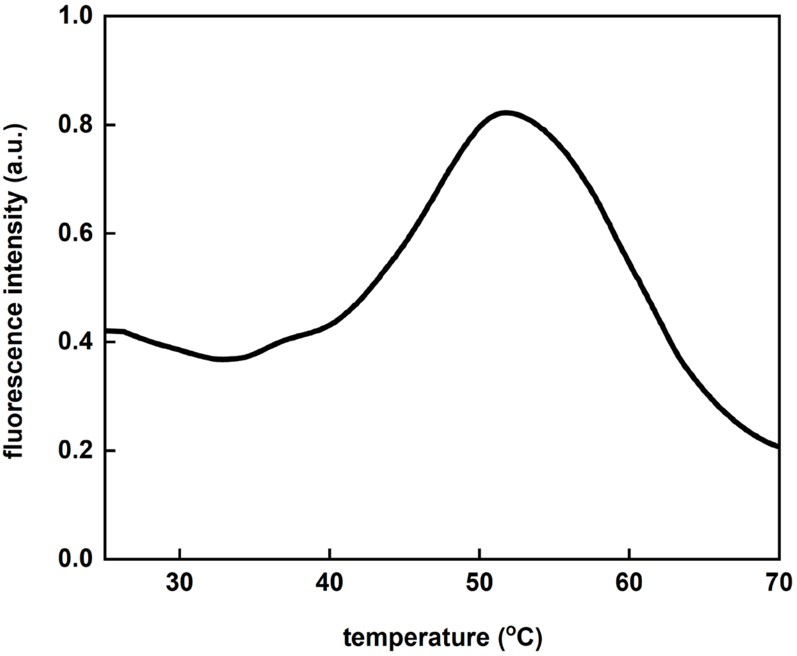

Figure 6.4 Fluorescence melting curve of DNA-peptide-coated SNAs specific for the detection of vimentin mRNA. To determine the T_m, fully assembled DNA-peptide-coated SNAs were heated to 70 °C and the flare strand fluorescence was monitored.

A characteristic curve with a melting temperature of approximately 46 °C for vimentin DNA-peptide-coated SNAs was observed in **Figure 6.4** suggesting a successful flare hybridisation and a suitable probe for *in vitro* cell experiments. A melting temperature below 37 °C would lead to nonspecific flare release and a false positive fluorescence signal when used within live cells, as they were cultured at a constant temperature of 37 °C.

6.1.2 Stability of DNA-peptide-coated spherical nucleic acids against nuclease

The ability of the aforementioned probes to resist nuclease degradation was investigated as DNA-peptide-coated SNAs were incubated with DNase I at 37 °C. The fluorescence signal of the dye conjugated to the oligonucleotide strand (FAM) was monitored over a 72 h incubation period. When attached to the gold core, the fluorescence of the dye was quenched. Degradation due to enzymatic hydrolysis would result in fluorescence restoration since the dye-modified strands would be released and quenching would no longer be possible.

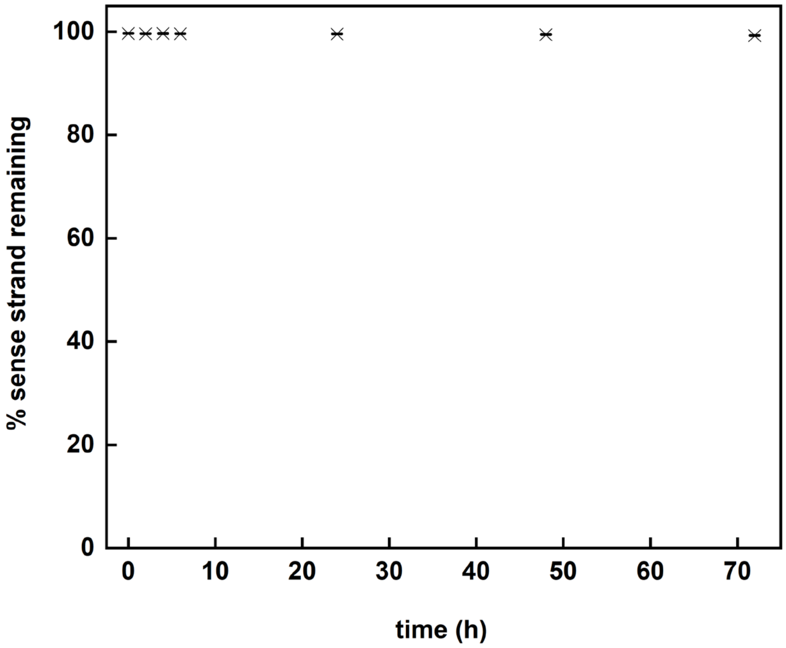

Figure 6.5 Susceptibility of DNA-peptide-coated SNAs towards degradation by DNase I. By monitoring the fluorescence intensity of the FAM dye on the sense strand, the % of oligonucleotides on the AuNP surface was determined. Data are shown as mean ± standard error of the mean (n = 3).

In **Figure 6.5** the percentage of oligonucleotide strands that remained attached to the AuNP surface is presented. There was no significant oligonucleotide loss over a 72 h incubation period with DNase I. The DNA-peptide-coated AuNPs preserve more than 99% of their initial DNA surface coverage thus demonstrating their high stability.

6.1.3 Specificity of DNA-peptide-coated spherical nucleic acids

DNA-coated AuNPs have high binding coefficients for complementary DNA and RNA sequences due to the 3D structure of the densely packed, highly oriented oligonucleotide shell on the surface of the particles [184]. As a result, the rapid and efficient specificity of the DNA-peptide-coated SNAs to detect mRNA within living cells was tested. Binding studies were performed in a tube using synthetic fully complementary oligonucleotide targets for vimentin mRNA. DNA-peptide-coated SNAs in PBS were incubated with an excess amount of fully complementary DNA and RNA targets.

Figure 6.6 demonstrates the ability of DNA-peptide-coated SNAs to respond with an increase in the Cy5 fluorescence signal upon recognition and binding within the first 2 min in the presence of the fully complementary DNA and RNA targets. This observation confirmed their efficiency at signalling in the presence of a specific target in buffered conditions within a tube.

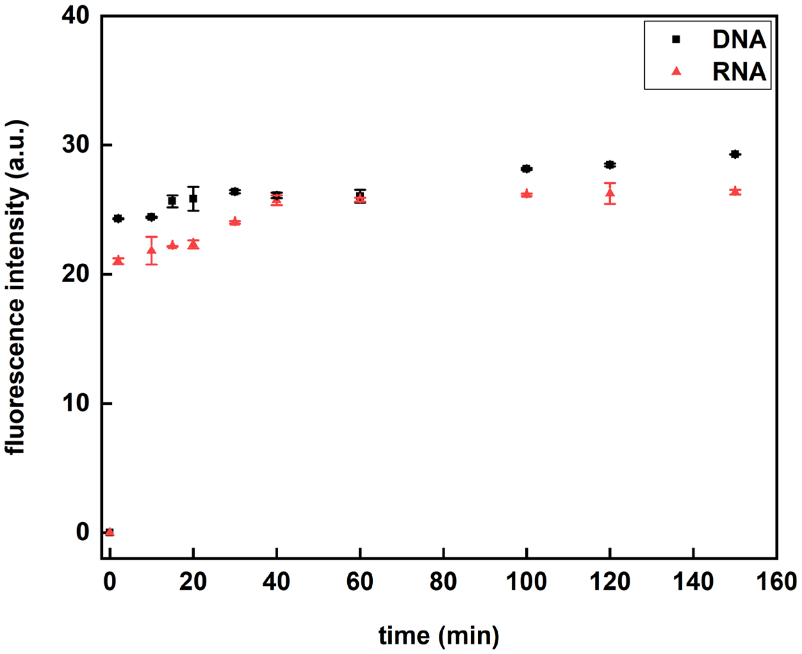

Figure 6.6 Time course of fluorescence associated with flare release when DNA-peptide-coated SNAs were incubated with synthetic and fully complementary oligonucleotide DNA and RNA sequences within a tube leading to the displacement of the vimentin flare. Data are shown as mean ± standard error of the mean (n = 3).

6.1.4 Interaction of DNA-peptide-coated spherical nucleic acids with mammalian cells

Having checked that the DNA-peptide-coated SNAs present increased stability, specificity and selectivity in an extracellular environment, their ability to detect mRNA targets was then studied in living cells. As previously mentioned the oligonucleotide sequences on the surface of the DNA-peptide-coated SNAs were designed to detect vimentin mRNAs. The A 549 cell line was chosen as a model that strongly expresses vimentin. A µ-slide with 8 wells and a glass bottom was used to grow cells at 90% confluency. Once cells reached the desired confluency, they were incubated with Hoechst 33342 (2 µL, 30 min) to stain the nuclei. The medium was then replaced by a fresh medium containing DNA modified AuNPs (0.7 pmol, 52.08 µL) or DNA-peptide modified AuNPs (0.7 pmol, 40.27 µL) and were monitored over a 7 h period. Vimentin DNA-coated SNAs were incubated with A 549 cells and used as control probes, to test the existence of any significant difference in fluorescence signal following live cell mRNA detection. The flare release that corresponds to mRNA detection, was monitored *via* confocal microscopy for a period of 7 h after initial incubation. The imaging was performed on a Leica SP8 confocal microscope at 37 °C under a constant flow of CO_2 to provide a healthy environment for the cells.

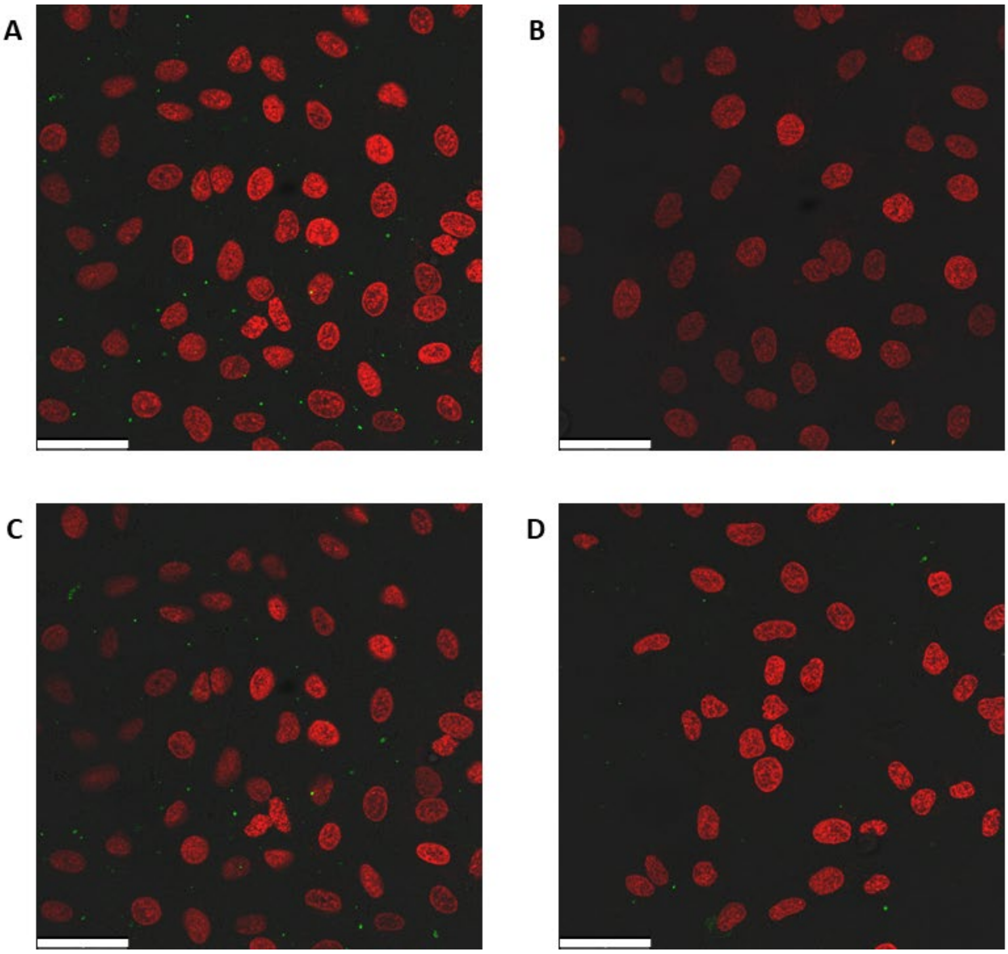

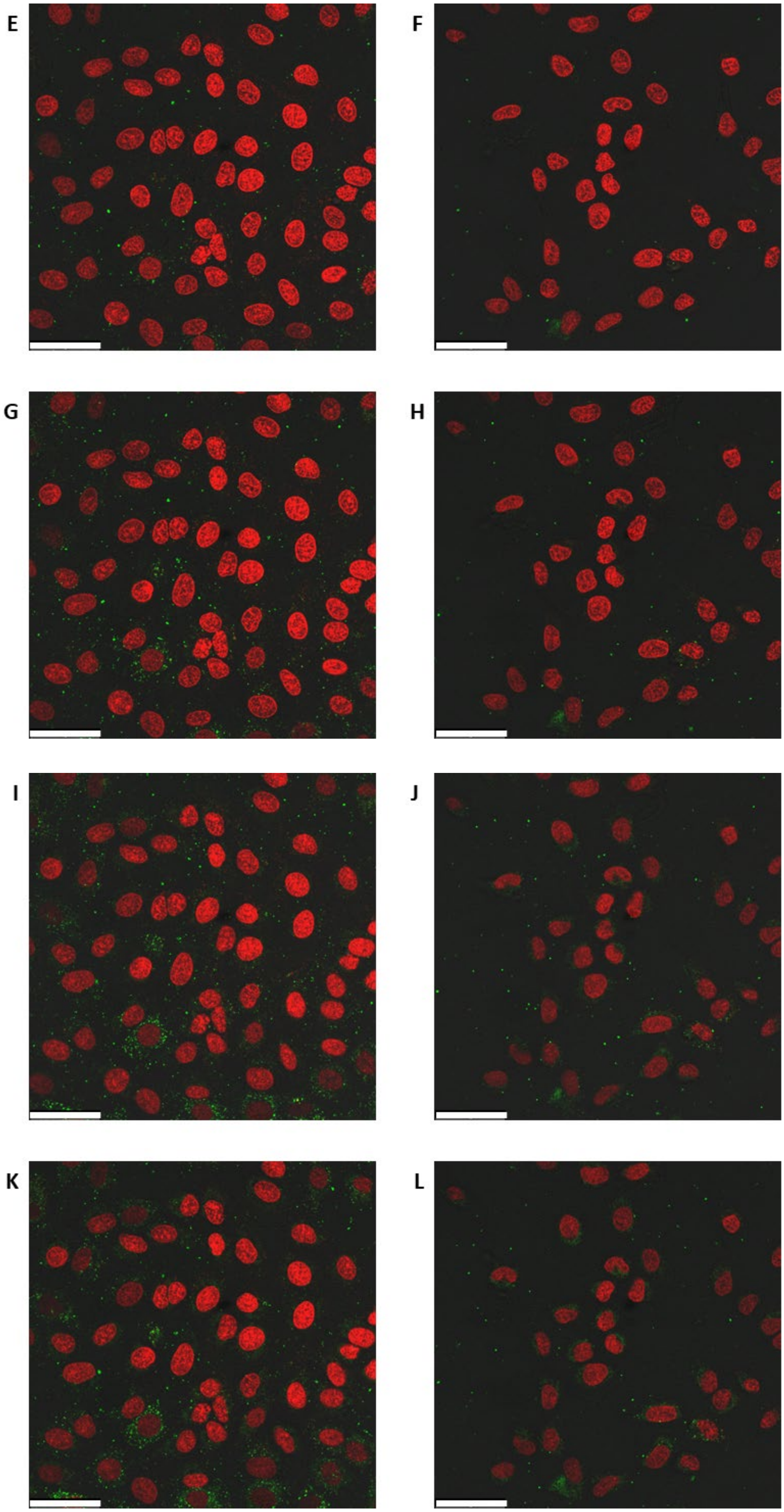
E
F
G
H
I
J
K
L

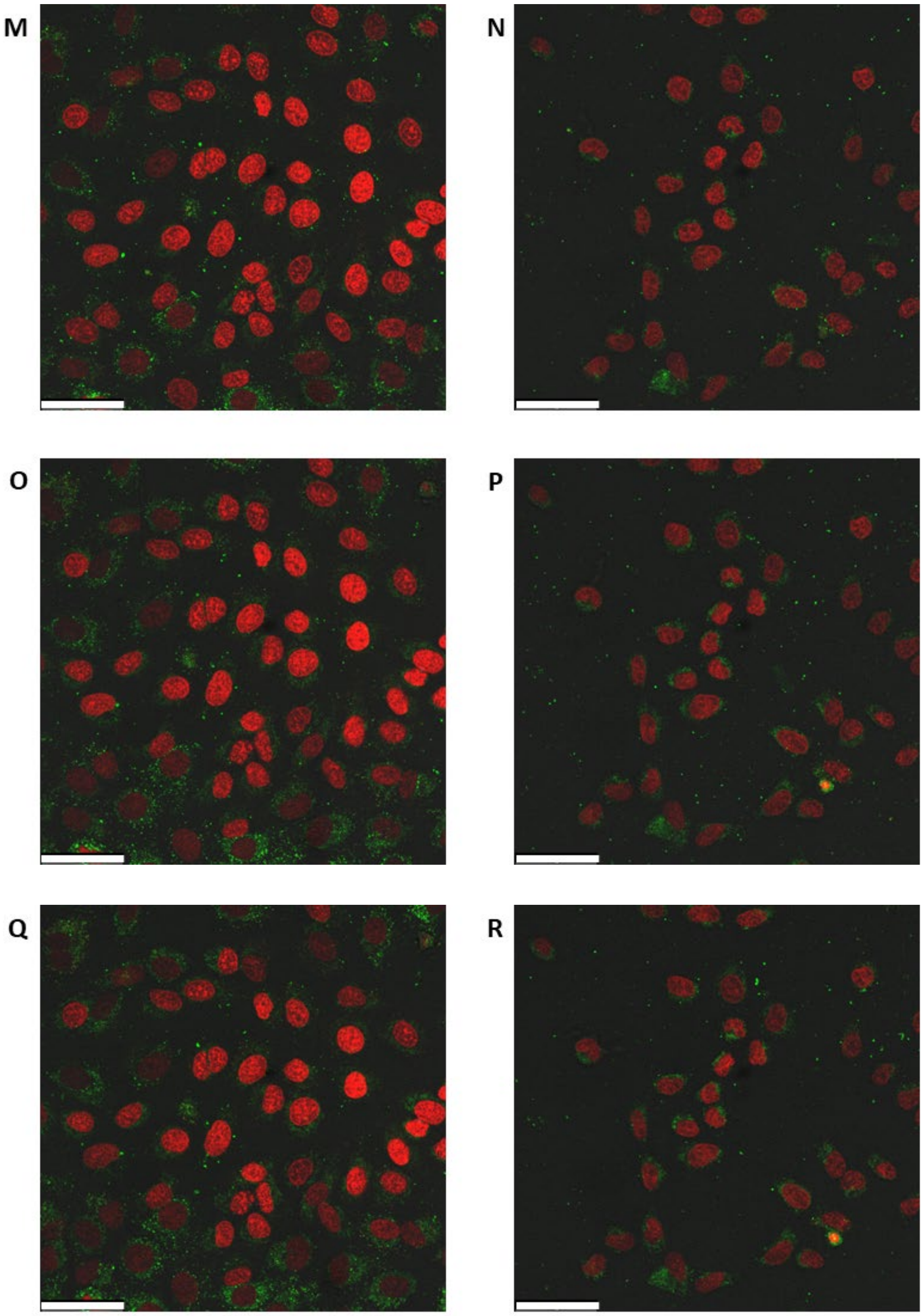

Figure 6.7 Fluorescence time-lapse study of live A 549 cells incubated with DNA-coated AuNPs (left column) and DNA-peptide-coated AuNPs (right column) specific for the detection of vimentin. Confocal microscopy images show cells before incubation (**A**-**B**) and flare release after 20 (**C**-**D**), 60 (**E**-**F**), 120 (**G**-**H**), 180 (**I**-**J**), 240 (**K**-**L**), 300 (**M**-**N**), 360 (**O**-**P**) and 420 min (**Q**-**R**) post-incubation. Colour guide: Hoechst nuclear counterstain – red, vimentin flare release – green. Scale bar is 49 µm.

By observing the fluorescence signal of the DNA-coated AuNPs (left column) and DNA-peptide-coated AuNPs (right column) shown in **Figure 6.7**, a slightly stronger signal for the DNA-coated

AuNPs sample was recorded at 7 h post-incubation. However, both the DNA-coated AuNPs and the DNA-peptide-coated AuNPs were able to detect vimentin mRNA in cells. According to previous studies, the functionalisation of AuNPs with only peptide sequences was a successful strategy for increased endosomal escape and the ability of the AuNPs-KT2-PEG conjugates to induce MDA-MB-231 human breast cancer cell death [351] or the capability of peptide-coated AuNPs to display a wound healing activity on a keratinocytes monolayer [352]. In our study, the peptides were not able to increase the number of nanoparticles escaping the endosomes. This small difference in fluorescence intensity led to the hypothesis that the short peptide strand used in this study was sterically hindered by the longer DNA strand while they were attached to the AuNP surface. DNA-peptide-coated SNAs were able to detect mRNA in live cells although the increase in the number of nanoparticles escaping the endosomes was not allowed by the design of the probe.

6.2 Surface Modification of 15 ± 1 nm Spherical Gold Nanoparticles with Peptide-DNA Conjugate Sequences

6.2.1 Synthesis and characterisation of peptide-DNA conjugate spherical nucleic acids

Based on the confocal results in **Section 6.1.4**, the DNA-peptide-coated SNAs were redesigned. Our strategy was based on the conjugation of the peptide on the 5′ end of the DNA strand to improve the spatial position of the peptide and avoid potential steric hindrance by the oligonucleotides. Spherical AuNPs with a size of 15 ± 1 nm were functionalised with both synthetic oligonucleotides and peptide oligonucleotide conjugates in different mixing ratios. The synthetic oligonucleotides had a terminal 3′ thiol modification and a terminal 5′ FAM dye. The peptide sequence was conjugated on the 5′ end after the FAM dye and consequently, it had a terminal 3′ thiol modification (see **Table 3.2** for the conjugate sequence). All the sequences directly attached to the AuNP surface were termed “sense” strands. The DNA sequence of the sense strand was designed to bind only vimentin mRNA (see **Table 3.1** for oligonucleotide sequence). The 3 different mixing ratios of DNA and peptide-DNA conjugate strands used in this study were 1% peptide-DNA conjugate & 99% vimentin DNA coated AuNPs, 5% peptide-DNA conjugate & 95% vimentin DNA coated AuNPs and 10% peptide-DNA conjugate & 90% vimentin DNA coated AuNPs.

Shorter oligonucleotide complementary strands (flare strands) modified with a Cy5 dye at their 5′ end were hybridised into the sense strands. The oligonucleotide dyes were quenched (OFF state) when the sense strands were bound to the AuNP surface due to close proximity. In the presence of the mRNA target, the flare strand was released and the target mRNA was bound to the sense strand due to competitive hybridisation [236, 237]. The increase in fluorescence at the wavelength of the Cy5 dye (ON state) was recorded as demonstrated in **Figure 6.8**. The fluorophore on the flare strand

(Cy5) acted as a reporter while the FAM dye on the sense strands was used as a control to monitor the integrity of the sense strands.

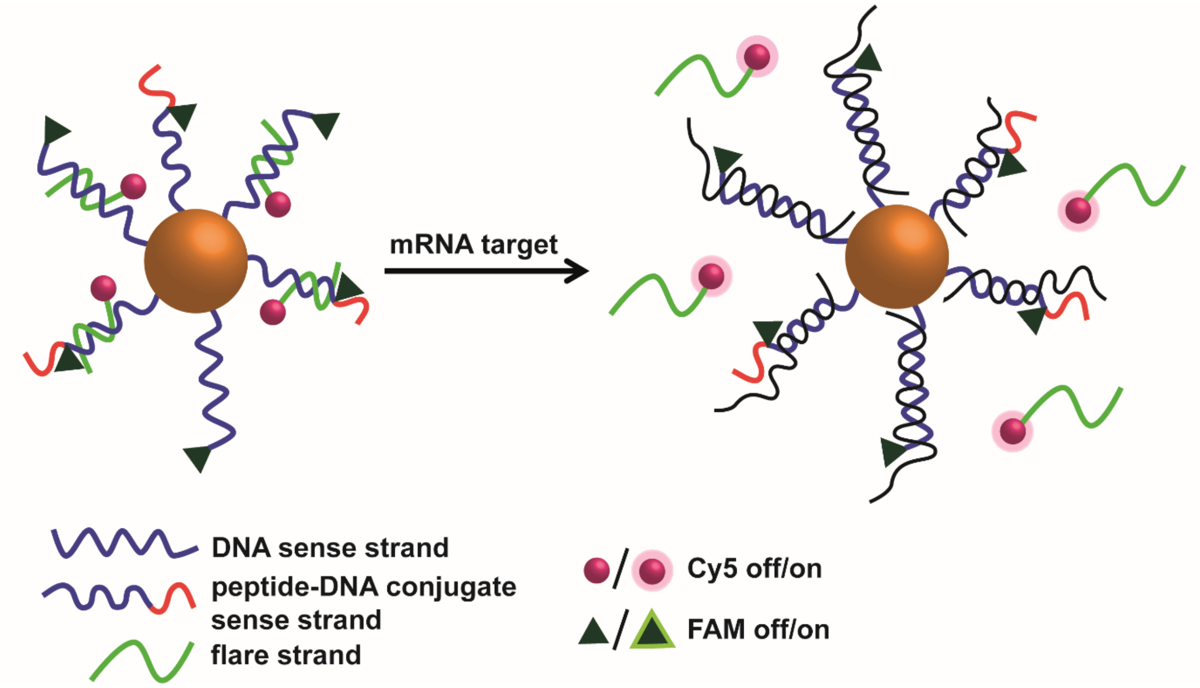

Figure 6.8 Schematic illustration of peptide-DNA conjugate SNAs for live mRNA detection. When both sense and flare strands are close to the AuNP core, fluorescence is quenched. When the target mRNA binds to the sense strand, the release of the flare can be detected as an increase in its fluorescence signature.

The successful 3D conjugation of the sense strands to the AuNP surface was qualitatively observed by UV-Vis. UV-Vis analysis of peptide-DNA conjugate SNAs revealed a sharp peak that was slightly red-shifted compared to BSPP functionalised AuNPs (**Figure 6.9**).

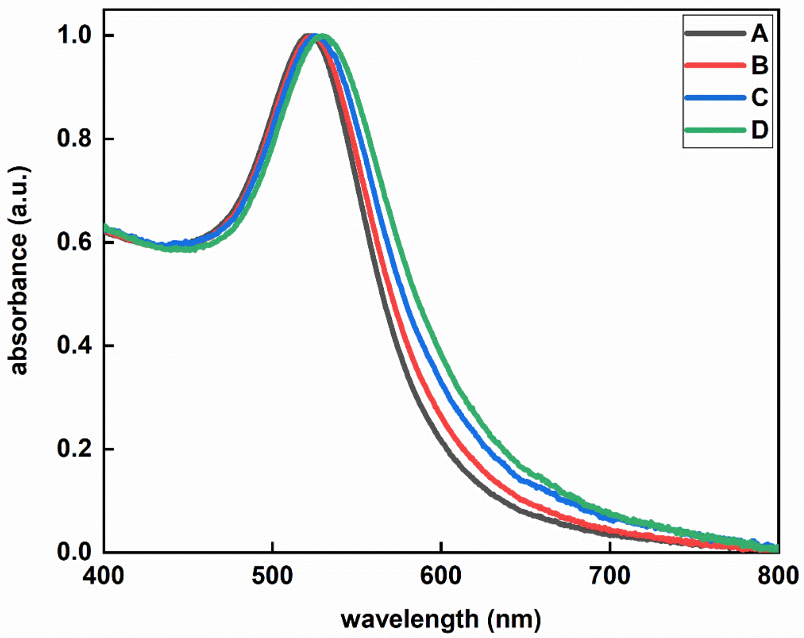

Figure 6.9 Normalized visible spectra of (**A**) BSPP coated AuNPs, (**B**) 1% peptide-DNA conjugate & 99% vimentin DNA coated AuNPs, (**C**) 5% peptide-DNA conjugate & 95% vimentin DNA coated AuNPs and (**D**) 10% peptide-DNA conjugate & 90% vimentin DNA coated AuNPs.

As discussed in **Section 6.1.1** the control of the temperature is important for maintaining the double-stranded helix of the probes together. An increase in temperature can break the bonds and dissociate the double-strand. As a result, the measurement of the T_m when designing these probes for *in vitro* applications is essential. **Figure 6.10** shows the melting curves of the three different types of peptide-DNA conjugate SNAs where the T_m corresponds to the mid-point of a smooth transition. This suggested a successful flare hybridisation and a suitable probe for *in vitro* cell experiments. All melting temperatures were above 37 °C which was desirable as peptide-DNA conjugate SNAs were cultured with live cells at a constant temperature of 37 °C. A decrease in fluorescence intensity in the melting curve was again observed for higher temperatures. After reaching and surpassing the T_m, the peptide-DNA conjugate SNA duplex disassociated and the donor Cy5 fluorophore strand was released into the solution. Consequently, the fluorophore concentration in the solution was increased which resulted in self-quenching [349, 350].

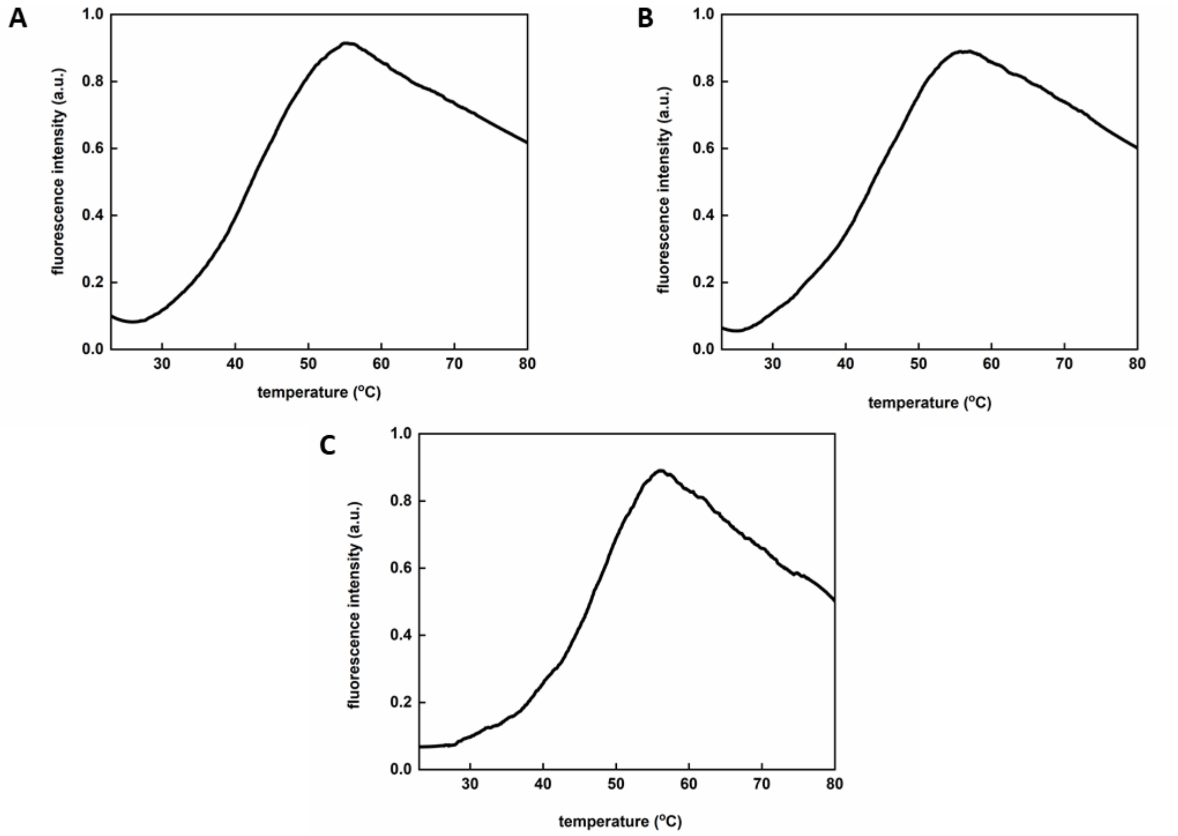

Figure 6.10 Fluorescence melting curves of (**A**) 1% peptide-DNA conjugate & 99% vimentin DNA coated AuNPs, (**B**) 5% peptide-DNA conjugate & 95% vimentin DNA coated AuNPs and (**C**) 10% peptide-DNA conjugate & 90% vimentin DNA coated AuNPs. To determine the T_m, fully assembled peptide-DNA conjugate SNAs were heated to 80 °C and the flare strand fluorescence was monitored.

6.2.2 Stability of peptide-DNA conjugate spherical nucleic acids against nuclease

Peptide-DNA conjugate SNAs were incubated with DNase I at 37 °C to test the stability of the probes against nuclease degradation. The fluorescence signal of the FAM dye conjugated to the sense strands was monitored over a 72 h incubation period. The percentage of sense strands that remained attached to the AuNP surface is presented in **Figure 6.11**. There was no significant sense strand loss over a 72 h incubation period with DNase I. The peptide-DNA conjugate SNAs maintained more than 99% of their initial surface coverage which confirmed their high stability.

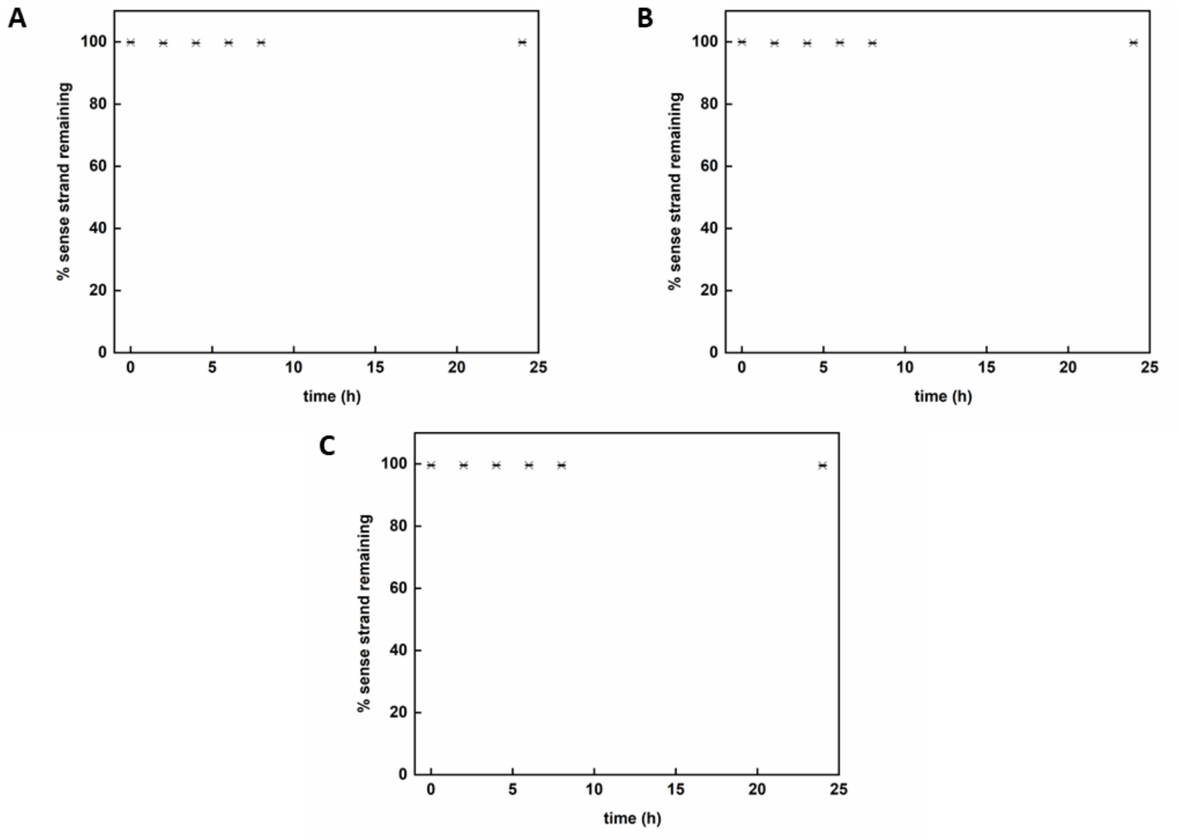

Figure 6.11 Susceptibility of (**A**) 1% peptide-DNA conjugate & 99% vimentin DNA coated AuNPs, (**B**) 5% peptide-DNA conjugate & 95% vimentin DNA coated AuNPs and (**C**) 10% peptide-DNA conjugate & 90% vimentin DNA coated AuNPs towards degradation by DNase I. By monitoring the fluorescence intensity of the FAM dye on the sense strand, the % of oligonucleotides on the AuNP surface was determined. Data are shown as mean ± standard error of the mean (n = 3).

6.2.3 Specificity of peptide-DNA conjugate spherical nucleic acids

The peptide-DNA conjugate SNAs were tested for their efficiency to detect mRNA within living cells. Binding studies were performed in a tube using synthetic fully complementary oligonucleotide targets for vimentin mRNA. Peptide-DNA conjugate SNAs in PBS were incubated with an excess amount of fully complementary DNA target. The ability of peptide-DNA conjugate SNAs to respond upon recognition and binding within the first 2 min in the presence of the fully complementary DNA target is presented in **Figure 6.12**. This observation confirmed their efficiency at signalling in the presence of a specific target in buffered conditions within a tube.

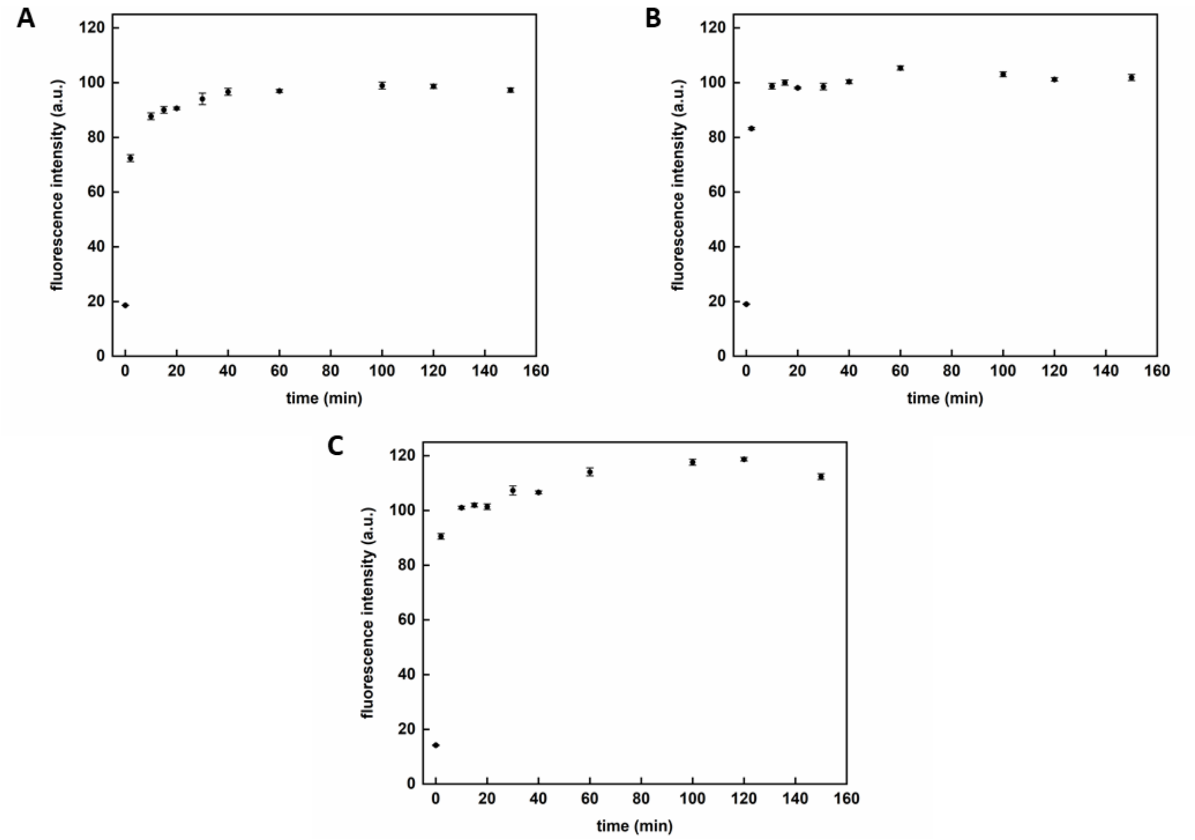

Figure 6.12 Time course of fluorescence associated with flare release when (**A**) 1% peptide-DNA conjugate & 99% vimentin DNA coated AuNPs, (**B**) 5% peptide-DNA conjugate & 95% vimentin DNA coated AuNPs and (**C**) 10% peptide-DNA conjugate & 90% vimentin DNA coated AuNPs were incubated with a synthetic and fully complementary oligonucleotide sequence within a tube leading to the displacement of the vimentin flare. Data are shown as mean ± standard error of the mean (n = 3).

6.2.4 Interaction of peptide-DNA conjugate spherical nucleic acids with mammalian cells

As previously mentioned the oligonucleotide sequences on the surface of the peptide-DNA conjugate SNAs were designed to detect vimentin mRNAs. Two cell lines, A 549 and SAOS-2, were used for this study. Both cell lines have an epithelial morphology and express vimentin. A 549 and SAOS-2 cells were incubated with the three different mixing ratios of peptide-DNA conjugate SNAs for the detection of vimentin mRNA such as the 1% peptide-DNA conjugate & 99% vimentin DNA coated AuNPs, the 5% peptide-DNA conjugate & 95% vimentin DNA coated AuNPs and the 10% peptide-DNA conjugate & 90% vimentin DNA coated AuNPs. Vimentin DNA-coated AuNPs were also incubated with A 549 and SAOS-2 cells and used as control probes, to test the existence of any significant difference in fluorescence signal following live cell mRNA detection. The flare release that corresponds to mRNA detection, was visualised *via* confocal microscopy after 18 h of initial incubation.

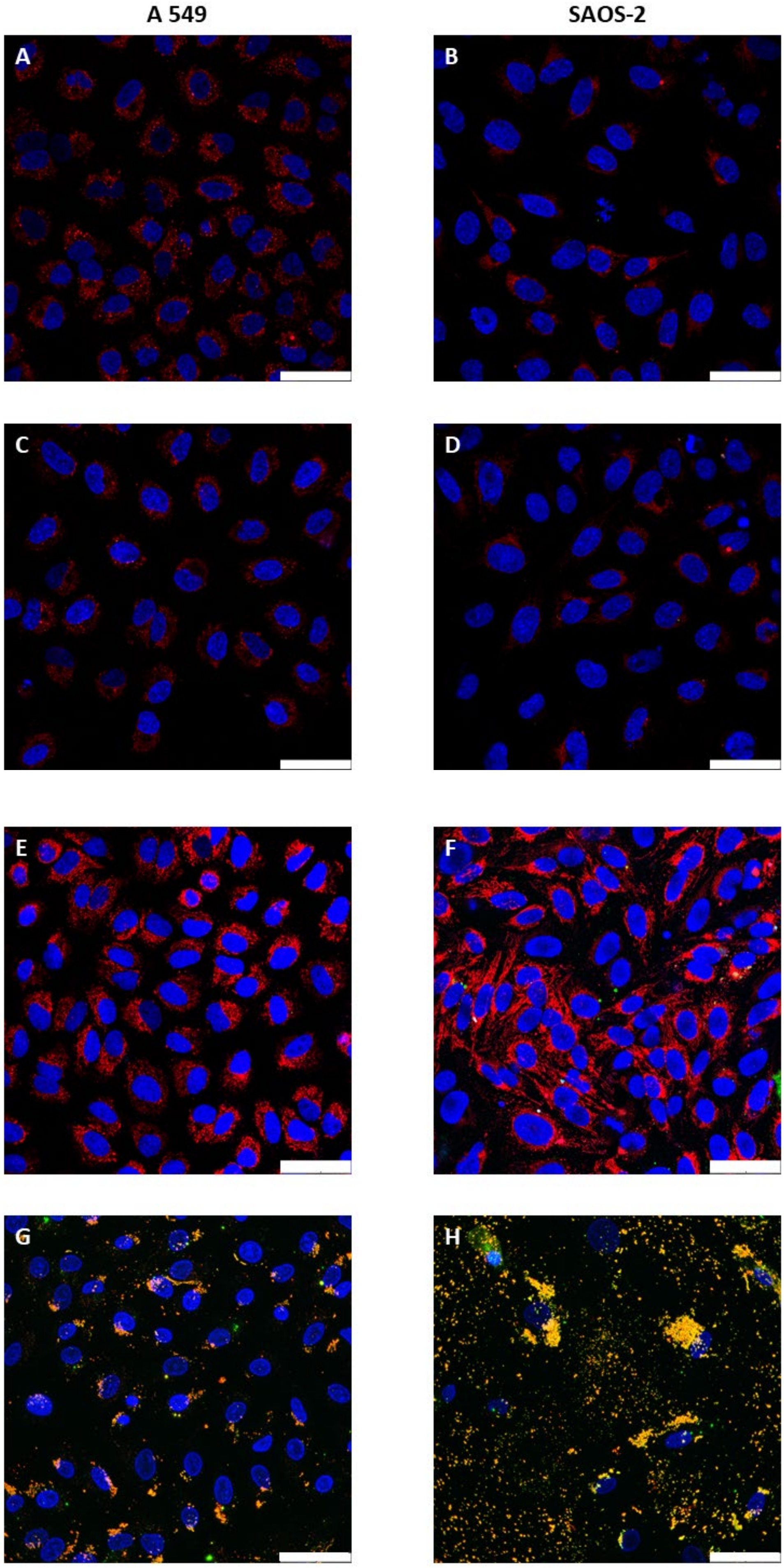
A 549
SAOS-2
A
B
C
D
E
F
G
H

Figure 6.13 Confocal microscopy images of A 549 (left column) and SAOS-2 (right column) live cells incubated with (**A** and **B**) vimentin DNA-coated AuNPs, (**C** and **D**) 1% peptide-DNA conjugate & 99% vimentin DNA coated AuNPs, (**E** and **F**) 5% peptide-DNA conjugate & 95% vimentin DNA coated AuNPs and (**G** and **H**) 10% peptide-DNA conjugate & 90% vimentin DNA coated AuNPs after 18 h post-incubation. Colour guide: Hoechst nuclear counterstain – blue, vimentin flare release – red, vimentin sense strand – green. Scale bar is 49 µm.

Confocal microscopy images of the flare release that corresponds to mRNA detection are demonstrated in **Figure 6.13** after 18 h of initial incubation. Both A 549 and SAOS-2 cells displayed a fluorescence signal (red) corresponding to the detection of vimentin mRNA for all kinds of probes. In the case of 10% peptide-DNA conjugate & 90% vimentin DNA coated AuNPs, a fluorescence signal from the sense strands (green) was also observed in both cell lines. This was due to partial degradation of the sense strands from the AuNP surface. As a consequence of the lack of stability of the 10% peptide-DNA conjugate & 90% vimentin DNA coated AuNPs after 18 h post-incubation, this probe was unsuitable for vimentin mRNA detection. Concerning the 1% peptide-DNA conjugate & 99% vimentin DNA coated AuNPs, the fluorescence signal was quite similar to the control vimentin DNA-coated AuNPs. By comparing the fluorescence signal intensity of the vimentin DNA-coated AuNPs and peptide-DNA conjugate coated AuNPs presented in **Figure 6.13**, a stronger signal for the 5% peptide-DNA conjugate & 95% vimentin DNA coated AuNPs sample was recorded in both A 549 and SAOS-2 cell lines after 18 h post-incubation. This led to the hypothesis that the structure of the 5% peptide-DNA conjugate & 95% vimentin DNA coated AuNPs enhanced the effective escape within cells in comparison with the control vimentin DNA-coated AuNPs.

After checking the ability of the peptide-DNA conjugate SNAs to detect mRNA in live cells, studies focused on investigating their intracellular fate. By understanding the interactions between the conjugate SNAs and live cells, the design of the probes could be further optimised toward the processes of nanoparticle uptake or endosomal escape. Several types of functional nanoparticles, mainly coated by peptides or other transfection agents, can escape endosomes following endocytosis, however, it has not been reported yet a mechanism for the process of endosomal escape [330, 353, 354]. To reassure that the difference in fluorescence intensity between the DNA-coated AuNPs and the peptide-DNA conjugate coated AuNPs after 18 h of initial incubation was significant, the ultra-thin sectioning of cells for TEM analysis was followed as presented in **Figure 6.14** for A 549 cells and **Figure 6.15** for SAOS-2 cells. This method was used to shed more light on the cellular location of mRNA sensing and observe any increase in the number of nanoparticles escaping the endosomes (see **Section 3.4.3** for experimental details).

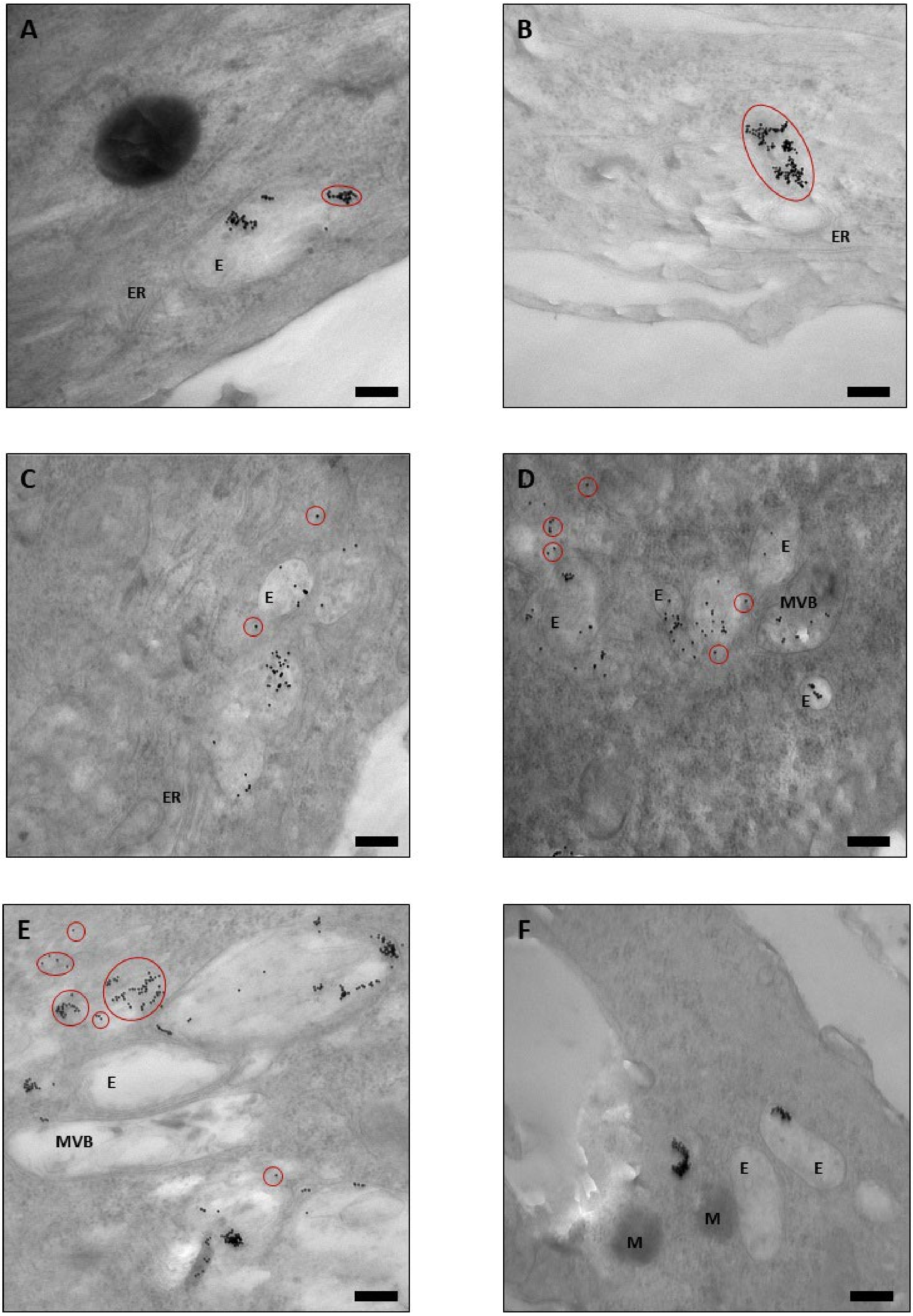

Figure 6.14 TEM images of A 549 cells incubated with (**A** and **B**) vimentin DNA-coated AuNPs, (**C** and **D**) 1% peptide-DNA conjugate & 99% vimentin DNA coated AuNPs and (**E** and **F**) 5% peptide-DNA conjugate & 95% vimentin DNA coated AuNPs. ER: Endoplasmic

Reticulum, E: Endosomes, M: Mitochondria, MVB: MultiVesicular Body. Red circles indicate peptide-DNA conjugate SNAs with a cytoplasmic location. Scale bar is 200 nm.

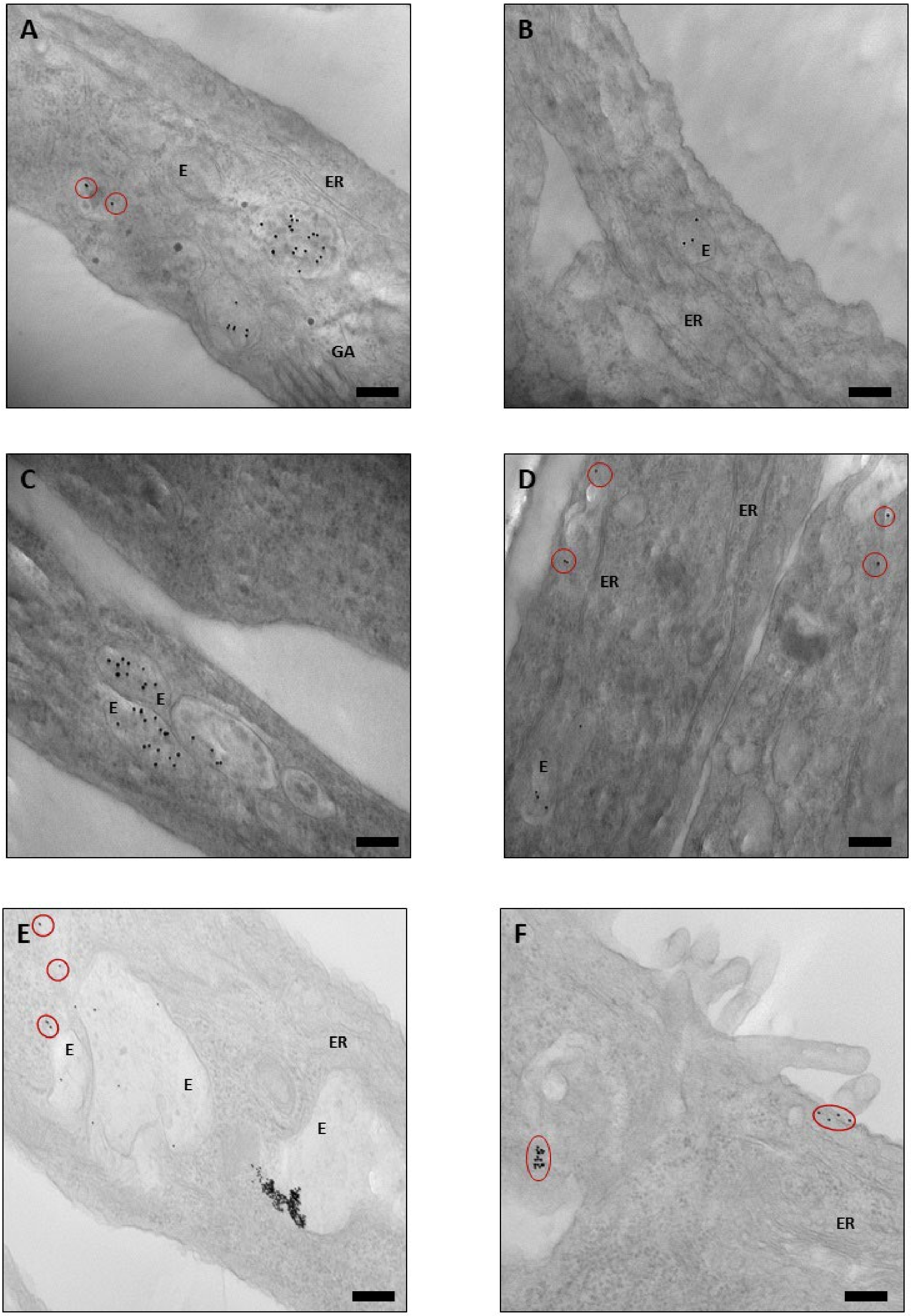

Figure 6.15 TEM images of SAOS-2 cells incubated with (**A** and **B**) vimentin DNA-coated AuNPs, (**C** and **D**) 1% peptide-DNA conjugate & 99% vimentin DNA coated AuNPs and (**E** and **F**) 5% peptide-DNA conjugate & 95% vimentin DNA coated AuNPs. ER: Endoplasmic Reticulum, E: Endosomes, GA: Golgi Apparatus. Red circles indicate peptide-DNA conjugate SNAs with a cytoplasmic location. Scale bar 200 nm.

The TEM analysis of many different images showed that 3.64% of vimentin DNA-coated AuNPs, 3.75% of 1% peptide-DNA conjugate & 99% vimentin DNA coated AuNPs and 3.97% of 5% peptide-DNA conjugate & 95% vimentin DNA coated AuNPs were found outside endosomes in A 549 cells after an 18 h incubation period. For the SAOS-2 cell line, it was found that 3.12% of vimentin DNA-coated AuNPs, 3.34% of 1% peptide-DNA conjugate & 99% vimentin DNA coated AuNPs and 3.67% of 5% peptide-DNA conjugate & 95% vimentin DNA coated AuNPs were outside endosomes after 18 h of initial incubation. For this study, three grids from three separate experiments per cell type for each experimental condition were analysed (~2,000 particles per experiment). As a result, the majority of particles were located in vesicles while a small percentage of particles appeared to be located in the cytosol. The percentage difference between the control sample of vimentin DNA-coated AuNPs and the peptide-DNA conjugate coated AuNPs was not significant regardless of the cell line. Nevertheless, despite their low abundance, it is considered that the particles located within the cells’ cytosol are responsible for the highly specific mRNA detection after 18 h of initial incubation.

Overall, this chapter describes the surface functionalisation of spherical AuNPs with a cell-penetrating peptide. The integration of the cell-penetrating peptide Aurein 1.2, which promotes efficient escape within cells, was inspired by the need for a novel design approach to enhance the endosomal escape of DNA functionalised AuNPs. Two different approaches to surface functionalisation using peptide Aurein 1.2 are covered in this chapter. In the first case, cell-penetrating peptides with cysteine ends were added after thiol-terminated DNA strands to modify AuNPs. However, the peptides on the surface of the AuNPs were not able to increase the number of nanoparticles escaping the endosomes. As a result, in the second case, AuNPs were functionalised using these peptide oligonucleotide conjugates and DNA strands in various mixing ratios after the peptide sequence was attached to the 5' end of the DNA strand. After incubation with cells, it was found that the majority of particles were located in vesicles with only a small percentage appearing to be in the cytosol.

Chapter 7 Design of Functionalised Upconversion Nanoparticles for Oligonucleotide Detection

The development of sensors for the detection of biomolecules is of increasing interest in order to achieve early disease diagnosis in clinical testing, environmental monitoring and food safety [355-360]. The biomolecules that have attracted more attention for detection are DNA and RNA due to their involvement in many biological processes such as protein production, gene regulation and various diseases such as cancer [13-15]. Previously, Alonso-Cristobal and co-workers reported a sensor that combined the emissive optical properties of UCNPs and the quenching ability of graphene oxide (GO) for the detection of polyA sequences in the picomolar range [361]. Then, the development of a sensor that detected specific mRNA biomarkers present in Alzheimer's disease and prostate cancer was fabricated and optimized for use in blood plasma and cell lysate [362]. Furthermore, Giust *et al*. developed a portable UCNPs/GO sensor for the field detection of messenger RNA biomarkers related to nutritional deficiencies in crops [156]. Based on these studies, the development of a sensor for the use of other types of two-dimensional materials as quenchers is investigated in this chapter. Moreover, during the COVID-19 pandemic, the development of a DNA sensor for SARS-CoV-2 oligonucleotide detection is especially beneficial. This chapter includes the results and discussion of the fabrication of a DNA sensor that is based on the optical interactions occurring between oligonucleotide-coated $NaYF_4$: Yb^{3+}; Er^{3+} UCNPs and the two-dimensional materials (**Section 7.1**). The surface modification of UCNPs with PAA and synthetic oligonucleotides is discussed in **Section 7.2** and **Section 7.3**, respectively. In **Section 7.4** the fluorescence intensity of the oligonucleotide coated UCNPs is monitored after increasing the concentration of two-dimensional materials. The ability of oligonucleotide coated UCNPs to detect a DNA target and SARS-CoV-2 oligonucleotides is presented in **Section 7.5**. The first part of this chapter's results has been published in the article: ''A DNA sensor based on upconversion nanoparticles and two-dimensional dichalcogenide materials'', Konstantina Alexaki, Davide Giust, Maria-Eleni Kyriazi, Afaf H. El-Sagheer, Tom Brown, Otto L. Muskens, and Antonios G. Kanaras, *Frontiers of Chemical Science and Engineering* **2021** *15*, 935–943, DOI: https://doi.org/10.1007/s11705-020-2023-9. The other part of this chapter's results has been published in the article: ''A SARS-CoV-2 sensor based on upconversion nanoparticles and graphene oxide'', Konstantina Alexaki, Maria-Eleni Kyriazi, Joshua Greening, Lapatrada Taemaitree, Afaf H. El-Sagheer, Tom Brown, Xunli Zhang, Otto L. Muskens, and Antonios G. Kanaras, *RSC Advances* **2022** *12*, 18445-18449, DOI: https://doi.org/10.1039/D2RA03599E.

7.1 A DNA Sensor Based on Upconversion Nanoparticles and Two-Dimensional Materials

There are several biosensors capable of detecting DNA or RNA targets based on electrochemical, mass-based or optical methods [15]. Electrochemical sensors are a class of sensors that monitor variations in current in a solution containing the target [363]. These sensors are notable because of their small-size dimensions in portable devices and real-time monitoring; low production thin-film applications; fast analysis and durability. However electrochemical sensors have a limited natural life, are easily affected by temperature changes [364] and show a lower sensitivity compared to other biosensors [365, 366]. Surface acoustic wave sensors are mass-based biosensors that can detect acoustic waves generated by mass loading on their surface [367]. While these sensors have significant advantages as they are rapid and label-free [368], their weakness of being mechanical unstable and fragile [369, 370] limits their widespread use. Optical DNA or RNA sensors are based on the interaction of the optical field with nucleic acids [371]. They represent a significant alternative for the detection of biomolecules as they have high sensitivity and specificity [372]. There are two common types of optical sensors, label-free systems that are based on plasmon resonance or optical resonance [373], and label-based systems that rely on the use of fluorophores, enzymes or nanoparticles [374]. LSPR detection is based on the measurement of binding-induced refractive index changes in a sample region. The quantitative and kinetic measurement of molecular interactions in real-time is due to this type of detection [375]. Since the molecular weight of the target should be large enough to generate a measurable signal change, it is quite challenging to develop LSPR sensors for small molecules at low concentrations [376]. Other common optical biosensors use organic dyes and rely on the existence of an energy transfer pair where the fluorescence of a donor is quenched by an acceptor — a process called Förster resonance energy transfer (FRET) [377]. However, the lack of stability due to photo-bleaching and photo-blinking can arise after the use of organic dyes [378]. Also, the use of organic dyes is limited in complex biological environments due to the presence of undesired background autofluorescence deriving from proteins, cells and other biomolecules since the photo-excitation happens in the UV-visible wavelength range [379].

To overcome the aforementioned difficulties with organic fluorophores, lanthanide-doped UCNPs have been used as reliable options. UCNPs can convert near-infrared light into visible light. Near-infrared excitation radiation is used for more efficient penetration into biological samples in comparison to visible light due to the optically transparent window of the electromagnetic spectrum in biological tissues [380]. Also, UCNPs have narrow emissions in the visible area and they express high resistance to photo-bleaching or photo-blinking, which enables their fluorescent signal stable and easily detectable in multiplexing biosensors [381, 382]. As a result, highly efficient UCNPs are used in a wide range of biological applications [383-385].

In the early 20th century, Perrin first discovered the Förster resonance energy transfer (FRET) theory and then in the 1950s Förster founded it [386]. FRET is a physical process where the excited state energy of a chromophore molecule, the donor, can be transferred to a proximal chromophore, the acceptor, in the ground state. This emission can happen when the two molecules are in close proximity usually between 10 and 100 Å *via* radiative or nonradiative processes [387]. The radiative energy transfer involves the emission of a photon from the donor and then the absorption of that photon by the acceptor [388]. The efficiency of this process is determined by the quantum yield which is the number of emitted photons relative to the number of absorbed photons. In this phenomenon, it is not required a significant interaction between the acceptor and the donor, hence radiative energy transfer can take place over large separations of donor and acceptor [389]. On the contrary, the nonradiative energy transfer does not involve the emission or reabsorption of photons and is strongly distance-dependent. In the nonradiative energy transfer process, the deactivation of the donor and the excitation of the acceptor occur simultaneously while the energy transfers [390]; if the acceptor is non-fluorescent, only quenching of the donor emission is observed following interactions. The nonradiative energy transfer emerges from the dipolar coupling of the excited states of donor and acceptor. This coupling has both quantum mechanical (Dexter exchange mechanism) and electrostatic parts [391]. In Förster's theory, only the electrostatic coupling is taken into consideration [386] which is called the 'weak coupling regime' since the energy levels of the donor and the acceptor are not perturbed by the electrostatic coupling. Consequently, energy transfer can be conceived with the aid of the classical approach of two oscillators (dipoles) in resonance [392]. The FRET efficiency is inversely proportional to the distance between the donor and the acceptor molecule and is described in **Equation 7.1**.

$$E = \frac{1}{1 + \left(\frac{R}{R_0}\right)^6}$$

Equation 7.1 Förster resonance energy transfer efficiency, where E = efficiency of the FRET events, R = distance between the acceptor and the donor molecules and R_0 = Förster distance of this specific pair involved in FRET.

Various two-dimensional materials can be utilised as effective acceptors that quench the fluorescence emission of the donor UCNP. In several studies, UCNPs functionalised with single-stranded DNA can adsorb onto the surface of GO *via* hydrogen bonding and π-π stacking generated interactions between the nucleobases of DNA strand and the aromatic group of GO [156, 362, 393, 394]. The quenching of UCNPs' fluorescence is a result of the close proximity of the UCNPs to the

GO surface [395]. This π-π interaction can be diminished when dsDNA coated UCNPs are formed after hybridisation as the nucleobases are efficiently shielded within the negatively charged phosphate backbone of dsDNA [396]. Thus, the UCNPs do not interact with the GO surface and retain their fluorescence in the presence of the complementary oligonucleotide sequence [361]. This strategy has been used by Zhang *et al*. to develop a glucose sensor based on FRET between concanavalin A-labelled upconverting phosphor nanocrystals and chitosan-labelled GO [397]. By following the same methodology, Huang and co-workers constructed a sensor for the detection of endonucleases using DNA coated UCNPs and GO as a FRET pair. The sensitivity of the resulting biosensor was high with a limit of detection of $1 \times 10^{-4}\ \mathrm{U/mL}$ for S1 nuclease [398]. The same approach has also been used for the sensitive detection of messenger RNA biomarkers, related to Alzheimer’s disease and prostate cancer, in complex media such as blood plasma and cell lysate [362]. Furthermore, Giust *et al*. fabricated a portable sensor for the field detection of messenger RNA biomarkers related to crops’ nutritional deficiencies [156].

Other two-dimensional materials that can be used as quenchers for UCNPs have been investigated for the fabrication of FRET assays. The large surface area, the ease of synthesis of large single sheets and the increased affinity towards biomolecules render two-dimensional dichalcogenide materials as ideal energy transfer acceptors. MoS_2 and WS_2 are two-dimensional materials that can work as excellent quenchers in the area of optical biosensors [399, 400]. UCNPs functionalised with single-stranded DNA can adsorb onto the surface of MoS_2 or WS_2 *via* van der Waals forces [401, 402]. MoS_2 and WS_2 are quite different from GO as GO can adsorb DNA *via* π-π stacking and hydrogen bonding with DNA bases, while MoS_2 and WS_2 are nonaromatic and can adsorb DNA *via* van der Waals forces. The study of the adsorption/desorption behaviour of single-stranded DNA with two-dimensional materials was carried out by Lu and co-workers by varying the ionic strength, the denaturing agents and the DNA length or sequence. In this study GO exhibited the highest affinity for DNA compared to MoS_2 and WS_2 while the detection limit of these three sensors was quite similar when using the same fluorescent DNA probe [401]. According to the available literature, two-dimensional materials behave as very good quenchers in the area of optical aptamer-based sensors. By using single-layer MoS_2 nanosheets and a single-stranded aptamer probe labelled with the fluorescent dye, fluorescein, Kenry’s group studied the fluorescence detection of Plasmodium lactose dehydrogenase protein, a highly expressed malarial biomarker. A heterogeneous mixture of proteins was used to test this sensing platform which was able to distinguish the target Plasmodium lactose dehydrogenase protein [403]. An aptamer-based sensor was also presented by Lv and co-workers for the detection of microcystin-LR, a representative toxin released by Cyanobacteria in water, using MoS_2 and DNA coated UCNPs. This sensor tested and worked efficiently even in ‘real’ samples such as tap and lake water [400]. Yuan *et al*. focused on the use of

MoS_2 and UCNPs as a FRET pair for the detection of the tumour marker $VEGF_{165}$ [404]. As a result, by exploiting the interactions occurring between single-stranded DNA coated UCNPs and MoS_2/WS_2 in solution, the detection of a polyA DNA target in PBS was investigated (see **Section 7.5.1**).

In late 2019, coronavirus disease (COVID-19) produced by the severe acute respiratory syndrome coronavirus 2 (SARS-CoV-2) became a global public health threat. The pathogen causing COVID-19 can create respiratory and intestinal illnesses in both humans and animals [405]. Since the outbreak of this pandemic, the need for fast and accurate testing for COVID-19 has been vital. To date, several testing methods are being utilised based on the available diagnostic tools. RT-PCR is the most widely used technique for testing COVID-19 infections due to its high specificity and sensitivity [406]. However, it is a time-consuming process that requires laboratory facilities, expensive fluorescent tags, trained personnel and extensive sample preparation [407]. Antigen lateral flow testing is another method for COVID-19 detection that can provide useful information as point-of-care testing. This technique offers rapid results but suffers from inferior sensitivity and specificity to RT-PCR [408]. Therefore, the need for a rapid and low-cost technique with high specificity and sensitivity remains for monitoring the spread of COVID-19. Two-dimensional materials-based innovative biosensors have already been developed by several groups [409]. Recently, Chen *et al*. reported single-stranded DNA functionalised two-dimensional transition-metal carbides used as a chemoresistive biosensing platform for the highly sensitive and fast detection of the SARS-CoV-2 N gene [410]. Seo and co-workers introduced a highly sensitive biosensor for rapid COVID-19 detection which was produced by coating anti-spike protein antibodies onto graphene sheets [411]. Moreover, the use of field-effect transistors based on the semiconducting transition metal dichalcogenide WSe_2 was reported by Fathi-Hafshejani *et al*. as a promising biosensor for the detection of SARS-CoV-2 *in vitro*. This sensor was developed by functionalising the WSe_2 monolayers with a monoclonal antibody against the SARS-CoV-2 spike protein [412]. Consequently, the use of GO and DNA functionalised UCNPs can lead to an alternative or a complementary alternative solution for detecting and continuous monitoring COVID-19 (see **Section 7.5.2**).

The working mechanism of the biosensor is demonstrated in **Figure 7.1**. When a two-dimensional material (MoS_2, WS_2, GO) is present, the single-stranded DNA coated UCNPs adsorb onto the surface of the material resulting in the quenching of the UCNPs' fluorescence. In the presence of a complementary DNA or RNA target, the hybridised double-stranded coated UCNPs do not adsorb to the surface of the two-dimensional materials, hence their fluorescence is retained. When a non-complementary sequence is present, the single-stranded DNA coated UCNPs adsorb onto the surface of the two-dimensional material and the fluorescence of the UCNPs is quenched as no fluorescent signal is detected. This demonstrates the target specificity of the sensor.

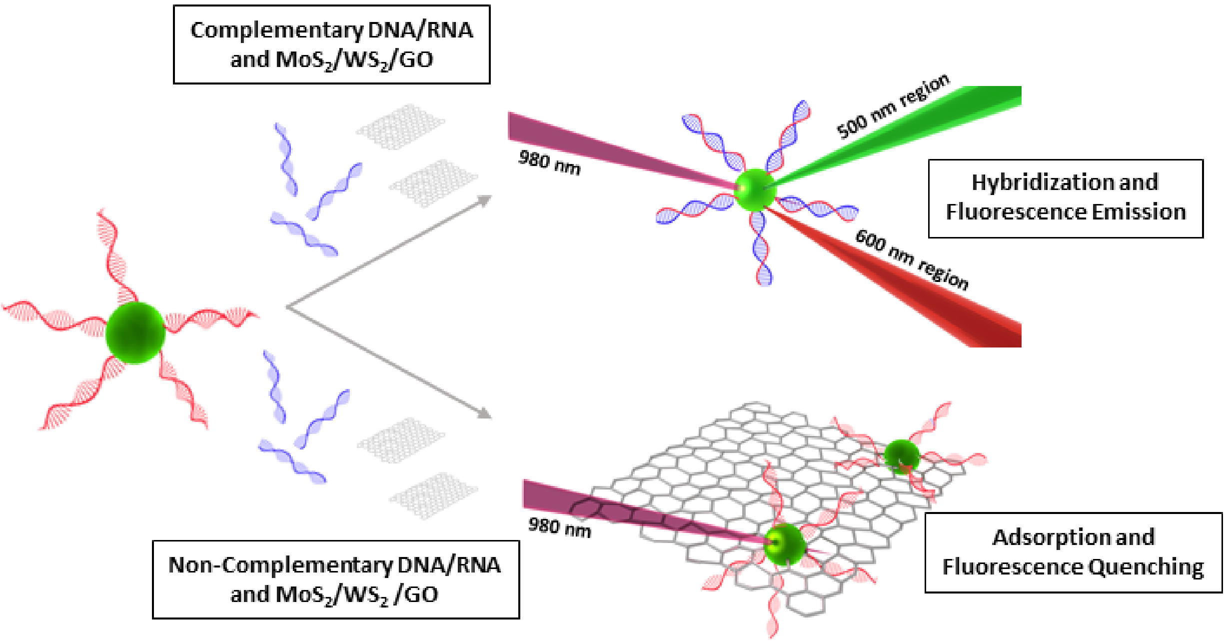

Figure 7.1 Schematic illustration presenting the working principle of the sensor. When a complementary DNA or RNA target is absent, two-dimensional material quenches the UCNP emitted fluorescence. In the presence of the complementary DNA or RNA target, the double-stranded DNA coated UCNPs do not adsorb to the surface of the two-dimensional materials and therefore their fluorescence is retained.

7.2 Ligand Exchange on Core-Shell Upconversion Nanoparticles

Hexagonal phase core-shell UCNPs were synthesised to investigate the interactions between single-stranded DNA coated UCNPs and two-dimensional materials. A ligand exchange procedure was followed for the removal of the attached capping molecules on the nanoparticles' surface with another set of ligands that have a higher affinity for the UCNPs' surface. The oleic acid ligands were replaced by PAA to enable nanoparticle solubility in water. The introduction of the functional group of -COOH facilitated further functionalisation of the UCNPs with amino-modified oligonucleotide sequences [156, 362]. The ligand exchange is a one-step method to bring the UCNPs into the water for further modification by EDC/sulfo-NHS coupling with amine-modified oligonucleotide sequences. FT-IR spectroscopy was used to verify the ligand exchange. FT-IR spectroscopic measurements of oleate-capped core-shell UCNPs and PAA coated core-shell UCNPs are presented in **Figure 7.2**. All the characteristic peaks of core-shell UCNPs were identified in the FT-IR spectrum. The C-H stretching vibration bands of unsaturated -CH_3 and -CH_2- were located at 2927 and 2852 cm^{-1}, respectively, and the asymmetric and symmetric COO- stretching appeared at 1549 and 1432 cm^{-1} of oleic acid molecules [224]. According to the spectrum of PAA coated UCNPs, the presence of PAA on the surface of the UCNPs was confirmed by the appearance of a strong peak at 1700 cm^{-}

^{1} which could be attributed to the C=O stretching mode of protonated carboxylate groups (-COOH) in PAA [413]. The two peaks at 1130 and 1250 cm^{-1} corresponded to C-O stretching bands while the absorption peak of asymmetric stretching vibration of methylene (-CH$_2$-) was at 2921 cm^{-1} [414].

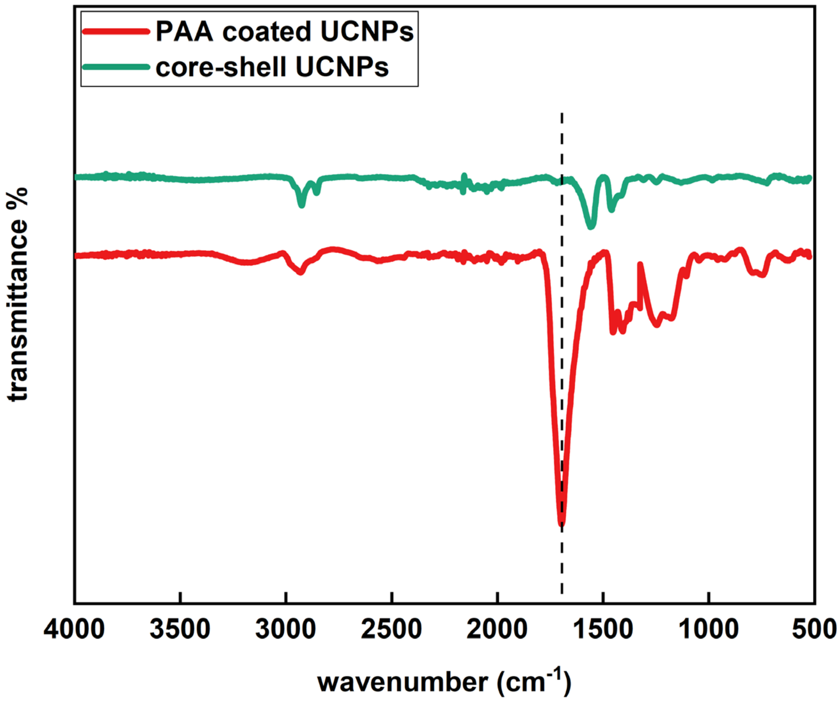

Figure 7.2 FT-IR spectra of oleate-capped core-shell UCNPs (green line) and PAA coated core-shell UCNPs (red line). The strong -COOH peak at 1700 cm^{-1} verifies the presence of PAA molecules. The above spectra are offset in the y axis for better visualisation.

7.3 Surface Modification of Upconversion Nanoparticles with Synthetic Oligonucleotides

7.3.1 Synthesis and characterisation of single-stranded DNA/PAA coated core-shell upconversion nanoparticles

Following the successful carboxylation of the UCNPs' surface, an EDC/sulfo-NHS reaction was followed to attach the amino-modified single-stranded DNA. This coupling was realised by following a previously established protocol [362] and the experimental details are described in **Section 3.2.9**. The first step of this process included the incubation of the UCNPs with EDC and sulfo-NHS to allow the formation of the reactive intermediate for 1 h. Then, an amino-modified polyT sequence (see **Table 3.1** for oligonucleotide sequence) was added to the solution and left overnight. Purification by centrifugation was followed to remove the unbound excess of DNA. The successful coupling was firstly confirmed by zeta potential measurements. Upon attachment of the polyT sequences to the UCNPs' surface, the zeta potential showed a decrease in the net charge in comparison with the value for the PAA coated UCNPs. This shift indicated the binding of the highly negative oligonucleotides to the surface of the nanoparticles (**Figure 7.3**). FT-IR spectroscopic analysis was also used to characterise the DNA coupling where the characteristic peak of the carboxyl group of the PAA (1700 cm^{-1}) disappeared after the EDC/sulfo-NHS reaction (**Figure 7.4**). The appearance of the peaks at 1560 cm^{-1} and 1650 cm^{-1} was related to the C=O and the N-H bonds of the amide groups due to the conjugation of the amino-modified oligonucleotides *via* EDC coupling [156].

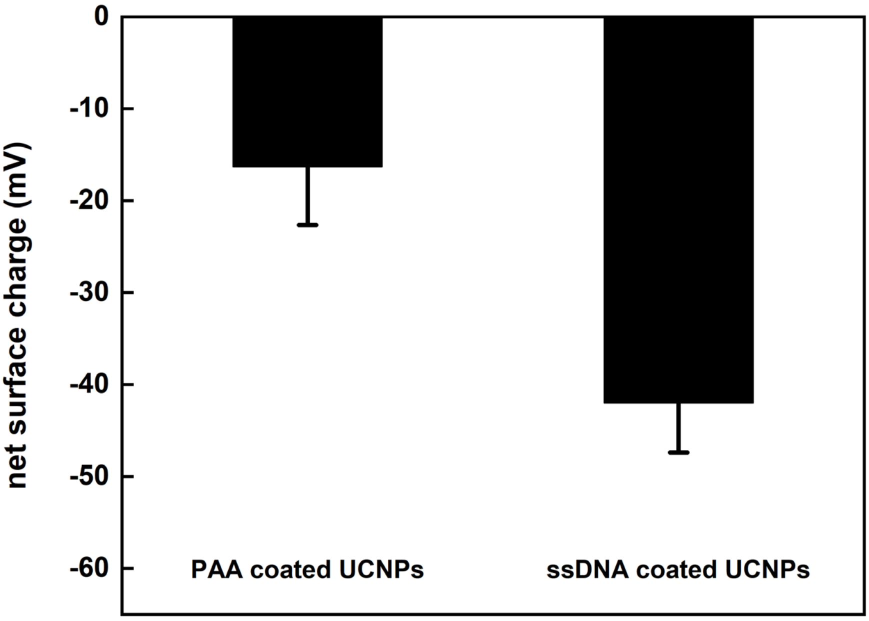

Figure 7.3 Zeta potential measurements of PAA coated core-shell UCNPs and single-stranded DNA/PAA coated core-shell UCNPs (0.5 mg/mL). The zeta potential for the single-stranded DNA/PAA coated core-shell UCNPs shows a decrease in the net charge in comparison with the value for the PAA coated core-shell UCNPs.

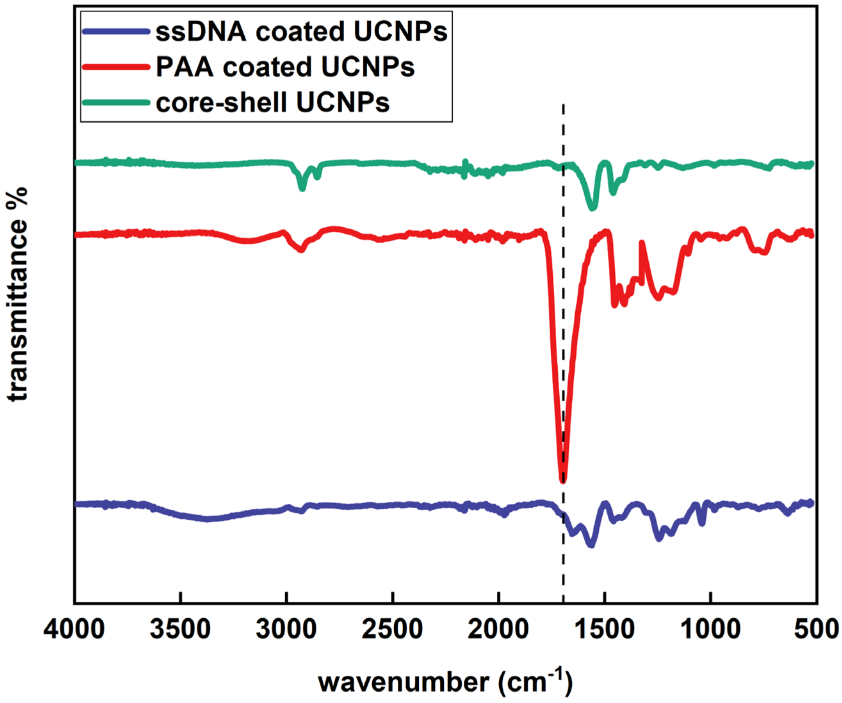

Figure 7.4 FT-IR spectra of oleate-capped core-shell UCNPs (green line), PAA coated core-shell UCNPs (red line) and single-stranded DNA coated core-shell UCNPs (blue line). The characteristic peak at 1700 cm^{-1} of the carboxyl group of the PAA disappeared after the EDC/sulfo-NHS reaction and the formation of 1560 cm^{-1} and 1650 cm^{-1} peaks confirm the successful DNA coupling. The above spectra are offset in the y axis for better visualisation.

7.3.2 Synthesis and characterisation of single-stranded DNA/PAA coated core-shell upconversion nanoparticles for SARS-CoV-2 oligonucleotide detection

An EDC/sulfo-NHS reaction was also followed to attach the amino-modified single-stranded SARS-CoV-2 DNA (see **Table 3.1** for oligonucleotide sequence) to the carboxylic group of the PAA ligands on the UCNPs surface after carboxylation (see **Section 3.2.9** for experimental details). PAA coated UCNPs were incubated with EDC and sulfo-NHS to allow the formation of the reactive intermediate for 1 h. Then, the amino-modified single-stranded SARS-CoV-2 DNA was added to the solution and left overnight. The solution was purified by centrifugation to remove the unbound excess of DNA. This amino-modified single-stranded DNA was chosen to be specific to the RNA-dependent RNA polymerase (RdRp) / Helicase (Hel) gene of SARS-CoV-2, a biomarker also used in RT-qPCR [415-417]. Zeta potential and FT-IR measurements were recorded to confirm the successful coupling. In **Figure 7.5** the zeta potential data demonstrate the decrease in the net charge for single-stranded

SARS-CoV-2 DNA coated UCNPs in comparison with the measurement for the PAA coated UCNPs. This shift was due to the binding of the highly negative oligonucleotides to the surface of the nanoparticles. In **Figure 7.6** the FT-IR data show the appearance of the characteristic peak (1700 cm^{-1}) of the carboxyl group for the PAA coated core-shell UCNPs which was not present after the EDC/sulfo-NHS reaction. The appearance of the peaks at 1560 cm^{-1} and 1650 cm^{-1} was related to the C=O and the N-H bonds of the amide groups due to the conjugation of the amino-modified SARS-CoV-2 oligonucleotides [156].

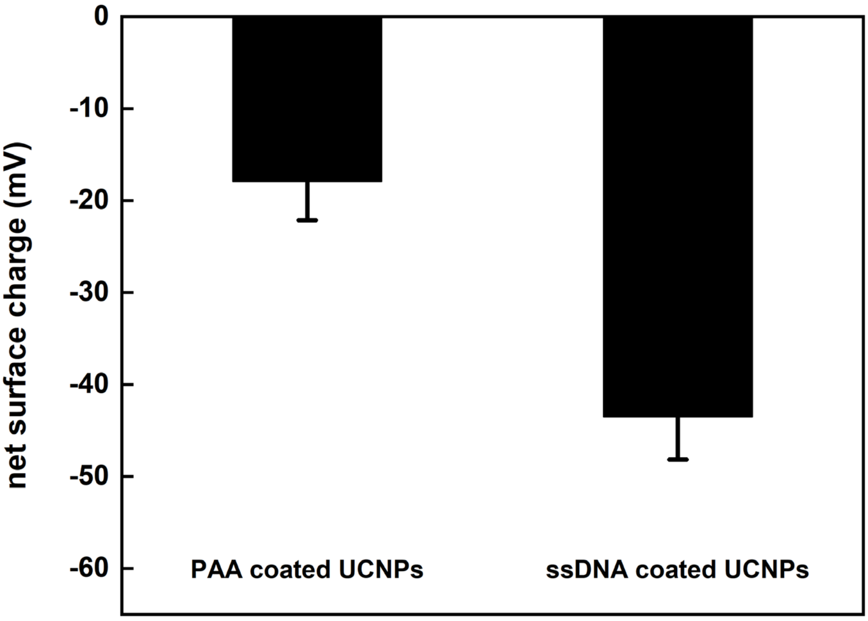

Figure 7.5 Zeta potential measurements of PAA coated core-shell UCNPs and single-stranded SARS-CoV-2 DNA/PAA coated core-shell UCNPs (0.5 mg/mL). The zeta potential for the single-stranded SARS-CoV-2 DNA/PAA coated core-shell UCNPs shows a decrease in the net charge in comparison with the value for the PAA coated core-shell UCNPs.

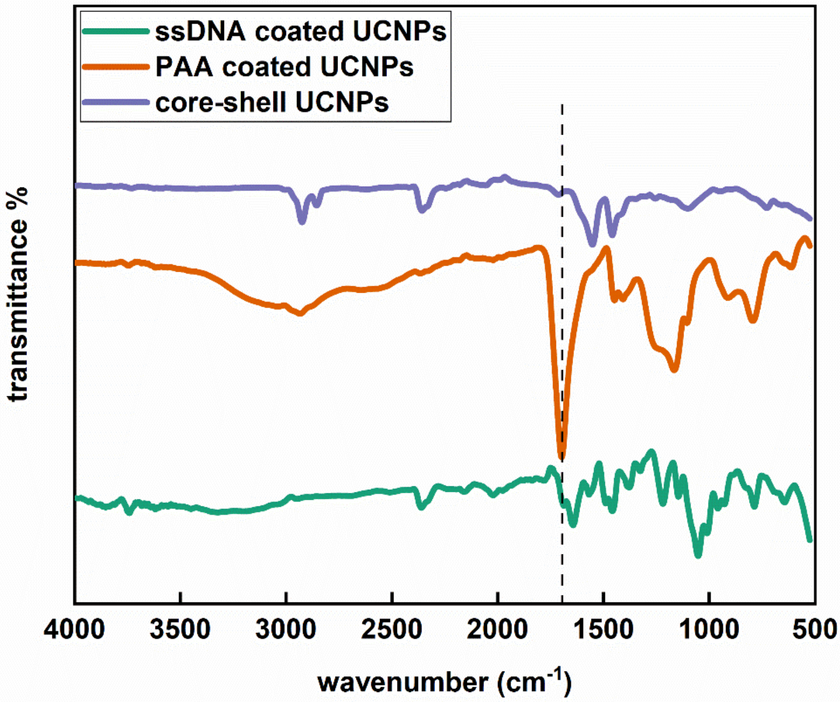

Figure 7.6 FT-IR spectra of oleate-capped core-shell UCNPs (purple line), PAA coated core-shell UCNPs (orange line) and single-stranded SARS-CoV-2 DNA/PAA coated core-shell UCNPs (green line). The conjugation of the amino-modified single-stranded SARS-CoV-2 oligonucleotides *via* EDC coupling is confirmed by the appearance of the peaks due to the creation of amide bonds at 1560 cm^{-1} and 1650 cm^{-1}. The above spectra are offset in the y axis for better visualisation.

7.4 Quenching of Upconversion Nanoparticles' Fluorescence by Two-Dimensional Materials

The successful synthesis and characterisation of single-stranded DNA coated UCNPs were followed by the incubation with the two-dimensional materials. To investigate the energy transfer between the UCNPs and two-dimensional materials, we fixed the concentration of single-stranded DNA coated UCNPs (0.5 mg/mL) and varied the concentration of two-dimensional materials. In **Section 7.4.1**, it is demonstrated the detection of a polyA DNA target in PBS by exploiting the interactions occurring between single-stranded DNA coated UCNPs and MoS_2/WS_2 in solution. The absorption spectra of the two-dimensional materials, MoS_2 and WS_2, are presented in **Figure 7.7 (A)** and **(B)** which correspond well with the typical spectra in the literature [418-420]. The next detection system is based on the detection of SARS-CoV-2 DNA and RNA targets in sterile DNase/RNase free Milli-Q water by investigating the interactions occurring between single-stranded DNA coated

UCNPs and GO (see **Section 7.4.2**). Coronaviruses are a family of single-stranded RNA viruses that express and replicate their genomic RNA to produce full-length copies that are incorporated into newly produced viral particles [421]. The detection of SARS-CoV-2 RNA targets was chosen as a sequence that is closest to the actual virus form while the detection of SARS-CoV-2 DNA targets was chosen as a more stable system. The absorption spectrum of GO is presented in **Figure 7.7 (C)** which is in agreement with the typical spectrum in the literature [361, 422].

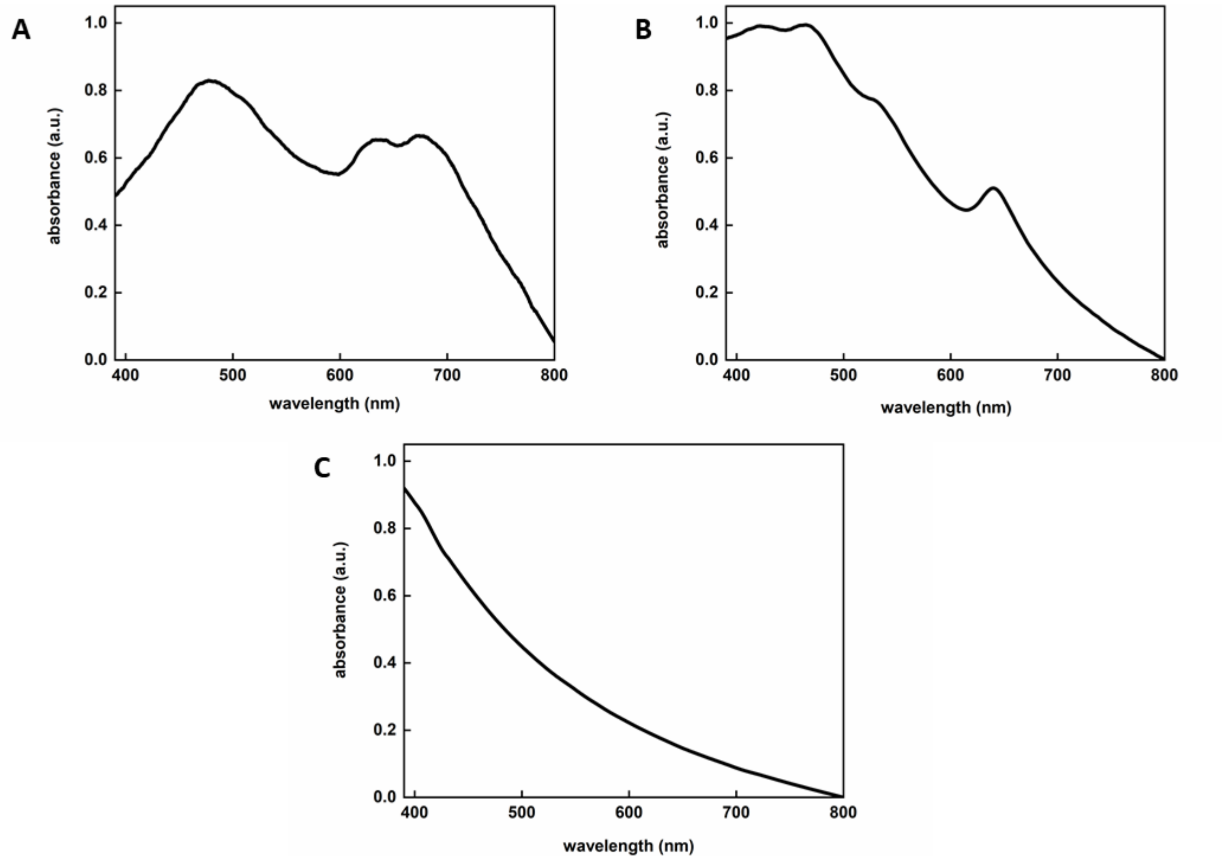

Figure 7.7 Normalised UV-Vis spectra of (**A**) MoS_2, (**B**) WS_2 and (**C**) GO dispersed in PBS (0.5 mg/mL). MoS_2 is dark green whereas WS_2 appears brown and GO is black when dispersed in PBS.

7.4.1 Quenching of upconversion nanoparticles' fluorescence by MoS_2 and WS_2

The recorded fluorescence spectra of single-stranded DNA coated UCNPs (0.5 mg/mL) in the presence of various concentrations of MoS_2 and WS_2 are presented in **Figure 7.8**. A steady decrease in the fluorescence intensity of the UCNPs was observed upon increasing the concentration of two-dimensional materials, whilst maintaining the same concentration of single-stranded DNA coated UCNPs (0.5 mg/mL). This is a strong indication that the interactions between the two-dimensional materials and single-stranded DNA coated UCNPs were within the distance required for a nonradiative energy transfer (see **Section 7.1**), which resulted in fluorescence quenching [423].

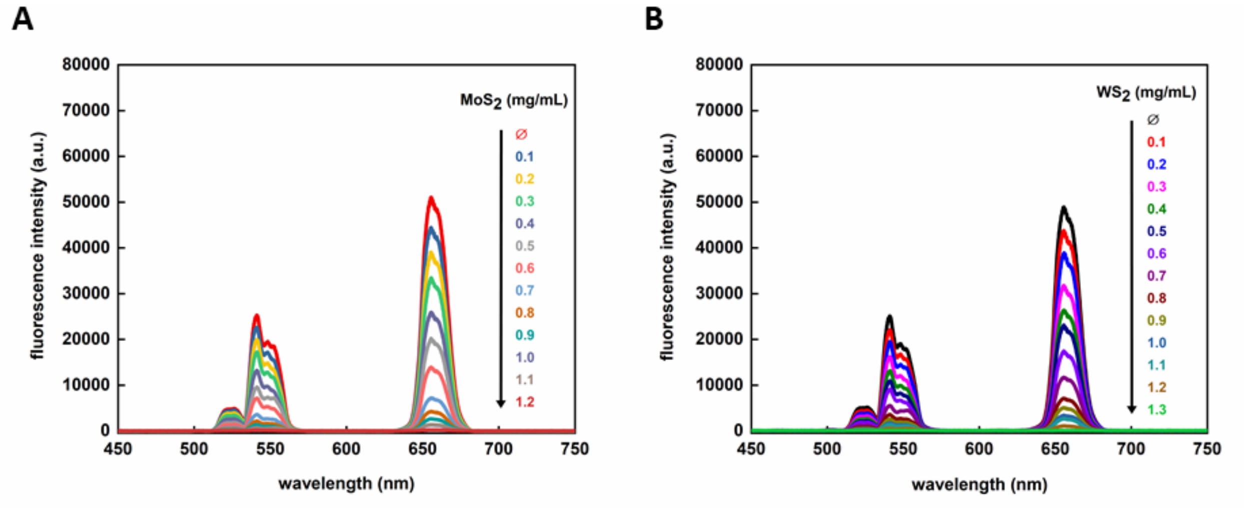

Figure 7.8 Representative fluorescence emission spectra from single-stranded DNA coated UCNPs (0.5 mg/mL) in the presence of increasing concentrations of (**A**) MoS_2 or (**B**) WS_2. As the concentration of two-dimensional materials was increasing, there was a decrease in the fluorescence intensity of the single-stranded DNA coated UCNPs.

The intensity at lambda max for each UCNP emission peak observed in the fluorescence spectra was correlated with the quenching ability of MoS_2 and WS_2 in order to further explore the nature of the interactions occurring between the single-stranded DNA coated UCNPs and the two-dimensional dichalcogenides. **Figure 7.9** shows the analysis of fluorescence quenching of single-stranded DNA coated UCNPs at wavelengths of 540 and 655 nm as a function of MoS_2 and WS_2 concentration. Upon the addition of 1.2 mg/mL of MoS_2 or 1.3 mg/mL of WS_2, a quenching ability of more than 99% was observed. This degree of quenching correlates well with the quenching effect previously reported for GO against the UCNPs' emitted fluorescence as a result of the FRET process occurring between the donor (UCNPs) and the acceptor (two-dimensional material). The UCNPs fluorescence quenching followed the same trend as previously observed, which indicated that this quenching was due to a FRET process [361, 401].

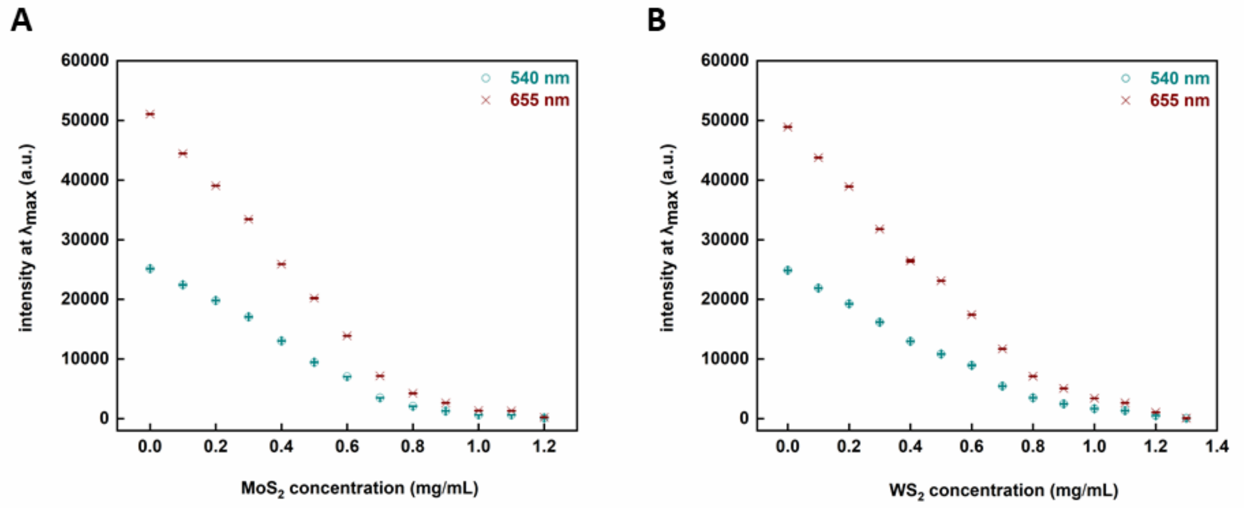

Figure 7.9 Correlated fluorescence emission spectra from single-stranded DNA coated UCNPs (0.5 mg/mL) showing the decreasing fluorescence emission of the λ_{max} of the two typical UCNPs peaks (655 nm, red points; 540 nm, cyan points) in the presence of an increasing concentration of (**A**) MoS_2 or (**B**) WS_2 as indicated in the graph.

7.4.2 Quenching of upconversion nanoparticles' fluorescence by graphene oxide

The strong dependence on the GO concentration of the quenching efficiency is presented in **Figure 7.10 (A)**. Upon increasing concentrations of GO, whilst maintaining the same concentration of single-stranded DNA coated UCNPs (0.5 mg/mL), a steady decrease in the fluorescence intensity of the UCNPs was recorded. This is again a strong indication that energy is transferred from the excited state of the donor to the ground state of the acceptor in a nonradiative way (see **Section 7.1**). This fluorescence quenching process occurs when the distance between the UCNP and the GO is below 10 nm [423, 424].

In order to further investigate the nature of the interactions occurring between the single-stranded DNA coated UCNPs and GO, the intensity at lambda max for each UCNP emission peak observed in the fluorescence spectra was correlated with the quenching ability of GO. **Figure 7.10 (B)** presents the analysis of fluorescence quenching of single-stranded DNA coated UCNPs at wavelengths of 540 and 655 nm as a function of GO concentration. A quenching ability of more than 98% was observed upon the addition of 0.6 mg/mL of GO, which was in good agreement with the quenching effect of previous studies [361, 401].

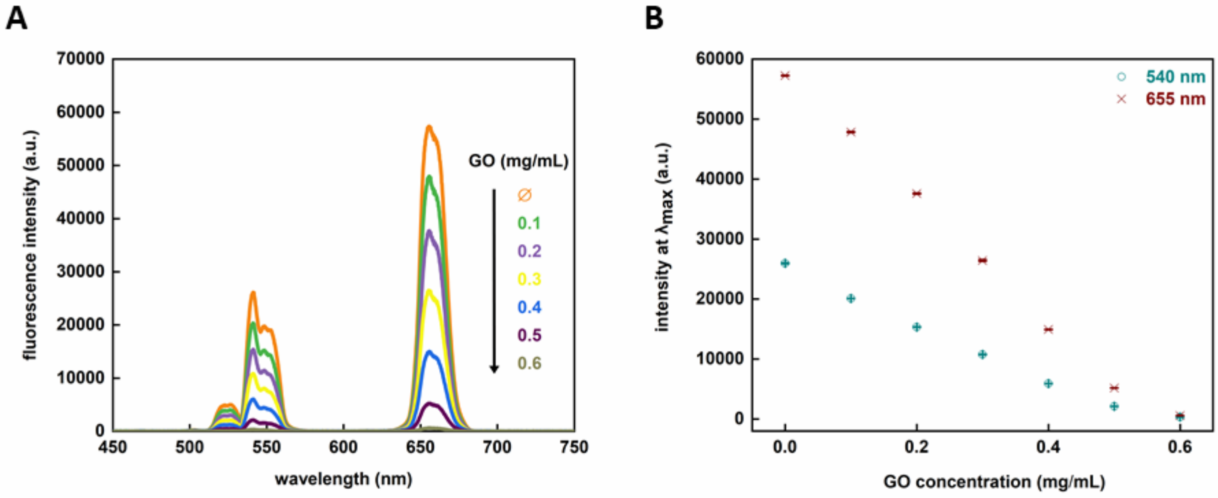

Figure 7.10 (**A**) Representative fluorescence emission spectrum from single-stranded DNA coated UCNPs (0.5 mg/mL) in the presence of increasing concentrations of GO and (**B**) the correlated fluorescence emission spectrum from single-stranded DNA coated UCNPs (0.5 mg/mL) showing the decreasing fluorescence emission of the λ_{max} of the two

typical UCNPs peaks (655 nm, red points; 540 nm, cyan points) in the presence of an increasing concentration of GO.

7.5 Oligonucleotide Target Detection

To fully investigate the ability of single-stranded DNA coated UCNPs to induce interaction with the chosen two-dimensional materials, MoS_2, WS_2 or GO were incubated at concentrations previously determined to induce the most effective quenching with functionalised UCNPs.

7.5.1 Targeted oligonucleotide detection using DNA coated upconversion nanoparticles

The distinct fluorescence emission of UCNPs was significantly quenched when coated with a monolayer of single-stranded DNA indicating that the main driving forces relied on van der Waals interactions between the single-stranded DNA and the two-dimensional surface as shown in **Figure 7.9** [401, 423]. Single-stranded DNA coated UCNPs were hybridized to their complementary sequences (see **Table 3.1** for oligonucleotide sequences) and then MoS_2 or WS_2 were added to further investigate the presence of such interactions. **Figure 7.11** presents the results obtained after hybridisation with an increasing concentration of complementary DNA target for 30 min. A decrease in the quenching efficiency of MoS_2 (**Figure 7.11 (A)**) and WS_2 (**Figure 7.11 (B)**) over both characteristic peaks was observed when the concentration of the target was increased from 5 fM to 50 nM. This happened due to the conformational change taking place upon DNA duplex formation, which prevented adsorption of the double-stranded DNA coated UCNPs onto the MoS_2 or WS_2 surface thus retaining their fluorescence properties.

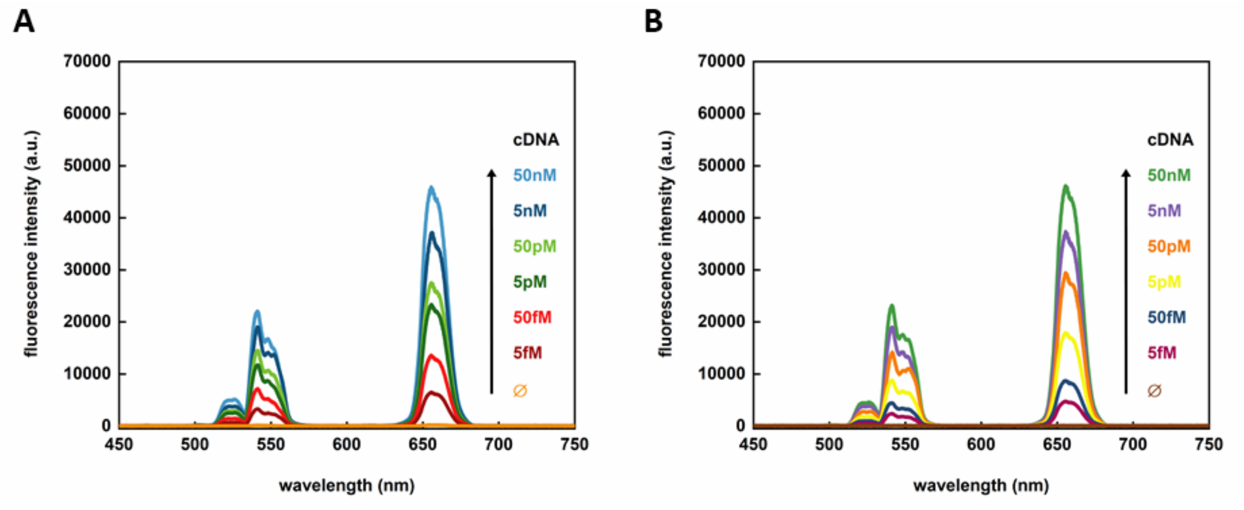

Figure 7.11 Representative fluorescence spectra of single-stranded DNA coated UNCPs (0.5 mg/mL) in the presence of increasing concentrations of complementary DNA targets for (**A**) MoS_2 and (**B**) WS_2.

The maximum intensity recorded for each peak at wavelengths of 540 and 655 nm was plotted against the target concentration as shown in **Figure 7.12**. By plotting a semi-log graph, a similar trend was observed for both MoS_2 (**Figure 7.12 (A)**) and WS_2 (**Figure 7.12 (B)**). Fluorescence recovery was less efficient for lower target concentrations due to the potential lower number of hybridisation events occurring. Consequently, the quenching by MoS_2 and WS_2 due to adsorption of single-stranded DNA coated UCNPs onto the surface was still observed at such complementary DNA concentrations demonstrating that fluorescence intensity is dependent on target detection.

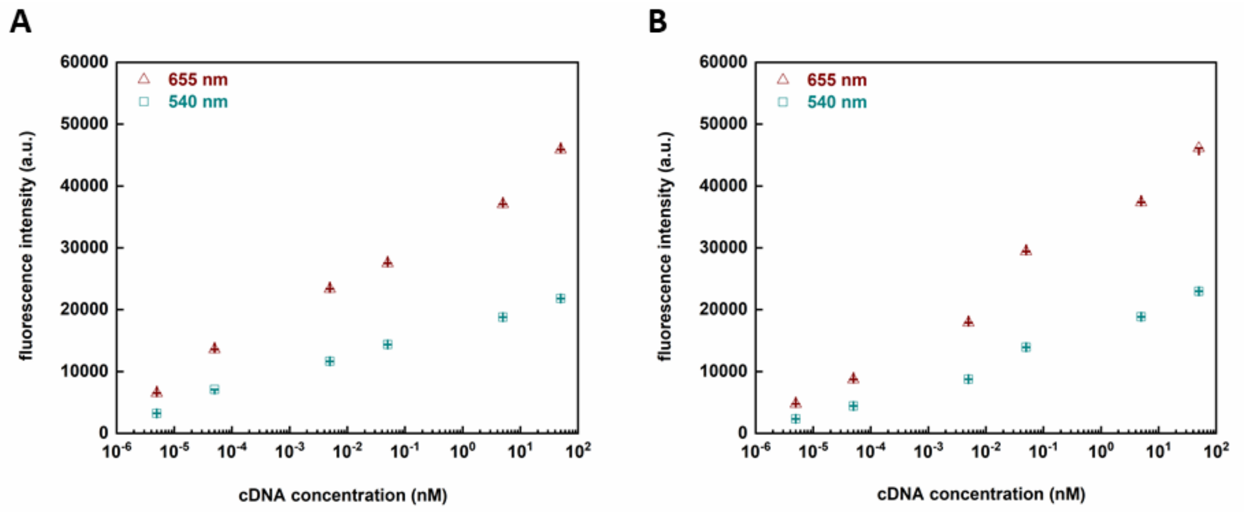

Figure 7.12 Graphs of the maximum nanoparticle fluorescence intensity bands measured at 540 (cyan points) and 655 nm (red points) for (**A**) MoS_2 and (**B**) WS_2 as a function of complementary DNA concentration. There was a decrease in the quenching efficiency of both MoS_2 and WS_2 when the concentration of the target was increased from 5 fM to 50 nM.

A control experiment was performed to further confirm the specificity of this system where single-stranded DNA coated UCNPs (0.5 mg/mL) were incubated with a non-complementary target sequence before the addition of MoS_2 and WS_2. **Figure 7.13** demonstrates the fluorescence emission spectra recorded following incubation with DNA concentrations ranging from 5 to 1000 nM. No fluorescence was observed (**Figure 7.13**) regardless of the concentration of the non-complementary DNA target initially added for both two-dimensional materials. This indicated that no DNA duplex formation took place and the UCNP surface remained single-stranded, which permitted adsorption onto the surface of MoS_2 and WS_2 respectively, thus rendering their fluorescence quenched.

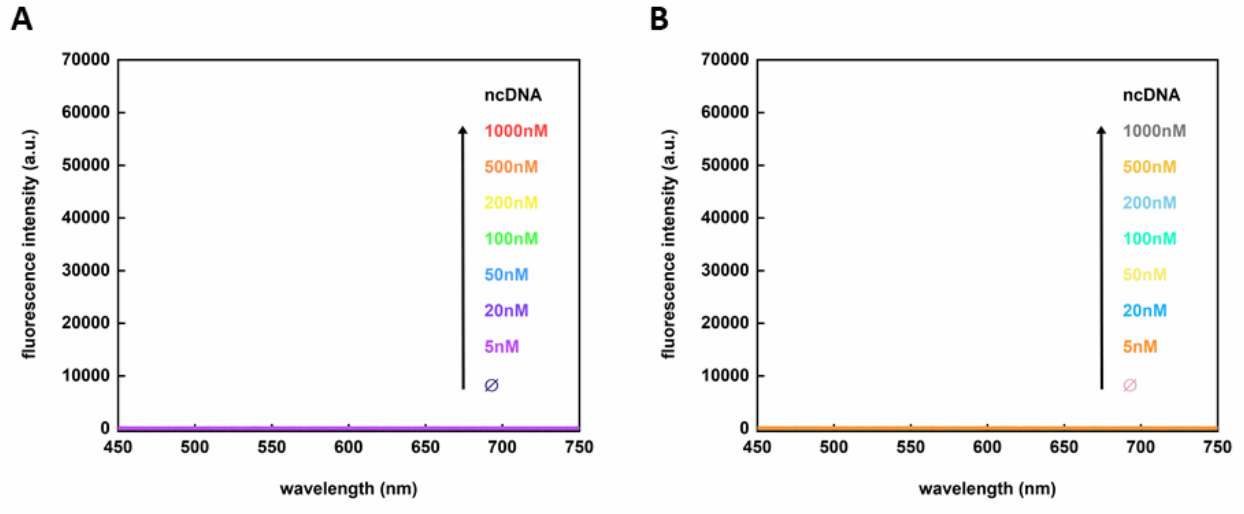

Figure 7.13 Fluorescence spectra of single-stranded DNA coated UCNPs (0.5 mg/mL) in the presence of various concentrations of the noncomplementary target for (**A**) 1.2 mg/mL MoS_2 and (**B**) 1.3 mg/mL WS_2.

To sum up, the development and use of an optical DNA sensor made from single-stranded DNA coated UCNPs and two-dimensional dichalcogenides (MoS_2 and WS_2) were demonstrated. The emissive properties of UCNPs and the quenching ability of GO have been further exploited by implementing alternative two-dimensional materials. The working principle of the sensor is based on the property of dichalcogenides to adsorb single-stranded DNA to their surface *via* van der Waals interactions. By using this sensor, the detection of target DNAs within a few minutes at the 5 fM range was possible. These results can pave the way toward the development of oligonucleotide sensors that involve other dichalcogenide materials such as TaS_2 and TiS_2, which have already been found to serve as suitable energy transfer acceptors upon their interaction with dye-modified oligonucleotides [425].

7.5.2 Targeted SARS-CoV-2 oligonucleotide detection using DNA coated upconversion nanoparticles

The distinct fluorescence emission of UCNPs was significantly quenched when coated with a monolayer of single-stranded SARS-CoV-2 DNA indicating that the main driving mechanism relied on π-π stacking between DNA and GO surface as shown in **Figure 7.10 (B)**. Before testing the sensor for detecting actual SARS-CoV-2 viral targets, its ability was optimised by using a synthesised perfect target. Single-stranded DNA coated UCNPs were hybridized to their complementary sequences (see **Table 3.1** for oligonucleotide sequences) and then GO was added to further investigate the presence of such interactions. The results obtained after hybridisation with an increasing concentration of complementary DNA or RNA target for 30 min are presented in **Figure 7.14**. A decrease in the quenching efficiency of GO (**Figure 7.14**) over both characteristic peaks was observed when the concentration of the target was increased from 5 fM to 50 nM for both SARS-CoV-2 DNA and RNA. This was due to the conformational change taking place upon duplex formation, which prevented adsorption of the double-stranded DNA/RNA coated UCNPs onto the GO surface thus retaining their fluorescence properties.

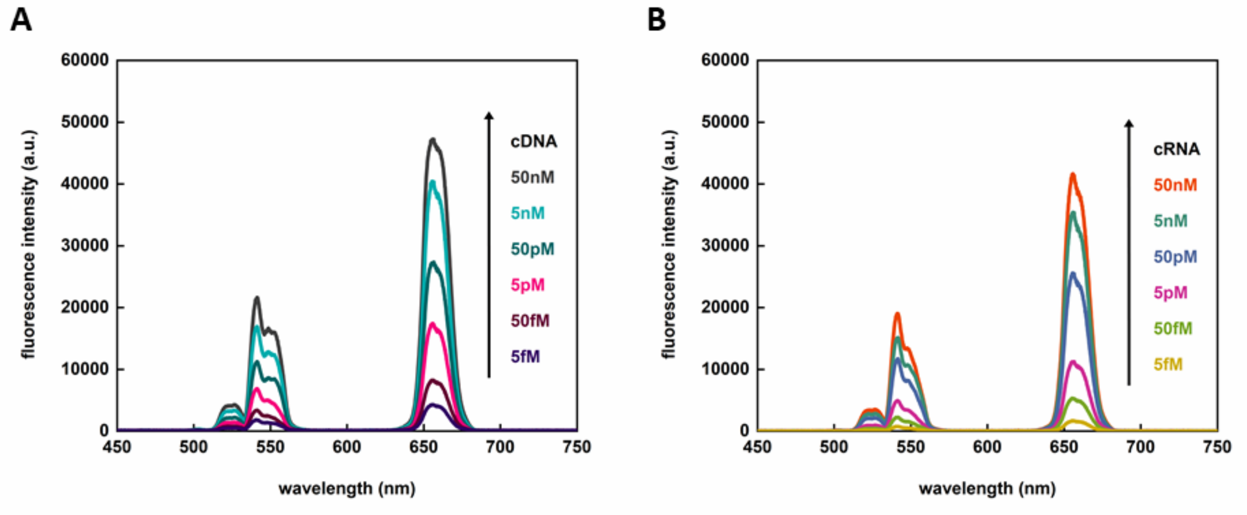

Figure 7.14 Representative fluorescence spectra of single-stranded DNA coated UNCPs (0.5 mg/mL) after incubation with increasing concentrations of SARS-CoV-2 complementary (**A**) DNA and (**B**) RNA targets in the presence of GO.

Figure 7.15 demonstrates the maximum intensity recorded for each peak at wavelengths of 540 and 655 nm as a function of the SARS-CoV-2 DNA or RNA target concentration. The fluorescence intensity of the single-stranded DNA coated UCNPs shows a gradual recovery with increasing concentrations of the complementary DNA (**Figure 7.15 (A)**) or RNA (**Figure 7.15 (B)**). For low target concentrations, fluorescence recovery was less efficient due to the potential lower number of hybridisation events occurring. Thus quenching by GO due to adsorption of single-stranded DNA coated UCNPs onto the surface was still observed at such complementary DNA concentrations demonstrating that fluorescence intensity is dependent on target detection.

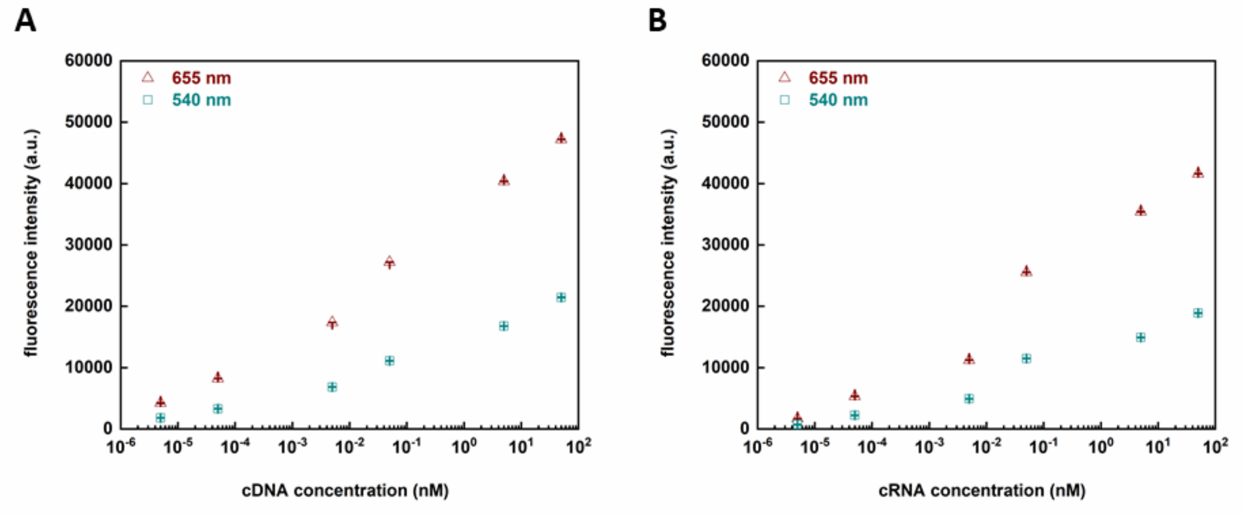

Figure 7.15 Graphs of the maximum nanoparticle fluorescence intensity bands measured at 540 (cyan points) and 655 nm (red points) after incubation with increasing concentrations of complementary SARS-CoV-2 (**A**) DNA and (**B**) RNA targets in the presence of GO. There was a decrease in the quenching efficiency of GO when the concentration of the target was increased from 5 fM to 50 nM for both SARS-CoV-2 DNA and RNA.

The specificity of this system was further confirmed by performing a control experiment where single-stranded DNA coated UCNPs (0.5 mg/mL) were incubated with a non-complementary target sequence prior to the addition of GO. The fluorescence emission spectra were recorded following incubation with DNA concentrations ranging from 5 to 1000 nM as presented in **Figure 7.16**. There was no significant fluorescence observed regardless of the concentration of the non-complementary DNA target initially added. This indicated the predominant existence of single-stranded DNA on the UCNP surface, which permitted their adsorption onto the surface of GO, thus rendering their fluorescence quenched. These observations demonstrate the high target selectivity of this biosensor platform for synthetic oligonucleotides for SARS-CoV-2.

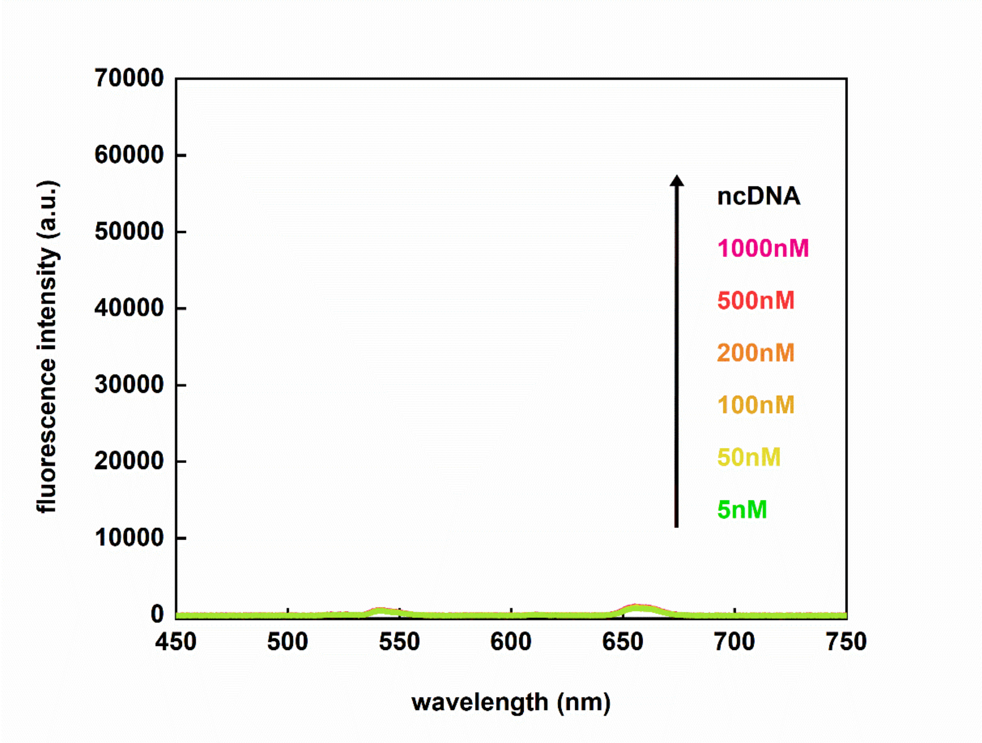

Figure 7.16 Fluorescence spectrum of single-stranded DNA coated UCNPs (0.5 mg/mL) in the presence of various concentrations of the noncomplementary DNA target for 0.6 mg/mL GO.

In conclusion, the development and use of an optical DNA sensor made from single-stranded DNA coated UCNPs and GO was presented for the targeted SARS-CoV-2 oligonucleotide detection. The working principle of the sensor is based on the property of GO to adsorb single-stranded DNA to its surface *via* π-π stacking and hydrogen bonding. In the absence of a target DNA or RNA, single-stranded DNA coated UCNPs were adsorbed onto the surface of GO and their fluorescence was quenched. In the presence of a complementary DNA or RNA target hybridized to the oligonucleotides on the surface of the UCNPs, the particles could no longer adsorb to the surface of GO and their fluorescence was retained. By using this sensor, the detection of DNA and RNA targets within a few minutes at the 5 fM range can facilitate the development of oligonucleotide sensors for other viruses.

Overall, a biomolecule detection sensor that combines the quenching capacity of two-dimensional materials with the emissive optical features of UCNPs is described in this chapter. Two different detection sensors were developed. In the first case, single-stranded DNA-coated UCNPs were adsorbed onto the surface of MoS_2 or WS_2 and their fluorescence was quenched. In the presence of the complementary polyA target hybridised to the oligonucleotides on the surface of the UCNPs, the particles could no longer adhere to the dichalcogenides' surface and their fluorescence was detected. In the second case, a sensor able to detect a segment of the SARS-CoV-2 virus genome coding for RdRp was developed. Single-stranded DNA-coated UCNPs were adsorbed onto the surface of GO and their fluorescence was quenched. The particles could no longer adhere to the surface of the GO in the presence of the complementary target hybridised to the oligonucleotides on the surface of the UCNPs. Both sensors were able to detect a target concentration as low as 5 fM within a few minutes, proving their sensitivity and efficiency. Finally, the inherent specificity of the sensors' DNA was confirmed since fluorescence quenching was maintained after UCNPs were incubated with a non-complementary target in the presence of two-dimensional materials.

Chapter 8 Summary and Outlook

Significant development has been achieved in the field of nanoscience over the last decades, resulting in the availability of a wide range of inorganic particles in terms of morphology and chemical composition, and hence properties. Furthermore, a better knowledge of nanoparticle surface chemistry has enabled the development of functional systems that have been effectively used in a variety of biomedical applications ranging from sensing to gene regulation to drug delivery. In this thesis, research has focused on the synthesis and functionalisation of AuNPs and UCNPs with oligonucleotides for the detection of biomolecules. A summary of produced results and an outlook for future work are presented below.

8.1 Summary of Results

The synthesis and characterisation of different types of colloidal nanoparticles such as spherical AuNPs, AuNRs and branched AuNPs as well as core and core-shell UCNPs, are demonstrated in **Chapter 4**. The synthesis of these biocompatible nanoparticles was carried out using modified synthetic techniques. The development of functional nanomaterials requires the fabrication of highly monodisperse nanoparticles with exact control over size, shape, and surface chemistry.

In **Chapter 5**, the surface functionalisation of AuNPs with a dense shell of oligonucleotides was achieved resulting in the development of SNAs for the detection of specific mRNA targets, runx2 and hspa8, in human BM stromal populations. This specific mRNA detection enabled the isolation and enrichment of human SSCs. By using FACS separation, fluorescent cells (Cy5 positive) were isolated after a short incubation period with runx2 and hspa8 SNAs with human BMSCs. The CFU-F formation was significantly enriched after plating the isolated mRNA target positive cells. Despite the limited number of SSCs in human BM, we showed by using this method that up to 1 in 200 of the Cy5 positive cells identified by FACS formed colonies with significant CFU-F levels on culture. As a result, the ability of SNAs to isolate and enrich skeletal stem cell populations enables their use in clinical applications.

The surface functionalisation of AuNPs with a cell-penetrating peptide is presented in **Chapter 6**. The need for a novel design approach for improving the endosomal escape of DNA functionalised AuNPs resulted in the incorporation of a cell-penetrating peptide, Aurein 1.2, that facilitates effective escape within cells. This chapter discusses two different methods of surface functionalisation with peptides. In the first case, AuNPs were firstly modified with thiol terminated DNA strands and then with cysteine terminated cell-penetrating peptides. These DNA-peptide-coated SNAs could detect mRNA in cells. However, the intensity of the detection signal of DNA-peptide-coated SNAs when incubated with cells showed no significant difference compared to SNAs without peptides. This suggested that the peptides on the surface of the AuNPs were not able to increase the number of nanoparticles escaping the endosomes, which may be related to the steric hindrance of the short peptide by the longer DNA strand while they were attached to the AuNP surface. In the second case, the peptide sequence was conjugated on the 5′ end of the DNA strand and then AuNPs were functionalised with these peptide oligonucleotide conjugates and DNA strands in different mixing ratios. The three different mixing ratios of DNA and peptide-DNA conjugate strands used in this study were 1% peptide-DNA conjugate & 99% vimentin DNA coated AuNPs, 5% peptide-DNA conjugate & 95% vimentin DNA coated AuNPs and 10% peptide-DNA conjugate & 90% vimentin DNA coated AuNP. This strategy focused on the improvement of the spatial position of the peptide. After incubation with cells, 10% peptide-DNA conjugate & 90% vimentin DNA coated AuNPs showed a lack of stability after 18 h post-incubation. The 5% peptide-DNA conjugate & 95% vimentin DNA coated AuNPs expressed a stronger signal compared to the 1% peptide-DNA conjugate & 99% vimentin DNA coated AuNPs after 18 h post-incubation. The ultra-thin sectioning of cells for TEM analysis was employed to ensure the difference in fluorescence intensity between the DNA-coated AuNPs and the peptide-DNA conjugate coated AuNPs after 18 hours of initial incubation was significant. After 18 h incubation of vimentin DNA-coated AuNPs, 1% peptide-DNA conjugate & 99% vimentin DNA coated AuNPs and 5% peptide-DNA conjugate & 95% vimentin DNA coated AuNPs with two different cell lines, it was observed that the majority of particles were located in vesicles with only a small percentage appearing to be in the cytosol. All of the above probes had similar stability towards degradation by endocellular enzymes and similar specificity towards the detection of specific mRNA targets.

Chapter 7 describes a biomolecule detection sensor that combines the emissive optical properties of UCNPs with the quenching ability of two-dimensional materials. Two different detection sensors were developed in this chapter. In the first case, the fabrication and use of a single-stranded DNA-coated UCNPs and two-dimensional dichalcogenides-based optical DNA sensor were presented. The sensor's working principle is based on dichalcogenides' ability (MoS_2 and WS_2) to adsorb single-stranded DNA to their surfaces *via* van der Waals interactions. In the absence of a target DNA, single-stranded DNA coated UCNPs were adsorbed onto the surface of MoS_2 or WS_2 and their fluorescence was quenched. The particles could no longer adsorb to the surface of the dichalcogenides in the presence of the complementary polyA target hybridised to the oligonucleotides on the surface of the UCNPs. As a result, the fluorescence of the UCNPs was detected. In the second case, a DNA sensor for the detection of an oligonucleotide target, a fingerprint of the SARS-CoV-2 virus was developed. The FRET donor was UCNPs, which were functionalised with oligonucleotides designed to detect a segment of the virus genome coding for RdRp, while GO was the acceptor. The working principle of the sensor is based on the property of single-stranded oligonucleotides to adsorb onto the GO surface *via* π-π stacking interactions. In both sensors, the detection of a target concentration as low as 5fM within a few minutes was achieved thus demonstrating its sensitivity and efficiency. Moreover, fluorescence quenching was retained after incubation of UCNPs with a non-complementary target in the presence of two-dimensional materials, confirming the sensors' DNA inherent specificity.

8.2 Outlook and Future Work

Taking into consideration the need for a new design approach for improving the endosomal escape of DNA functionalised AuNPs, further work will focus on the investigation of highly stable DNA-peptide-coated SNAs. The use of multiple mixing ratios of DNA and peptide strands as well as the position of peptide sequence will be explored.

Following the experiments from **Section 6.2.4,** there was a need to track the time point of the flare release after initial incubation with cells. Hence a fluorescent time-lapse study was realised. Live A 549 and SAOS-2 cells incubated with 1% peptide-DNA conjugate & 99% vimentin DNA coated AuNPs and 5% peptide-DNA conjugate & 95% vimentin DNA coated AuNPs were imaged over a period of 5 h after initial incubation. The flare release corresponding to mRNA detection was evaluated *via* confocal microscopy as presented in **Figure 8.1** for A 549 cells and **Figure 8.2** for SAOS-2 cells.

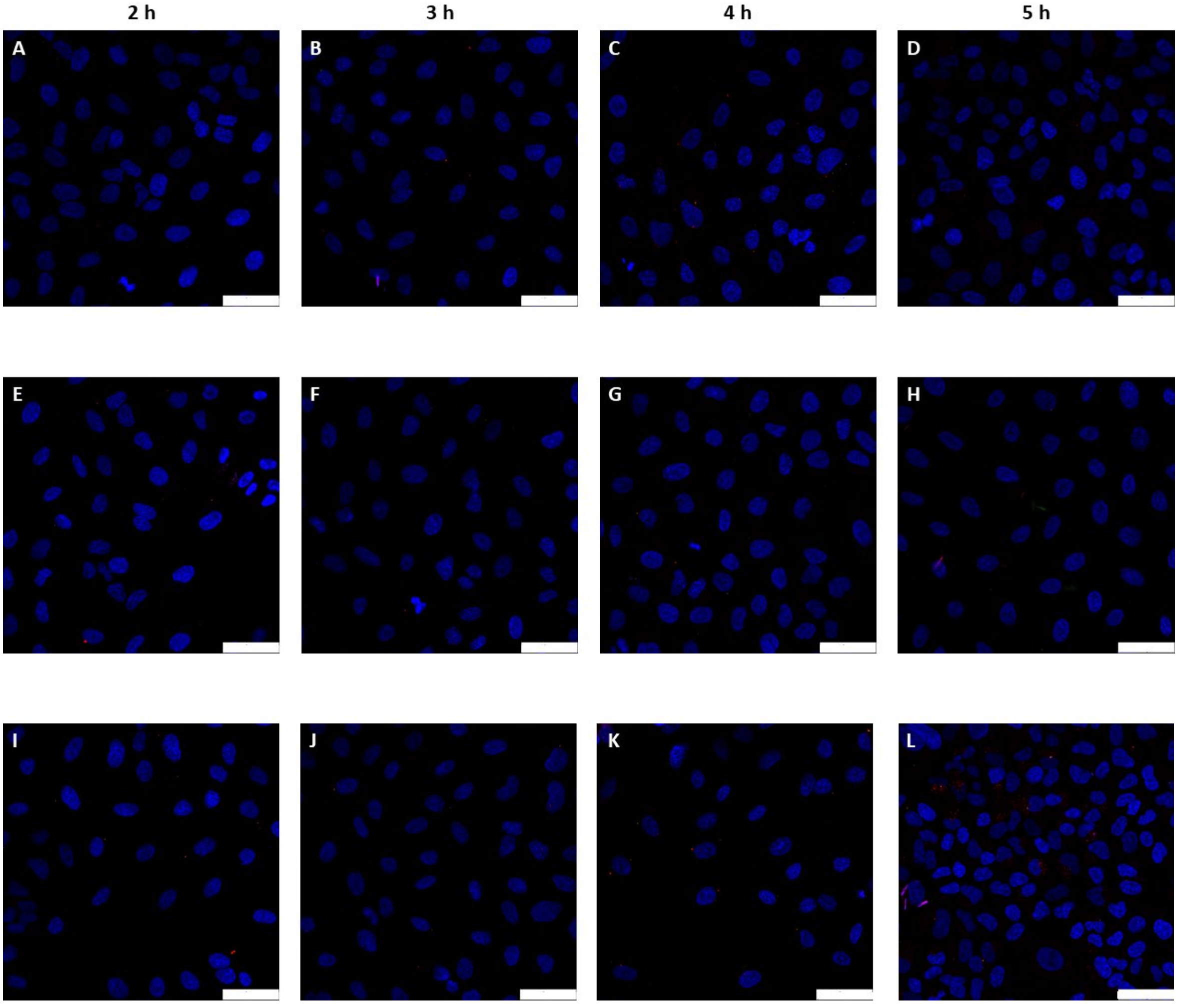

Figure 8.1 Fluorescent time-lapse study of live A 549 cells incubated with (**A**-**D**) vimentin DNA-coated AuNPs, (**E**-**H**) 1% peptide-DNA conjugate & 99% vimentin DNA coated AuNPs and (**I**-**L**) 5% peptide-DNA conjugate & 95% vimentin DNA coated AuNPs. Confocal microscopy images show flare release after 2 (**A**, **E**, **I**), 3 (**B**, **F**, **J**), 4 (**C**, **G**, **K**) and 5 h (**D**, **H**, **L**) post-incubation. Colour guide: Hoechst nuclear counterstain – blue, vimentin flare release – red. Scale bar is 49 µm.

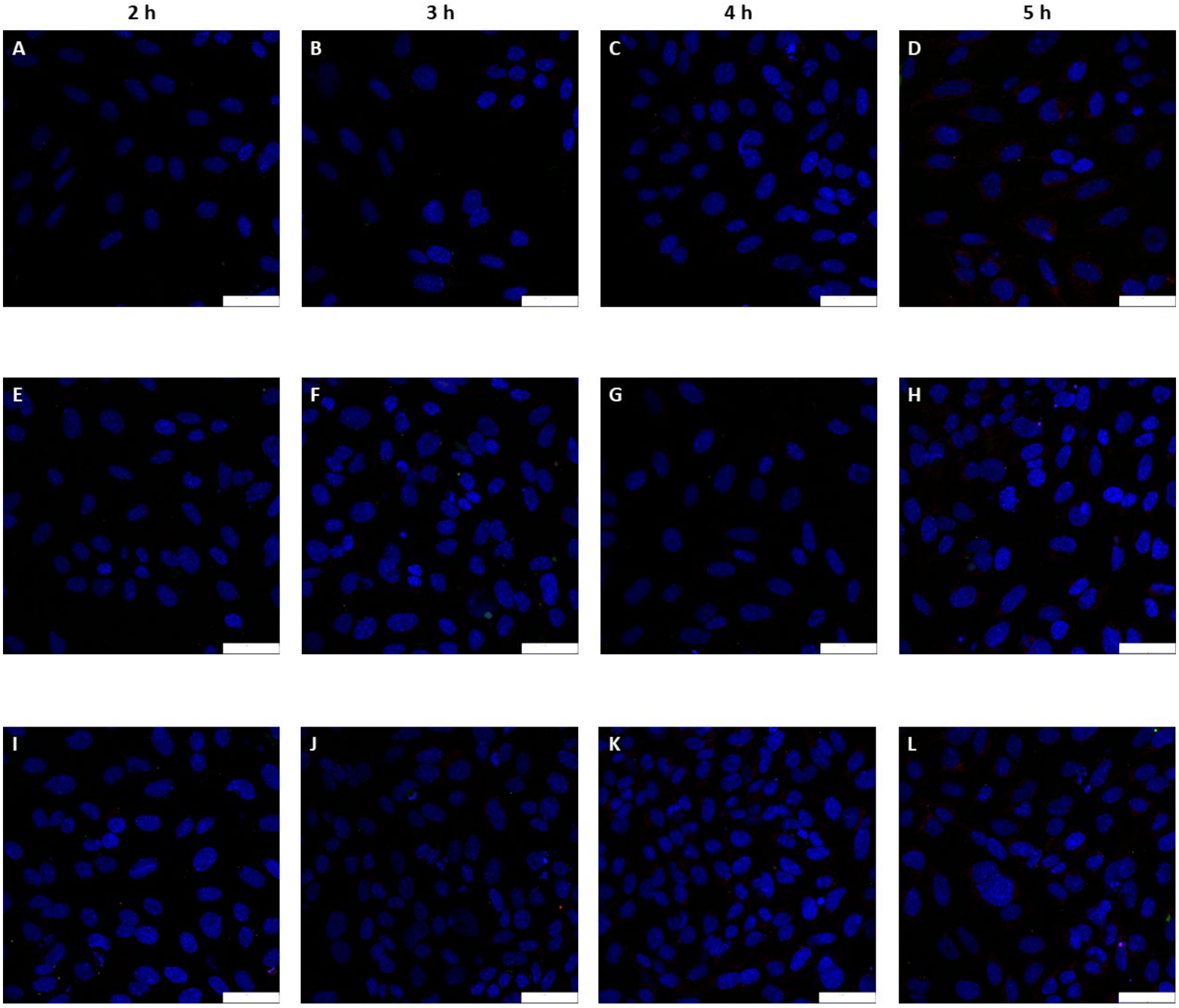

Figure 8.2 Fluorescent time-lapse study of live SAOS-2 cells incubated with (**A**-**D**) vimentin DNA-coated AuNPs, (**E**-**H**) 1% peptide-DNA conjugate & 99% vimentin DNA coated AuNPs and (**I**-**L**) 5% peptide-DNA conjugate & 95% vimentin DNA coated AuNPs. Confocal microscopy images show flare release after 2 (**A**, **E**, **I**), 3 (**B**, **F**, **J**), 4 (**C**, **G**, **K**) and 5 h (**D**, **H**, **L**) post-incubation. Colour guide: Hoechst nuclear counterstain – blue, vimentin flare release – red. Scale bar is 49 µm.

However, from the time-lapse images shown in **Figure 8.1** for A 549 cells and **Figure 8.2** for SAOS-2 cells, there was no fluorescence signal detectable after 5 h of initial incubation not even for the vimentin DNA-coated AuNPs. The lack of fluorescence signal for the vimentin DNA-coated AuNPs is contrary to the literature [313]. Hence further investigation of the gradual increase of the fluorescence intensity should be realised in order to obtain more information on the nanoparticles' location. Such an analysis can provide important information regarding the uptake pathway.

Another approach to increase the efficiency of the endosomal escape will be to increase the amount of peptide-DNA conjugate in the ratio of the probe. The synthesis of multiple probes with different mixing ratios of DNA and peptide-DNA conjugates can be developed for a live cell incubation. Given successful synthesis, their stability toward enzymatic degradation will be assessed *in vitro* and will be compared to DNA-coated AuNPs whilst cell viability assays will ensure the viability of cells.

Finally, the use of other cell-penetrating peptides already established in the literature for the development of DNA-peptide conjugate strands should be investigated. This work will therefore prove that new systems will be expandable to the detection of any mRNA sequence more efficiently.

After providing a good understanding of the design of these probes and a high level of expertise relating to nanoparticle surface chemistry and its manipulation, future research will provide some experimental recommendations for the increased efficiency of mRNA detection.

Appendix A List of Suppliers and Reagents

All chemical reagents were used as received without further purification and were obtained from commercial sources.

Agar Scientific: SPURR resin, osmium tetroxide, glutaraldehyde, formaldehyde, piperazine-N,N'-bis(2-ethanesulfonic acid) (PIPES buffer), uranyl acetate, 400 mesh copper/nickel grid

Alfa Aesar: yttrium(III) chloride hexahydrate (99.9%), ytterbium(III) chloride hexahydrate (99.9%), erbium(III) chloride hexahydrate (99.9%), thullium(III) chloride hexahydrate (99.9%), ammonium fluoride (98%), 1-octadecene (90%), oleic acid (90%), methanol (99%), chloroform (99.8%), n-hexane (95+%), tetrahydrofuran (THF, 99.8%), boric acid (99.99%), 1-(3-dimethylaminopropyl)-3-ethylcarbodiimide hydrochloride (EDC, 98+%), N-hydroxysulfosuccinimide sodium salt (sulfo-NHS, 97%)

Merck: sodium tetrachloroaurate (III) dihydrate (99%), bis(psulfonatophenyl) phenyl phosphine dihydrate dipotassium salt (BSPP), sodium citrate dihydrate (≥ 99%), sodium dodecyl sulphate (SDS), ficoll, 2-(N-Morpholino) ethanesulfonic acid, 4-Morpholineethanesulfonic acid (MES), sodium borate, sodium chloride, DNase I, tris base, (ethylenedinitrilo)tetraacetic acid (EDTA), magnesium chloride ($MgCl_2$), L-ascorbic acid (99%), agarose, silver nitrate (98%), ammonium persulfate (APS), N,N,N',N'-tetramethylethylenediamine (TEMED), sodium borohydride ($NaBH_4$, 99.99%), sodium hydroxide (97%), poly(acrylic acid) (PAA, MW ≈ 1.8 kDa), monobasic phosphate (99%), dibasic phosphate (99%)

Promega: 10bp DNA Step Ladder

Thermo Fisher Scientific: phosphate buffer saline (PBS) tablets, potassium iodide, acrylamide: bis-acrylamide 19:1 solution 40%, Thermo Scientific™ O'RangeRuler DNA Ladder, minimum essential medium (MEM), Pen/Strep, L glutamine, trypsin, nystatin, fetal bovine serum (FBS), Hank's Balanced Salt Solution (HBSS), Hoechst 33342, trypan blue, ethanol (≥ 99%)

ACS Material: MoS_2, WS_2 (black powders of monolayer sheets dispersed in PBS before use) – MoS_2 monolayers exhibit a diameter between 1 – 3 µm, with a thickness of ~1 nm and a monolayer ratio ≥ 90% while WS_2 monolayers exhibit a diameter between 0.1 – 4 µm, a thickness of ~1 nm and a monolayer ratio of ≥ 90%.

Graphene Supermarket: graphene oxide (GO, black powder of monolayer sheets dispersed in PBS before use) – GO monolayers exhibit a flake size between 0.2 – 2 µm with a monolayer ratio of at least 80%.

Oligonucleotides including their modifications were synthesised by Dr Afaf El-Sagheer at the University of Oxford.

A 549 cell line was provided by Dr Peter Lackie based at the Biomedical Imaging Unit, Southampton General Hospital. SAOS-2 cell line was provided by Prof. Richard Oreffo based at Cancer Research Building, Southampton General Hospital.

Schematic illustrations that are presented in this work were produced by Adobe Illustrator CS6.

Appendix B Error Analysis

As part of the data analysis, it's important to present the accuracy or proximity of the sample data to the whole population. The two terms of the standard deviation and the standard error of the mean are usually confused.

The standard deviation measures the dispersion (variability) of the data in relation to the mean. In simple terms, the closest to zero the standard deviation is the more close to the mean the values in the studied dataset are.

The formula to calculate the standard deviation (σ) is:

$$\sigma = \sqrt{\frac{\sum_{i=1}^{n}(x_i - \bar{x})^2}{n-1}}$$

where:

$$x_i = \text{each value}$$

$$\bar{x} = \text{the sample's mean}$$

$$n = \text{the sample size}$$

The standard error of the mean is a measure of the dispersion of sample means around the population mean. In other words, the standard error of the mean demonstrates how accurately your sample data represents the whole population.

The formula to calculate the standard error of the mean ($\sigma_{\bar{x}}$) is:

$$\sigma_{\bar{x}} = \frac{\sigma}{\sqrt{n}}$$

where:

$$\sigma = \text{the standard deviation}$$

$$n = \text{the sample size}$$

The standard error of the mean was used throughout the work presented in this thesis as we were interested in finding how precise the sample mean was. At greater length, standard deviation describes variability within a single sample, while standard error of the mean describes variability across multiple samples of a population [426].

Appendix C Laser Setup

Fluorescence spectra of UCNPs suspended in solution were acquired on a home-built setup presented in **Figure C.1.** The excitation source was a diode laser (Thorlabs) of continuous wave 980 nm (300 mW). The emission signal was monitored by a fibre-coupled grating SpectraSuite Spectrometer detector (USB4000, OceanOptics, USA) and was collected at an angle of 90° using a 35 mm focal length lens. The laser beam was guided through a short pass IR-blocking filter (Schott KG3) and a narrowband optical filter centred at 545 nm (Thorlabs) in order to suppress scattered excitation light and collect only the fluorescence emission. Prof. Otto Muskens built and aligned the aforementioned setup. All samples were measured with a quartz cuvette with a path length of 10 mm. Each measurement was performed with 1 second of integration time and 10 scans to average.

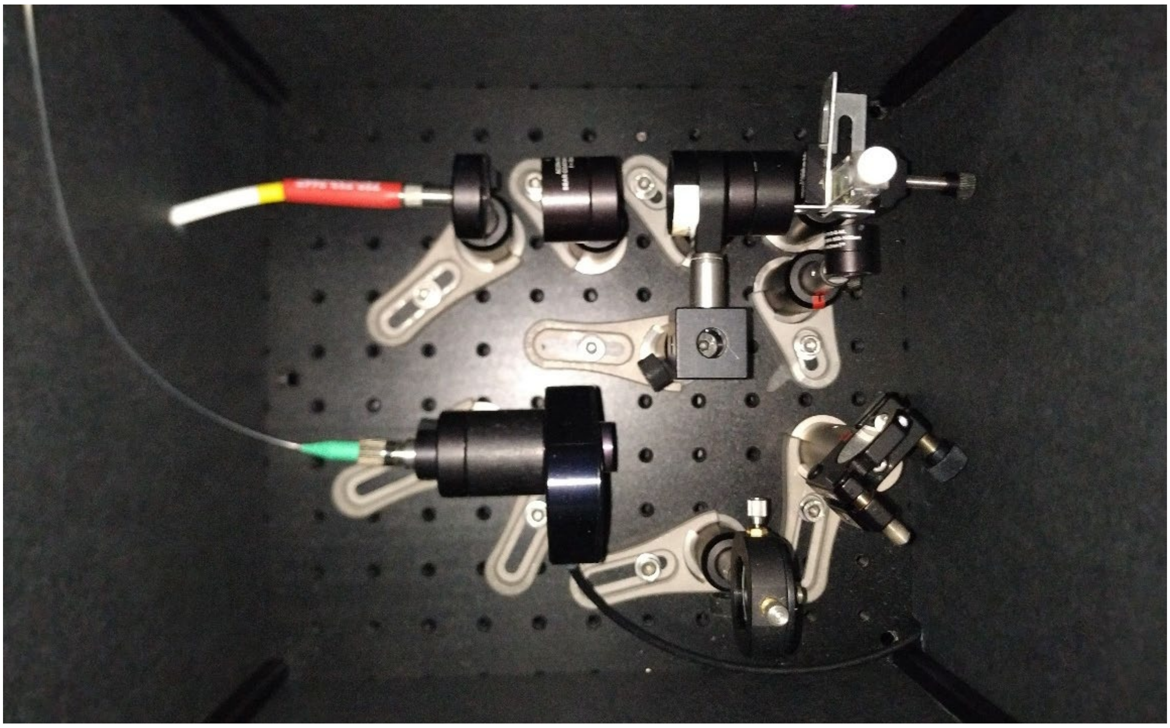

Figure C.1 Digital image of the home-built setup with a 980 nm laser used for fluorescence measurements of UCNPs in solution.

Appendix D Experimental Methods for Enrichment of Skeletal Stem Cells from Human Bone Marrow Using Spherical Nucleic Acids

These experimental methods were carried out by the collaborators in Prof. Richard Oreffo's lab based at Cancer Research Building, Southampton General Hospital.

D.1 Incubation of Spherical Nucleic Acids with Bone Marrow Stromal Cells in Suspension

The SNAs were added to the BMSC suspension (at 106 cells per mL) to the required final concentration of 0.2 nM and for the appropriate incubation time. Then, cells were washed in basal medium and re-suspended in FACS solution (0.5% BSA, 2 mM EDTA in 1 × PBS) before FACS analysis. A FACS Aria cytometer (Becton Dickinson, Wokingham, UK) was used to acquire 20,000 cells with data analyzed using the FlowJo software version 10.6.1. All washing stages were at 400g for 5 min.

D.2 Processing of Human Bone Marrow Samples

BM samples were obtained from hematologically healthy patients undergoing hip replacement surgery with local ethics committee approval (LREC194/99/1 and 18/NW/0231 and 210/01) and informed patient consent. In detail, BM was washed at least three times in 50 mL of α-MEM medium to remove fat and then passed through a 70 µm cell strainer. Marrow cells were re-suspended in 10 mL of α-MEM and subjected to density centrifugation using 20 mL of Lymphoprep (Lonza) at 800g for 20 min with no braking on the centrifuge. The buffy coat layer, containing BM mononuclear cells, was washed in 5 mL of basal medium (α-MEM containing 10% FBS, 100 U/mL penicillin and 100 µg/mL streptomycin; Lonza). All washing stages were at 400g for 5 min.

D.3 Colony Forming Units Fibroblast Assay

SNA positive and negative cells from human BM samples were collected by a FACS Aria cytometer. Cells were gated for monocytes, single cells and Cy5 fluorescence. Positive samples were deemed to be the top 15% of Cy5 fluorescent cells and negative samples were deemed to be the lower 15% of Cy5 fluorescent cells collected. Cy5 positive and negative cells were collected by FACS sorting. Each well of a 6-well tissue culture plate was seeded with 10,000 cells containing 2 mL of basal medium. Cells were grown for 14 days, with a medium change after 7 days. On day 14, all wells were washed with 3 mL of PBS and then fixed with 1 mL of 95% EtOH for 10 min. Next, 1 mL of 0.05% crystal violet solution was added to each well for 1 min after air-drying all the wells. Finally, the wells were washed again twice with 2 mL of distilled water and the number of visible colonies was determined by eye.

D.4 Osteogenic Differentiation Assay

Passage 1 cells were cultured at 37 °C in a 5% CO_2 atmosphere in a Sanyo CO_2 incubator until confluent. Then, cells were seeded at 10,000 cells per well on a 12-well plate followed by culture in basal medium for 24 h. Next, they were cultured in an osteoinductive medium (basal medium with 50 µM ascorbic acid 2-phosphate and 10 nM vitamin D_3) for 14 days at 37 °C in a 5% CO_2 atmosphere with a medium change every 3 - 4 days. Finally, cells were washed in PBS, fixed with 95% EtOH, and stained with alkaline phosphatase.

D.5 Adipogenic Differentiation Assay

Passage 1 cells were cultured at 37 °C in a 5% CO_2 atmosphere in a Sanyo CO_2 incubator until confluent. Then, cells were seeded at 10,000 cells per well on a 12-well plate followed by culture in a basal medium until 80% confluent, after approximately 3 - 5 days. Then, cells were cultured in an adipogenic medium (basal medium with 100 nM dexamethasone, 500 µM IBMX, 3 µg/mL ITS solution, and 1 µM rosiglitazone) for 14 days at 37 °C in a 5% CO_2 atmosphere with a medium change every 3 - 4 days. Following the washing of cells with PBS, they were fixed with 4% paraformaldehyde, washed again with PBS, and then stained with Oil Red O.

D.6 Chondrogenic Differentiation Assay

Passage 2 cells were cultured at 37 °C in a 5% CO_2 atmosphere in a Sanyo CO_2 incubator until confluent. Then, cells were diluted to 500,000 cells per mL in chondrogenic media (α-MEM containing 100 U/mL penicillin and 100 µg/mL streptomycin, 100 µM ascorbic acid 2-phosphate, 10 ng/mL TGF-B_3, 10 µg/mL ITS solution and 10 nM dexamethasone) in a universal container. Cells were centrifuged at 400g for 10 min to form a cell pellet and all but 1 mL of media was removed. In the next step, the cells were cultured with the tube cap loose for 14 days at 37 °C in a 5% CO_2 atmosphere with a media change every 2 days. Finally, cells were washed in PBS, fixed in 95% EtOH and stained with alcian blue and Sirius red.

D.7 Statistical Analysis

Wilcoxon-Mann-Whitney statistical analysis and ANOVA were performed where appropriate using the SPSS for Windows program version 23 (IBM Corp, Portsmouth, Hampshire, UK). All experiments and measurements were performed at least three times and the data were presented as mean value ± standard error of the mean (see **Appendix B**). Significance was determined with a *p*-level of 0.05 or lower.

Appendix E Theoretical Molecular Weight of Hexagonal $NaYF_4$:RE Upconversion Nanoparticles

UCNPs are used in biological imaging, sensing and therapeutic applications, however, their molecular weight has not been widely used. For the experiments in this thesis, the concentration of hexagonal $NaYF_4$:Yb^{3+} (20%), Er^{3+} (2%) UCNPs in solution is calculated by weighting an amount of UCNPs in solid form (usually in mg) and then adding a specific volume of solvent (usually in mL). Thus the concentration is reported as the weight of UCNPs per volume of solvent (mg/mL). The molar concentration and the absolute number of UCNPs in solution have not been taken into consideration. In 2018, Mackenzie *et al*. presented a theoretical method based on UCNP crystal structure taking into account the UCNP composition and morphology in order to calculate the molecular weight of UCNPs [427]. TEM and X-ray diffraction (XRD) measurements were used to determine the crystalline structure of UCNPs. As a result, the total atomic weight within a single $NaYF_4$:RE unit cell and the total number of unit cells within a UCNP can be estimated. By adding the total molecular weight contained within all unit cells in a UCNP, the theoretical molecular weight of UCNPs can be calculated.

Calculating the number of unit cells in a UCNP

It is assumed that UCNPs are spherical and the volume is calculated by using the formula for the volume of a sphere:

$$\mathrm{V_{UCNP}} = \frac{4}{3}\pi \mathrm{r}^3$$

where r is the radius of the UCNP.

In the case of UCNPs with hexagonal unit cells, the volume of a hexagonal unit cell is:

$$\mathrm{V_{unit\ cell}} = \frac{2\sqrt{3}}{4}\ \mathrm{a_h^2\ c_h}$$

where a_h and c_h are the lattice parameters that describe the hexagonal unit cells.

Hence, the number of unit cells in a UCNP is: $\mathrm{N_{unit\ cell}} = \frac{\mathrm{V_{UCNP}}}{\mathrm{V_{unit\ cell}}}$

The effects of crystal dislocations and a rounding error in the total number of unit cells are assumed to be insignificant in this calculation. Also, it is assumed that lattice parameters are accurate and that UCNPs are made entirely of hexagonal unit cells since hybrid crystal phase UCNPs have not been reported.

Calculating the total atomic weight within a single unit cell

The atomic weight of a single hexagonal $NaYF_4$ unit cell, assuming no RE dopants, is given by:

$$\mathrm{AW_{unit\,cell}} = (1.5 \cdot \mathrm{AW_{Na}}) + (1.5 \cdot \mathrm{AW_{Y}}) + (6 \cdot \mathrm{AW_{F}})$$

where AW_{Na}, AW_{Y} and AW_{F} are the atomic weight (g/mol) of Sodium, Yttrium and Fluorine, respectively.

When RE dopant ions are added during UCNP synthesis, a part of Y^{3+} ions is replaced with RE^{3+} dopant ions, resulting in a change in the average atomic weight of unit cells within UCNPs. To account for this RE doping, a total additive factor (af) is defined:

$$\mathrm{af} = \mathrm{fRE_{d1}} + \mathrm{fRE_{d2}} + \cdots + \mathrm{fRE_{dn}}$$

where fRE_{d1}, fRE_{d2}, …, fRE_{dn} is the fractional percentage of an arbitrary number (n) of RE dopants.

The total additive factor is a quantitative value between 0 and 1, corresponding to the theoretical extremes of 0% and 100% substitution of Y, respectively.

Hence, the atomic weight of a single hexagonal unit cell with RE dopants is:

$$\begin{aligned}\mathrm{AW_{unit\,cell}RE_{doped}} &= (1.5 \cdot \mathrm{AW_{Na}}) + (6 \cdot \mathrm{AW_{F}}) + [1.5 \cdot (1 - \mathrm{af}) \cdot \mathrm{AW_{Y}}] + \left(1.5 \cdot \mathrm{fRE_{d1}} \cdot \mathrm{AW_{RE_{d1}}}\right) \\ &\quad + \left(1.5 \cdot \mathrm{fRE_{d2}} \cdot \mathrm{AW_{RE_{d2}}}\right) + \cdots + \left(1.5 \cdot \mathrm{fRE_{dn}} \cdot \mathrm{AW_{RE_{dn}}}\right)\end{aligned}$$

where $AW_{unit\,cell}RE_{doped}$ is the average atomic weight of RE doped hexagonal unit cells.

Calculating the theoretical molecular weight of a UCNP

The theoretical molecular weight of a hexagonal lattice UCNP (MW) can be estimated by adding the total number of unit cells within a UCNP (N) and the total atomic weight (AW) within each individual unit cell.

$$\mathrm{MW} = \mathrm{AW_{unit\,cell}RE_{doped}} \cdot \mathrm{N_{unit\,cell}}$$

Another simpler approach for estimating the theoretical molecular weight of UCNPs was used by Bao and co-workers in 2021 [428]. The nanoparticle volume is calculated by using a spherical approximation:

$$\mathrm{V_{UCNP}} = \frac{4}{3}\pi \mathrm{r}^3$$

where r is the radius of the UCNP.

According to the literature the $NaYF_4$ has a density of $\rho = 4.21\ \mathrm{g/cm^3}$ [428].

The average weight of a single UCNP is: $\mathrm{m} = \rho \cdot \mathrm{V_{UCNP}}$

Hence the average molecular weight of UCNPs is: $\mathrm{MW_{UCNP}} = \mathrm{m} \cdot \mathrm{N_A}$

where $\mathrm{N_A} = 6.02 \cdot 10^{23}$ is the Avogadro constant.

List of References

1. Zhao, X., et al., *Recent Developments in Detection Using Noble Metal Nanoparticles.* Crit Rev Anal Chem, 2020. **50**(2): p. 97-110.

2. Bouzigues, C., T. Gacoin, and A. Alexandrou, *Biological applications of rare-earth based nanoparticles.* ACS Nano, 2011. **5**(11): p. 8488-505.

3. Giljohann, D.A., et al., *Gold nanoparticles for biology and medicine.* Angew Chem Int Ed Engl, 2010. **49**(19): p. 3280-94.

4. Chinen, A.B., et al., *Nanoparticle Probes for the Detection of Cancer Biomarkers, Cells, and Tissues by Fluorescence.* Chem Rev, 2015. **115**(19): p. 10530-74.

5. Myroshnychenko, V., et al., *Modelling the optical response of gold nanoparticles.* Chem Soc Rev, 2008. **37**(9): p. 1792-805.

6. Quidant, R., *Optical and Thermal Properties of Gold Nanoparticles for Biology and Medicine.* Gold Nanoparticles for Physics, Chemistry and Biology, 2012: p. 273-298.

7. Huang, X., et al., *Gold nanoparticles: interesting optical properties and recent applications in cancer diagnostics and therapy.* Nanomedicine (Lond), 2007. **2**(5): p. 681-93.

8. Daniel, M.C. and D. Astruc, *Gold nanoparticles: assembly, supramolecular chemistry, quantum-size-related properties, and applications toward biology, catalysis, and nanotechnology.* Chem Rev, 2004. **104**(1): p. 293-346.

9. Katz, E. and I. Willner, *Integrated nanoparticle-biomolecule hybrid systems: synthesis, properties, and applications.* Angew Chem Int Ed Engl, 2004. **43**(45): p. 6042-108.

10. Kang, D., et al., *Lanthanide-Doped Upconversion Nanomaterials: Recent Advances and Applications.* Biochip Journal, 2020. **14**(1): p. 124-135.

11. Liang, L., et al., *Facile Assembly of Functional Upconversion Nanoparticles for Targeted Cancer Imaging and Photodynamic Therapy.* ACS Appl Mater Interfaces, 2016. **8**(19): p. 11945-53.

12. Rao, L., et al., *Erythrocyte Membrane-Coated Upconversion Nanoparticles with Minimal Protein Adsorption for Enhanced Tumor Imaging.* ACS Appl Mater Interfaces, 2017. **9**(3): p. 2159-2168.

13. Contag, C.H. and M.H. Bachmann, *Advances in in vivo bioluminescence imaging of gene expression.* Annu Rev Biomed Eng, 2002. **4**: p. 235-60.

14. Heuer-Jungemann, A., et al., *Selective killing of cells triggered by their mRNA signature in the presence of smart nanoparticles.* Nanoscale, 2016. **8**(38): p. 16857-16861.

15. Halo, T.L., et al., *NanoFlares for the detection, isolation, and culture of live tumor cells from human blood.* Proc Natl Acad Sci U S A, 2014. **111**(48): p. 17104-9.

16. Liz-Marzan, L.M., *Nanometals formation and color.* Materials Today, 2004. **7**(2): p. 26-31.

17. Thompson, D., *Michael Faraday's recognition of ruby gold: the birth of modern nanotechnology.* Gold Bulletin, 2007. **40**(4): p. 267-269.

18. Turkevich, J., P.C. Stevenson, and J. Hillier, *A study of the nucleation and growth processes in the synthesis of colloidal gold* Discussions of the Faraday Society 1951. **11**(0): p. 20.

19. Turkevich, J., P.C. Stevenson, and J. Hillier, *The Formation of Colloidal Gold.* The Journal of Physical Chemistry, 1953. **57**(7): p. 3.

20. Frens, G., *Controlled Nucleation for Regulation of Particle-Size in Monodisperse Gold Suspensions.* Nature-Physical Science, 1973. **241**(105): p. 20-22.

21. Schulz, F., et al., *Little adjustments significantly improve the Turkevich synthesis of gold nanoparticles.* Langmuir, 2014. **30**(35): p. 10779-84.

22. Ji, X., et al., *Size control of gold nanocrystals in citrate reduction: the third role of citrate.* J Am Chem Soc, 2007. **129**(45): p. 13939-48.

23. Kumar, S., K.S. Gandhi, and R. Kumar, *Modeling of formation of gold nanoparticles by citrate method.* Industrial & Engineering Chemistry Research, 2007. **46**(10): p. 3128-3136.

24. Xia, H., et al., *Synthesis of monodisperse quasi-spherical gold nanoparticles in water via silver(I)-assisted citrate reduction.* Langmuir, 2010. **26**(5): p. 3585-9.

25. Biggs, S., et al., *The Role of Colloidal Stability in the Formation of Gold Sols.* Journal of Colloid and Interface Science, 1993. **160**(2): p. 511-513.

26. Privman, V.V., et al., *Mechanism of Formation of Monodispersed Colloids by Aggregation of Nanosize Precursors.* J Colloid Interface Sci, 1999. **213**(1): p. 36-45.

27. Li, G.T., et al., *Spherical and planar gold(0) nanoparticles with a rigid gold(I)-anion or a fluid gold (0)-acetone surface.* Langmuir, 2003. **19**(16): p. 6483-6491.

28. Frens, G., *Particle-Size and Sol Stability in Metal Colloids.* Kolloid-Zeitschrift and Zeitschrift Fur Polymere, 1972. **250**(7): p. 736-+.

29. Bastus, N.G., J. Comenge, and V. Puntes, *Kinetically controlled seeded growth synthesis of citrate-stabilized gold nanoparticles of up to 200 nm: size focusing versus Ostwald ripening.* Langmuir, 2011. **27**(17): p. 11098-105.

30. Brown, K.R., D.G. Walter, and M.J. Natan, *Seeding of colloidal Au nanoparticle solutions. 2. Improved control of particle size and shape.* Chemistry of Materials, 2000. **12**(2): p. 306-313.

31. Ziegler, C. and A. Eychmuller, *Seeded Growth Synthesis of Uniform Gold Nanoparticles with Diameters of 15-300 nm.* Journal of Physical Chemistry C, 2011. **115**(11): p. 4502-4506.

32. Brown, K.R., et al., *Hydroxylamine seeding of colloidal au nanoparticles. 3. Controlled formation of conductive Au films.* Chemistry of Materials, 2000. **12**(2): p. 314-323.

33. Brown, K.R. and M.J. Natan, *Hydroxylamine seeding of colloidal Au nanoparticles in solution and on surfaces.* Langmuir, 1998. **14**(4): p. 726-728.

34. Jana, N.R., L. Gearheart, and C.J. Murphy, *Seeding growth for size control of 5-40 nm diameter gold nanoparticles.* Langmuir, 2001. **17**(22): p. 6782-6786.

35. Rodriguez-Fernandez, J., et al., *Seeded growth of submicron Au colloids with quadrupole plasmon resonance modes.* Langmuir, 2006. **22**(16): p. 7007-10.

36. Voorhees, P.W., *The Theory of Ostwald Ripening.* Journal of Statistical Physics, 1985. **38**(1-2): p. 231-252.

37. Jana, N.R., L. Gearheart, and C.J. Murphy, *Seed-mediated growth approach for shape-controlled synthesis of spheroidal and rod-like gold nanoparticles using a surfactant template.* Advanced Materials, 2001. **13**(18): p. 1389-1393.

38. Gole, A. and C.J. Murphy, *Seed-mediated synthesis of gold nanorods: Role of the size and nature of the seed.* Chemistry of Materials, 2004. **16**(19): p. 3633-3640.

39. Murphy, C.J., et al., *One-dimensional colloidal gold and silver nanostructures.* Inorg Chem, 2006. **45**(19): p. 7544-54.

40. Orendorff, C.J. and C.J. Murphy, *Quantitation of metal content in the silver-assisted growth of gold nanorods.* J Phys Chem B, 2006. **110**(9): p. 3990-4.

41. Liu, M. and P. Guyot-Sionnest, *Mechanism of silver(I)-assisted growth of gold nanorods and bipyramids.* J Phys Chem B, 2005. **109**(47): p. 22192-200.

42. Nikoobakht, B. and M.A. El-Sayed, *Preparation and growth mechanism of gold nanorods (NRs) using seed-mediated growth method.* Chemistry of Materials, 2003. **15**(10): p. 1957-1962.

43. Hao, F., et al., *Plasmon resonances of a gold nanostar.* Nano Lett, 2007. **7**(3): p. 729-32.

44. Guerrero-Martinez, A., et al., *Nanostars shine bright for you Colloidal synthesis, properties and applications of branched metallic nanoparticles.* Current Opinion in Colloid & Interface Science, 2011. **16**(2): p. 118-127.

45. Cheng, K., et al., *Construction and validation of nano gold tripods for molecular imaging of living subjects.* J Am Chem Soc, 2014. **136**(9): p. 3560-71.

46. Chen, S., et al., *Monopod, bipod, tripod, and tetrapod gold nanocrystals.* J Am Chem Soc, 2003. **125**(52): p. 16186-7.

47. Barbosa, S., et al., *Tuning size and sensing properties in colloidal gold nanostars.* Langmuir, 2010. **26**(18): p. 14943-50.

48. Sau, T.K. and C.J. Murphy, *Room temperature, high-yield synthesis of multiple shapes of gold nanoparticles in aqueous solution.* J Am Chem Soc, 2004. **126**(28): p. 8648-9.

49. Day, H.A., et al., *Controlling the three-dimensional morphology of nanocrystals.* Crystengcomm, 2010. **12**(12): p. 4312-4316.

50. Kuo, C.H. and M.H. Huang, *Synthesis of branched gold nanocrystals by a seeding growth approach.* Langmuir, 2005. **21**(5): p. 2012-6.

51. Pastoriza-Santos, I. and L.M. Liz-Marzan, *N,N-Dimethylformamide as a Reaction Medium for Metal Nanoparticle Synthesis.* Advanced Functional Materials, 2009. **19**(5): p. 679-688.

52. Senthil Kumar, P., et al., *High-yield synthesis and optical response of gold nanostars.* Nanotechnology, 2008. **19**(1): p. 015606.

53. Zou, X., E. Ying, and S. Dong, *Seed-mediated synthesis of branched gold nanoparticles with the assistance of citrate and their surface-enhanced Raman scattering properties.* Nanotechnology, 2006. **17**(18): p. 4758-64.

54. Yuan, H., et al., *Shape and SPR evolution of thorny gold nanoparticles promoted by silver ions.* Chemistry of Materials, 2007. **19**(7): p. 1592-1600.

55. Haase, M. and H. Schafer, *Upconverting nanoparticles.* Angew Chem Int Ed Engl, 2011. **50**(26): p. 5808-29.

56. Menyuk, N., J.W. Pierce, and K. Dwight, *Nayf4-Yb,Er - Efficient Upconversion Phosphor.* Applied Physics Letters, 1972. **21**(4): p. 159-&.

57. Kano, T., H. Yamamoto, and Y. Otomo, *NALNF4-YB3+, ER3+(LN-Y,GD,LA) - EFFICIENT GREEN-EMITTING INFRARED-EXCITED PHOSPHORS.* Journal of the Electrochemical Society, 1972. **119**(3): p. C100-&.

58. Liang, L., et al., *Enhanced blue and green upconversion in hydrothermally synthesized hexagonal NaY1−xYbxF4:Ln3+ (Ln3+ = Er3+ or Tm3+).* Journal of Alloys and Compounds, 2004. **368**(1-2): p. 94-100.

59. Zhou, J., et al., *Upconversion luminescent materials: advances and applications.* Chem Rev, 2015. **115**(1): p. 395-465.

60. Wang, F. and X. Liu, *Multicolor tuning of lanthanide-doped nanoparticles by single wavelength excitation.* Acc Chem Res, 2014. **47**(4): p. 1378-85.

61. Chen, G., et al., *Upconversion nanoparticles: design, nanochemistry, and applications in theranostics.* Chem Rev, 2014. **114**(10): p. 5161-214.

62. Zhu, X., et al., *Recent Progress of Rare-Earth Doped Upconversion Nanoparticles: Synthesis, Optimization, and Applications.* Adv Sci (Weinh), 2019. **6**(22): p. 1901358.

63. Martin, N., et al., *Preparation of fluorides at 80 degrees C in the NaF-(Y,Yb,Pr)F-3 system.* Journal of Materials Chemistry, 1999. **9**(1): p. 125-128.

64. Stouwdam, J.W. and F.C.J.M. van Veggel, *Near-infrared emission of redispersible Er3+, Nd3+, and Ho3+ doped LaF3 nanoparticles.* Nano Letters, 2002. **2**(7): p. 733-737.

65. Yi, G.S. and G.M. Chow, *Colloidal LaF3 : Yb,Er, LaF3 : Yb,Ho and LaF3 : Yb,Tm nanocrystals with multicolor upconversion fluorescence.* Journal of Materials Chemistry, 2005. **15**(41): p. 4460-4464.

66. Zeng, J.H., et al., *Synthesis and upconversion luminescence of hexagonal-phase NaYF4 : Yb, Er3+, phosphors of controlled size and morphology.* Advanced Materials, 2005. **17**(17): p. 2119-+.

67. Yi, G.S., et al., *Synthesis, characterization, and biological application of size-controlled nanocrystalline NaYF4 : Yb,Er infrared-to-visible up-conversion phosphors.* Nano Letters, 2004. **4**(11): p. 2191-2196.

68. Heer, S., et al., *Highly efficient multicolour upconversion emission in transparent colloids of lanthanide-doped NaYF4 nanocrystals.* Advanced Materials, 2004. **16**(23-24): p. 2102-+.

69. Heer, S., et al., *Blue, green, and red upconversion emission from lanthanide-doped LuPO4 and YbPO4 nanocrystals in a transparent colloidal solution.* Angew Chem Int Ed Engl, 2003. **42**(27): p. 3179-82.

70. Li, Z. and Y. Zhang, *An efficient and user-friendly method for the synthesis of hexagonal-phase NaYF(4):Yb, Er/Tm nanocrystals with controllable shape and upconversion fluorescence.* Nanotechnology, 2008. **19**(34): p. 345606.

71. Li, Z.Q., Y. Zhang, and S. Jiang, *Multicolor Core/Shell-Structured Upconversion Fluorescent Nanoparticles.* Advanced Materials, 2008. **20**(24): p. 4765-+.

72. Wang, F., et al., *Synthesis of polyethylenimine/NaYF4 nanoparticles with upconversion fluorescence.* Nanotechnology, 2006. **17**(23): p. 5786-5791.

73. Li, Z. and Y. Zhang, *Monodisperse silica-coated polyvinylpyrrolidone/NaYF(4) nanocrystals with multicolor upconversion fluorescence emission.* Angew Chem Int Ed Engl, 2006. **45**(46): p. 7732-5.

74. Wang, F. and X. Liu, *Upconversion multicolor fine-tuning: visible to near-infrared emission from lanthanide-doped NaYF4 nanoparticles.* J Am Chem Soc, 2008. **130**(17): p. 5642-3.

75. Boyer, J.C., et al., *Synthesis of colloidal upconverting NaYF4 nanocrystals doped with Er3+, Yb3+ and Tm3+, Yb3+ via thermal decomposition of lanthanide trifluoroacetate precursors.* J Am Chem Soc, 2006. **128**(23): p. 7444-5.

76. Zhang, Y.W., et al., *Single-crystalline and monodisperse LaF3 triangular nanoplates from a single-source precursor.* J Am Chem Soc, 2005. **127**(10): p. 3260-1.

77. Liu, Y., et al., *A strategy for accurate detection of glucose in human serum and whole blood based on an upconversion nanoparticles-polydopamine nanosystem.* Nano Research, 2018. **11**(6): p. 3164-3174.

78. Zhu, Y.R., et al., *Enhancing Upconversion Luminescence of LiYF4:Yb,Er Nanocrystals by Cd2+ Doping and Core-Shell Structure.* Journal of Physical Chemistry C, 2017. **121**(34): p. 18909-18916.

79. Zhou, B., et al., *Enhanced green upconversion luminescence in tetrahedral LiYF4:Yb/Er nanoparticles by manganese(ii)-doping: the key role of the host lattice.* Nanoscale, 2018. **10**(6): p. 2834-2840.

80. Mai, H.X., et al., *High-quality sodium rare-earth fluoride nanocrystals: controlled synthesis and optical properties.* J Am Chem Soc, 2006. **128**(19): p. 6426-36.

81. Mai, H.X., et al., *Size- and phase-controlled synthesis of monodisperse NaYF4 : Yb,Er nanocrystals from a unique delayed nucleation pathway monitored with upconversion spectroscopy.* Journal of Physical Chemistry C, 2007. **111**(37): p. 13730-13739.

82. Wang, F. and X. Liu, *Recent advances in the chemistry of lanthanide-doped upconversion nanocrystals.* Chem Soc Rev, 2009. **38**(4): p. 976-89.

83. DaCosta, M.V., et al., *Lanthanide upconversion nanoparticles and applications in bioassays and bioimaging: a review.* Anal Chim Acta, 2014. **832**: p. 1-33.

84. Xie, M.G., et al., *Phase and morphology evolution of NaGdF4:Yb,Er nanocrystals with power density-dependent upconversion fluorescence via one-step microwave-assisted solvothermal method.* Journal of Luminescence, 2021. **239**.

85. Savchuk, O.A., et al., *Mapping Temperature Distribution Generated by Photothermal Conversion in Graphene Film Using Er,Yb:NaYF4 Nanoparticles Prepared by Microwave-Assisted Solvothermal Method.* Frontiers in Chemistry, 2019. **7**.

86. Reddy, K.L., et al., *Microwave-assisted one-step synthesis of acetate-capped NaYF4:Yb/Er upconversion nanocrystals and their application in bioimaging.* Journal of Materials Science, 2017. **52**(10): p. 5738-5750.

87. Wang, H.Q. and T. Nann, *Monodisperse upconverting nanocrystals by microwave-assisted synthesis.* ACS Nano, 2009. **3**(11): p. 3804-8.

88. Wang, H.Q., R.D. Tilley, and T. Nann, *Size and shape evolution of upconverting nanoparticles using microwave assisted synthesis.* Crystengcomm, 2010. **12**(7): p. 1993-1996.

89. Sun, C.N., et al., *Solvothermal Synthesis of Lanthanide-doped NaYF4 Upconversion Crystals with Size and Shape Control: Particle Properties and Growth Mechanism.* Chemnanomat, 2021. **7**(2): p. 174-183.

90. Xie, J., et al., *Selective growth and upconversion photoluminescence of Y-based fluorides: from NaYF4: Yb/Er to YF3: Yb/Er crystals.* Nanotechnology, 2020. **31**(50).

91. Mallqui, C.R., et al. *Synthesis of NaYF4: Yb, Tm Nanoparticles by Solvothermal Method and Characterization by Upconversion Visible Radiation Fluorescence*. in *16th Meeting of Physics*. 2017. Lima, PERU.

92. Wang, X., et al., *A general strategy for nanocrystal synthesis.* Nature, 2005. **437**(7055): p. 121-4.

93. Lin, M., et al., *Recent advances in synthesis and surface modification of lanthanide-doped upconversion nanoparticles for biomedical applications.* Biotechnol Adv, 2012. **30**(6): p. 1551-61.

94. Link, S. and M.A. El-Sayed, *Size and temperature dependence of the plasmon absorption of colloidal gold nanoparticles.* Journal of Physical Chemistry B, 1999. **103**(21): p. 4212-4217.

95. Yang, X., et al., *Gold Nanomaterials at Work in Biomedicine.* Chem Rev, 2015. **115**(19): p. 10410-88.

96. Cobley, C.M., et al., *Gold nanostructures: a class of multifunctional materials for biomedical applications.* Chem Soc Rev, 2011. **40**(1): p. 44-56.

97. Kelly, K.L., et al., *The optical properties of metal nanoparticles: The influence of size, shape, and dielectric environment.* Journal of Physical Chemistry B, 2003. **107**(3): p. 668-677.

98. Xia, Y.N. and N.J. Halas, *Shape-controlled synthesis and surface plasmonic properties of metallic nanostructures.* Mrs Bulletin, 2005. **30**(5): p. 338-344.

99. Kreibig, U., et al., *Optical properties of free and embedded metal clusters: Recent results.* Large Clusters of Atoms and Molecules, 1996. **313**: p. 475-493.

100. Ghosh, S.K. and T. Pal, *Interparticle coupling effect on the surface plasmon resonance of gold nanoparticles: from theory to applications.* Chem Rev, 2007. **107**(11): p. 4797-862.

101. Louis, C. and O. Pluchery, *Gold Nanoparticles for Physics, Chemistry and Biology.* Gold Nanoparticles for Physics, Chemistry and Biology, 2012: p. 1-395.

102. Link, S. and M.A. El-Sayed, *Shape and size dependence of radiative, non-radiative and photothermal properties of gold nanocrystals.* International Reviews in Physical Chemistry, 2000. **19**(3): p. 409-453.

103. Link, S. and M.A. El-Sayed, *Optical properties and ultrafast dynamics of metallic nanocrystals.* Annu Rev Phys Chem, 2003. **54**: p. 331-66.

104. Shao, L., et al., *Plasmonic properties of single multispiked gold nanostars: correlating modeling with experiments.* Langmuir, 2012. **28**(24): p. 8979-84.

105. Nehl, C.L. and J.H. Hafner, *Shape-dependent plasmon resonances of gold nanoparticles.* Journal of Materials Chemistry, 2008. **18**(21): p. 2415-2419.

106. Xin, N., et al., *Upconversion nanomaterials: a platform for biosensing, theranostic and photoregulation.* Materials Today Chemistry, 2020. **17**.

107. Reddy, K.L., et al., *Lanthanide Doped Near Infrared Active Upconversion Nanophosphors: Fundamental Concepts, Synthesis Strategies, and Technological Applications.* Small, 2018. **14**(37).

108. Zheng, X., et al., *Lanthanides-doped near-infrared active upconversion nanocrystals: Upconversion mechanisms and synthesis.* Coordination Chemistry Reviews, 2021. **438**.

109. Chen, J. and J.X. Zhao, *Upconversion nanomaterials: synthesis, mechanism, and applications in sensing.* Sensors (Basel), 2012. **12**(3): p. 2414-35.

110. Liang, G., et al., *Recent progress in the development of upconversion nanomaterials in bioimaging and disease treatment.* J Nanobiotechnology, 2020. **18**(1): p. 154.

111. Chen, G., et al., *Ultrasmall monodisperse NaYF(4):Yb(3+)/Tm(3+) nanocrystals with enhanced near-infrared to near-infrared upconversion photoluminescence.* ACS Nano, 2010. **4**(6): p. 3163-8.

112. Wang, M., et al., *Upconversion nanoparticles: synthesis, surface modification and biological applications.* Nanomedicine, 2011. **7**(6): p. 710-29.

113. Wang, L. and Y. Li, *Green upconversion nanocrystals for DNA detection.* Chem Commun (Camb), 2006(24): p. 2557-9.

114. Kramer, K.W., et al., *Hexagonal sodium yttrium fluoride based green and blue emitting upconversion phosphors.* Chemistry of Materials, 2004. **16**(7): p. 1244-1251.

115. Suyver, J.F., et al., *Upconversion spectroscopy and properties of NaYF4 doped with , and/or.* Journal of Luminescence, 2006. **117**(1): p. 1-12.

116. Lee, C., et al., *Origin of strong red emission in Er3+-based upconversion materials: role of intermediate states and cross relaxation.* Physical Chemistry Chemical Physics, 2019. **21**(43): p. 24026-24033.

117. Huang, F., et al., *Temperature sensitive cross relaxation between Er3+ ions in laminated hosts: a novel mechanism for thermochromic upconversion and high performance thermometry.* Journal of Materials Chemistry C, 2018. **6**(45): p. 12364-12370.

118. Dwivedi, Y., S.N. Thakur, and S.B. Rai, *Study of frequency upconversion in Yb3+/Eu3+ by cooperative energy transfer in oxyfluoroborate glass matrix.* Applied Physics B-Lasers and Optics, 2007. **89**(1): p. 45-51.

119. Xue, X.J., et al., *Upconversion emissions from high energy levels of Tb3+ under near-infrared laser excitation at 976 nm.* Optical Materials Express, 2015. **5**(12): p. 2768-2776.

120. Tiwari, S.P., et al., *Future prospects of fluoride based upconversion nanoparticles for emerging applications in biomedical and energy harvesting.* Journal of Vacuum Science & Technology B, 2018. **36**(6).

121. Mehrdel, B., et al., *Upconversion lanthanide nanomaterials: basics introduction, synthesis approaches, mechanism and application in photodetector and photovoltaic devices.* Nanotechnology, 2022. **33**(8).

122. Zheng, K.Z., et al., *Recent advances in upconversion nanocrystals: Expanding the kaleidoscopic toolbox for emerging applications.* Nano Today, 2019. **29**.

123. Capobianco, J.A., et al., *Enhancement of red emission (F-4(9/2)-> I-4(15/2)) via upconversion in bulk and nanocrystalline cubic Y2O3 : Er3+.* Journal of Physical Chemistry B, 2002. **106**(6): p. 1181-1187.

124. van De Rijke, F., et al., *Up-converting phosphor reporters for nucleic acid microarrays.* Nat Biotechnol, 2001. **19**(3): p. 273-6.

125. Wang, G., Q. Peng, and Y. Li, *Upconversion luminescence of monodisperse CaF2:Yb(3+)/Er(3+) nanocrystals.* J Am Chem Soc, 2009. **131**(40): p. 14200-1.

126. Strohhofer, C. and A. Polman, *Absorption and emission spectroscopy in Er3+-Yb3+ doped aluminum oxide waveguides.* Optical Materials, 2003. **21**(4): p. 705-712.

127. Tikhomirov, V.K., et al., *Preparation and up-conversion luminescence of 8 nm rare-earth doped fluoride nanoparticles.* Opt Express, 2008. **16**(19): p. 14544-9.

128. Auzel, F., *Upconversion and anti-Stokes processes with f and d ions in solids.* Chem Rev, 2004. **104**(1): p. 139-73.

129. Shalav, A., et al. *Improvements of an up-conversion NaYF4 : Er3+ phosphor/silicon solar cell system for an enhanced response in the near-infrared*. in *31st IEEE Photovoltaic Specialists Conference*. 2005. Lake Buena Vista, FL.

130. Dong, H., L.D. Sun, and C.H. Yan, *Basic understanding of the lanthanide related upconversion emissions.* Nanoscale, 2013. **5**(13): p. 5703-14.

131. Lu, H.Z., et al., *Sensitization, energy transfer and infra-red emission decay modulation in Yb3+-doped NaYF4 nanoparticles with visible light through a perfluoroanthraquinone chromophore.* Scientific Reports, 2017. **7**.

132. Wang, F., et al., *Upconversion nanoparticles in biological labeling, imaging, and therapy.* Analyst, 2010. **135**(8): p. 1839-54.

133. Achatz, D.E., R. Ali, and O.S. Wolfbeis, *Luminescent chemical sensing, biosensing, and screening using upconverting nanoparticles.* Top Curr Chem, 2011. **300**: p. 29-50.

134. Bogdan, N., et al., *Synthesis of ligand-free colloidally stable water dispersible brightly luminescent lanthanide-doped upconverting nanoparticles.* Nano Lett, 2011. **11**(2): p. 835-40.

135. Boyer, J.C., L.A. Cuccia, and J.A. Capobianco, *Synthesis of colloidal upconverting NaYF4: Er3+/Yb3+ and Tm3+/Yb3+ monodisperse nanocrystals.* Nano Lett, 2007. **7**(3): p. 847-52.

136. Joubert, M.F., *Photon avalanche upconversion in rare earth laser materials.* Optical Materials, 1999. **11**(2-3): p. 181-203.

137. Watson, J.D. and F.H. Crick, *Molecular structure of nucleic acids: a structure for deoxyribose nucleic acid.* Clin Orthop Relat Res, 2007. **462**(462): p. 3-5.

138. Alberts, B., et al., *Molecular Biology of the Cell, Sixth Edition.* Molecular Biology of the Cell, Sixth Edition, 2015: p. 1-1342.

139. Carmody, S.R. and S.R. Wente, *mRNA nuclear export at a glance.* J Cell Sci, 2009. **122**(Pt 12): p. 1933-7.

140. Kresge, N., R.D. Simoni, and R.L. Hill, *Chargaff's rules: the work of Erwin Chargaff - The separation and quantitative estimation of purines and pyrimidines in minute amounts (Vischer, E. and Chargaff, E. (1948) J. Biol. Chem. 176, 703-714).* Journal of Biological Chemistry, 2005. **280**(24).

141. Gumport, R.I., *Nucleic-Acids in Chemistry and Biology - Blackburn,Gm, Gait,Mj.* Nature, 1991. **350**(6320): p. 667-667.

142. Kool, E.T., *Hydrogen bonding, base stacking, and steric effects in dna replication.* Annu Rev Biophys Biomol Struct, 2001. **30**: p. 1-22.

143. Owczarzy, R., et al., *Predicting stability of DNA duplexes in solutions containing magnesium and monovalent cations.* Biochemistry, 2008. **47**(19): p. 5336-5353.

144. Florescu, A.M. and M. Joyeux, *Thermal and mechanical denaturation properties of a DNA model with three sites per nucleotide.* J Chem Phys, 2011. **135**(8): p. 085105.

145. Owczarzy, R., et al., *Predicting stability of DNA duplexes in solutions containing magnesium and monovalent cations.* Biochemistry, 2008. **47**(19): p. 5336-53.

146. Ansevin, A.T., et al., *High-resolution thermal denaturation of DNA. I. Theoretical and practical considerations for the resolution of thermal subtransitions.* Biopolymers, 1976. **15**(1): p. 153-74.

147. D'Abramo, M., et al., *On the nature of DNA hyperchromic effect.* J Phys Chem B, 2013. **117**(29): p. 8697-704.

148. Kibbe, W.A., *OligoCalc: an online oligonucleotide properties calculator.* Nucleic Acids Res, 2007. **35**(Web Server issue): p. W43-6.

149. Pon, R.T., N. Usman, and K.K. Ogilvie, *Derivatization of controlled pore glass beads for solid phase oligonucleotide synthesis.* Biotechniques, 1988. **6**(8): p. 768-75.

150. Caruthers, M.H., *Gene synthesis machines: DNA chemistry and its uses.* Science, 1985. **230**(4723): p. 281-5.

151. Damha, M.J., P.A. Giannaris, and S.V. Zabarylo, *An improved procedure for derivatization of controlled-pore glass beads for solid-phase oligonucleotide synthesis.* Nucleic Acids Res, 1990. **18**(13): p. 3813-21.

152. Hall, L.M., M. Gerowska, and T. Brown, *A highly fluorescent DNA toolkit: synthesis and properties of oligonucleotides containing new Cy3, Cy5 and Cy3B monomers.* Nucleic Acids Res, 2012. **40**(14): p. e108.

153. Shelbourne, M., et al., *Fast copper-free click DNA ligation by the ring-strain promoted alkyne-azide cycloaddition reaction.* Chem Commun (Camb), 2011. **47**(22): p. 6257-9.

154. Hakkinen, H., *The gold-sulfur interface at the nanoscale.* Nat Chem, 2012. **4**(6): p. 443-55.

155. Dougan, J.A., et al., *Enhanced oligonucleotide-nanoparticle conjugate stability using thioctic acid modified oligonucleotides.* Nucleic Acids Res, 2007. **35**(11): p. 3668-75.

156. Giust, D., et al., *Graphene Oxide-Upconversion Nanoparticle Based Portable Sensors for Assessing Nutritional Deficiencies in Crops.* ACS Nano, 2018. **12**(6): p. 6273-6279.

157. Green, M. and P.M. Loewenstein, *AUTONOMOUS FUNCTIONAL DOMAINS OF CHEMICALLY SYNTHESIZED HUMAN IMMUNODEFICIENCY VIRUS TAT TRANS-ACTIVATOR PROTEIN.* Cell, 1988. **55**(6): p. 1179-1188.

158. Frankel, A.D. and C.O. Pabo, *CELLULAR UPTAKE OF THE TAT PROTEIN FROM HUMAN IMMUNODEFICIENCY VIRUS.* Cell, 1988. **55**(6): p. 1189-1193.

159. Bechara, C. and S. Sagan, *Cell-penetrating peptides: 20 years later, where do we stand?* Febs Letters, 2013. **587**(12): p. 1693-1702.

160. Lindgren, M., et al., *Cell-penetrating peptides.* Trends in Pharmacological Sciences, 2000. **21**(3): p. 99-103.

161. Kim, H., M. Kitamatsu, and T. Ohtsuki, *Enhanced intracellular peptide delivery by multivalent cell-penetrating peptide with bioreducible linkage.* Bioorganic & Medicinal Chemistry Letters, 2018. **28**(3): p. 378-381.

162. Borrelli, A., et al., *Cell Penetrating Peptides as Molecular Carriers for Anti-Cancer Agents.* Molecules, 2018. **23**(2).

163. Milletti, F., *Cell-penetrating peptides: classes, origin, and current landscape.* Drug Discovery Today, 2012. **17**(15-16): p. 850-860.

164. Guidotti, G., L. Brambilla, and D. Rossi, *Cell-Penetrating Peptides: From Basic Research to Clinics.* Trends in Pharmacological Sciences, 2017. **38**(4): p. 406-424.

165. Lundberg, P. and U. Langel, *A brief introduction to cell-penetrating peptides.* Journal of Molecular Recognition, 2003. **16**(5): p. 227-233.

166. Pouny, Y., et al., *INTERACTION OF ANTIMICROBIAL DERMASEPTIN AND ITS FLUORESCENTLY LABELED ANALOGS WITH PHOSPHOLIPID-MEMBRANES.* Biochemistry, 1992. **31**(49): p. 12416-12423.

167. Matsuzaki, K., et al., *Transbilayer transport of ions and lipids coupled with mastoparan X translocation.* Biochemistry, 1996. **35**(25): p. 8450-8456.

168. Lee, M.T., et al., *Many-body effect of antimicrobial peptides: On the correlation between lipid's spontaneous curvature and pore formation.* Biophysical Journal, 2005. **89**(6): p. 4006-4016.

169. Hirose, H., et al., *Transient Focal Membrane Deformation Induced by Arginine-rich Peptides Leads to Their Direct Penetration into Cells.* Molecular Therapy, 2012. **20**(5): p. 984-993.

170. Ter-Avetisyan, G., et al., *Cell Entry of Arginine-rich Peptides Is Independent of Endocytosis.* Journal of Biological Chemistry, 2009. **284**(6): p. 3370-3378.

171. Mishra, A., et al., *Translocation of HIV TAT peptide and analogues induced by multiplexed membrane and cytoskeletal interactions.* Proceedings of the National Academy of Sciences of the United States of America, 2011. **108**(41): p. 16883-16888.

172. Derossi, D., G. Chassaing, and A. Prochiantz, *Trojan peptides: the penetratin system for intracellular delivery.* Trends in Cell Biology, 1998. **8**(2): p. 84-87.

173. Elmquist, A., M. Hansen, and U. Langel, *Structure-activity relationship study of the cell-penetrating peptide pVEC.* Biochimica Et Biophysica Acta-Biomembranes, 2006. **1758**(6): p. 721-729.

174. Gessner, I. and I. Neundorf, *Nanoparticles Modified with Cell-Penetrating Peptides: Conjugation Mechanisms, Physicochemical Properties, and Application in Cancer Diagnosis and Therapy.* International Journal of Molecular Sciences, 2020. **21**(7).

175. Rozek, T., et al., *The antibiotic and anticancer active aurein peptides from the Australian Bell Frogs Litoria aurea and Litoria raniformis - The solution structure of aurein 1.2.* European Journal of Biochemistry, 2000. **267**(17): p. 5330-5341.

176. Lorenzon, E.N., et al., *Effect of dimerization on the mechanism of action of aurein 1.2.* Biochimica Et Biophysica Acta-Biomembranes, 2016. **1858**(6): p. 1129-1138.

177. Laadhari, M., et al., *Interaction of the antimicrobial peptides caerin 1.1 and aurein 1.2 with intact bacteria by H-2 solid-state NMR.* Biochimica Et Biophysica Acta-Biomembranes, 2016. **1858**(12): p. 2959-2964.

178. Li, M., et al., *Discovery and Characterization of a Peptide That Enhances Endosomal Escape of Delivered Proteins in Vitro and in Vivo.* Journal of the American Chemical Society, 2015. **137**(44): p. 14084-14093.

179. Cutler, J.I., E. Auyeung, and C.A. Mirkin, *Spherical nucleic acids.* J Am Chem Soc, 2012. **134**(3): p. 1376-91.

180. Mirkin, C.A., et al., *A DNA-based method for rationally assembling nanoparticles into macroscopic materials.* Nature, 1996. **382**(6592): p. 607-9.

181. Alivisatos, A.P., et al., *Organization of 'nanocrystal molecules' using DNA.* Nature, 1996. **382**(6592): p. 609-11.

182. Rosi, N.L., et al., *Oligonucleotide-modified gold nanoparticles for intracellular gene regulation.* Science, 2006. **312**(5776): p. 1027-30.

183. Jin, R., et al., *What controls the melting properties of DNA-linked gold nanoparticle assemblies?* J Am Chem Soc, 2003. **125**(6): p. 1643-54.

184. Lytton-Jean, A.K. and C.A. Mirkin, *A thermodynamic investigation into the binding properties of DNA functionalized gold nanoparticle probes and molecular fluorophore probes.* J Am Chem Soc, 2005. **127**(37): p. 12754-5.

185. Li, Z., et al., *Multiple thiol-anchor capped DNA-gold nanoparticle conjugates.* Nucleic Acids Research, 2002. **30**(7): p. 1558-1562.

186. Sato, K., K. Hosokawa, and M. Maeda, *Rapid aggregation of gold nanoparticles induced by non-cross-linking DNA hybridization.* Journal of the American Chemical Society, 2003. **125**(27): p. 8102-8103.

187. Lee, J.S., et al., *Silver nanoparticle-oligonucleotide conjugates based on DNA with triple cyclic disulfide moieties.* Nano Letters, 2007. **7**(7): p. 2112-2115.

188. Mitchell, G.P., C.A. Mirkin, and R.L. Letsinger, *Programmed assembly of DNA functionalized quantum dots.* Journal of the American Chemical Society, 1999. **121**(35): p. 8122-8123.

189. Xue, C., et al., *Self-assembled monolayer mediated silica coating of silver triangular nanoprisms.* Advanced Materials, 2007. **19**(22): p. 4071-+.

190. Cutler, J.I., et al., *Polyvalent Oligonucleotide Iron Oxide Nanoparticle "Click" Conjugates.* Nano Letters, 2010. **10**(4): p. 1477-1480.

191. Cao, Y.W., R. Jin, and C.A. Mirkin, *DNA-modified core-shell Ag/Au nanoparticles.* Journal of the American Chemical Society, 2001. **123**(32): p. 7961-7962.

192. Yin, Y.D., et al., *Synthesis and characterization of stable aqueous dispersions of silver nanoparticles through the Tollens process.* Journal of Materials Chemistry, 2002. **12**(3): p. 522-527.

193. Demers, L.M., et al., *A fluorescence-based method for determining the surface coverage and hybridization efficiency of thiol-capped oligonucleotides bound to gold thin films and nanoparticles.* Anal Chem, 2000. **72**(22): p. 5535-41.

194. Hurst, S.J., A.K. Lytton-Jean, and C.A. Mirkin, *Maximizing DNA loading on a range of gold nanoparticle sizes.* Anal Chem, 2006. **78**(24): p. 8313-8.

195. Elghanian, R., et al., *Selective colorimetric detection of polynucleotides based on the distance-dependent optical properties of gold nanoparticles.* Science, 1997. **277**(5329): p. 1078-81.

196. Park, J.W. and J.S. Shumaker-Parry, *Strong resistance of citrate anions on metal nanoparticles to desorption under thiol functionalization.* ACS Nano, 2015. **9**(2): p. 1665-82.

197. Nuzzo, R.G., B.R. Zegarski, and L.H. Dubois, *Fundamental-Studies of the Chemisorption of Organosulfur Compounds on Au(111) - Implications for Molecular Self-Assembly on Gold Surfaces.* Journal of the American Chemical Society, 1987. **109**(3): p. 733-740.

198. Tagliazucchi, M. and I. Szleifer, *Stimuli-responsive polymers grafted to nanopores and other nano-curved surfaces: structure, chemical equilibrium and transport.* Soft Matter, 2012. **8**(28): p. 7292-7305.

199. Hill, H.D., et al., *The role radius of curvature plays in thiolated oligonucleotide loading on gold nanoparticles.* ACS Nano, 2009. **3**(2): p. 418-24.

200. Giljohann, D.A., et al., *Oligonucleotide loading determines cellular uptake of DNA-modified gold nanoparticles.* Nano Lett, 2007. **7**(12): p. 3818-21.

201. Seferos, D.S., et al., *Polyvalent DNA nanoparticle conjugates stabilize nucleic acids.* Nano Lett, 2009. **9**(1): p. 308-11.

202. Shi, J., et al., *Fluorescence Lifetime Imaging of Nanoflares for mRNA Detection in Living Cells.* Anal Chem, 2016. **88**(4): p. 1979-83.

203. Zwanikken, J.W., et al., *Local Ionic Environment around Polyvalent Nucleic Acid-Functionalized Nanoparticles.* Journal of Physical Chemistry C, 2011. **115**(33): p. 16368-16373.

204. Lee, O.S. and G.C. Schatz, *Molecular Dynamics Simulation of DNA-Functionalized Gold Nanoparticles.* Journal of Physical Chemistry C, 2009. **113**(6): p. 2316-2321.

205. Kewalramani, S., et al., *Counterion distribution surrounding spherical nucleic acid-Au nanoparticle conjugates probed by small-angle x-ray scattering.* ACS Nano, 2013. **7**(12): p. 11301-9.

206. Cutler, J.I., et al., *Polyvalent nucleic acid nanostructures.* J Am Chem Soc, 2011. **133**(24): p. 9254-7.

207. Kyriazi, M.E., et al., *An Investigation into the Resistance of Spherical Nucleic Acids against DNA Enzymatic Degradation.* Bioconjug Chem, 2022. **33**(1): p. 219-225.

208. Kanaras, A.G., et al., *Towards multistep nanostructure synthesis: programmed enzymatic self-assembly of DNA/gold systems.* Angew Chem Int Ed Engl, 2003. **42**(2): p. 191-4.

209. Zhang, X., M.R. Servos, and J. Liu, *Instantaneous and quantitative functionalization of gold nanoparticles with thiolated DNA using a pH-assisted and surfactant-free route.* J Am Chem Soc, 2012. **134**(17): p. 7266-9.

210. Liu, B. and J. Liu, *Freezing Directed Construction of Bio/Nano Interfaces: Reagentless Conjugation, Denser Spherical Nucleic Acids, and Better Nanoflares.* J Am Chem Soc, 2017. **139**(28): p. 9471-9474.

211. Liu, B. and J. Liu, *Freezing-Driven DNA Adsorption on Gold Nanoparticles: Tolerating Extremely Low Salt Concentration but Requiring High DNA Concentration.* Langmuir, 2019. **35**(19): p. 6476-6482.

212. Vives, E., J. Schmidt, and A. Pelegrin, *Cell-penetrating and cell-targeting peptides in drug delivery.* Biochim Biophys Acta, 2008. **1786**(2): p. 126-38.

213. Hostetler, M.J., A.C. Templeton, and R.W. Murray, *Dynamics of place-exchange reactions on monolayer-protected gold cluster molecules.* Langmuir, 1999. **15**(11): p. 3782-3789.

214. Levy, R., et al., *Rational and combinatorial design of peptide capping Ligands for gold nanoparticles.* Journal of the American Chemical Society, 2004. **126**(32): p. 10076-10084.

215. Krpetic, Z., et al., *A Multidentate Peptide for Stabilization and Facile Bioconjugation of Gold Nanoparticles.* Bioconjugate Chemistry, 2009. **20**(3): p. 619-624.

216. Peng, L.H., et al., *TAT conjugated cationic noble metal nanoparticles for gene delivery to epidermal stem cells.* Biomaterials, 2014. **35**(21): p. 5605-5618.

217. Khamehchian, S., et al., *Enhanced and selective permeability of gold nanoparticles functionalized with cell penetrating peptide derived from maurocalcine animal toxin.* Journal of Biomedical Materials Research Part A, 2016. **104**(11): p. 2693-2700.

218. Boussoufi, F., et al., *Synthesis and study of cell-penetrating peptide- modified gold nanoparticles.* International Journal of Nanomedicine, 2018. **13**: p. 6199-6205.

219. Kumar, M., et al., *Insights into cell penetrating peptide conjugated gold nanoparticles for internalization into bacterial cells.* Biophysical Chemistry, 2018. **237**: p. 38-46.

220. Yan, X.X., et al., *Redox-Responsive Multifunctional Polypeptides Conjugated with Au Nanoparticles for Tumor-Targeting Gene Therapy and Their 1+1 > 2 Synergistic Effects.* Acs Biomaterials Science & Engineering, 2020. **6**(1): p. 463-473.

221. Xie, W., et al., *Nuclear Targeted Nanoprobe for Single Living Cell Detection by Surface-Enhanced Raman Scattering.* Bioconjugate Chemistry, 2009. **20**(4): p. 768-773.

222. Yi, G.S. and G.M. Chow, *Synthesis of hexagonal-phase NaYF4 : Yb,Er and NaYF4 : Yb,Tm nanocrystals with efficient up-conversion fluorescence.* Advanced Functional Materials, 2006. **16**(18): p. 2324-2329.

223. Kong, W., et al., *A General Strategy for Ligand Exchange on Upconversion Nanoparticles.* Inorg Chem, 2017. **56**(2): p. 872-877.

224. Duong, H.T.T., et al., *Systematic investigation of functional ligands for colloidal stable upconversion nanoparticles.* Rsc Advances, 2018. **8**(9): p. 4842-4849.

225. Jurga, N., et al., *Improvement of ligand-free modification strategy to obtain water-stable up-converting nanoparticles with bright emission and high reaction yield.* Sci Rep, 2021. **11**(1): p. 18846.

226. Buchner, M., et al., *Photosensitiser functionalised luminescent upconverting nanoparticles for efficient photodynamic therapy of breast cancer cells.* Photochem Photobiol Sci, 2019. **18**(1): p. 98-109.

227. Jin, J., et al., *Polymer-coated NaYF(4):Yb(3)(+), Er(3)(+) upconversion nanoparticles for charge-dependent cellular imaging.* ACS Nano, 2011. **5**(10): p. 7838-47.

228. Naccache, R., et al., *Controlled Synthesis and Water Dispersibility of Hexagonal Phase NaGdF4:Ho3+/Yb3+ Nanoparticles.* Chemistry of Materials, 2009. **21**(4): p. 717-723.

229. Xiong, L., et al., *Long-term in vivo biodistribution imaging and toxicity of polyacrylic acid-coated upconversion nanophosphors.* Biomaterials, 2010. **31**(27): p. 7078-85.

230. Shen, J., et al., *Engineering the Upconversion Nanoparticle Excitation Wavelength: Cascade Sensitization of Tri-doped Upconversion Colloidal Nanoparticles at 800 nm.* Advanced Optical Materials, 2013. **1**(9): p. 644-650.

231. Johnson, N.J., et al., *Facile ligand-exchange with polyvinylpyrrolidone and subsequent silica coating of hydrophobic upconverting beta-NaYF(4):Yb(3+)/Er(3+) nanoparticles.* Nanoscale, 2010. **2**(5): p. 771-7.

232. Johnson, N.J.J., et al., *Size-Tunable, Ultrasmall NaGdF4 Nanoparticles: Insights into Their T1 MRI Contrast Enhancement.* Chemistry of Materials, 2011. **23**(16): p. 3714-3722.

233. Bogdan, N., et al., *Carbohydrate-coated lanthanide-doped upconverting nanoparticles for lectin recognition.* Journal of Materials Chemistry, 2010. **20**(35): p. 7543-7550.

234. Liras, M., et al., *Thin Amphiphilic Polymer-Capped Upconversion Nanoparticles: Enhanced Emission and Thermoresponsive Properties.* Chemistry of Materials, 2014. **26**(13): p. 4014-4022.

235. Hermanson, G.T., *Bioconjugate Techniques, 3rd Edition.* Bioconjugate Techniques, 3rd Edition, 2013: p. 1-1146.

236. Seferos, D.S., et al., *Nano-flares: probes for transfection and mRNA detection in living cells.* J Am Chem Soc, 2007. **129**(50): p. 15477-9.

237. Prigodich, A.E., et al., *Nano-flares for mRNA regulation and detection.* ACS Nano, 2009. **3**(8): p. 2147-52.

238. Mokhtarzadeh, A., et al., *Applications of Spherical Nucleic Acid Nanoparticles as Delivery Systems.* Trends in Molecular Medicine, 2019. **25**(12): p. 1066-1079.

239. Pan, W., et al., *Multiplexed detection and imaging of intracellular mRNAs using a four-color nanoprobe.* Anal Chem, 2013. **85**(21): p. 10581-8.

240. Li, N., et al., *A Multicolor Nanoprobe for Detection and Imaging of Tumor-Related mRNAs in Living Cells (vol 51, pf 7426, 2012).* Angewandte Chemie-International Edition, 2012. **51**(44): p. 10922-10922.

241. Tyagi, S. and F.R. Kramer, *Molecular beacons: probes that fluoresce upon hybridization.* Nat Biotechnol, 1996. **14**(3): p. 303-8.

242. Sokol, D.L., et al., *Real time detection of DNA.RNA hybridization in living cells.* Proc Natl Acad Sci U S A, 1998. **95**(20): p. 11538-43.

243. Santangelo, P.J., et al., *Dual FRET molecular beacons for mRNA detection in living cells.* Nucleic Acids Res, 2004. **32**(6): p. e57.

244. Heuer-Jungemann, A., et al., *Gold nanoparticles and fluorescently-labelled DNA as a platform for biological sensing.* Nanoscale, 2013. **5**(20): p. 9503-10.

245. Narayan, S.P., et al., *The Sequence-Specific Cellular Uptake of Spherical Nucleic Acid Nanoparticle Conjugates.* Small, 2015. **11**(33): p. 4173-82.

246. Choi, C.H., et al., *Mechanism for the endocytosis of spherical nucleic acid nanoparticle conjugates.* Proc Natl Acad Sci U S A, 2013. **110**(19): p. 7625-30.

247. Song, W.C., et al., *Backbone-modified oligonucleotides for tuning the cellular uptake behaviour of spherical nucleic acids.* Biomaterials Science, 2017. **5**(3): p. 412-416.

248. Altieri, D.C., *Survivin, versatile modulation of cell division and apoptosis in cancer.* Oncogene, 2003. **22**(53): p. 8581-9.

249. Li, N., et al., *A tumour mRNA-triggered nanocarrier for multimodal cancer cell imaging and therapy.* Chem Commun (Camb), 2014. **50**(56): p. 7473-6.

250. Li, S., et al., *Precision Spherical Nucleic Acids Enable Sensitive FEN1 Imaging and Controllable Drug Delivery for Cancer-Specific Therapy.* Analytical Chemistry, 2021. **93**(32): p. 11275-11283.

251. Lee, J.M., et al., *The epithelial-mesenchymal transition: new insights in signaling, development, and disease.* J Cell Biol, 2006. **172**(7): p. 973-81.

252. Kalluri, R., *EMT: when epithelial cells decide to become mesenchymal-like cells.* J Clin Invest, 2009. **119**(6): p. 1417-9.

253. Lamouille, S., J. Xu, and R. Derynck, *Molecular mechanisms of epithelial-mesenchymal transition.* Nat Rev Mol Cell Biol, 2014. **15**(3): p. 178-96.

254. Kalluri, R. and R.A. Weinberg, *The basics of epithelial-mesenchymal transition.* J Clin Invest, 2009. **119**(6): p. 1420-8.

255. Zhang, Y. and R.A. Weinberg, *Epithelial-to-mesenchymal transition in cancer: complexity and opportunities.* Frontiers of Medicine, 2018. **12**(4): p. 361-373.

256. Yang, J., et al., *Guidelines and definitions for research on epithelial-mesenchymal transition.* Nat Rev Mol Cell Biol, 2020. **21**(6): p. 341-352.

257. Zeisberg, M. and E.G. Neilson, *Biomarkers for epithelial-mesenchymal transitions.* J Clin Invest, 2009. **119**(6): p. 1429-37.

258. Katsumoto, T., A. Mitsushima, and T. Kurimura, *The role of the vimentin intermediate filaments in rat 3Y1 cells elucidated by immunoelectron microscopy and computer-graphic reconstruction.* Biol Cell, 1990. **68**(2): p. 139-46.

259. Ivaska, J., et al., *Novel functions of vimentin in cell adhesion, migration, and signaling.* Exp Cell Res, 2007. **313**(10): p. 2050-62.

260. Satelli, A. and S. Li, *Vimentin in cancer and its potential as a molecular target for cancer therapy.* Cell Mol Life Sci, 2011. **68**(18): p. 3033-46.

261. Liu, C.Y., et al., *Vimentin contributes to epithelial-mesenchymal transition cancer cell mechanics by mediating cytoskeletal organization and focal adhesion maturation.* Oncotarget, 2015. **6**(18): p. 15966-83.

262. Arodin Selenius, L., et al., *The Cell Culture Medium Affects Growth, Phenotype Expression and the Response to Selenium Cytotoxicity in A549 and HepG2 Cells.* Antioxidants (Basel), 2019. **8**(5).

263. Qin, Y.F., et al., *DEHP-elicited small extracellular vesicles miR-26a-5p promoted metastasis in nearby normal A549 cells.* Environmental Pollution, 2021. **272**.

264. Raimondi, L., et al., *Potential Anti-Metastatic Role of the Novel miR-CT3 in Tumor Angiogenesis and Osteosarcoma Invasion.* Int J Mol Sci, 2022. **23**(2).

265. Dauphin, M., et al., *Vimentin expression predicts the occurrence of metastases in non small cell lung carcinomas.* Lung Cancer, 2013. **81**(1): p. 117-22.

266. Buccheri, G. and D. Ferrigno, *Lung tumor markers of cytokeratin origin: an overview.* Lung Cancer, 2001. **34 Suppl 2**: p. S65-9.

267. Karantza, V., *Keratins in health and cancer: more than mere epithelial cell markers.* Oncogene, 2011. **30**(2): p. 127-38.

268. John, C.L., et al., *Reproducibly synthesize gold nanorods and maintain their stability.* Rsc Advances, 2013. **3**(27): p. 10909-10918.

269. Kawamura, G., et al., *Shape control synthesis of multi-branched gold nanoparticles.* Materials Chemistry and Physics, 2009. **115**(1): p. 229-234.

270. Wang, F., R. Deng, and X. Liu, *Preparation of core-shell NaGdF4 nanoparticles doped with luminescent lanthanide ions to be used as upconversion-based probes.* Nat Protoc, 2014. **9**(7): p. 1634-44.

271. Bian, W., et al., *Direct Identification of Surface Defects and Their Influence on the Optical Characteristics of Upconversion Nanoparticles.* ACS Nano, 2018. **12**(4): p. 3623-3628.

272. Lin, W., et al., *Highly luminescent lead sulfide nanocrystals in organic solvents and water through ligand exchange with poly(acrylic acid).* Langmuir, 2008. **24**(15): p. 8215-9.

273. Lee, P.Y., et al., *Agarose gel electrophoresis for the separation of DNA fragments.* J Vis Exp, 2012(62).

274. Hanauer, M., et al., *Separation of nanoparticles by gel electrophoresis according to size and shape.* Nano Lett, 2007. **7**(9): p. 2881-5.

275. Stellwagen, N.C. and E. Stellwagen, *Effect of the matrix on DNA electrophoretic mobility.* J Chromatogr A, 2009. **1216**(10): p. 1917-29.

276. Liu, X., et al., *Extinction coefficient of gold nanoparticles with different sizes and different capping ligands.* Colloids Surf B Biointerfaces, 2007. **58**(1): p. 3-7.

277. Tataurov, A.V., Y. You, and R. Owczarzy, *Predicting ultraviolet spectrum of single stranded and double stranded deoxyribonucleic acids.* Biophys Chem, 2008. **133**(1-3): p. 66-70.

278. Cavaluzzi, M.J. and P.N. Borer, *Revised UV extinction coefficients for nucleoside-5'-monophosphates and unpaired DNA and RNA.* Nucleic Acids Res, 2004. **32**(1): p. e13.

279. Cho, E.C., et al., *Understanding the role of surface charges in cellular adsorption versus internalization by selectively removing gold nanoparticles on the cell surface with a I2/KI etchant.* Nano Lett, 2009. **9**(3): p. 1080-4.

280. Chen, C., et al., *Kinetics and thermodynamics of DNA hybridization on gold nanoparticles.* Nucleic Acids Res, 2009. **37**(11): p. 3756-65.

281. Al-Johani, H., et al., *The structure and binding mode of citrate in the stabilization of gold nanoparticles.* Nat Chem, 2017. **9**(9): p. 890-895.

282. Clayden, J., et al., *Organic Chemistry*

1st ed. 2001, New York: Oxford University Press. 1512.

283. Barreto, A., et al., *Behavior of colloidal gold nanoparticles in different ionic strength media.* Journal of Nanoparticle Research, 2015. **17**(12).

284. Schmid, G., et al., *LIGAND-STABILIZED BIMETALLIC COLLOIDS IDENTIFIED BY HRTEM AND EDX.* Angewandte Chemie-International Edition, 1991. **30**(7): p. 874-876.

285. Yon, M., et al., *Easy colorimetric detection of gadolinium ions based on gold nanoparticles: key role of phosphine-sulfonate ligands.* Nanoscale Advances, 2020. **2**(10): p. 4671-4681.

286. Loweth, C.J., et al., *DNA-Based Assembly of Gold Nanocrystals.* Angew Chem Int Ed Engl, 1999. **38**(12): p. 1808-1812.

287. Heuer-Jungemann, A., et al., *The Role of Ligands in the Chemical Synthesis and Applications of Inorganic Nanoparticles.* Chem Rev, 2019. **119**(8): p. 4819-4880.

288. Li, X., et al., *Localized surface plasmon resonance (LSPR) of polyelectrolyte-functionalized gold-nanoparticles for bio-sensing.* Colloids and Surfaces a-Physicochemical and Engineering Aspects, 2009. **332**(2-3): p. 172-179.

289. Jain, P.K., et al., *Calculated absorption and scattering properties of gold nanoparticles of different size, shape, and composition: applications in biological imaging and biomedicine.* J Phys Chem B, 2006. **110**(14): p. 7238-48.

290. Jain, P.K. and M.A. Ei-Sayed, *Surface plasmon resonance sensitivity of metal nanostructures: Physical basis and universal scaling in metal nanoshells.* Journal of Physical Chemistry C, 2007. **111**(47): p. 17451-17454.

291. Park, K., et al., *Growth Mechanism of Gold Nanorods.* Chemistry of Materials, 2013. **25**(4): p. 555-563.

292. Tong, W.M., et al., *Control of Symmetry Breaking Size and Aspect Ratio in Gold Nanorods: Underlying Role of Silver Nitrate.* Journal of Physical Chemistry C, 2017. **121**(6): p. 3549-3559.

293. Stefan Kooij, E. and B. Poelsema, *Shape and size effects in the optical properties of metallic nanorods.* Phys Chem Chem Phys, 2006. **8**(28): p. 3349-57.

294. Shenashen, M.A., S.A. El-Safty, and E.A. Elshehy, *Synthesis, Morphological Control, and Properties of Silver Nanoparticles in Potential Applications.* Part. Part. Syst. Char., 2014. **31**(3): p. 293-316.

295. Xia, Y., et al., *Shape-controlled synthesis of metal nanocrystals: simple chemistry meets complex physics?* Angew Chem Int Ed Engl, 2009. **48**(1): p. 60-103.

296. Huang, X.Y. and J. Lin, *Active-core/active-shell nanostructured design: an effective strategy to enhance Nd3+/Yb3+ cascade sensitized upconversion luminescence in lanthanide-doped nanoparticles.* Journal of Materials Chemistry C, 2015. **3**(29): p. 7652-7657.

297. Nie, Z.Y., et al., *NaYF4:Yb,Er,Nd@NaYF4:Nd Upconversion Nanocrystals Capped with Mn:TiO2 for 808 nm NIR-Triggered Photocatalytic Applications.* Journal of Physical Chemistry C, 2019. **123**(37): p. 22959-22970.

298. Lezhnina, M.M., et al., *Efficient luminescence from rare-earth fluoride nanoparticles with optically functional shells.* Advanced Functional Materials, 2006. **16**(7): p. 935-942.

299. Yi, G.S. and G.M. Chow, *Water-soluble NaYF4 : Yb,Er(Tm)/NaYF4/polymer core/shell/shell nanoparticles with significant enhancement of upconversion fluorescence.* Chemistry of Materials, 2007. **19**(3): p. 341-343.

300. Dong, C.H., et al., *Cation Exchange: A Facile Method To Make NaYF4:Yb,Tm-NaGdF4 Core-Shell Nanoparticles with a Thin, Tunable, and Uniform Shell.* Chemistry of Materials, 2012. **24**(7): p. 1297-1305.

301. Boyer, J.C., et al., *Synthesis, characterization, and spectroscopy of NaGdF4: Ce3+, Tb3+/NaYF4 core/shell nanoparticles.* Chemistry of Materials, 2007. **19**(14): p. 3358-3360.

302. Liu, S.B., et al., *Controlling upconversion in emerging multilayer core-shell nanostructures: from fundamentals to frontier applications.* Chemical Society Reviews, 2022. **51**(5): p. 1729-1765.

303. Fan, Y., L. Liu, and F. Zhang, *Exploiting lanthanide-doped upconversion nanoparticles with core/shell structures.* Nano Today, 2019. **25**: p. 68-84.

304. Elahi, N., M. Kamali, and M.H. Baghersad, *Recent biomedical applications of gold nanoparticles: A review.* Talanta, 2018. **184**: p. 537-556.

305. McNamara, K. and S.A.M. Tofail, *Nanoparticles in biomedical applications.* Advances in Physics-X, 2017. **2**(1): p. 54-88.

306. Li, F., et al., *Thermal Stability of DNA Functionalized Gold Nanoparticles.* Bioconjugate Chemistry, 2013. **24**(11): p. 1790-1797.

307. Pensa, E., et al., *The chemistry of the sulfur-gold interface: in search of a unified model.* Acc Chem Res, 2012. **45**(8): p. 1183-92.

308. Liu, B. and J.W. Liu, *Methods for preparing DNA-functionalized gold nanoparticles, a key reagent of bioanalytical chemistry.* Analytical Methods, 2017. **9**(18): p. 2633-2643.

309. Wang, C.C., et al., *Biomedical Applications of DNA-Conjugated Gold Nanoparticles.* Chembiochem, 2016. **17**(12): p. 1052-62.

310. Lahm, H., et al., *Live fluorescent RNA-based detection of pluripotency gene expression in embryonic and induced pluripotent stem cells of different species.* Stem Cells, 2015. **33**(2): p. 392-402.

311. Wang, Z., et al., *Bioinspired nanocomplex for spatiotemporal imaging of sequential mRNA expression in differentiating neural stem cells.* ACS Nano, 2014. **8**(12): p. 12386-96.

312. Vilela, P., et al., *Sensing of Vimentin mRNA in 2D and 3D Models of Wounded Skin Using DNA-Coated Gold Nanoparticles.* Small, 2018. **14**(12): p. e1703489.

313. Kyriazi, M.E., et al., *Multiplexed mRNA Sensing and Combinatorial-Targeted Drug Delivery Using DNA-Gold Nanoparticle Dimers.* ACS Nano, 2018. **12**(4): p. 3333-3340.

314. Xu, J., et al., *Potential mechanisms underlying the Runx2 induced osteogenesis of bone marrow mesenchymal stem cells.* Am J Transl Res, 2015. **7**(12): p. 2527-35.

315. Dalle Carbonare, L., G. Innamorati, and M.T. Valenti, *Transcription factor Runx2 and its application to bone tissue engineering.* Stem Cell Rev Rep, 2012. **8**(3): p. 891-7.

316. Lucero, C.M., et al., *The cancer-related transcription factor Runx2 modulates cell proliferation in human osteosarcoma cell lines.* J Cell Physiol, 2013. **228**(4): p. 714-23.

317. Stein, G.S., et al., *Runx2 control of organization, assembly and activity of the regulatory machinery for skeletal gene expression.* Oncogene, 2004. **23**(24): p. 4315-29.

318. Fitter, S., et al., *The Mesenchymal Precursor Cell Marker Antibody STRO-1 Binds to Cell Surface Heat Shock Cognate 70.* Stem Cells, 2017. **35**(4): p. 940-951.

319. Gothard, D., et al., *Regionally-derived cell populations and skeletal stem cells from human foetal femora exhibit specific osteochondral and multi-lineage differentiation capacity in vitro and ex vivo.* Stem Cell Res Ther, 2015. **6**: p. 251.

320. Xavier, M., R.O.C. Oreffo, and H. Morgan, *Skeletal stem cell isolation: A review on the state-of-the-art microfluidic label-free sorting techniques.* Biotechnol Adv, 2016. **34**(5): p. 908-923.

321. Ambrosi, T.H., M.T. Longaker, and C.K.F. Chan, *A Revised Perspective of Skeletal Stem Cell Biology.* Front Cell Dev Biol, 2019. **7**: p. 189.

322. Cutler, J.I., E. Auyeung, and C.A. Mirkin, *Spherical Nucleic Acids.* J. Am. Chem. Soc., 2012. **134**(3): p. 1376-1391.

323. Pellegrino, T., et al., *Gel electrophoresis of gold-DNA nanoconjugates.* J Biomed Biotechnol, 2007. **2007**: p. 26796.

324. Mergny, J.L., et al., *Fluorescence energy transfer as a probe for nucleic acid structures and sequences.* Nucleic Acids Res, 1994. **22**(6): p. 920-8.

325. Junowicz, E. and J.H. Spencer, *Studies on bovine pancreatic deoxyribonuclease A. II. The effect of different bivalent metals on the specificity of degradation of DNA.* Biochim Biophys Acta, 1973. **312**(1): p. 85-102.

326. Suck, D., *DNA recognition by structure-selective nucleases.* Biopolymers, 1997. **44**(4): p. 405-21.

327. Rittie, L. and B. Perbal, *Enzymes used in molecular biology: a useful guide.* J Cell Commun Signal, 2008. **2**(1-2): p. 25-45.

328. Zheng, D., et al., *Aptamer nano-flares for molecular detection in living cells.* Nano Lett, 2009. **9**(9): p. 3258-61.

329. Barnaby, S.N., et al., *Design Considerations for RNA Spherical Nucleic Acids (SNAs).* Bioconjug Chem, 2016. **27**(9): p. 2124-31.

330. Wu, X.A., et al., *Intracellular fate of spherical nucleic acid nanoparticle conjugates.* J Am Chem Soc, 2014. **136**(21): p. 7726-33.

331. Hassan, H.T. and M. El-Sheemy, *Adult bone-marrow stem cells and their potential in medicine.* J R Soc Med, 2004. **97**(10): p. 465-71.

332. Bonnet, D., *Biology of human bone marrow stem cells.* Clin Exp Med, 2003. **3**(3): p. 140-9.

333. Birbrair, A. and P.S. Frenette, *Niche heterogeneity in the bone marrow.* Ann N Y Acad Sci, 2016. **1370**(1): p. 82-96.

334. Bianco, P., *Stem cells and bone: a historical perspective.* Bone, 2015. **70**: p. 2-9.

335. Bianco, P. and P.G. Robey, *Skeletal stem cells.* Development, 2015. **142**(6): p. 1023-7.

336. Jones, E. and D. McGonagle, *Human bone marrow mesenchymal stem cells in vivo.* Rheumatology (Oxford), 2008. **47**(2): p. 126-31.

337. Bianco, P., et al., *The meaning, the sense and the significance: translating the science of mesenchymal stem cells into medicine.* Nat Med, 2013. **19**(1): p. 35-42.

338. Pan, J. and J. Wan, *Methodological comparison of FACS and MACS isolation of enriched microglia and astrocytes from mouse brain.* J Immunol Methods, 2020. **486**: p. 112834.

339. Shi, S. and S. Gronthos, *Perivascular niche of postnatal mesenchymal stem cells in human bone marrow and dental pulp.* J Bone Miner Res, 2003. **18**(4): p. 696-704.

340. Friedenstein, A.J., et al., *Stromal cells responsible for transferring the microenvironment of the hemopoietic tissues. Cloning in vitro and retransplantation in vivo.* Transplantation, 1974. **17**(4): p. 331-40.

341. Xavier, M., et al., *Size and dielectric properties of skeletal stem cells change critically after enrichment and expansion from human bone marrow: consequences for microfluidic cell sorting.* J R Soc Interface, 2017. **14**(133).

342. Janeczek, A.A., et al., *Transient Canonical Wnt Stimulation Enriches Human Bone Marrow Mononuclear Cell Isolates for Osteoprogenitors.* Stem Cells, 2016. **34**(2): p. 418-30.

343. Patel, P.C., et al., *Peptide antisense nanoparticles.* Proc Natl Acad Sci U S A, 2008. **105**(45): p. 17222-6.

344. Tkachenko, A.G., et al., *Cellular trajectories of peptide-modified gold particle complexes: comparison of nuclear localization signals and peptide transduction domains.* Bioconjug Chem, 2004. **15**(3): p. 482-90.

345. Yang, C., M. Neshatian, and M. van Prooijen, *Cancer nanotechnology: enhanced therapeutic response using peptide-modified gold nanoparticles.* J Nanosci Nanotechnol, 2014. **14**(7): p. 4813-9.

346. Nativo, P., I.A. Prior, and M. Brust, *Uptake and intracellular fate of surface-modified gold nanoparticles.* ACS Nano, 2008. **2**(8): p. 1639-44.

347. Fernandez, D.I., et al., *The antimicrobial peptide aurein 1.2 disrupts model membranes via the carpet mechanism.* Phys Chem Chem Phys, 2012. **14**(45): p. 15739-51.

348. Apponyi, M.A., et al., *Host-defence peptides of Australian anurans: structure, mechanism of action and evolutionary significance.* Peptides, 2004. **25**(6): p. 1035-54.

349. Howell, W.M., *Detection of DNA hybridization using induced fluorescence resonance energy transfer.* Methods in Molecular Biology, 2006. **335**: p. 33-41.

350. Bae, W., T.Y. Yoon, and C. Jeong, *Direct evaluation of self-quenching behavior of fluorophores at high concentrations using an evanescent field.* PLoS One, 2021. **16**(2): p. e0247326.

351. Maraming, P., J. Daduang, and J.C.Y. Kah, *Conjugation with gold nanoparticles improves the stability of the KT2 peptide and maintains its anticancer properties.* Rsc Advances, 2021. **12**(1): p. 319-325.

352. Casciaro, B., et al., *Gold-nanoparticles coated with the antimicrobial peptide esculentin-1a(1-21)NH2 as a reliable strategy for antipseudomonal drugs.* Acta Biomater, 2017. **47**: p. 170-181.

353. Gilleron, J., et al., *Image-based analysis of lipid nanoparticle-mediated siRNA delivery, intracellular trafficking and endosomal escape.* Nat Biotechnol, 2013. **31**(7): p. 638-46.

354. Blanco, E., H. Shen, and M. Ferrari, *Principles of nanoparticle design for overcoming biological barriers to drug delivery.* Nat Biotechnol, 2015. **33**(9): p. 941-51.

355. Wang, J., *DNA biosensors based on peptide nucleic acid (PNA) recognition layers. A review.* Biosens Bioelectron, 1998. **13**(7-8): p. 757-62.

356. Leatherbarrow, R.J. and P.R. Edwards, *Analysis of molecular recognition using optical biosensors.* Current Opinion in Chemical Biology, 1999. **3**(5): p. 544-547.

357. Akyilmaz, E., E. Yorganci, and E. Asav, *Do copper ions activate tyrosinase enzyme? A biosensor model for the solution.* Bioelectrochemistry, 2010. **78**(2): p. 155-60.

358. Soraya, G.V., et al., *An interdigitated electrode biosensor platform for rapid HLA-B*15:02 genotyping for prevention of drug hypersensitivity.* Biosens Bioelectron, 2018. **111**: p. 174-183.

359. Wang, J., et al., *DNA electrochemical biosensors for environmental monitoring. A review.* Analytica Chimica Acta, 1997. **347**(1-2): p. 1-8.

360. Mishra, G.K., et al., *Food Safety Analysis Using Electrochemical Biosensors.* Foods, 2018. **7**(9).

361. Alonso-Cristobal, P., et al., *Highly Sensitive DNA Sensor Based on Upconversion Nanoparticles and Graphene Oxide.* ACS Appl Mater Interfaces, 2015. **7**(23): p. 12422-9.

362. Vilela, P., et al., *Graphene Oxide-Upconversion Nanoparticle Based Optical Sensors for Targeted Detection of mRNA Biomarkers Present in Alzheimer's Disease and Prostate Cancer.* ACS Sens, 2017. **2**(1): p. 52-56.

363. Blair, E.O. and D.K. Corrigan, *A review of microfabricated electrochemical biosensors for DNA detection.* Biosens Bioelectron, 2019. **134**: p. 57-67.

364. Mehrvar, M. and M. Abdi, *Recent developments, characteristics, and potential applications of electrochemical biosensors.* Anal Sci, 2004. **20**(8): p. 1113-26.

365. Matharu, Z., et al., *Nanoporous-Gold-Based Electrode Morphology Libraries for Investigating Structure-Property Relationships in Nucleic Acid Based Electrochemical Biosensors.* ACS Appl Mater Interfaces, 2017. **9**(15): p. 12959-12966.

366. Garcia, T., et al., *Disposable DNA biosensor based on thin-film gold electrodes for selective Salmonella detection.* Sensors and Actuators B-Chemical, 2012. **161**(1): p. 1030-1037.

367. Lange, K., B.E. Rapp, and M. Rapp, *Surface acoustic wave biosensors: a review.* Anal Bioanal Chem, 2008. **391**(5): p. 1509-19.

368. Ten, S.T., et al., *Highly sensitive Escherichia coli shear horizontal surface acoustic wave biosensor with silicon dioxide nanostructures.* Biosens Bioelectron, 2017. **93**: p. 146-154.

369. Zhang, Y., et al., *A surface acoustic wave biosensor synergizing DNA-mediated in situ silver nanoparticle growth for a highly specific and signal-amplified nucleic acid assay.* Analyst, 2017. **142**(18): p. 3468-3476.

370. Afzal, A., et al., *Gravimetric Viral Diagnostics: QCM Based Biosensors for Early Detection of Viruses.* Chemosensors, 2017. **5**(1).

371. Damborsky, P., J. Svitel, and J. Katrlik, *Optical biosensors.* Essays Biochem, 2016. **60**(1): p. 91-100.

372. Dey, D. and T. Goswami, *Optical biosensors: a revolution towards quantum nanoscale electronics device fabrication.* J Biomed Biotechnol, 2011. **2011**: p. 348218.

373. Shin, Y., A.P. Perera, and M.K. Park, *Label-free DNA sensor for detection of bladder cancer biomarkers in urine.* Sensors and Actuators B-Chemical, 2013. **178**: p. 200-206.

374. Petty, J.T., et al., *DNA-Templated Molecular Silver Fluorophores.* J Phys Chem Lett, 2013. **4**(7): p. 1148-1155.

375. Nguyen, H.H., et al., *Surface plasmon resonance: a versatile technique for biosensor applications.* Sensors (Basel), 2015. **15**(5): p. 10481-510.

376. Patil, P.O., et al., *Graphene-based nanocomposites for sensitivity enhancement of surface plasmon resonance sensor for biological and chemical sensing: A review.* Biosens Bioelectron, 2019. **139**: p. 111324.

377. Shi, J., et al., *Nanoparticle based fluorescence resonance energy transfer (FRET) for biosensing applications.* J Mater Chem B, 2015. **3**(35): p. 6989-7005.

378. Schuster, J., J. Brabandt, and C. von Borczyskowski, *Discrimination of photoblinking and photobleaching on the single molecule level.* Journal of Luminescence, 2007. **127**(1): p. 224-229.

379. Frangioni, J.V., *In vivo near-infrared fluorescence imaging.* Curr Opin Chem Biol, 2003. **7**(5): p. 626-34.

380. Smith, A.M., M.C. Mancini, and S. Nie, *Bioimaging: second window for in vivo imaging.* Nat Nanotechnol, 2009. **4**(11): p. 710-1.

381. Binnemans, K., *Lanthanide-based luminescent hybrid materials.* Chem Rev, 2009. **109**(9): p. 4283-374.

382. Wang, X., et al., *Dye-sensitized lanthanide-doped upconversion nanoparticles.* Chem Soc Rev, 2017. **46**(14): p. 4150-4167.

383. Wang, Y.F., et al., *Nd(3+)-sensitized upconversion nanophosphors: efficient in vivo bioimaging probes with minimized heating effect.* ACS Nano, 2013. **7**(8): p. 7200-6.

384. Liu, J., et al., *Ultrasensitive nanosensors based on upconversion nanoparticles for selective hypoxia imaging in vivo upon near-infrared excitation.* J Am Chem Soc, 2014. **136**(27): p. 9701-9.

385. Chen, Z., et al., *Versatile synthesis strategy for carboxylic acid-functionalized upconverting nanophosphors as biological labels.* J Am Chem Soc, 2008. **130**(10): p. 3023-9.

386. Forster, T., *Energy migration and fluorescence.* Journal of Biomedical Optics, 2012. **17**(1).

387. Clegg, R.M., *Forster resonance energy transfer-FRET what is it, why do it, and how it's done.* Fret and Flim Techniques, 2009. **33**: p. 1-57.

388. Ray, P.C., et al., *Nanoscopic optical rulers beyond the FRET distance limit: fundamentals and applications.* Chemical Society Reviews, 2014. **43**(17): p. 6370-6404.

389. Omary, M.A. and H.H. Patterson, *Luminescence, Theory.* Encyclopedia of Spectroscopy and Spectrometry, 3rd Edition, Vol 2: G-M, 2017: p. 636-653.

390. Zhang, C., et al., *Rare earth upconversion nanophosphors: synthesis, functionalization and application as biolabels and energy transfer donors.* Journal of Rare Earths, 2010. **28**(6): p. 807-819.

391. Scholes, G.D. and K.P. Ghiggino, *RATE EXPRESSIONS FOR EXCITATION TRANSFER .1. RADIATIONLESS TRANSITION THEORY PERSPECTIVE.* Journal of Chemical Physics, 1994. **101**(2): p. 1251-1261.

392. Sisamakis, E., et al., *Accurate Single-Molecule Fret Studies Using Multiparameter Fluorescence Detection.* Methods in Enzymology, Vol 475: Single Molecule Tools, Pt B, 2010. **475**: p. 455-514.

393. Mendez-Gonzalez, D., et al., *Contribution of resonance energy transfer to the luminescence quenching of upconversion nanoparticles with graphene oxide.* J Colloid Interface Sci, 2020. **575**: p. 119-129.

394. Liu, C., et al., *Efficient fluorescence resonance energy transfer between upconversion nanophosphors and graphene oxide: a highly sensitive biosensing platform.* Chem Commun (Camb), 2011. **47**(16): p. 4661-3.

395. Huang, Y., et al., *A novel single-layered MoS2 nanosheet based microfluidic biosensor for ultrasensitive detection of DNA.* Nanoscale, 2015. **7**(6): p. 2245-9.

396. Wu, M., et al., *Adsorption and desorption of DNA on graphene oxide studied by fluorescently labeled oligonucleotides.* Langmuir, 2011. **27**(6): p. 2731-8.

397. Zhang, C., et al., *Biosensing platform based on fluorescence resonance energy transfer from upconverting nanocrystals to graphene oxide.* Angew Chem Int Ed Engl, 2011. **50**(30): p. 6851-4.

398. Huang, L.J., et al., *A turn-on upconversion fluorescence resonance energy transfer biosensor for ultrasensitive endonuclease detection.* Analytical Methods, 2015. **7**(18): p. 7474-7479.

399. Wang, F.F., et al., *Upconversion nanoparticles-MoS2 nanoassembly as a fluorescent turn-on probe for bioimaging of reactive oxygen species in living cells and zebrafish.* Sensors and Actuators B-Chemical, 2018. **274**: p. 180-187.

400. Lv, J., et al., *Upconversion nanoparticles grafted molybdenum disulfide nanosheets platform for microcystin-LR sensing.* Biosens Bioelectron, 2017. **90**: p. 203-209.

401. Lu, C., et al., *Comparison of MoS2, WS2, and Graphene Oxide for DNA Adsorption and Sensing.* Langmuir, 2017. **33**(2): p. 630-637.

402. Zhao, L.J., et al., *Interface interaction of MoS2 nanosheets with DNA based aptameric biosensor for carbohydrate antigen 15-3 detection.* Microchemical Journal, 2020. **155**.

403. Kenry, et al., *Highly Sensitive and Selective Aptamer-Based Fluorescence Detection of a Malarial Biomarker Using Single-Layer MoS2 Nanosheets.* Acs Sensors, 2016. **1**(11): p. 1315-1321.

404. Yuan, Y., H. Yu, and Y. Yin, *A highly sensitive aptasensor for vascular endothelial growth factor based on fluorescence resonance energy transfer from upconversion nanoparticles to MoS2 nanosheets.* Anal Methods, 2020. **12**(36): p. 4466-4472.

405. Swelum, A.A., et al., *COVID-19 in Human, Animal, and Environment: A Review.* Front Vet Sci, 2020. **7**: p. 578.

406. Crozier, A., et al., *Put to the test: use of rapid testing technologies for covid-19.* BMJ, 2021. **372**: p. n208.

407. Mardian, Y., et al., *Review of Current COVID-19 Diagnostics and Opportunities for Further Development.* Front Med (Lausanne), 2021. **8**: p. 615099.

408. Mertens, P., et al., *Development and Potential Usefulness of the COVID-19 Ag Respi-Strip Diagnostic Assay in a Pandemic Context.* Front Med (Lausanne), 2020. **7**: p. 225.

409. Wang, W., et al., *Two-dimensional material-based virus detection.* Sci China Chem, 2022: p. 1-17.

410. Chen, W.Y., et al., *DNA-Functionalized Ti3C2Tx MXenes for Selective and Rapid Detection of SARS-CoV-2 Nucleocapsid Gene.* Acs Applied Nano Materials, 2021.

411. Seo, G., et al., *Correction to Rapid Detection of COVID-19 Causative Virus (SARS-CoV-2) in Human Nasopharyngeal Swab Specimens Using Field-Effect Transistor-Based Biosensor.* ACS Nano, 2020. **14**(9): p. 12257-12258.

412. Fathi-Hafshejani, P., et al., *Two-Dimensional-Material-Based Field-Effect Transistor Biosensor for Detecting COVID-19 Virus (SARS-CoV-2).* ACS Nano, 2021. **15**(7): p. 11461-11469.

413. Ju, Q., et al., *An upconversion nanoprobe operating in the first biological window.* J Mater Chem B, 2015. **3**(17): p. 3548-3555.

414. Liu, Y., et al., *Affinity binding-mediated fluorometric protein assay based on the use of target-triggered DNA assembling probes and aptamers labelled with upconversion nanoparticles: application to the determination of platelet derived growth factor-BB.* Mikrochim Acta, 2019. **187**(1): p. 9.

415. Gand, M., et al., *Use of Whole Genome Sequencing Data for a First in Silico Specificity Evaluation of the RT-qPCR Assays Used for SARS-CoV-2 Detection.* Int J Mol Sci, 2020. **21**(15).

416. Chan, J.F., et al., *Improved Molecular Diagnosis of COVID-19 by the Novel, Highly Sensitive and Specific COVID-19-RdRp/Hel Real-Time Reverse Transcription-PCR Assay Validated In Vitro and with Clinical Specimens.* J Clin Microbiol, 2020. **58**(5).

417. Cho, H., et al., *Positive control synthesis method for COVID-19 diagnosis by one-step real-time RT-PCR.* Clin Chim Acta, 2020. **511**: p. 149-153.

418. Dumcenco, D., et al., *Large-Area Epitaxial Monolayer MoS2.* ACS Nano, 2015. **9**(4): p. 4611-20.

419. Dong, N., et al., *Optical Limiting and Theoretical Modelling of Layered Transition Metal Dichalcogenide Nanosheets.* Sci Rep, 2015. **5**: p. 14646.

420. Mishra, A.K., K.V. Lakshmi, and L. Huang, *Eco-friendly synthesis of metal dichalcogenides nanosheets and their environmental remediation potential driven by visible light.* Sci Rep, 2015. **5**: p. 15718.

421. V'Kovski, P., et al., *Coronavirus biology and replication: implications for SARS-CoV-2.* Nat Rev Microbiol, 2021. **19**(3): p. 155-170.

422. Ciplak, Z., N. Yildiz, and A. Calimli, *Investigation of Graphene/Ag Nanocomposites Synthesis Parameters for Two Different Synthesis Methods.* Fullerenes Nanotubes and Carbon Nanostructures, 2015. **23**(4): p. 361-370.

423. Neema, P.M., A.M. Tomy, and J. Cyriac, *Chemical sensor platforms based on fluorescence resonance energy transfer (FRET) and 2D materials.* Trac-Trends in Analytical Chemistry, 2020. **124**.

424. Arai, M.S. and A.S.S. de Camargo, *Exploring the use of upconversion nanoparticles in chemical and biological sensors: from surface modifications to point-of-care devices.* Nanoscale Advances, 2021. **3**(18): p. 5135-+.

425. Hu, Y.L., et al., *Two-dimensional transition metal dichalcogenide nanomaterials for biosensing applications.* Materials Chemistry Frontiers, 2017. **1**(1): p. 24-36.

426. Altman, D.G. and J.M. Bland, *Standard deviations and standard errors.* BMJ, 2005. **331**(7521): p. 903.

427. Mackenzie, L.E., et al., *The theoretical molecular weight of NaYF4: RE upconversion nanoparticles.* Scientific Reports, 2018. **8**.

428. Bao, G.C., et al., *Enhancing Hybrid Upconversion Nanosystems via Synergistic Effects of Moiety Engineered NIR Dyes.* Nano Letters, 2021. **21**(23): p. 9862-9868.